# THE RELATIONSHIP BETWEEN ORDERED INTERMETALLIC NANOPARTICLE SYNTHESIS AND THE BULK PHASE DIAGRAM

A Dissertation

Presented to the Faculty of the Graduate School

of Cornell University

In Partial Fulfillment of the Requirements for the Degree of

Doctor of Philosophy

by

Douglas York DeSario

AUGUST 2014

# THE RELATIONSHIP BETWEEN ORDERED INTERMETALLIC NANOPARTICLE SYNTHESIS AND THE BULK PHASE DIAGRAM

Douglas York DeSario, Ph. D.

Cornell University 2014

In this thesis, a surfactant-free synthesis of binary and ternary metal nanoparticles via co-reduction of metal chloride precursors is used to investigate the relationship between the bulk phase diagram and the formation of ordered intermetallic structures. The majority of the synthesized phases are binary materials of the formula Pt-M (M = Sn, Sb, In, Bi), because of their propensity to form single-phase regions with very narrow phase widths, known as "line phases". These line phases are thermodynamically stable according to the bulk phase diagram; however, the relationship between bulk stability and stability in the nanoparticle regime - and the implications for nanoparticle growth and ordering behavior - have not been fully explored. The 1:1 Pt-Sn phase (PtSn) forms ordered intermetallic nanoparticles with small domain sizes (4.3 nm) at room temperature, without any thermal annealing required. $Pt_3Sn$ similarly orders at low temperature (200 $^oC$), in contrast to the three Pt-rich line phases, all of which require higher annealing temperatures to form the intermetallic phase. Other Pt-M phases show varying degrees of ordering, but none are observed to have the same low-temperature ordering as the Pt-rich Pt-Sn phases. This behavior is extremely rare, with only one other phase to our knowledge (Pt-Bi) forming the intermetallic without annealing, and only under specific conditions. It is possible to make qualitative statements concerning which phases should easily order and form phase-pure products; however, in order to more quantitatively predict these

patterns, a multivariate analysis utilizing many physical properties (e.g., melting point, whether a phase melts congruently or incongruently, crystal structure, etc) was conducted. Using principal components analysis, partial least squares regression, and logistic regression techniques, a model was constructed to determine which properties would be most predictive of phases that were able to be synthesized as pure ordered intermetallics.

## BIOGRAPHICAL SKETCH

Douglas York DeSario was born on October 13, 1987, in New Jersey, where he lived throughout his childhood and high school years. In high school, he found a mentor in Ms. Georgia Muhs, his AP Chemistry teacher, who encouraged him to pursue chemistry and to apply to her alma mater, the University of Delaware. He enrolled at the UDel in 2005, where he was introduced to college-level general chemistry by Prof. Burnaby Munson. Douglas had enrolled as a chemistry major, but Prof. Munson's "study breaks", unorthodox laboratory demonstrations, and frequent urgings to "just go do it," solidified his desire to be a chemist. In sophomore year, Douglas met his friend and future wife Marianna Lios DeSario. He also opted out of a second semester of organic chemistry laboratory in favor of becoming an undergraduate research assistant in organic chemistry. After initially deciding to spend a summer at Delaware continuing his research, Douglas unexpectedly received a callback from Merck & Co. to join in an 8-week internship program at their campus in West Point, PA. Having always wanted to eventually work in industry, Douglas accepted, and spent that summer working in the Quality Assurance department, updating the API database and assisting with internal audits. The following year, Douglas was invited back to Merck - this time to Rahway, NJ - to research alternative detectors for HPLC. By this point, Douglas had also begun his undergraduate thesis research on the multivariate analysis of the fluorescence decay of 3-hydroxyflavone under Prof. Sharon Neal at Delaware. Douglas graduated from the University of Delaware Magna Cum Laude with a Bachelor's of Science in Chemistry in 2009, and that summer moved to Ithaca, NY to attend Cornell University. He joined Prof. Frank DiSalvo's research group, primarily out of his desire to work on alternative energy sources and energy efficiency. Though he has moved from analytical to synthetic inorganic chemistry, he has never lost his interest in computational methods and programming.

ACKNOWLEDGMENTS

I would first like to thank my group, and especially my advisor Prof. Frank DiSalvo. In my biographical sketch, I mentioned that I joined the DiSalvo group out of a desire to work on energy materials, which is true, but my conversations with Prof. DiSalvo during visiting weekends and my first semester here played just as large a role in my decision, and even in my decision to come to Cornell. I had never before met a man who is so happy to sit and discuss literally anything that you happen to have an interest in. Thank you for your support throughout the years, it has truly been invaluable, particularly while writing this dissertation. Additionally, I would like to thank the other members of my committee - Prof. Hector Abruña and Prof. Richard Robinson - for their experience and guidance.

To the rest of my group, most of whom are long graduated, thank you as well for your help, your advice, your time, and your friendship. In particular, I would like to thank Dr. Brian Leonard for originally teaching a clueless first year how to work in a glove box and perform the syntheses that form the basis of my research, Drs. Hao Chen and Minh Nguyen for developing the synthetic technique, Dr. Minghui Yang for his explanations of Rietveld analysis, Dr. Zhiming Cui for his help with in-house electrochemistry, and Dr. Raymond Burns, Dr. Chinmayee Subban, and Ryo Wakabayashi for their good advice on everything to do with graduate school, safety, and research in general. Lastly, to the members of the group who helped synthesize some of the phases present in this work - Amy Frankhouser, Weitian Zhao, and Daniel Marshall - thank you very much for all of your efforts, they have made an enormous difference.

There are so many groups and individuals at Cornell who have contributed directly or

indirectly to this work. In no particular order, I would like to thank Yingchao Yu for his help with HAADF and HRTEM images and analysis (supported by the DOE Energy Frontiers Research Center, Grant DE-SC0001086); Mick Thomas and John Grazul for teaching me how to take microscopy images and for managing the Cornell Center for Materials Research Shared Experimental Facilities (partially supported through the NSF MRSEC program, DMR-0520404 and DMR-1120296); Deniz Gunceler for the J-DFT collaboration; Ivan Keresztes for figuring out how to make $^{119}$Sn NMR work; and all of the members and administrators of the Energy Materials Center at Cornell ($EMC^2$). This work was supported by the Basic Energy Sciences Division of the Department of Energy through Grant DE-FG02-87ER45298.

The multivariate analyses presented in Chapter 5 are the direct result of my exposure to similar mathematical and computational techniques as an undergraduate at the University of Delaware. In particular, I would like to thank my advisor, Prof. Sharon Neal; the graduate student who taught me the generalized rank annihilation method and how to use Matlab in general, Dr. Carol Roach; and Prof. Steven Brown, whose Chemometrics course made me truly value Matlab, and whose M-files were frequently referenced while writing this dissertation. Special thanks to Julie Nevins for consultations on proper methods of analysis and regression.

Lastly, I would like to thank my wonderful wife Marianna for all of her love, kindness, support, and understanding over the years. I am so happy in my life with you. Last time I wrote about you in an acknowledgments section, I asked if you were ready to do it all over again. Well, you were. I don't even feel the need to ask this time; I am just looking forward to the next chapter of our lives together.

TABLE OF CONTENTS

# CHAPTER 1

# INTRODUCTION

## *1.1 Energy and Fuel Cells*

### *1.1.1 Growing Needs and Potential Solutions*

To begin with the most basic and uncontroversial of facts, the global demand for energy is increasing[1,2], as shown in Figure 1.1. Economics, environmental science, and politics all indicate that the current situation with regards to energy is untenable in the long term[3,4]. It is not within the scope of this dissertation to prove the necessity of updating energy production and infrastructure to meet increased demand; from whichever perspective the reader chooses to view the issue, the benefits of decreased utilization of fossil fuels and increased energy efficiency in general are evident.

The first and most direct avenue by which we can reduce the consumption of non-renewable energy is the development of new sources of power. These encompass solar, wind, geothermal, tidal, biofuel generation, and other renewables. The second method is by improving the efficiency of our current technologies, or replacing them with new and more efficient technologies. Fuel cells exist under the latter heading.

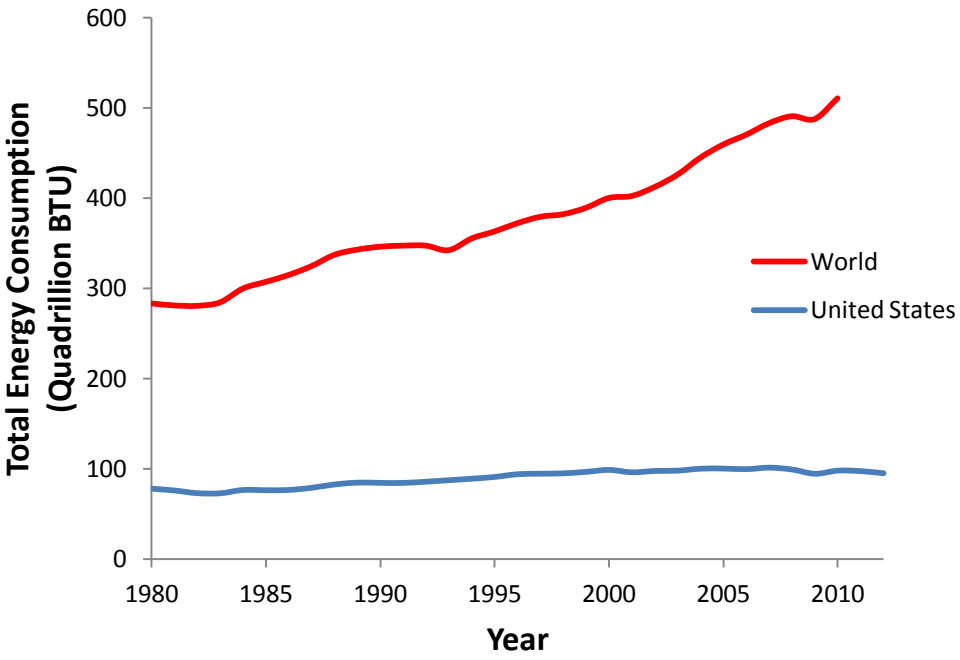


**Figure 1.1 -** Total global energy consumption (red) over the past three decades, compared to US energy consumption (blue). Global consumption grew 80% from 1980 to 2010, whereas US consumption remained relatively constant (and decreased on a per-capita basis). Adapted from data from the US Energy Information Administration[1].

Fuel cells are not energy sources, rather they are energy conversion devices; they require a fuel to operate. Fuel cells share similar characteristics with batteries. They are capable of directly transforming the stored chemical energy of molecular bonds into electrical energy through redox reactions. Both have two electrodes – a negative anode and a positive cathode. These basic cells can be "stacked" in series to increase the voltage of a power pack, or connected in parallel to increase the current output of the power pack. Most batteries have chemical "fuels" (reactants) included within the battery container. Secondary (rechargeable) batteries can regenerate the reactants inside the cell when external power is applied. In contrast, fuel cells store the fuel externally, though one type of battery - flow batteries - also stores the fuel outside the battery.

The largest difference between batteries and fuel cells is the need for catalysts in the latter. One highly promising type of fuel cell is a polymer electrolyte membrane fuel cell (PEMFC) that uses hydrogen gas as the fuel and oxygen gas from air as the oxidizing agent. This system will be used to illustrate the fundamental principles common to fuel cells in general.

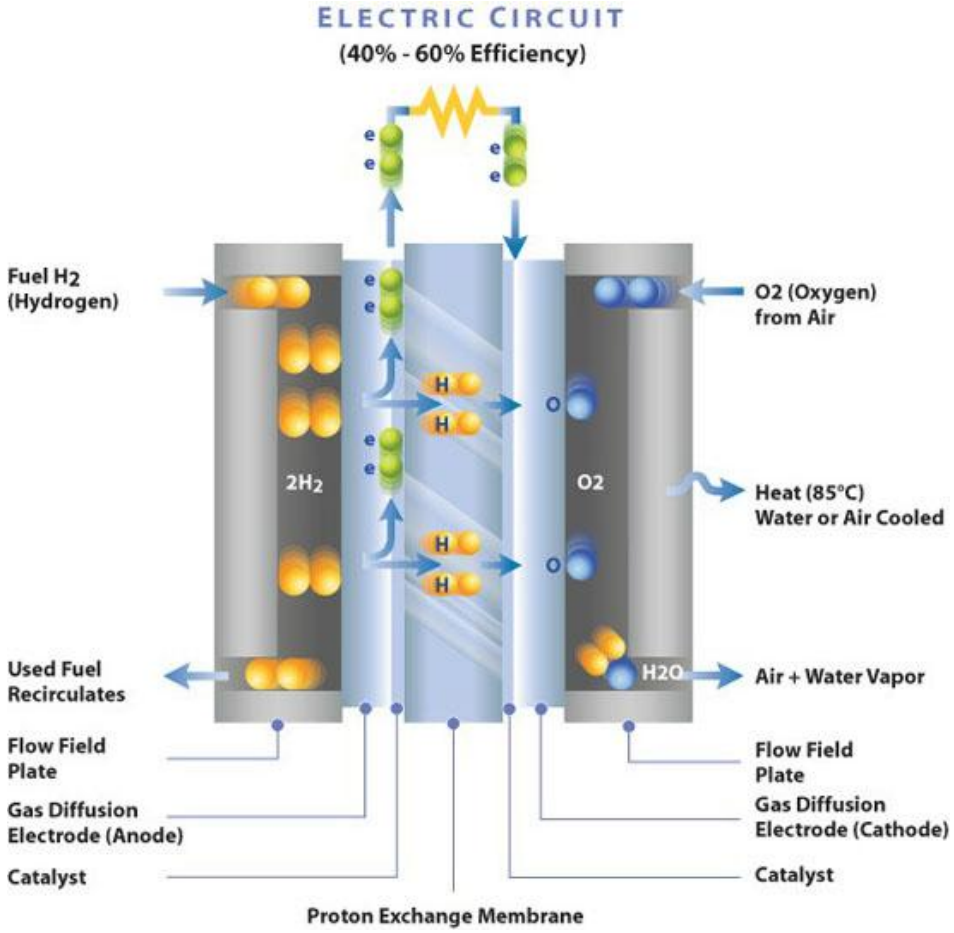


**Figure 1.2** Schematic of a model polymer electrolyte membrane fuel cell. Taken from Ballard[5].

A model PEMFC is shown in Figure 1.2. The first step of the process is the oxidation of the fuel ($H_2$). The fuel must diffuse from the flow channels through what is called the gas diffusion layer to the anode. The anode contains a catalyst, usually nano-particles of platinum on a porous carbon support, that very efficiently promotes the oxidation of the hydrogen. Upon oxidization,

hydrogen gives up its valence electron and those electrons are conducted into the external circuit to do useful work, and the remaining hydrated protons are transported across the electrolyte membrane that is selectively permeable to cations.

On the other side of the membrane, oxygen is reduced by the electrons that flowed through the external circuit to form $O^{-2}$, and at the same time the protons that came across the membrane combine with these oxygen anions to form water ($H_2O$) . Again a platinum containing catalyst is used to promote the reduction of the oxygen. The precise mechanism by which this cathode reaction occurs is a complex multi-step process and is still the subject of research, though it invariably involves as a first step the adsorption of the $O_2$ molecule to the cathode catalyst[6–8]. Incomplete reduction of oxygen can result in reactive byproducts such as hydrogen peroxide ($H_2O_2$), a side-reaction that captures only about half of the energy of the desired reaction. Further, peroxide is one cause of membrane degradation through chemical attack and is a factor that limits fuel cell life[9]. Combining the desired half reactions of the anode and cathode gives the overall reaction, which is essentially the combustion of $H_2$.

$$H_2 \rightarrow 2H^+ + 2e^- \qquad E^o = 0 \text{ V vs. SHE (Eq. 1.1)}$$

$$4H^+ + 4e^- + O_2 \rightarrow 2H_2O \qquad E^o = 1.23 \text{ V vs. SHE (Eq. 1.2)}$$

$$2H_2 + O_2 \rightarrow 2H_2O \qquad E^o = 1.23 \text{ V vs. SHE (Eq. 1.3)}$$

*1.1.2 Benefits of Fuel Cells*

As previously stated, fuel cells directly convert chemical energy to electrical energy. This conversion avoids transforming the energy into the high-entropy form of heat, as do combustion engines. The maximum efficiency of any heat engine is theoretically limited by that obtained in a reversible Carnot cycle. The limit is simple to determine and states that any process that uses heat energy to generate work is limited in maximum efficiency by the equation:

$$\eta = \frac{T_H - T_C}{T_H} \qquad \text{(Eq. 1.4)}$$

where η is the maximum theoretical efficiency, $T_H$ is the temperature of the hot reservoir in Kelvin, and $T_C$ is the temperature of the cold reservoir in Kelvin. In real systems there are always parasitic losses due to friction and irreversibility of some chemical steps in the process. Conceptually, the Carnot principle says that only a fraction of the heat generated can be turned into useful work. Under operational conditions and with current materials, automobile engines have efficiencies of roughly 25%. The hot temperature is determined by an average temperature of the internal gases in the cylinder and the cold temperature by the block cooling temperature of about 120 $^{o}$C. Large scale steam turbines are able to operate at roughly 50% efficiency.[10] These limits are defined by the thermal durability of the relatively inexpensive materials used to make the engines, and by the temperature of the cold reservoir.

A fuel cell, however, is not limited by Carnot considerations. A fuel cell has a maximum theoretical Gibbs free energy efficiency of 100 %, ignoring overpotential losses (ie, at low currents). This does not, however, mean that all the heat energy is available to do work. If efficiency is measured by the fraction of the enthalpy of combustion of hydrogen that is turned into useful energy, the maximum theoretical efficiency (electrical work divided by the enthalpy) of a hydrogen fuel cell is roughly 83%.[10] This is the ratio between the theoretical cell potential (1.23 V) of the overall reaction, and the thermoneutral potential (1.48 V). This ratio is dependent on both temperature and pressure and arises from the change in entropy in the fuel cell reaction.

While there are many factors that reduce overall efficiency, which we will discuss in detail later, the fuel cell is at least theoretically a more efficient system for converting a fuel into useful work

than a combustion engine or even a gas fired turbine. Current research on fuel cells focuses on understanding and controlling the irreversible processes that lead to unwanted energy loss. This is intimately connected with the behavior and performance of the catalysts, especially for the reduction of oxygen. Other challenges include improving the durability under prolonged operation, in addition to lowering materials, ancillary system and manufacturing costs

Beyond the promise of high efficiency, fuel cells have a number of other positive qualities. Hydrogen fuel cells are zero-$CO_2$ emission devices. On the other hand the production of hydrogen usually produces $CO_2$. 90 % of hydrogen is currently produced by the steam reforming of natural gas; $CO_2$ is a by-product of the synthesis. The remaining 10 % is produced by electrolysis, which could in principle be driven by renewable electrical sources such as solar PV or hydropower[11,12]. Fuel cells also benefit from the fact that they are open systems, which means that their capacity can be scaled up on demand, and they can be recharged quickly from high pressure hydrogen storage tanks or instantaneously by switching from one hydrogen storage tank to another with no recharge time. The recharge time of batteries is a challenge for some applications, such as in electric vehicles.

### *1.1.3 Challenges Facing Fuel Cells*

In PEMFCs that use hydrogen gas as a fuel and platinum based nanoparticle catalysts are the current industry standard. The immediate disadvantage of using platinum is cost; platinum is a rare noble metal, and the cost of the catalyst is a significant barrier to mass adoption of the technology.

A perfect catalyst would still be useful even if it were expensive; however, platinum is far from a perfect catalyst. The oxidation rate of hydrogen on the Pt surface is about as fast a rate as can be expected in an electrochemical reaction in acid (the exchange current density is about $10^{-3}$ A/cm$^2$). But the reduction rate for oxygen, by comparison to hydrogen, is horribly slow (exchange current density of about $10^{-9}$ A/cm$^2$).[13] This slow rate results in a high overpotential when the reaction occurs at a useful current density (or equivalently at useful power densities). Overpotentials of 300 to 400 mV are necessary to achieve current densities approaching the mass transport limit of the device. These overpotentials result in ohmic heating losses directly reducing voltage and power and decreasing efficiency. The excess heat must be removed by cooling systems that are larger for larger losses and that add complexity, weight and cost to the system.

This is not to say that Pt nanoparticles make perfect anode catalysts, either. The Pt catalytic surface is prone to poisoning (the surface is covered by a strongly bound contaminant that prevents hydrogen from reaching the surface) by air-born pollutants like $SO_x$, $NO_x$, CO, and certain organics[14–17]. In an $H_2$ fuel cell, therefore, the fuel stream needs to be free of these contaminants - which often exist in trace amounts in hydrogen produced via fossil fuels. For example – CO must be below a few parts per million (ppm) or S below a few parts per billion (ppb), or the efficiency and lifetime of the Pt catalysts will be significantly reduced. In fuel cells utilizing more complex organic fuels such as methanol or ethanol, the possibility exists for incomplete oxidation that produces CO that poisons the surface of Pt and Pt alloys. This poisoning is in addition to the higher overpotential from the slower kinetics of oxidizing these other organic compared to hydrogen, particularly for reactions that involve breaking carbon-

carbon bonds[18–21].

In order to address these issues, fuel cell catalysts made from platinum mixed with other elements has become a widely explored topic of research[22–27]. Decreasing the Pt content of the catalyst and replacing it with some cheaper element may decrease the overall cost of the catalyst if the activity of the catalyst is not significantly reduced by the added elements. The exchange current density of some Pt based binary or ternary compositions has been shown to meet or exceed that of pure platinum at operational voltages for both the anodic and cathodic reactions in PEMFCs. This behavior is hypothesized to be due to surface strain at the nanoparticle surface caused by changes in lattice parameters upon alloying or by the modifying the electronic structure, particularly of the Pt based d-bands. Such considerations have lead to many researchers' pursuit of new catalysts that follow to so-called "volcano plots", which have sought to quantify and predict these effects[22], as shown in Figure 1.3. Additionally, inclusion of other elements may also lower susceptibility to poisoning[28]. These benefits may be expected for both alloys and ordered intermetallics of Pt, but at this point only experiments are able to determine the relative improvements that come with such modifications of Pt.

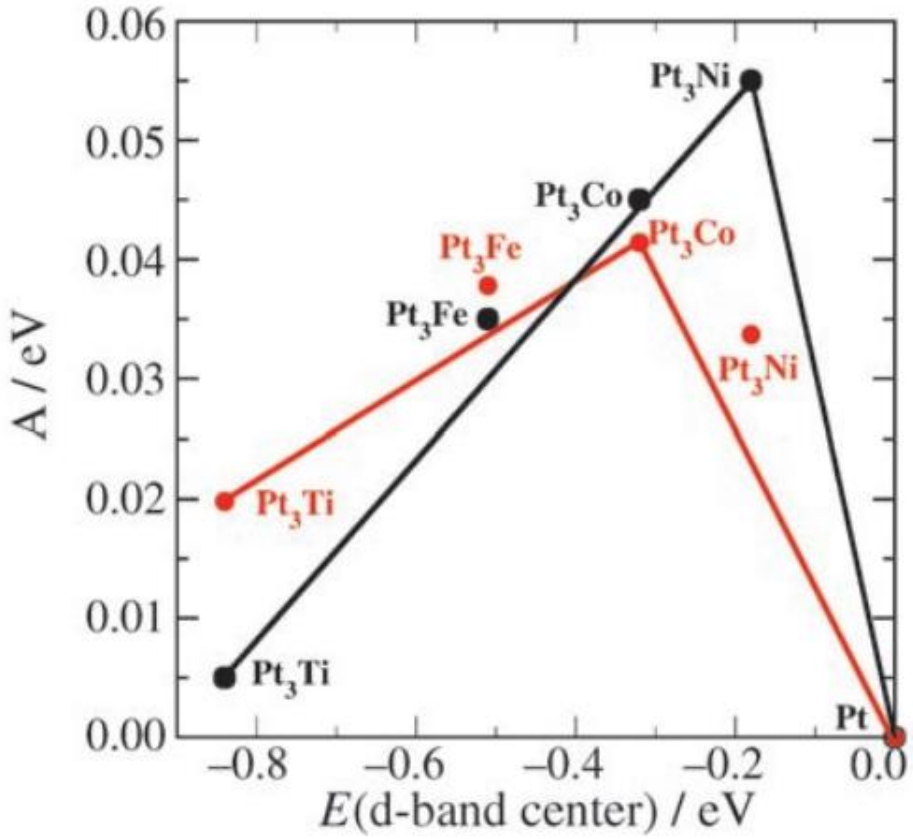


**Figure 1.3** A characteristic "volcano plot" showing the theoretically (black) and experimentally (red) determined reactivity of various bimetallic Pt-containing catalysts for ORR vs. a measure of the energy of the Pt based d-band . Taken from the work of Stamenkovic et. al[22].

### *1.2 Alloys vs. Intermetallics*

#### *1.2.1 Definitions and Structure*

Alloys, also called solid solutions, are crystalline compounds composed of two or more metals where some or all of the Wycoff positions in the unit cell are randomly occupied by metal atoms. As seen in Figure 1.4, in materials with only one Wycoff position (as is the case for binary alloys of platinum) the probability for any individual site to be occupied by an element is equal to the

stoichiometric ratio of that element in the overall alloy. This means that local composition can vary dramatically across the surface on the atomic scale, resulting in localized clusters with higher concentrations of one element or the other.

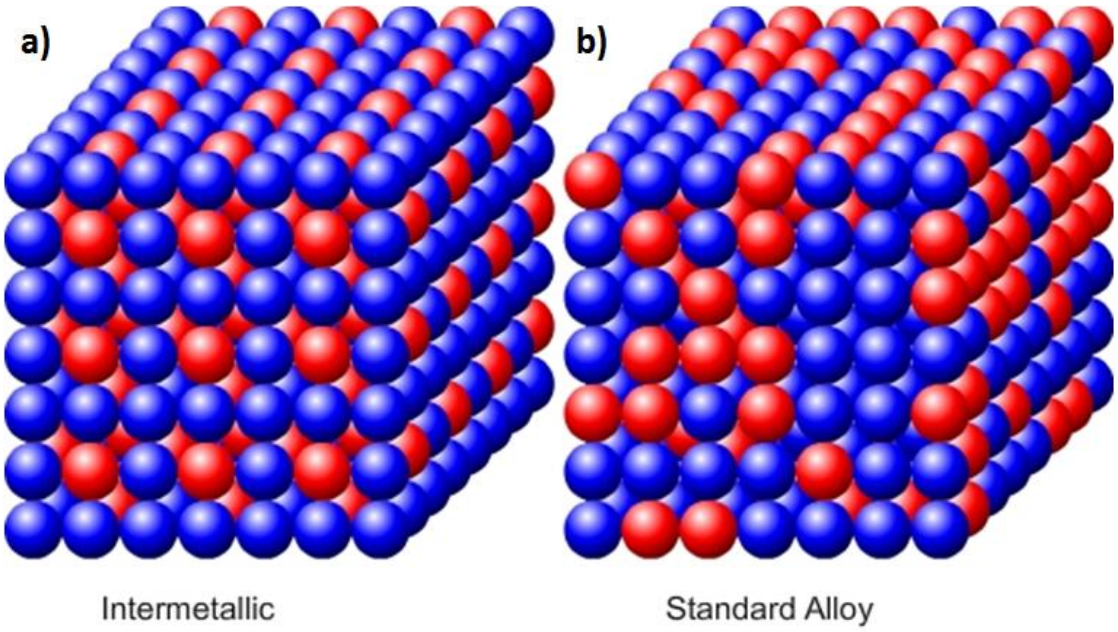


**Figure 1.4** A comparison of two cubic binary 1:1 materials, a) an ordered intermetallic, and b) a possible local structure in a random alloy. Modified from spaceflight.esa.int[29]

Ordered intermetallics, in contrast, are homogenous in composition on both the atomic- and macroscale. Each element occupies its own Wycoff position in binary or ternary compositions. Intermetallic surfaces, prior to any changes due to chemical or electrochemical leaching, are therefore exactly defined based on the exposed facets of the catalyst particle. Pseudo-ternaries are related structures where one element sits on one Wycoff position and the other two elements are distributed randomly on another Wycoff position. The basic structure is one that is adopted by a binary compound. A true ternary compound has each of the three elements occupying their own distinct Wycoff positions, adopting a structure not seen in binary compounds. Pseudo-

ternary structures often occur when two elements in a three-element mixture are of similar size or electronic configuration, and thus there is a small energy difference between states where the atoms exchange lattice positions.

Ordered phases are thermodynamically favored (have the lowest free energy of formation) at room temperature when they have large negative enthalpies of formation resulting from strong intermetallic bonds; ordered intermetallics maximize the number and strength of these bonds. The second component of the free energy is the entropy. The entropy is maximized by disordered atomic arrangements. The entropy of randomness in a binary phase is maximized at a 50:50 composition and is equal to 2R*ln2 per mole of alloy (e.g. composition of $A_{(1-x)}B_x$ at x = 0.5). The entropic contribution to the free energy is equal to the entropy times the temperature. At room temperature the above entropic contribution to the free energy is about 1.8 kJ/mole, a rather small energy compared to most bond enthalpies.

The magnitude of the *relative* bond enthalpies determine when and if disorder is favored over order. The entropy of disorder can favor the alloy phase at high temperatures and the intermetallic phase at lower temperature, sometimes leading to order-disorder transitions at temperatures below the melting point of the solid. It is important to note that the order-disorder temperature has no direct relationship to the melting point, but rather to how similar the constituent elements are to each other. However, when the order-disorder temperature is low, slow kinetics can inhibit the transition in real materials. Copper-platinum alloys, for instance, are preferentially disordered at very low temperatures[30,31], whereas $Pt_3Ti$ favors the ordered phase up to the melting point[32,33]. Almost all theoretical and experimental work on these order-disorder phenomena have been conducted on bulk phases or extended surfaces, rather than on

nanoparticles. We expect modifications to such behavior when the difference in surface energies of various nano-structures are comparable to bulk or surface ordering energies. For example, Ag-Pt will not form an alloy or intermetallic in the bulk; the maximum miscibility is about 2-5 % of either element present as a dopant[34,35]. However, in the nanoparticle regime, it is possible to create Ag-Pt alloys, core-shell structures, and intermetallics with a wide range of compositions[36].

*1.2.2 Analytical Evidence for Ordered Intermetallics*

Multiple techniques can be used to distinguish between ordered intermetallic structures and disordered alloys. The primary technique used in this work is powder X-ray diffractometry (pXRD), which is discussed in detail in Chapter 2. In FCC alloys - such as is found in nanoparticles of $Pt_3Sn$ prepared at room temperature - the powder pattern will look very similar to that of a face centered cubic crystal - such as Pt - with the peaks shifted slightly due to differences in the size of Pt and Sn and thus the resulting lattice parameter, which usually follow Vegard's Law[37,38]. However, when ordering occurs additional peaks (referred to as "ordering peaks" or "superlattice peaks") are usually detectable. In the case of $Pt_3Sn$, which orders by adopting the simple cubic $Cu_3Au$ structure (space group Pm-3m), these weak peaks are indicative of the loss of some symmetry elements within the FCC structure (space group Fm-3m). Figure 1.5 is a theoretical comparison of $Pt_3Sn$ ordered and disordered pXRD patterns made with the crystal structure visualization software Mercury. The disordered pattern (red) was calculated from a theoretical crystal with the same lattice parameters as ordered $Pt_3Sn$, with one atom (Pt) chosen to fill both Pt and Sn sites. The ordering removes the six weak superlattice peaks from the pattern in the 2-theta range shown. Similar analyses can be performed on other crystal structures, though additional considerations arise when dealing with non-cubic ordered

structures; these will be discussed in Chapter 3.

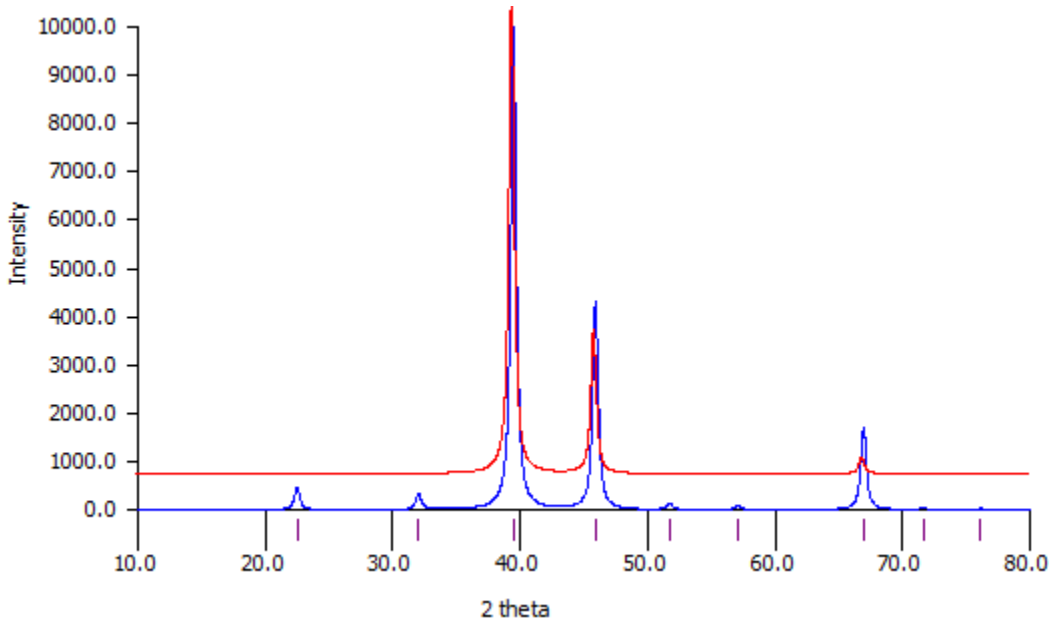


**Figure 1.5** Comparison of theoretical $Pt_3Sn$ ordered (blue) and disordered alloy (red) pXRD patterns calculated with Mercury.

Elemental analysis via energy dispersive X-ray spectroscopy (EDX) in an SEM or microprobe is another important technique for use in confirming the identity of nanoparticle phases. Ordering requires precise ratios of elements in order to be consistent across the entire sample; as such, most intermetallics have little or no composition width (often called "line phases"), so that deviations from stoichiometry are accommodated by the appearance of a second phase. If there is a measurable composition width, some site alloying, vacancies or interstitials occur to accommodate the stoichiometric variability. This means that large aggregations of nanoparticles can be quickly scanned with EDX to determine whether or not the ratio of the constituents elements matches the expected ratio for the desired phase. Significant deviations are indicative of multi-phase products, or alloys. But this method generally averages over a sample volume of a cubic micron, which may contain up to $10^9$ nano-particles. Thus, unless there is macroscopic

phase separation, we obtain only the average composition of the nano-particles.

Individual nanoparticles can be examined via high-resolution spectroscopic methods such as transmission electron microscopy (TEM), scanning transmission electron microscopy (STEM), and high angle annular dark field STEM (HAADF-STEM). Coupling these techniques with atomic-resolution electron energy loss spectroscopy (EELS) allows mapping of the different elements present in individual nanoparticles. Uniform naono-particle composition is highly likely if 10s of particles show the same composition which agrees with the average composition obtained by microprobe. These techniques can also definitively show the difference between ordered intermetallics and disordered alloys in compounds with high Z-contrast between their constituent elements. More detailed descriptions of all of these analytical techniques are found in the following chapter.

### *1.2.3 Comparison as Catalysts*

An important question one might ask themselves at this time is: "Why care so much about ordered intermetallics if it's easier to form alloys?" First, in proposing mechanisms for a particular catalytic reaction, it is very helpful to know that the local surface structure is well known, rather than the statistical variations that occur on the surface of a random alloy. Because intermetallics have (theoretically) well defined surfaces, the active sites of one particle are the same as the active sites of another particle with identical crystallinity and composition. In other words, the atomic scale properties are directly linked to the macroscale properties. Any alloy does not possess this quality. When the site occupancy pattern changes on a surface, it is to be expected that the catalytic behavior will change as well.

For instance, carbon monoxide (CO) has been shown to strongly bond to the Pt surface in a number of configurations, which are dependent on surface coverage of CO, and the surface structure of Pt. There are two main modes by which CO bonds to the surface: 1. perpendicular to the metal surface, and 2. lying parallel to the surface. Both of these have surface bonding energies of roughly 30-35 kcal/mole[17]. A CO molecule lying on the surface will involve bonding with multiple adjacent Pt atoms[39]. Therefore, if one of the Pt atoms were replaced by another atom that binds less strongly to CO, the overall binding energy of CO to the surface would drop significantly, and indeed it has been shown that on a variety of Pt-M alloy and intermetallic surfaces, electrochemical CO stripping is generally more favorable[28,40–43].

Intermetallics are also generally more thermodynamically stable under fuel cell conditions. Nanoparticle alloys of Pt with more oxophilic elements, such as the 3d and main group metals, typically display irreversible leeching of the non-Pt atoms on exposing to oxidizing agents such as nitric acid or even to long term air exposure or on electrochemical cycling to a composition dependent positive potential, particularly when those non-Pt atoms make up greater than 50 % of the total composition[44]. Leaching can occur in just the top surface monolayers, or extend into the bulk of the nanoparticle. Especially the latter results in a high-surface area Pt nanoparticles with some fraction of the non-Pt metal still remaining, and which can show much higher catalytic activity (the result of a dramatic increase in surface area)[45,46]; however, the spongy structure can collapse during electrochemical cycling, reducing the apparent activity. Recent work suggests that intermetallics show less leaching than alloys of the same composition under oxidizing conditions and on electrochemical cycling up to 1.2 V vs. the standard hydrogen electrode

(SHE)[47].

### *1.3 Phase diagrams and Nanophase Deviations*

#### *1.3.1 Introduction to Phase Diagrams and the Phase Rule*

Phase diagrams are maps of thermodynamic stability under different experimentally controlled conditions. The controllable parameters are usually temperature, pressure, and multiple components or elements. While the kinds of phase behavior reported in such diagrams seems vast, there are theoretical limits that are derived from thermodynamics, as embodied in concepts such as the phase rule. Gibbs' phase rule is summarized in a simple but powerful equation (Eq 1.5), where F is the degrees of freedom, C is the number of components in the system, and P is the number of phases in thermodynamic equilibrium.

$$F = C - P + 2 \qquad \text{(Eq. 1.5)}$$

The degrees of freedom are defined as the number of independent intensive variables that may be changed while maintaining the same phase(s) and crystal structures; in other words, in how many directions on the phase diagram is the system allowed to move without resulting in a change in the number of phases? Components are chemically distinct and independent species that are added to the reaction mixture and that maintain their identity under the conditions explored. . For example, if a system consists of two ions that originate from dissolving the same salt, those ions together count as one component. Phases are homogenous physical states (generally classified as solids, liquids, and gases). Immiscible solids and liquids in a system count as separate phases for the phase rule.

The phase rule is the mathematical representation of the simple but important thermodynamic concept that phases in equilibrium are constrained in terms of some (though not necessarily the same) intensive properties. A mixture of water and ice that is chilled to exactly 0 $^{o}$C at atmospheric pressure will remain in equilibrium until the temperature is changed. For such a system, F = 1 , since C = 1 and P = 2. Pressure and temperature, the two relevant intensive properties for the system, can therefore not be altered independently; if one is held constant, the other must be held constant, and if one is changed, the other must be changed as well in order to keep the liquid water and solid ice present in the container.

However, phase diagrams do not take kinetics into account in any way. This is why, for example, graphite occupies the region of the carbon phase diagram at standard temperature and pressure. However, no one is concerned about diamonds suddenly turning into graphitic carbon, because the kinetics for that transformation are incredibly slow at room temperature and in air. Thermodynamics determines the most stable phase(s) at some fixed composition and external conditions such as temperature and pressure, but does not determine if there are meta-stable phases, although the phase diagram may indirectly suggest ways to get to the stable phase from the metastable phase(s).

Another caveat of predicting properties from phase diagrams is that all of the diagrams available are representative of the thermodynamics of bulk materials. Nanoparticles have a much greater fraction of atoms at the surface than bulk samples, so thermodynamic stability in the bulk does not necessarily translate to the nano-regime, and vice versa. As already mentioned, homogeneous alloy Ag-Pt nanoparticles can be prepared, but they are unstable (decomposing to two phases,

one Ag rich the other Pt rich in thebulk material[36]. Au-Pt nanoparticles have similar behavior[48], while the preparation of Au-Ag nanoparticles (elements which are completely miscible in the bulk) have posed some synthetic challenges[49].

*1.3.2 Binary Phase Diagrams*

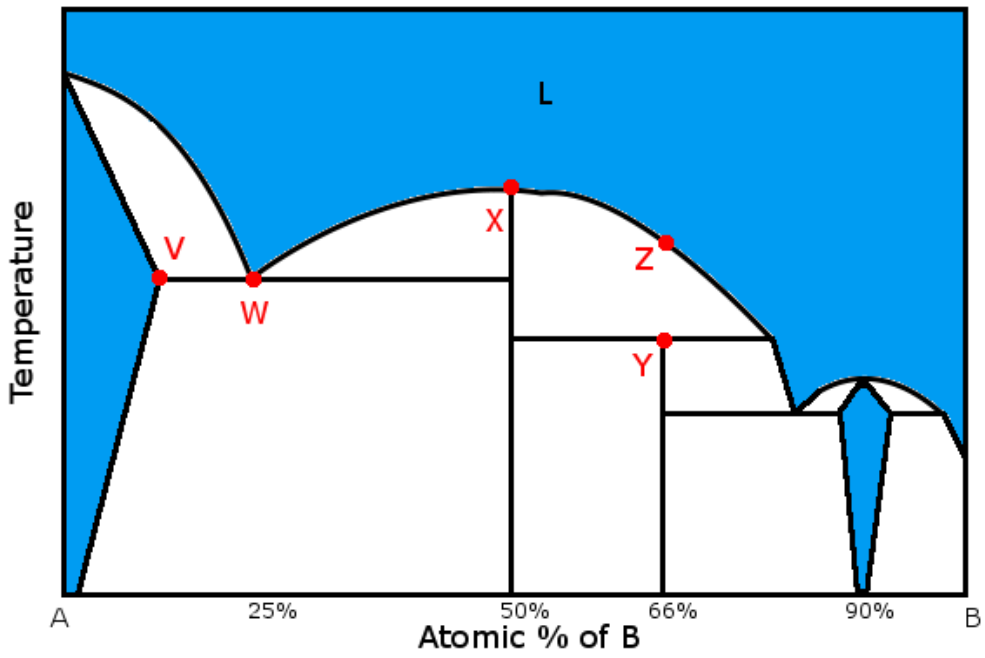


**Figure 1.6.** A mock phase diagram of the mixing of two phases, A and B. Blue regions are partial alloys or at high temperatures, homogeneous melts, and black vertical lines are single-phase ordered solids, white regions consist of two phases.

Figure 1.6 is a mock phase diagram. It will be used to illustrate several features that will be referred to while discussing binary phase diagrams and predictions that can be derived from them. The diagram shows the combination of two elements, A and B, across the entire composition range, from 100% A on the left to 100% B on the right. In this diagram, blue areas denote single-phase regions, whereas white regions consist of two separate phases. The phase

rule in this case (at a fixed pressure of 1 atm) says that the maximum number of phases that can co-exist in equilibrium is two.

Starting from pure A and progressively adding more of element B, the first notable feature is an extended region of blue. This region indicates that B is completely soluble in A as a solid solution, up to a maximum of about 10 % B at the eutectic temperature marked as point V; the solubility is temperature-dependent. Above this is a two-phase region where liquid B and a solid solution of B in A are in equilibrium. The minimum, or eutectic, temperature at which a mixture of A and B with less than 50 % B will solidify is located at the eutectic composition A:B 3:1. The point on the phase diagram with the coordinates of the eutectic composition and temperature is known as the eutectic point, indicated here as the point W.

The next feature of note is the "line phase" at 50 % B. This phase, which can be called AB because the ratio of A:B is equal to 1:1, has a phase width so narrow that it cannot be seen on the scale of the phase diagram. By the phase rule, there must be *some* phase width, but the structure has low enough tolerance for extra A or B atoms that as far as we are concerned for the synthesis, the phase width is effectively zero. Also of note is the congruent melting point of AB at point X. The solid AB, upon heating, will change directly into a liquid with the same overall composition as the solid. This is called a congruently melting phase.

In contrast, the line phase at 66 % B ($AB_2$) is an incongruently melting phase. Upon heating, $AB_2$ will decompose at its Pertitectic decomposition temperature (point Y) into solid AB and a liquid with a higher concentration of B (roughly 75 %). As this mixture is heated further, AB continues

to dissolve into the melt until eventually it hits the liquidus line at point Z and melts completely into liquid A-B in a 1:2 ratio.

Finally, the blue region at 90% B is an alloy phase that has some line width. This phase may very well order at particular atomic ratios, but small deviations from those ratios will be incorporated into the lattice, most likely by replacing one element for another on a 1:1 basis (and disrupting the nanoscale order in the process). Also note on the far right side of the diagram that there is effectively zero solubility of A in pure B within the scale that we can resolve on the diagram (perhaps a percent or so resolution).

### 1.3.3 Melting Point and Ordering Temperature Trends

Vacancies in the structure of a material form when atoms become energetic enough to break the bonds in the lattice and move to the surface. According to the vacancy model of melting[50,51], as the number of vacancies increases, a point is reached where the crystal melts in a sudden transition at the melting point. This transition is first order (i.e. has an associated latent heat of melting).

Vacancy energies ($E_v$) are easy to calculate as the difference between the energy of the bonds surrounding an atom in the bulk crystal and the energy of the smaller number of bonds that same atom can make on the surface. The number of vacancies is proportional to $\exp(-E_v/kT)$[50]. This leads to a rapid increase in vacancy concentration as the temperature increases (typically doubling every 10 to 20 $^{o}$C).

Bulk diffusion rates are also determined in part by the number of vacancies in a material; it usually is much easier for an atom to jump to an empty atomic position than to push past another atom. The energy required for an atom to diffuse to an empty lattice point is not, however, zero; there is an activation energy of motion required to move past atoms in the lattice. The sum of the activation energy of motion and the energy required to make a vacancy is equal, the total energy required for an atom to move through the solid. Given this link between vacancies, bulk diffusion, and melting points, it is unsurprising that bulk diffusion rates in a given family of materials with the same structure tend to scale with the bulk melting point[52].

Furthermore, since activation energy of diffusion depends in part on the energy of breaking bonds in the lattice, it is evident that diffusion along a surface has a lower barrier (and is therefore faster) than diffusion in the bulk. There are fewer bonds to break for atoms on the surface than there are for atoms in the bulk. It is well known that, as the radius of a particle decreases from the bulk to the nanoparticle regime, the melting point of that particle decreases[53,54] due to an increase in the proportion of atoms located on the surface relative to the bulk.

At the same time, the atoms in an as-made alloy or amorphous nanoparticle must diffuse through the structure to rearrange into the ordered phase. Thus, we might generalize by supposing that alloys prepared at room temperature would order at annealing temperatures that scale with the melting point of the ordered bulk solid. This is the expected relationship; however, as we shall see, the empirical observation is that the relationship between bulk melting temperature and ordering behavior is far more complicated than expected.

### *1.4 Scope of Dissertation*

The following chapter will discuss the general synthetic procedure of intermetallic nanoparticles, in addition to notable experimental parameters and conditions, including the choice of solvent, precursors, reducing agents, annealing temperatures, and other factors that influence the structure, morphology, and reactivity of the final product. Subsequent chapters will focus on the syntheses of particular phases or groups of phases, paying close attention to the relationships between the parameters of the reaction and the bulk phase diagram. The overall goal of these chapters is to examine the relationship between the bulk phase diagram and nanoparticle composition and structure. In particular, products of low temperature solution phase syntheses may be metastable (amorphous, include bound solvent molecules, form alloys when intermetallic phases are expected, etc). Finally, the concluding chapter discusses a multivariate analysis of the data presented in chapters 3 and 4. The impetus behind this inclusion is to quantitatively demonstrate which physical properties - including those found in phase diagrams - are best able to describe if and how a phase will form ordered intermetallic nanoparticles using the borohydride co-reduction method.

REFERENCES


(1) U.S. Energy Information Administration International Energy Statistics. http://www.eia.gov/cfapps/ipdbproject/IEDIndex3.cfm (accessed Apr 23, 2014).
(2) Lewis, N. S.; Nocera, D. G. *Proc. Natl. Acad. Sci.* **2006**, *103*, 15729–15735.
(3) Wackernagel, M.; Schulz, N. B.; Deumling, D.; Linares, A. C.; Jenkins, M.; Kapos, V.; Monfreda, C.; Loh, J.; Myers, N.; Norgaard, R.; Randers, J. *Proc. Natl. Acad. Sci.* **2002**, *99*, 9266–9271.
(4) Brown, M. M.; Desai, N.; Doucet, G.; Goldemberg, J. *World Energy Assessment: Energy and the Challenge of Sustainability*; United Nations Development Programme, United Nations Department of Economic and Social Affairs, World Energy Council, 2000.
(4) Ballard: How a Fuel Cell Works. http://www.ballard.com/about-ballard/fuel-cell-education-resources/how-a-fuel-cell-works.aspx (accessed Apr 29, 2014).
(6) Yeh, K.-Y.; Wasileski, S. A.; Janik, M. J. *Phys. Chem. Chem. Phys.* **2009**, *11*, 10108.
(7) Strmcnik, D.; Escudero-Escribano, M.; Kodama, K.; Stamenkovic, V. R.; Cuesta, A.; Marković, N. M. *Nat. Chem.* **2010**, *2*, 880–885.
(8) Wang, X.-G.; Fisher, G. *Phys. Rev. Lett.* **2007**, *99*.
(9) Ramaswamy, N.; Hakim, N.; Mukerjee, S. *Electrochimica Acta* **2008**, *53*, 3279–3295.
(10) Zhang, J. *PEM Fuel Cell Electrocatalysts and Catalyst Layers: Fundamentals and Applications*; Springer, 2008.
(11) *Ullmann's Encyclopedia of Industrial Chemistry*; Wiley-VCH Verlag GmbH & Co. KGaA, Ed.; Wiley-VCH Verlag GmbH & Co. KGaA: Weinheim, Germany, 2000.
(12) Joosten, J.; Gross, P.; Kydes, A.; Maples, J. D. *The Impact of Increased Use of Hydrogen on Petroleum Consumption and Carbon Dioxide Emissions*; SR-OIAF-CNEAF/2008-04; U.S. Energy Information Administration, 2008.
(13) O'Hayre, R.; Cha, S.-W.; Colella, W.; Prinz, F. *Fuel Cell Fundamentals*; John Wiley & Sons, Inc: Hoboken, New Jersey, 2006.
(14) Dunleavy, J. K. *Platin. Met. Rev.* **2006**, *50*, 110–110.
(15) Minachev, K. M.; Shuikin, N. I.; Rozhdestivenskaya, I. D. *Bull. Acad. Sci. USSR Div. Chem. Sci.* **1952**, *1*, 567–575.
(16) Mohtadi, R.; Lee, W. K.; Cowan, S.; Van Zee, J. W.; Murthy, M. *Electrochem. Solid State Lett.* **2003**, *6*, A272–A274.
(17) Smith, G. W.; Carter, E. A. *J. Phys. Chem.* **1991**, *95*, 2327–2339.
(18) Antolini, E. *J. Power Sources* **2007**, *170*, 1–12.
(19) Rousseau, S.; Coutanceau, C.; Lamy, C.; Léger, J.-M. *J. Power Sources* **2006**, *158*, 18–24.
(20) Purgato, F. L. S.; Pronier, S.; Olivi, P.; de Andrade, A. R.; Léger, J. M.; Tremiliosi-Filho, G.; Kokoh, K. B. *J. Power Sources* **2012**, *198*, 95–99.
(21) Melke, J.; Schoekel, A.; Dixon, D.; Cremers, C.; Ramaker, D. E.; Roth, C. *J. Phys. Chem. C* **2010**, *114*, 5914–5925.

(22) Stamenkovic, V.; Mun, B. S.; Mayrhofer, K. J. J.; Ross, P. N.; Markovic, N. M.; Rossmeisl, J.; Greeley, J.; Nørskov, J. K. *Angew. Chem. Int. Ed.* **2006**, *45*, 2897–2901.
(23) Stamenkovic, V. R.; Mun, B. S.; Mayrhofer, K. J. J.; Ross, P. N.; Markovic, N. M. *J. Am. Chem. Soc.* **2006**, *128*, 8813–8819.
(24) Strasser, P.; Koh, S.; Anniyev, T.; Greeley, J.; More, K.; Yu, C.; Liu, Z.; Kaya, S.; Nordlund, D.; Ogasawara, H.; Toney, M. F.; Nilsson, A. *Nat. Chem.* **2010**, *2*, 454–460.
(25) Greeley, J.; Stephens, I. E. L.; Bondarenko, A. S.; Johansson, T. P.; Hansen, H. A.; Jaramillo, T. F.; Rossmeisl, J.; Chorkendorff, I.; Nørskov, J. K. *Nat. Chem.* **2009**, *1*, 552–556.
(26) Casado-Rivera, E.; Volpe, D. J.; Alden, L.; Lind, C.; Downie, C.; Vázquez-Alvarez, T.; Angelo, A. C. D.; DiSalvo, F. J.; Abruña, H. D. *J. Am. Chem. Soc.* **2004**, *126*, 4043–4049.
(27) Chen, H.; Wang, D.; Yu, Y.; Newton, K. A.; Muller, D. A.; Abruña, H.; DiSalvo, F. J. *J. Am. Chem. Soc.* **2012**.
(28) de-los-Santos-Álvarez, N.; Alden, L. R.; Rus, E.; Wang, H.; DiSalvo, F. J.; Abruña, H. D. *J. Electroanal. Chem.* **2009**, *626*, 14–22.
(29) ESA. It's Not a Solution! *IMPRESS: Supporting Education Across Europe*, 2010.
(30) Collings, E. .; Smith, R. .; Ho, J. . *J. Common Met.* **1976**, *46*, 189–195.
(31) Abe, T.; Sundman, B.; Onodera, H. *J. Phase Equilibria Diffus.* **2006**, *27*, 5–13.
(32) Duan, Z.; Zhong, J.; Wang, G. *J. Chem. Phys.* **2010**, *133*, 114701.
(33) Meschter, P. J.; Worrell, W. L. *Metall. Trans. A* **1976**, *7*, 299–305.
(34) Durussel, P.; Feschotte, P. *J. Alloys Compd.* **1996**, *239*, 226–230.
(35) Peng, Z.; Yang, H. *J. Solid State Chem.* **2008**, *181*, 1546–1551.
(36) Wojtysiak, S.; Solla-Gullón, J.; Dłużewski, P.; Kudelski, A. *Colloids Surf. Physicochem. Eng. Asp.* **2014**, *441*, 178–183.
(37) King, H. W. *J. Mater. Sci.* **1966**, *1*, 79–90.
(38) Vegard, L. *Z. F*[?]*r Phys.* **1921**, *5*, 17–26.
(39) Pedersen, M. .; Bocquet, M.-L.; Sautet, P.; Lægsgaard, E.; Stensgaard, I.; Besenbacher, F. *Chem. Phys. Lett.* **1999**, *299*, 403–409.
(40) Lim, D.-H.; Choi, D.-H.; Lee, W.-D.; Lee, H.-I. *Appl. Catal. B Environ.* **2009**, *89*, 484–493.
(41) Wakisaka, M.; Mitsui, S.; Hirose, Y.; Kawashima, K.; Uchida, H.; Watanabe, M. *J. Phys. Chem. B* **2006**, *110*, 23489–23496.
(42) Wang, D.; Subban, C. V.; Wang, H.; Rus, E.; DiSalvo, F. J.; Abruña, H. D. *J. Am. Chem. Soc.* **2010**, *132*, 10218–10220.
(43) Liu, Z.; Jackson, G. S.; Eichhorn, B. W. *Angew. Chem. Int. Ed.* **2010**, *49*, 3173–3176.
(44) Gregoire, J. M.; Kostylev, M.; Tague, M. E.; Mutolo, P. F.; Dover, R. B. van; DiSalvo, F. J.; Abruña, H. D. *J. Electrochem. Soc.* **2009**, *156*, B160–B166.
(45) Hong, J. W.; Kang, S. W.; Choi, B.-S.; Kim, D.; Lee, S. B.; Han, S. W. *ACS Nano* **2012**, *6*, 2410–2419.
(46) Peng, Z.; Wu, J.; Yang, H. *Chem. Mater.* **2010**, *22*, 1098–1106.

(47) Wang, D.; Xin, H. L.; Hovden, R.; Wang, H.; Yu, Y.; Muller, D. A.; DiSalvo, F. J.; Abruña, H. D. *Nat. Mater.* **2012**, *12*, 81–87.
(48) Wanjala, B. N.; Luo, J.; Fang, B.; Mott, D.; Zhong, C.-J. *J. Mater. Chem.* **2011**, *21*, 4012.
(49) Sun, L.; Luan, W.; Shan, Y. *Nanoscale Res. Lett.* **2012**, *7*, 225.
(50) Vaidya, S. N. *Pramana* **1979**, *12*, 23–32.
(51) Mei, Q. S.; Lu, K. *Prog. Mater. Sci.* **2007**, *52*, 1175–1262.
(52) Antczak, G.; Ehrlich, G. *Surf. Sci. Rep.* **2007**, *62*, 39–61.
(53) Koper, O.; Winecki, S. In *Nanoscale Materials in Chemistry*; 2001; pp. 263–277.
(54) Dick, K.; Dhanasekaran, T.; Zhang, Z.; Meisel, D. *J. Am. Chem. Soc.* **2002**, *124*, 2312–2317.

# CHAPTER 2

# SYNTHESIS AND CHARACTERIZATION OF NANOPARTICLES VIA CO-REDUCTION

## *2.1 Synthetic Methods for Intermetallics*

Because of their importance for catalysis, Pt and Pt-alloy nanoparticle synthetic methods are varied and abundant. Colloidal methods are some of the most well-developed of these. This category includes nano-encapsulations, "water in oil" microemulsions, and polyol reductions[1–7]. All of these methods involve the reduction of solvated Pt salts, inorganic coordination or organometallic compounds. Almost always some form of organic molecular component that coordinates to the particle surface is also employed as a surfactant to reduce the agglomeration of the resulting nanoparticles, or as a control agent to direct the growth of particular particle morphologies.

Co-reduction is itself a broad category that encompasses many different reactions[8,9]. It similarly involves the reduction of both solvated Pt and non-Pt species, but differences in the nature of the products are a function of the strength of the reducing agents and therefore the individual rates of reduction. An ideal co-reduction reaction removes kinetics as a consideration for the nucleation of nanoparticles, or more precisely that the rate of nucleation solely depends on mass transport, not the rate of reduction of the metal precursors. This is usually accomplished by reducing all metals in the solution

to their metallic form simultaneously (or at fast but similar rates), which typically requires a reducing agent with a reduction potential quite negative than that of all the solvated metal cation precursors.

If there are no barriers to the formation of metal-metal bonds, the seeds that are formed from this extremely fast reduction are more likely to be stoichiometrically-determined random mixtures near the desired composition. If surfactants are present, the situation becomes rapidly more complex, and rate and specificity of metal-metal bonding may be significantly perturbed.

Solution-phase reduction methods with reaction times of hours or days often will result in nanoparticle seeds primarily composed of the more easily reduced element, and the products of these reactions will therefore necessarily be inhomogeneous on some length scale and require annealing at high temperatures to form larger, but homogeneous particles that can adopt an alloy or ordered phase structure. This is not meant to imply that co-reduced nanoparticles do not require annealing to overcome the kinetic barriers to crystallization or ordering, but most of the time the annealing can be done at a lower temperature if the initial product of reduction has a homogeneous composition at the nanometer scale. Lower annealing temperatures result in less particle size growth (coarsening) and often less sintering and agglomeration, and therefore produce a final product that has smaller domain and particle sizes[10–12].

Surfactants are popular in nanoparticle synthesis, as they can be chosen to selectively

bind to all or selected facets, inhibiting the growth of the whole nanoparticle or allowing growth only in directions perpendicular to facets on which surfactants are only weakly bound. Synthesis of nanoparticles with defined structures often rely on this sort of control with organic[13] or inorganic[14] surface agents . However, these species need to be removed via chemical or electrochemical methods if they are used as catalysts. Such removal can change the surface structure and composition, or, particularly if annealed to high temperatures to decompose the surfactant, can leave carbonaceous deposits on the surface that physically block catalytic activity.

Co-reduction with soluble metal reactants, such as metal chlorides and soluble reducing agents, such as alkylborohydrides, in solvents such as tetrahydrofuran (THF). THF is both unreactive with most reduced metals (say those from group 3 to 15 in the periodic table) and is a weak surfactant, which greatly lowers the probability of surface contaminating species in the final annealed product. So this method generally produce nanoparticles with relatively clean surfaces. This method simplifies the growth kinetics of the nanoseeds, since the species that interact with the growing surface are only weakly bound and are sufficiently labile that particle surfaces can bind reduced metals and continue to grow during the reduction process.. The most challenging species that often bind to metal surfaces are anions, such as halides, which have increasing surface binding energies in the order $F < Cl < Br < I$ and also result in charged nanoparticles. Such charged particles repel each other in solution, possibly preventing aggregation or precipitation[15], though these effects can be managed. However, fluorides have extremely low solubility in THF and bromide and

iodide anions bind strongly to most clean metal surfaces. For all the above reasons, co-reduction of chlorides was selected as the best method to investigate the synthesis and crystallographic ordering behavior of platinum-containing binary and ternary intermetallic nanoparticles.

## *2.2 Experimental Synthetic Methods*

### *2.2.1 Co-Reduction*

As many of the reactants are air and/or water sensitive, all co-reductions were performed in a sealed glove box under an inert argon atmosphere. All solvents were purchased from Fisher and dispensed dry from a custom solvent system (Seca solvent system by Glass Contour). Metal chloride precursors (see Table 2.1) were dissolved in 30 mL of THF in the appropriate molar ratio to prepare the targeted composition. Certain chlorides are insoluble or only slightly soluble in THF.

Fortunately, we have found that the addition of lithium chloride (LiCl) usually improves the solubility of many binary metal chlorides, by forming large metal chloride anions such as $MCl_n^{-z}$ and $Li^+$ counter ions[15,16]. Since the cations and anions have very different effective radii, the dissolution is favored[17]. Previous members of the DiSalvo group have investigated the solubility of metal chlorides in THF across the periodic table, and their findings are summarized in the following fragment of the periodic table (Figure 2.1). Metal chlorides of the elements highlighted with a green background dissolve at sufficiently high concentration as a metal chloride to produce a

useful mass of product with reaction volumes of roughly 30 mL. Blue elements require the addition of lithium chloride to stirring THF in order to dissolve a high enough concentration. Red elements require synthesis of the ternary lithium metal chloride in order to obtain a high concentration of the metal in THF. White elements either have no data (Tc) or produce no soluble species through any of the three previous methods. Alkali (except for lithium) and alkaline-earth metal chlorides also have very low solublities in THF.

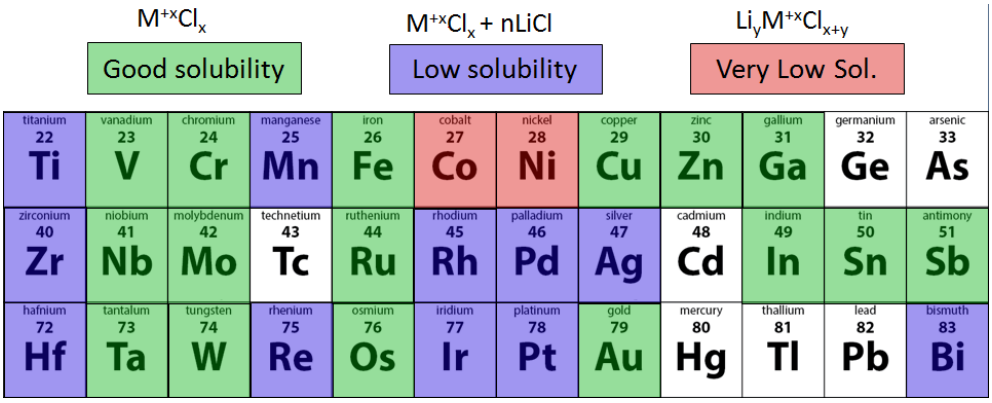


**Figure 2.1** Relative solubility of metal chlorides in THF. Courtesy Drs. Brian Leonard, Minh Nguyen, and Hao Chen.

A few salts used in this study are also indicated in Table 2.1. Typically, 30 mg of $PtCl_4$ was dissolved in 30 mL of THF and stoichiometric amounts of the second (and third, if applicable) metal chloride was simultaneously dissolved in the same flask.The resulting solution (often yellow orange in color due to the $PtCl_4$, if the other salts are colorless or weakly colored in solution) was stirred for 15 minutes. A borohydride reducing agent - either $LiBHEt_3$ (LBH) or $KBHEt_3$ (KBH) (Aldritch, 1M in THF) - was injected quickly (in a few seconds), with a 20 % excess. The excess is added to

reduce any acidic hydrogen of likely impurities, such as water, in the THF. The rapidly stirred solution typically turned black and opaque within a second after injection. The solution was then stirred for another 15 minutes, after which the resulting suspension and any precipitate were transferred to a centrifuge tube, which was then sealed with a rubber septum and removed from the glove box. Figure 2.2 outlines this portion of the experimental method.

| Chloride Precursor | Manufacturer | Soluble without LiCl? | $E^o$ (V) |
|---|---|---|---|
| **$PtCl_4$** | Alfa Aesar | Partially | 2.97 |
| **$SnCl_2$** | STREM | Yes | -0.14 |
| **$SnCl_4$** | Aldritch | Yes | 0.03 |
| **$SbCl_3$** | Alfa Aesar | Yes | 0.20 |
| **$BiCl_3$** | STREM | Partially | 0.32 |
| **$InCl_3$** | SREM | No | -0.34 |
| **$FeCl_3$** | Aldritch | Yes | -0.04 |
| **$NiCl_2$** | Aldritch | No | -0.25 |

**Table 2.1** Table of precursor chloride compounds utilized in this work.

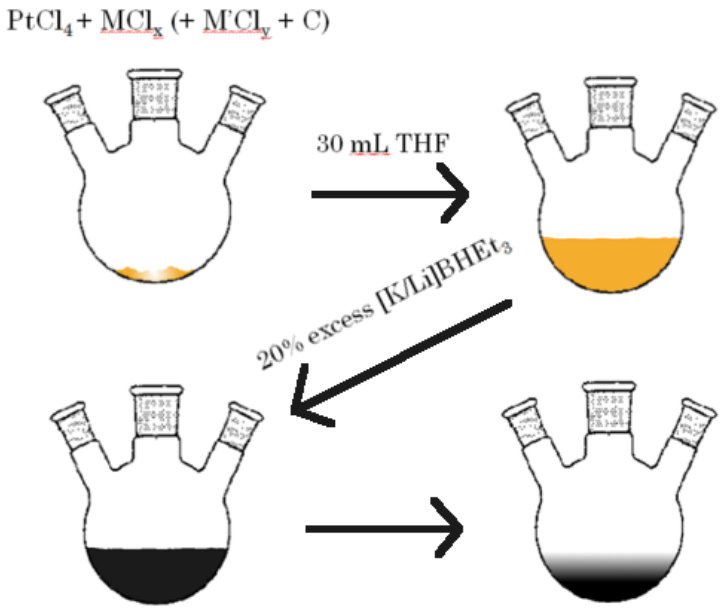


**Figure 2.2.** Reduction and precipitation of nanoparticles from metal chloride precursors.

*2.2.2 Post-Reduction Preparation and Annealing*

The centrifuge tube was spun (9000 rpm, 10 min) and the resulting clear supernatant was decanted under argon via cannula transfer. If the supernatant was not clear or more than lightly tea-colored - which most often happened with target phases using more than 50% non-Pt elements, or if the atmosphere in the glovebox had some air/water contamination, half of the solution was decanted, and then hexanes were added and the tube was re-centrifuged to try to precipitate as much of the product out of solution as possible prior to decanting. 30 mL of THF was then added to the black precipitate, the contents of the tube were stirred with a vortexer and then sonicated for 1 minute, and the tube was centrifuged again.

This washing procedure was repeated once more with THF, and finally once with pure hexane, unless the solution did not come out clear after the first centrifuging step. In this case, the washing procedures were performed with THF/hexane 50:50 mixtures. This reduced the dielectric constant of the wash liquid, which increases the electrostatic interactions between the charged nanoparticles and their counter ions, allowing them to assemble and precipitate. The washing procedure is diagramed in Figure 2.3.

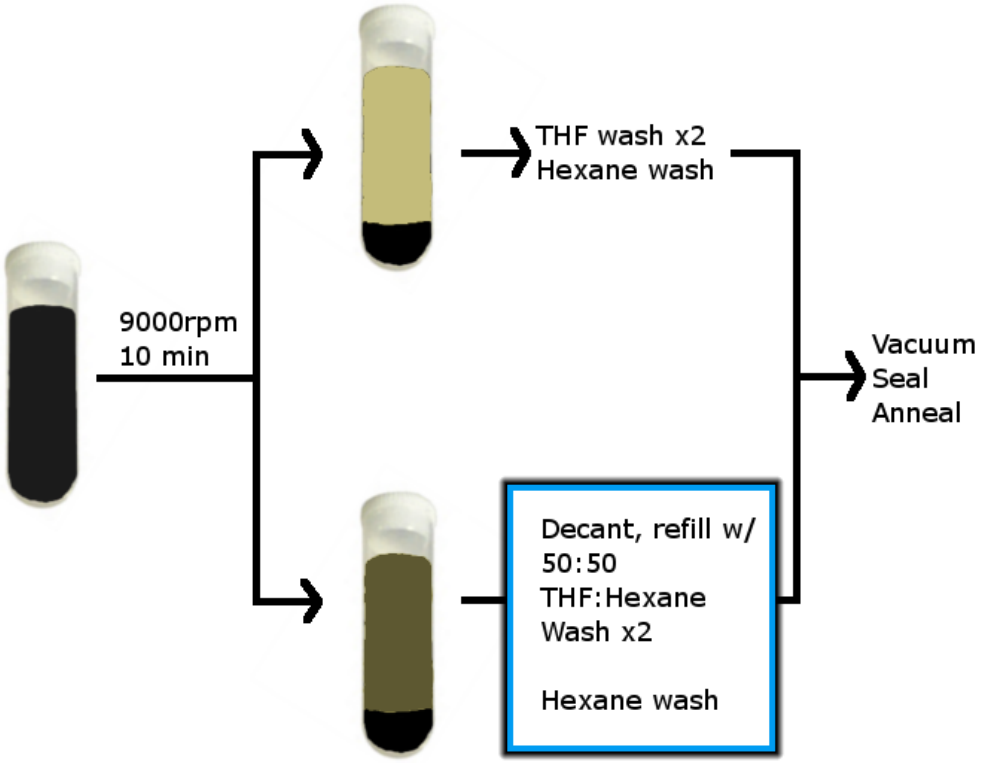


**Figure 2.3** Washing procedure for as-made nanoparticles prior to annealing

In the above reduction process, either THF soluble LiCl or insoluble KCl are produced as a by-product, depending on the reducing agent used. LiCl and organic species are completely removed by the above washing process, leaving only the $Pt_{(1-x)}M_x$ product as agglomerated nanoparticles (with some adsorbed chloride and their charge balancing cations on the surface of the nanoparticles). KCl, on the other hand, precipitates in THF as a crystalline salt matrix that encases the $Pt_{(1-x)}M_x$ nanoparticles, preventing the nanoparticles from agglomerating, and greatly slowing sintering of those nanoparticles upon annealing. The KCl can subsequently be removed by

washing in ethylene glycol or glycol/water mixtures[18]. As we will see, the as-made metal nanoparticle products produced by these different reducing agents at room temperature can be different, and also display different annealing behavior.

In either case, the resulting black product was dried under vacuum. Some products were not annealed, in which case the centrifuge tubes were backfilled with argon and then opened in air. Samples that were to be annealed at a higher temperature were transferred inside the glove box under argon to silica annealing tubes. These tubes were then removed from the glove box without exposure to air and sealed under vacuum using a hand held torch. Finally, they were heated to the desired temperature, and held there for 24 hours.

Supported Pt-Sn nanoparticles were synthesized using carbon black (Cabot**,** Vulcan XC-72). Carbon black was heated to 100$^{o}$C in air to remove adsorbates such as water, transferred to the glove box, and added to the stirring yellow-orange solution of metal chloride precursors. After this addition, $LiBHEt_3$ at 50% excess was added and workup of the reaction proceeded exactly as described above. We empirically found that this 50% excess reduced all metals, and accounted for possible competing reactions between the reducing agent and probable functional groups that contain acidic hydrogen (OH, COOH, etc.) on the carbon surface, with other species adsorbed on the carbon black, or on the container walls. Previous work in this group[6] also shows that nanoparticles can alternatively be released from a KCl matrix and dispersed onto carbon black supports without much agglomeration, but that method

was not specifically explored in this work.

## *2.3 Instrumentation and Analytical Software*

In the following subchapters, we will discuss the most common analytical instruments and software that will be used repeatedly throughout the thesis. Focus will be paid to benefits and limitations of each technique; specifically, what information can be derived from the use of each, and what information cannot.

### *2.3.1 Powder X-Ray Diffraction*

As previously mentioned in section 1.2.2, Powder X-Ray Diffraction (pXRD) is the most important and most prevalent technique used in this work for the identification of nanoparticle phases and purity. This is largely due to the speed at which a sample can be scanned with this non-destructive technique, and how little sample preparation is necessary to achieve optimal results. The fundamental principle on which pXRD is based is, unsurprisingly, diffraction: the property by which high-energy photons are "diffracted" (i.e., reflected at specific angles) by a crystal lattice in a regular and predictable fashion. Figure 2.4 is a cartoon used to explain why diffraction occurs.

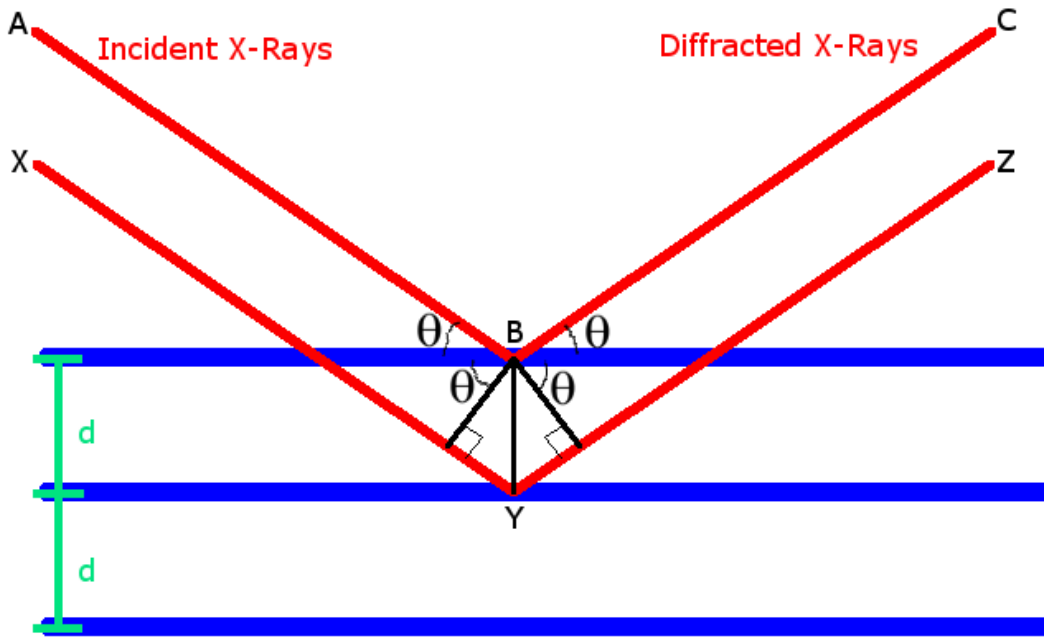


**Figure 2.4** A depiction of X-ray diffraction on a single crystal, using the terms found in Bragg's Law. The horizontal blue lines represent planes of atoms that are identical and repeated from one side of the crystal to the other. This periodic arrangement is the defining characteristic of a crystalline material.

When the difference between the path lengths ABC and XYZ are an integer multiple of the X-ray wavelength, the X-ray photons from each diffracting plane constructively interfere with each other. This condition is detected as a peak in the diffracted X-ray intensity at the angle of incidence at which this constructive interference occurs, which will also be dependent on the interplanar spacing of the crystal. The equation governing this constructive interference effect is known as Bragg's Law:

$$n\lambda = 2d \sin\theta \qquad \text{(Eq. 2.1)}$$

where λ is the wavelength of the incident x-ray, d is the interplanar spacing of the crystal, θ is the angle of incidence of the X-ray on the crystal, and n is any positive integer. The wavelength is a known value, defined by the X-ray source; for the Cu $K_\alpha$ X-ray tube (which is used for all patterns in this work), this wavelength is 1.542 Å. The penetration depth of these X-rays is dependent on the incident angle; however, the irradiated volume remains constant (as the spot size is also dependent on θ). The penetration depth is on the order of tens of micrometers[19], deep enough to obtain an average characterization of the bulk sample in the sample holder used, not just the surface of the nanoparticles.

The cartoon in Figure 2.4 represents diffraction from one crystal orientation. If θ is scanned from 0 to 90 $^{o}$ (impossible in practice; generally, scans are performed from 5 to 80 $^{o}$ at most), the ratio nλ/2d must be a positive number less than or equal to1 in order for diffraction to occur. Because this ratio is a constant for any given diffraction plane, a single set of Miller planes will diffract at a set of values of θ, one for each n, and have a (theoretical) intensity of 0 at all other angles of incidence. This is useful for determining the precise lattice spacing of a planes in a single crystal, but it is generally insufficient for identifying a particular structure or composition out of tens of thousands of known possibilities and almost impossible to determine the structure of a previously unknown crystalline compound.

Fortunately, we are not making single crystals. Nanoparticles are, obviously, agglomerations of huge numbers of individual crystals. Each particle can be

comprised of one or more domains, each of which will have a different orientation. Any given sample of nanoparticles can be assumed to contain all possible orientations of crystallites in a statistically random fashion (unless synthetic or growth conditions results in preferential orientation of the crystallized, as when the particles have a rod or platelet morphology, for example). To demonstrate this, assume a 10 mm x 10 mm x 100 μm sample of identical particles 10 μm in diameter. Such a sample would contain $(10*10^3)(10*10^3)(100)/(10^3) = 10^7$ nanoparticles, which is more than enough to assume every orientation has equal representation in the sample. Therefore, if the same diffraction experiment is conducted on such an assembly, the resulting diffraction peaks will contain peaks generated from all sets of Miller planes in the crystal. This is the principle behind pXRD.

pXRD can serve as a "fingerprint" to uniquely identify crystalline phases, as every crystal structure has a unique combination of lattice parameters and relative intensities of diffraction. One previously unmentioned factor that contributes to the fingerprint is the fact that different elements will diffract X-rays with different strengths. Generally, of the scattering amplitude increases linearly with atomic number Z and but dereases as angle of incidence θ increases (all atoms diffract more strongly at smaller angles than at higher angles).

Some further details regarding peak width and area are needed. First of all, it is important to recognize that symmetry-equivalent reflections will occur at the same value of 2θ. In a cubic crystal, for example, the value of the lattice spacing is equal to:

$$d = \frac{a}{\sqrt{h^2 + k^2 + l^2}} \quad \text{(Eq. 2.2)}$$

which means that the reflection (100) has five other reflections that show up at the same angle of incidence - (010), (001), (-100), (0-10), and (00-1). The multiplicity of this peak is, therefore, six. The intensity of any given peak is proportional, in part, to this multiplicity.

Up until now, the diffraction peaks have been treated as if they were infinitely narrow. This is obviously impossible in practice, though for perfect bulk samples (i.e., a single crystal of domain size greater than a micron or so, depending on the particular X-ray machine design) the width of the diffraction peak is effectively zero, limited only by the instrumental resolution. However, for nanoparticle assemblies, domain sizes are much smaller (generally between 2 and 50 nm). Peak broadening can come from a number of factors. In 1918, Paul Scherrer discovered that, if all other factors are accounted for, diffraction peak widths are inversely proportional to the domain size causing the reflection, following what is known as the Scherrer Equation:

$$\beta_L = \frac{K\lambda}{L\cos\theta} \quad \text{(Eq. 2.3)}$$

where L is the average domain size of the nanoparticles in Ångstroms, K is a constant that depends on the shape of the crystal (generally taken to be between 0.9 and 1), λ is the X-ray wavelength in Ångstroms, $\beta_L$ is the full width at half-maximum (FWHM, in radians) of the diffraction peaks *after* subtracting instrumental broadening, and θ is the angle of incidence.

As previously mentioned, Eq. 2.3 ignores other factors that can result in broadened peaks, such as strain, dislocations, grain boundaries, compositional inhomogeneity, and other imperfections in the crystal structure. Figure 2.5 illustrates how strain, for example, can affect the peak position and shape,

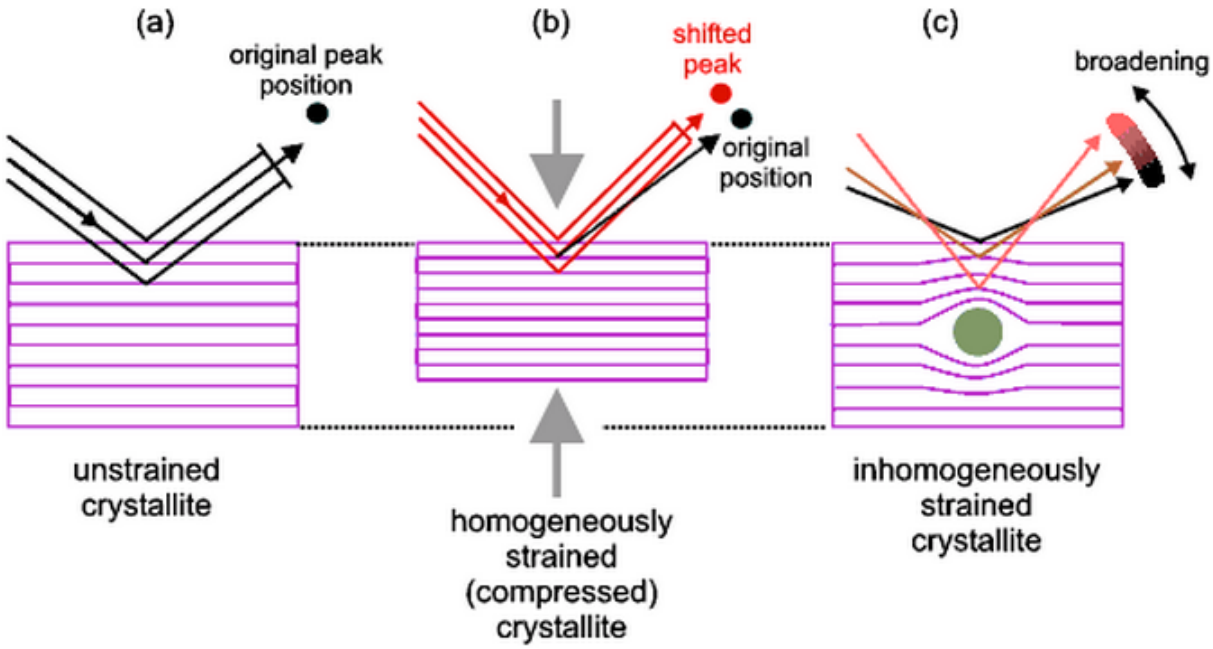


**Figure 2.5** An illustration of the effects of strain on peak position and broadening. Taken from Birkbeck College instructive materials[20].

Sample A in Figure 2.5 is a "normal" unstrained crystallite. Sample B is the same crystallite under homogenous compressive strain; note how the d-spacing of the refracting lattice plane has decreased, resulting in a shifting of the original peak position to a higher angle, following Eq. 2.1. Sample C is an inhomogenously strained crystal. The lattice is not uniformly deformed, resulting in a continuum of d-spacing

values. X-rays are diffracted at slightly different values, resulting in the peak smearing (broadening) across a range of 2θ values.

Nanoparticles often possess some strain in the lattice (surface strain is, after all, one of the primary reasons why they are considered to have good catalytic activity[21–23]). Strain is an inevitable concern in this domain, which is why the Scherrer equation is used in this work as a guideline to describe the relationship between the peak widths and domain sizes, and as a quick way to check domain size calculations. $\beta_L$ is more appropriately defined as the peak broadening due to domain size. The method utilized to calculate domain size in this work is the more sophisticated Williamson-Hall method[24], which comes standard in the PDXL whole-pattern powder-fitting software offered by Rigaku to go along with the Rigaku diffractometer that we use (Model ###). Williamson-Hall defines the broadening due to strain as a constant multiplied by the tangent of the angle of incidence.

$$\beta_e = C_e \tan\theta \qquad \text{(Eq. 2.4)}$$

Theoretically, it should be possible to deconvolute the peak broadening due to strain and domain size, if their effects on peak width simply sum together. Adding Eqs. 2.3 and 2.4 together and multiplying by cos(θ) gives the equation:

$$\beta_{tot} \cos\theta = C_e \sin\theta + \frac{K\lambda}{L} \qquad \text{(Eq. 2.5)}$$

where $\beta_{tot} = \beta_L + \beta_e$. This equation bears obvious similarities to the standard slope-intercept equation y = mx + b. Plotting $\beta_{tot} \cos\theta \; vs. \sin\theta$ will give a line with slope

$C_e$ and intercept $\frac{K\lambda}{L}$. Therefore, the intercept of such a plot (an example of which is given in Figure 2.6) will give the domain size of the particles free of the effects of strain, and as a side effect this method allows one to calculate the approximate degree of lattice strain present in the nanoparticles. Of course, this method has all of the difficulties inherent to any graphical method; namely, individual peaks with weak signals (and therefore high degrees of uncertainty in the FWHM) contribute equally to the line-fitting algorithm, which can easily result in domain sizes that are off by an order of magnitude. Checking the computer with an application of the Scherrerr equation on the strongest peaks is necessary.

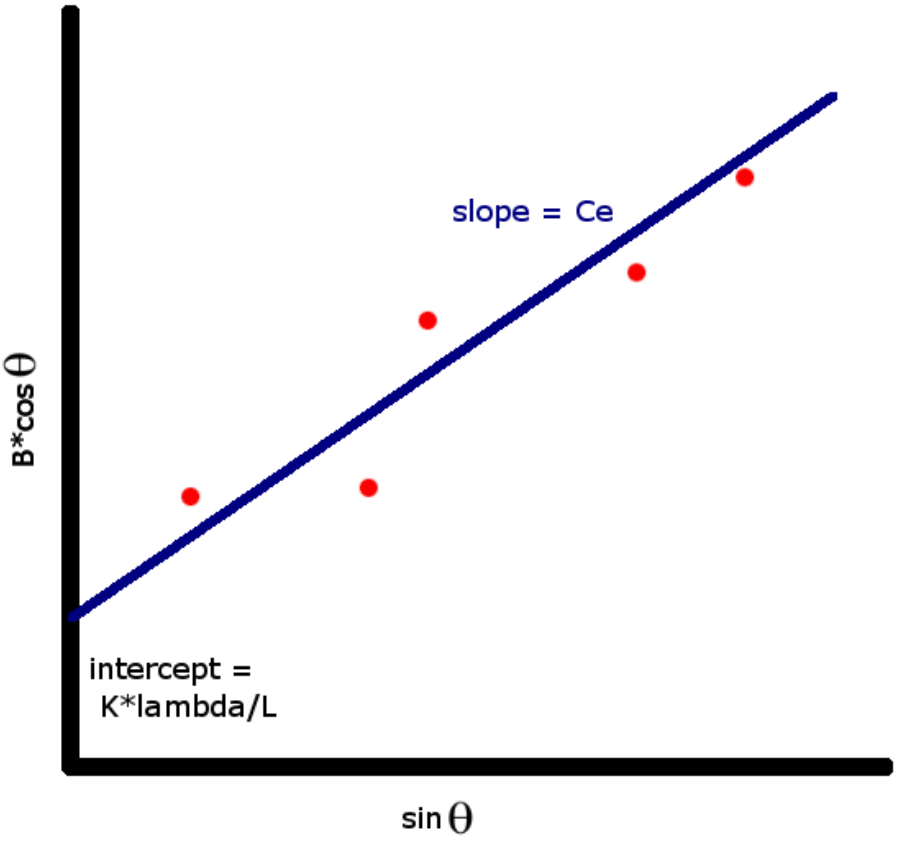


**Figure 2.6** An example of a Williamson-Hall plot used to determine the domain size L

of a nanoparticle ensemble. The red points are determined from individual peaks in the pXRD pattern. The regression line (blue) is calculated by PDXL automatically; outliers must be identified and removed in order to correctly determine the domain size.

Domain size and strain are not the only additional factors to look for in pXRD patterns after first considering peak positions and intensities. Asymmetry is another irregularity. When a peak has a "shoulder" - in other words, when one side of a peak has a different shape than the other side - it can signify a host of other defects or deviations from perfect crystallinity of particles, or a distribution in particle sizes, etc.[19]. Yet another irregularity to watch for is "conically" shaped peaks; i.e., peaks with broad bases but narrow FWHM and a sharp point. This shape is indicative of a superposition of peaks with a large distribution of FWHM values; in other words, a large distribution of domain sizes. When calculating the domain size of a phase with such peaks, the small domains make little or no contribution to the FWHM by the nature of the calculation. That is, those peaks with large FWHM have a low peak intensity, while peaks with small FWHM have a high peak intensity.

Thus we see why pXRD is such a useful and ubiquitous tool for analyzing nanoparticle samples. It is a fast, non-destructive technique that requires little sample preparation. It gives an accurate picture of all crystalline phases present in a sample and can therefore immediately identify whether or not the sample has multiple crystalline phases. Very little sample is required to achieve a high signal-to-noise

ratio; a few milligrams is sufficient. Lastly, the PDXL software package can use peak-fitting algorithms to calculate domain size, strain, percent phase composition, and shifted lattice parameters.

### *2.3.2 Thermogravimetric Analysis*

The synthetic method used in this work for the preparation of nanoparticles dispersed onto carbon black was described in section 2.2.3. While the amount of carbon black in the round-bottomed flask was carefully measured to give as close to the desired loading level as possible (generally 20 wt% by total metal content, unless otherwise specified), the fact that the nanoparticles were reduced *onto* the carbon leaves open the possibility of inhomogenous distribution of metal on carbon, both on the micro- and the macroscale. While the microscale distribution was investigated by high-resolution microscopy techniques (see the following sections), the macroscale ratios of metal to carbon were investigated with thermogravimetric analysis (TGA).

TGA is, in essence, a very finely tuned balance surrounded by an enclosed container and further enclosed by a heating element. The principle behind TGA is simple: heat a small amount of sample (under flowing argon or air) on a set heating profile, and measure the mass as a function of temperature. The benefit of this analysis is that carbon under flowing air will eventually oxidize to $CO_2$ and be swept out of the inner enclosure by the flowing gas, causing a reduction in the mass of the sample that can be measured and used to calculate the weight percentage of carbon in the original sample.

The sample mass can be accurately measured to +/- 1 microgram or less, a level of precision necessary when dealing with small changes of mass in samples that can be as light as a milligram. This is achieved by an internal balance system where an internal platinum pan on which an alumina or platinum dish holding the sample is placed. Due to the delicate nature of these very fine pieces of analytical equipment, all samples and pans must be handled by tweezers to avoid inadvertent bending or breaking or contamination from dirt, grease or other substances that may be on the operators hands or in the local environment.

The TGA used in this work is a TA Instruments TGA Q50. For all TGA analyses, roughly 6 mg of sample were heated at a rate of 10 $^{o}$C/min to a maximum temperature of 550 $^{o}$C, where it was held for an additional 30 minutes. In all cases, the mass remained constant during the hold period, which is an indication that any and all reactions had reached completion by that point. This is necessary to properly calculate the weight percentage. A sample TGA trace from this instrument (of the phase $Pt_3Sn$/C, prepared to attain 20 wt% loading) is shown in Figure 2.7.

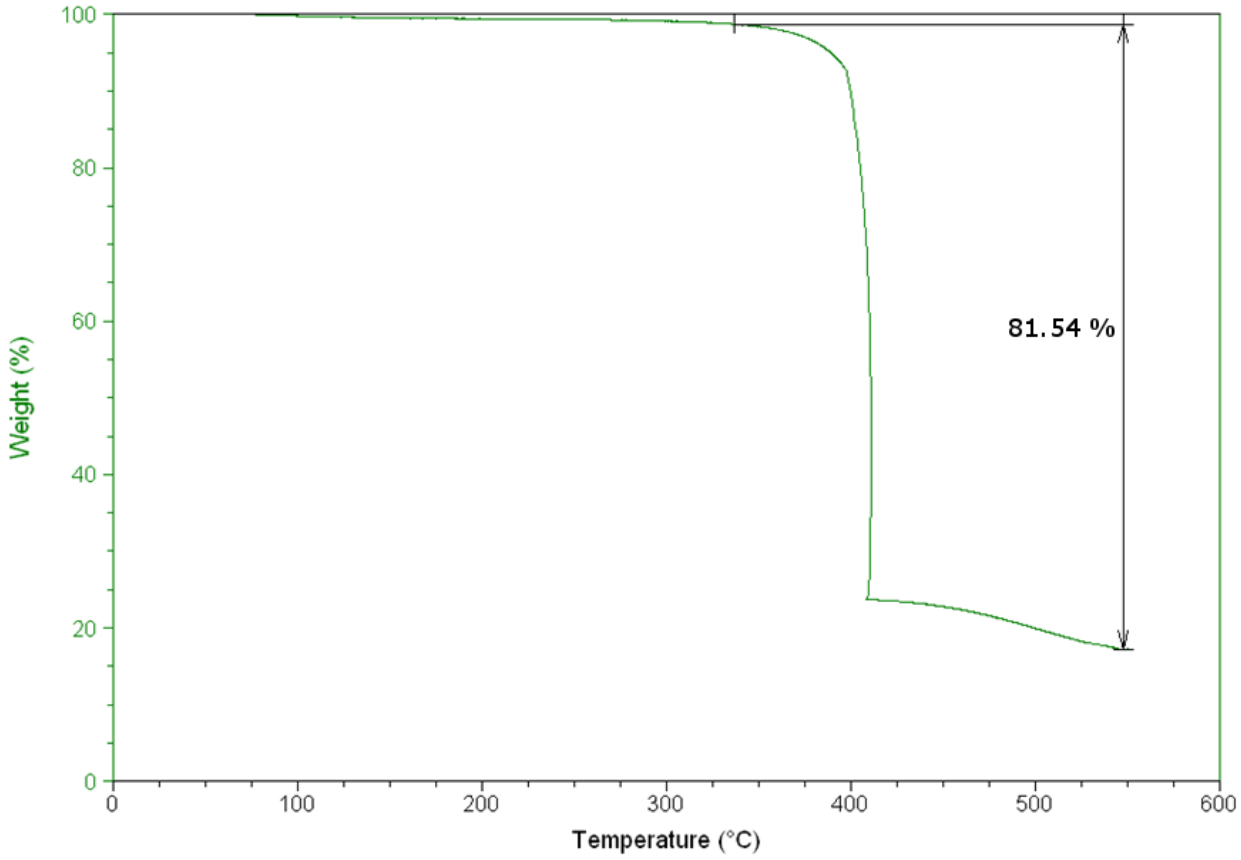


**Figure 2.7** Example TGA trace of $Pt_3Sn/C$ heated to 550 $^{o}C$ under flowing air.

The onset of mass loss at around 350 $^{o}C$ indicates the start of the oxidation of carbon black to $CO_2$. The rapid drop in mass near 420 $^{o}C$ then levels off to about an 82 % total drop in weight from before the onset to the final mass. As a first approximation, this is the mass of carbon lost to oxidation, so the loading of the sample is indeed roughly 20 wt%. However, there is another factor here: the oxidation of the metal itself. Platinum will not oxidize significantly under these conditions, but certain other non-noble metals (tin included) will. When metals oxidize, rather than decreasing the mass of the sample, they increase the mass by incorporating oxygen.

For example, assuming Sn oxidizes fully to $SnO_2$, the total weight loss observed by TGA of a given amount of $Pt_3Sn/C$ will be (assuming m(X) is the mass of component X):

$$obs.\ loss(\%) = \frac{m(initial) - m(final)}{m(initial)} \times 100\% \quad \text{(Eq. 2.6)}$$

$$obs.\ loss(\%) = \left\{1 - \frac{m(final)}{m(initial)}\right\} \times 100\%$$

$$obs.\ loss(\%) = \left\{1 - \frac{m(Pt) + m(Sn) + m(O)}{m(Pt) + m(Sn) + m(C)}\right\} \times 100\%$$

Set $m(Pt) + m(Sn) = x$, and $m(C) = y$, to make the following equations easier to follow. The mass of oxygen incorporated is proportional to the mass of $Pt_3Sn$ (ie, "x"). Assuming total oxidation of tin, which is supported by the TGA trace flattening before 550 $^{o}$C, and also that the entire sample is in a 3:1 ratio of Pt:Sn, the mass of oxygen is equal to:

$$m(O) = \frac{2 * MW(O)}{MW(Sn) + 3 * MW(Pt)} x = \frac{32}{704} x \quad \text{(Eq. 2.7)}$$

Substituting Eq. 2.7 into Eq. 2.6 gives:

$$obs.loss(\%) = \left\{1 - \frac{x + \frac{32}{704}x}{x + y}\right\} \times 100\% \quad \text{(Eq. 2.8)}$$

$$= \left\{1 - \frac{1.045x}{x + y}\right\} \times 100\%$$

The percent loading is given by the equation

$$loading(\%) = \frac{x}{x + y} \times 100\% \quad \text{(Eq. 2.9)}$$

Which means it is unnecessary to solve Eq. 2.9 completely; we need only rearrange Eqn 2.8 to find the loading in terms of the observed mass loss.

$$\frac{1 - obs.loss(\%)}{1.045} = \frac{x}{x+y} = \frac{loading(\%)}{100\%} \quad \text{(Eq. 2.10)}$$

Which, for the sample in Figure 2.4, gives a actual metal loading of 17.8%. Without taking the additional oxygen into account, the metal loading would be calculated to simply be 1-0.815 = 18.5%, roughly a 5% difference in the weight percent. The significance of the oxygen increases as the proportion of Sn in the nanoparticle increases.

*2.3.3 Scanning Electron Microscopy and Energy-Dispersive X-ray Spectroscopy*

The next two techniques that will be discussed were always performed in tandem: scanning electron microscopy (SEM) and energy-dispersive X-ray spectroscopy (EDX). SEM, as the name implies, uses electrons in place of photons to image surfaces at high resolution, on the order of a nanometer depending on the instrument and the parameters under which it is operated. A rigorous treatment of electron beam optics is beyond the scope of this dissertation; suffice it to say that an electron beam is directed at the surface of the analyte material in a high-vacuum chamber, which produces secondary electrons as ionization products through inelastic scattering. It is these secondary electrons that are used to produce the image of the sample (other detectors are possible, including back-scattered electrons, but secondary electron detection was the method used in this work for all SEM images).

As previously stated, SEM is a surface technique; visible secondary electrons are only produced in the first few nanometers of a metal, depending on the beam strength. The images also have a large depth of field. This means that topography and other physical surface characteristics can be investigated, as three-dimensional features are easily identified by eye. One can even note the presence of "shadows" where the electron beam is obstructed, which adds to the dimensionality of the image.

The voltage of the electron beam can be set to different values depending on the material under analysis, the desired images, and other factors (such as whether or not EDX is simultaneously occurring, which will be discussed later). Lower voltages (5-15 kV) is useful for specifically investigating the surface, as the topography and will be more distinct and the contrast will be greater. It is also good in cases where a sample is a poor conductor or is not in good electrical contact with the substrate; higher voltages will result in charging of the sample (a build-up of electron density due to ionization) which will result in columbic forces repelling incident electrons. However, a higher-energy electron beam (15-30 kV) can also be useful. The beam is narrower, resulting in higher resolution, particularly at edges. Furthermore, the beam energy must be high enough to produce secondary electrons. The stronger the beam, the stronger the secondary electron signal. Of course, samples that contain carbon or other organics can actually be destroyed by a high-energy beam.

Figure 2.8 is a representative SEM image of PtZn/C acquired at 10 kV at moderately high resolution using a LEO 1550 FESEM with an electron beam voltage of 10 kV.

Note how the topography of the sample is clearly distinguishable. The carbon support in the sample emits fewer secondary electrons, and is therefore darker than the bright metal nanoparticles, which show up as bright white dots distributed over the surface of the carbon black. The black void is the sticky carbon paper supporting the sample.

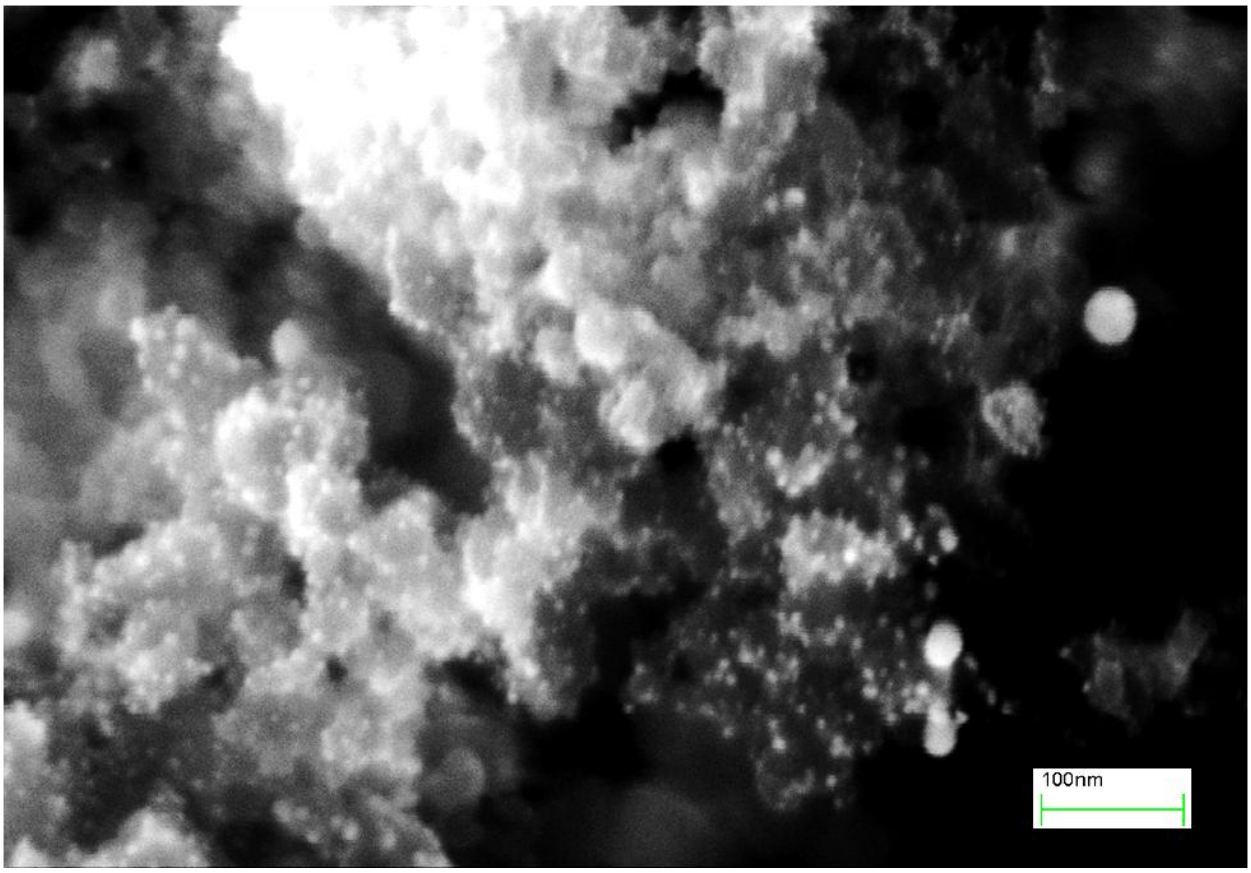


**Figure 2.8** SEM image of PtZn reduced onto carbon black.

EDX uses the same instrument equipped with a different detector. The incident electron beam produces characteristic X-rays from the sample, which are element-specific. By collecting these X-rays over a period of time - generally one minute, unless higher resolution is needed or the sample signal is poor - the atomic percentage of all elements in a sample can be calculated. An example of the data collected and

analyzed by EDX is shown in Figure 2.9. The extremely large peaks at low x-ray energies correspond to low-Z elements (C, O, N, S, etc) and are not included in the calculations for atomic ratio. These generally arise from surface contamination or the carbon support, or the carbon tape.

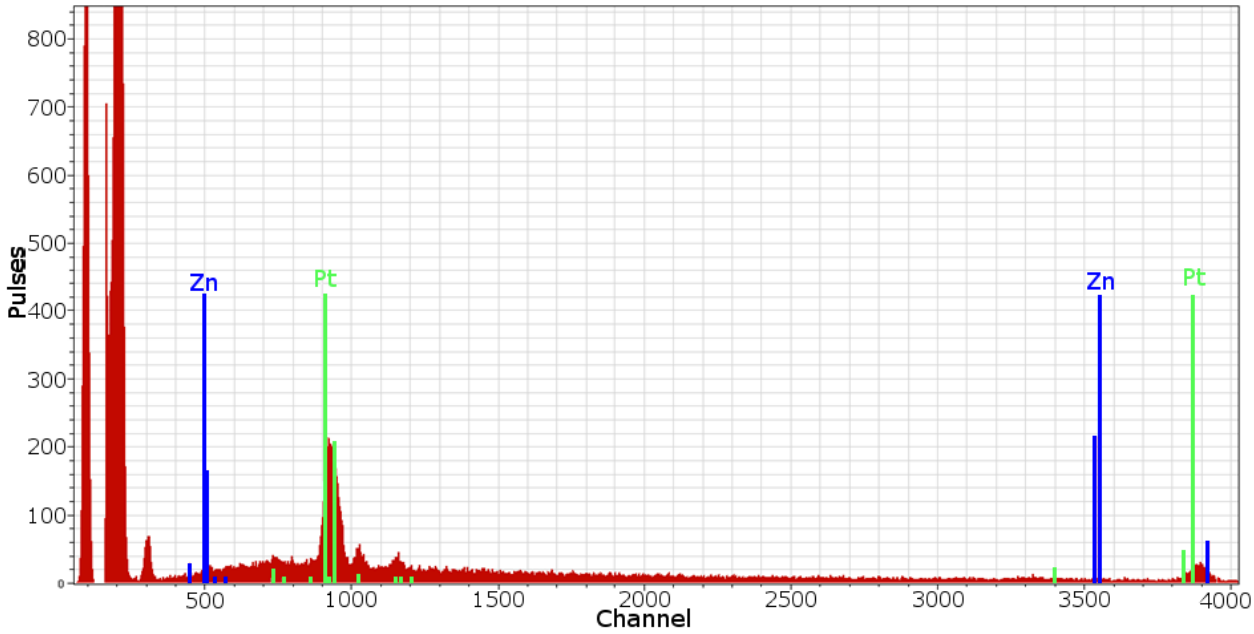


**Figure 2.9** EDX trace for PtZn/C. The x-axis is proportional to x-ray energy, and the y-axis is signal count.

There are a few caveats that need to be taken into account when performing this analysis. First of all, some elements have characteristic X-ray energies that are similar enough that they cannot be resolved. When this occurs, it is necessary to choose different characteristic X-rays to use for the elemental composition calculation. Note in Figure 2.6 how both Pt (green) and Zn (red) have two main visible peaks in the sample window. Increasing the incident electron energy increases the number of possible characteristic X-ray emissions that are visible. As a general rule, the electron

beam voltage should be set to a value at least three to five times greater in energy than the highest characteristic X-ray energy to be observed.

All scanning electron microscopy (SEM) images and energy dispersive X-ray analysis (EDX) data were acquired on a LEO-1550 field emission SEM. SEM specimens were prepared by attaching a piece of sticky carbon paper - an electrical conductor - to an aluminum stub, and gently dispersing less than a milligram of sample over the paper. This allows for easy sample immobilization, which is important for tiny amounts of nanoparticles which are easily blown around. Beam strength varied between 5 to 30 kV for the images depending on the sample, as did the working distance (the distance between the sample and the beam emitter). Later chapters will deal with the information that can be extracted from SEM images on a case-by-case basis, as much of the image analysis come down to inferences and the presence of individual features.

*2.3.4 Transmission Electron Microscopy*

Transmission Electron Microscopy (TEM) is similar to SEM in that it uses a focused electron beam in order to investigate samples, but instead of looking at secondary electrons excited from the surface, TEM uses electrons that go straight through the sample. These transmitted electrons are detected on the far side of the sample, and are used to construct the image. TEM beam voltages are necessarily much higher than SEM voltages, on the order of 100-300 kV. TEM samples must also be much thinner than SEM samples, typically less than 100 nm , as resolution and contrast are decreased significantly as electrons pass through the sample and are slowed by

inelastic interactions.

TEM, due to the much higher energy beam, can have much higher resolution than SEM. Properly calibrated, it is possible to observe individual atoms, and measure the d-spacing values (distance between Miller planes) of crystalline materials through what are called "lattice fringes". Some of the transmitted electrons are strongly scattered, with scattering increasing with atomic number (Z) of the element, which means that TEM also produces pictures with innate elemental differentiation. On the other hand, TEM has effectively zero topographical information, as every pixel is effectively a summation of the interactions of all atoms in that vertical slice of the sample travelled by the scattered electron. Because of this, nanoparticles must be separated (either by surfactants or by a support of some kind) in order to acquire decent TEM images; TEM of agglomerated nanoparticles provide very little useful information.

An example of the high resolution possible with TEM is shown in Figure 2.7. Continuing from the previous section's theme, Figure 2.10 is the same PtZn/C sample at high magnification. The lattice fringes can be used to identify the sample as pure PtZn. TEM is one of the most effective methods of determining particle size and distribution by measuring over an ensemble of particles (at least 100). The number of domains in a single particle can also be observed; in this case, the entire particle appears to be a single continuous crystalline domain. These are just a few of the characteristics that can be determined via TEM analysis.

Two separate TEM instruments were used in this work. The lower-resolution instrument was a FEI T12 Spirit TEM. The resolution of this instrument is not consistently high enough to determine the lattice spacings of crystalline domains; however, it is useful for determining particle size, distribution, homogeneity, and other properties. Higher resolution images (such as Figure 2.10) were taken on a FEI Tecnai F20 TEM STEM operated at 200 kV.

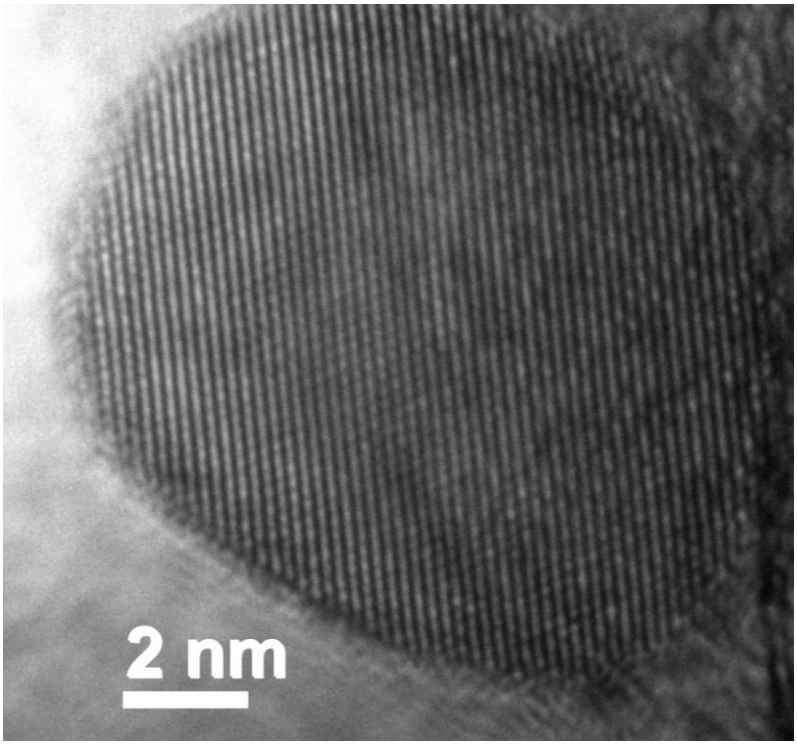


**Figure 2.10** TEM image of PtZn/C particle. The amorphous material on the right hand side of the image is the carbon support, and the light void on the left and bottom are the lacy carbon sample holder.

### *2.4 Conclusions*

The experimental synthetic procedure outlined above is a tunable, flexible method for the formation of intermetallic nanoparticles of many different compositions, both with and without a carbon black support. It can be adjusted on the fly to accommodate different solubilities and reactivities to produce the greatest yield of nanoparticles possible. It is also a very clean technique, limiting the number of species present in solution to the minimum necessary to prevent interference with the co-reduction reaction, and to produce nanoparticles with few, if any, surface impurities.

The analytical techniques are similarly broad in scope. pXRD is applicable to all crystalline samples and is the first technique used for sample identification in all cases. SEM, EDX, and TEM complement each other. They provide information about the sample's elemental composition; surface structure; crystallinity; particle size, distribution, and heterogeneity; and identify amorphous side products or impurities that pXRD cannot see. Together, these synthetic and analytical techniques describe the majority of the samples and data that will be presented in the next two chapters.

REFERENCES


(1) Coutanceau, C.; Baranton, S.; Napporn, T. *Nanoparticles/Book* **2011**, *2*.
(2) Zhang, X.; Chan, K.-Y. *Chem. Mater.* **2003**, *15*, 451–459.
(3) Capek, I. *Adv. Colloid Interface Sci.* **2004**, *110*, 49–74.
(4) Rioux, R. M.; Song, H.; Grass, M.; Habas, S.; Niesz, K.; Hoefelmeyer, J. D.; Yang, P.; Somorjai, G. A. *Top. Catal.* **2006**, *39*, 167–174.
(5) Chen, W.-X.; Lee, J. Y.; Liu, Z. *Mater. Lett.* **2004**, *58*, 3166–3169.
(6) Komarneni, S.; Li, D.; Newalkar, B.; Katsuki, H.; Bhalla, A. S. *Langmuir* **2002**, *18*, 5959–5962.
(7) Herricks, T.; Chen, J.; Xia, Y. *Nano Lett.* **2004**, *4*, 2367–2371.
(8) Sun, S.; Anders, S.; Thomson, T.; Baglin, J. E. E.; Toney, M. F.; Hamann, H. F.; Murray, C. B.; Terris, B. D. *J. Phys. Chem. B* **2003**, *107*, 5419–5425.
(9) Liu, Z.; Jackson, G. S.; Eichhorn, B. W. *Angew. Chem. Int. Ed.* **2010**, *49*, 3173–3176.
(10) Zhang, W. L.; Jiang, H. C.; Zhang, J. P.; Zhang, W. X. *J. Magn. Magn. Mater.* **2004**, *284*, 128–132.
(11) Jirkovský, J.; Makarova, M.; Krtil, P. *J. Electrochem. Soc.* **2005**, *152*, A1613.
(12) Mosleh, Z.; Kameli, P.; Ranjbar, M.; Salamati, H. *Ceram. Int.* **2014**, *40*, 7279–7284.
(13) Wang, K.-W.; Chung, S.-R.; Jang, L.-Y.; Lee, J.-F.; Perng, T.-P. *J. Alloys Compd.* **2006**, *426*, 341–344.
(14) Kim, J.; Lee, Y.; Sun, S. *J. Am. Chem. Soc.* **2010**, *132*, 4996–4997.
(15) Chen, H. A Surfactant-Free Strategy For Synthesizing And Processing Intermetallic Platinum-Based Nanoparticle Catalysts. Dissertation, Cornell University: Ithaca, NY, 2013.
(16) Nguyen, M. T. Synthesis of Carbon Supported Ordered Intermetallic Nanoparticles as Oxygen Reduction Catalysts in Polymer Electrolyte Membrane Fuel Cells. Dissertation, Cornell University: Ithaca, NY, 2014.
(17) Shriver, D. F.; Atkins, P. W.; Langford, C. H. *Inorganic Chemistry*; W. H. Freeman and Company: New York, NY, 1990.
(18) Chen, H.; Wang, D.; Yu, Y.; Newton, K. A.; Muller, D. A.; Abruña, H.; DiSalvo, F. J. *J. Am. Chem. Soc.* **2012**.
(19) Cullity, B. . *Elements of X-Ray Diffraction*; Addison-Wesley Series in metallurgy and Materials; 2nd ed.; Addison-Wesley Publishing Company, Inc.: Reading, Massachusetts, 1978.
(20) Barnes, P.; Jacques, S.; Vickers, M. Crystallite Size and Strain. *Birkbeck College, University of London*, 2006.
(21) Wang, J. X.; Inada, H.; Wu, L.; Zhu, Y.; Choi, Y.; Liu, P.; Zhou, W.-P.; Adzic, R. R. *J. Am. Chem. Soc.* **2009**, *131*, 17298–17302.
(22) Strasser, P.; Koh, S.; Anniyev, T.; Greeley, J.; More, K.; Yu, C.; Liu, Z.; Kaya, S.; Nordlund, D.; Ogasawara, H.; Toney, M. F.; Nilsson, A. *Nat. Chem.* **2010**, *2*, 454–460.

(23) Zhang, S.; Zhang, X.; Jiang, G.; Zhu, H.; Guo, S.; Su, D.; Lu, G.; Sun, S. *J. Am. Chem. Soc.* **2014**, *136*, 7734–7739.
(24) Williamson, G. .; Hall, W. . *Acta Metall.* **1953**, *1*, 22–31.

CHAPTER 3

THE PT-SN PHASE DIAGRAM: A MODEL SYSTEM

### *3.1 $Pt_{1-x}Sn_x$ Phases*

Pt-Sn was chosen as the main binary system to begin our exploration of the formation of ordered intermetallic nanoparticles for two reasons. First, the phase diagram (as seen in Figure 3.1) is comprised of five distinct "line phases" which adopt ordered, crystallographically distinct structures in the bulk when prepared by standard solid state, high temperature techniques. The primary goal of this work is to determine if these phases can be formed in the nanoparticle regime by co-reduction, and if so, can any useful information about the synthesis and properties of the resultant nanoparticles be reasonably predicted by the bulk phase diagram.

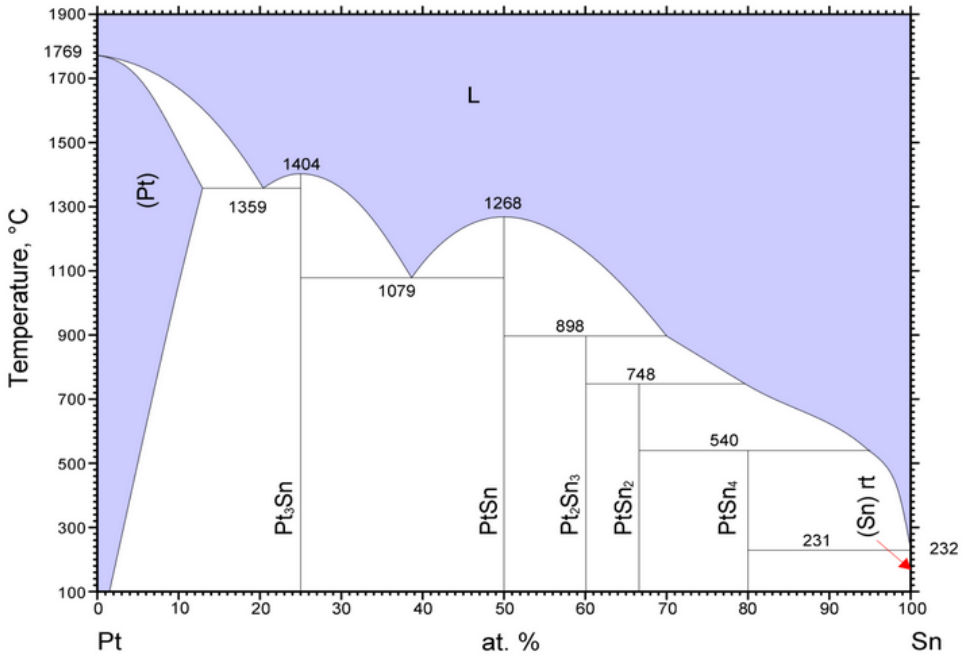


**Figure 3.1** The binary phase diagram of the Pt-Sn system. Dark areas represent single-phase regions. Taken with permission from ASM Alloy Phase Diagram Database[1].

Second, nanophase Pt-Sn compounds have been shown to be good catalysts for hydrogen, formic acid, methanol, and ethanol oxidation under PEMFC conditions[2–5], and also show activity for the oxygen reduction reaction[6]. Therefore, the facile synthesis of Pt-Sn nanoparticles is a step on the path to address the environmental and energy-related concerns highlighted in Chapter 1. Much of the data and analysis presented in this chapter has been recently published[7].

The co-reduction method was described in Chapter 2, utilizing lithium triethyl borohydride (LBH) and potassium triethyl borohydride (KBH) to rapidly reduce metal chloride precursors - platinum (IV) chloride ($PtCl_4$) and tin (II) chloride ($SnCl_2$) or tin (IV) chloride ($SnCl_4$) - in tetrahydrofuran (THF) to as-made nanoparticles, which were then sealed under vacuum and annealed at appropriate temperatures to form ordered intermetallic nanoparticles. Two equivalents of LiCl were added to improve the solubility of $PtCl_4$ in THF prior to the reduction. As is customary, we express the composition of the target binary phases in mole fractions: $Pt_{(1-x)}Sn_x$.

*3.1.1 x = 0 and 1 (i.e. elemental Pt and elemental Sn)*

To demonstrate the effectiveness of the reducing agent on the chloride precursors, the end members at x = 0 and x = 1 were explored first. For x = 0, platinum (IV) chloride was reduced The Pt chloride undergoes a facile, fast reduction to agglomerated as-made Pt nanoparticles. The nanoparticles prepared by LBH reduction were examined by pXRD, shown in Figure 3.2, and found to have an average domain size of 4.5 ± 1.0 nm via a Williamson-Hall analysis (see Chapter 2.3.1).

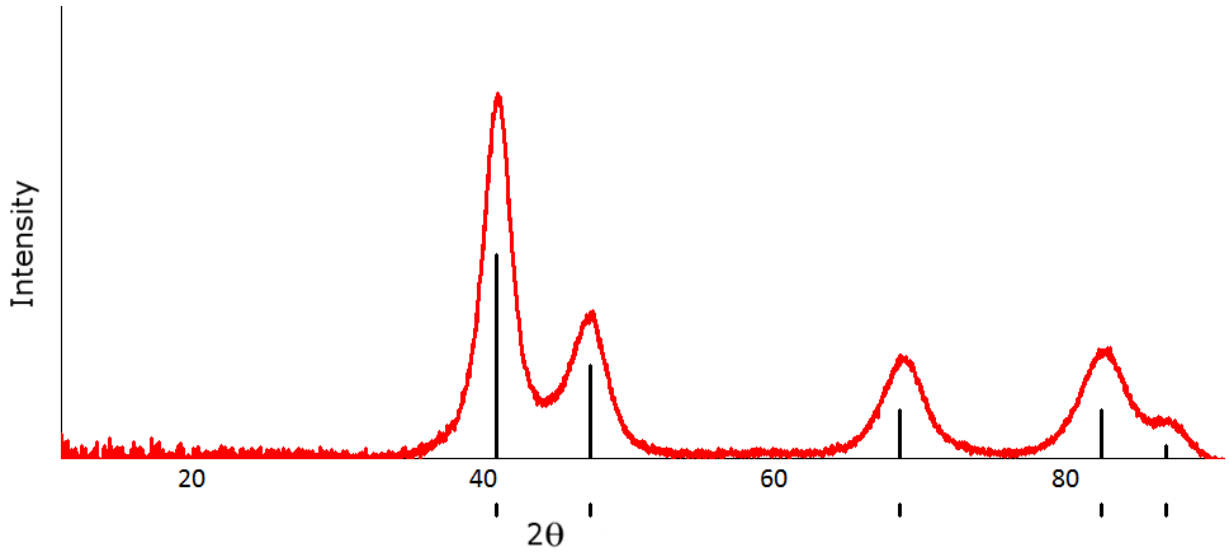


**Figure 3.2** The pXRD of Pt obtained by reduction of $PtCl_4$ via LBH at room temperature. The vertical black tick marks below the diffraction angles (10-90 $^{o}$ 2θ) show the expected position of the peaks observed for bulk FCC Pt powder (from PDF card# 04-016-6405). The black drop lines above the horizontal axis indicate relative intensities expected for bulk Pt.

Recall from Chapter 2 that KCl, unlike LiCl, is insoluble in THF. Reductions using the KBH reducing agent, therefore, result in an insoluble KCl matrix that traps the metal nanoparticles, limiting or preventing their agglomeration compared to the as-made nanoparticles synthesized with LBH (see Figure 3.3). This matrix can also serve to reduce the growth of nanoparticles on annealing, as demonstrated by Hao Chen's previous work in the group[8,9]. The domain size of as-made Pt nanoparticles reduced by KBH was found to be 3.1 ± 0.5 nm. Upon annealing to 200$^{o}$C, the domain size increased to 3.8 ± 0.4 nm (see Figure 3.4), which is still smaller than the domain sizes of particles reduced by LBH.

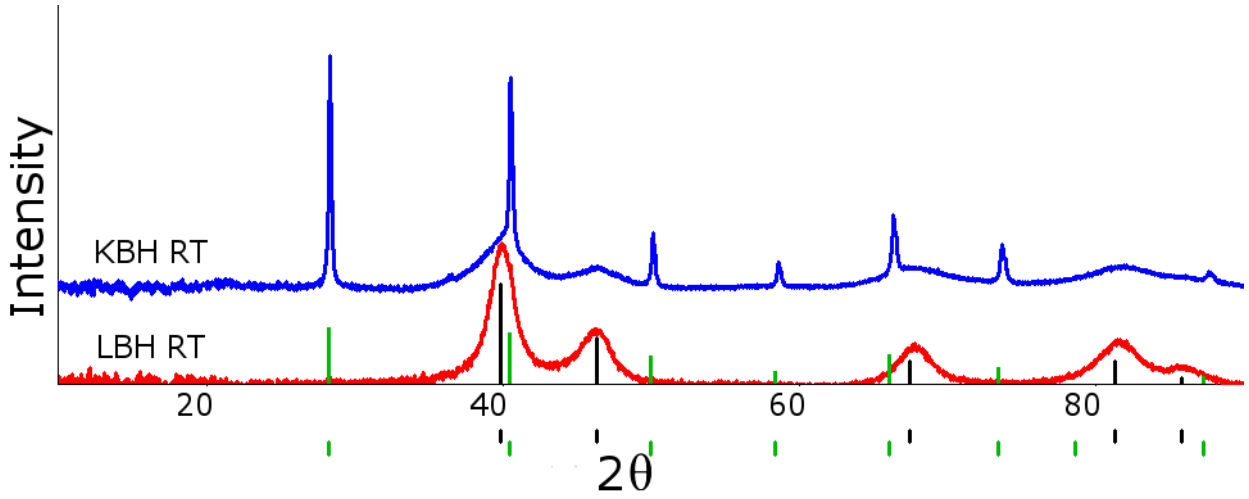


**Figure 3.3** A comparison of as-made nanoparticles of Pt reduced with KBH and LBH. The sharp peaks correspond to the KCl matrix (green tick marks and drop lines) encapsulating the particles. Black drop lines correspond to Pt standard.

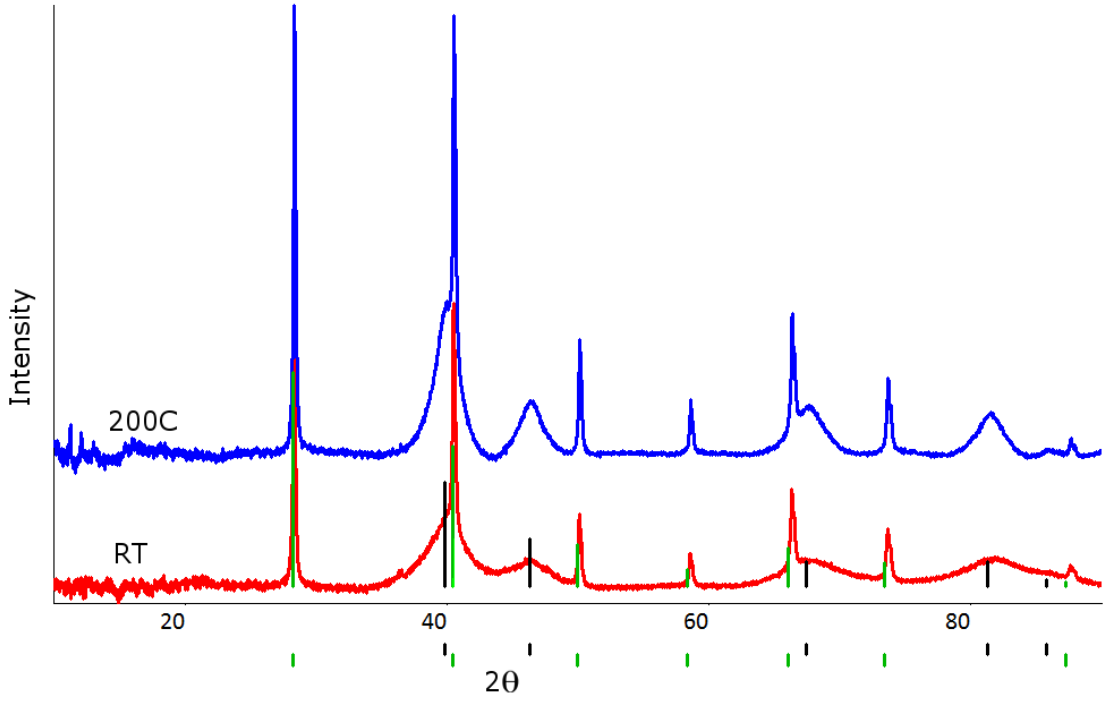


**Figure 3.4** A comparison of as-made Pt nanoparticles reduced with KBH with the same nanoparticles annealed to 200 $^{o}$C. The particles are separated from each other by the KCl matrix. Dark green lines indicate the peaks of the KCl matrix, black lines correspond to Pt.

Pure tin nanoparticles can be readily prepared via reduction by LBH at room temperature. These particles will oxidize quickly in air, forming a shell of tin oxide on the surface of the nanoparticles. To avoid this, the pXRD pattern was taken under air-free conditions by preparing the sample holder in the glovebox, and covering it with a Mylar film sealed with a thin layer of silicone grease. The Mylar film has broad diffraction peaks in the region of 15-30 $^{o}$ 2θ. The pXRD 2θ scan was chosen so that these peaks were minimized in Figure 3.5, and the remaining background was subtracted. The remaining sharper peaks match the pattern for Sn, with a relatively large domain size of 21 nm.

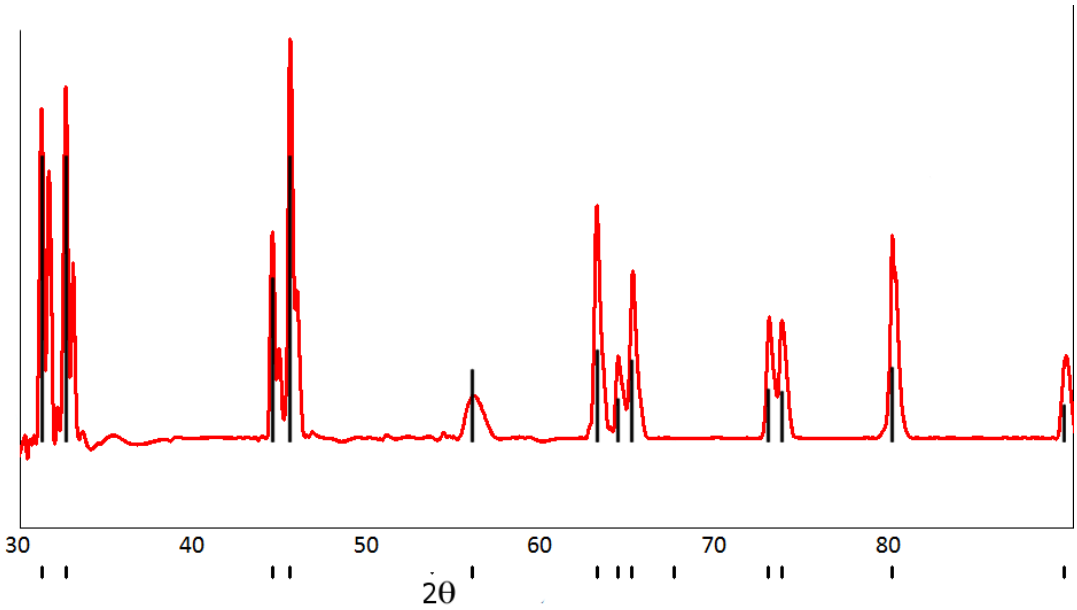


**Figure 3.5** Air-free powder XRD pattern of Sn nanoparticles reduced by LBH at room temperature. PDF card# 04-016-6444 (Sn).

3.1.2 $x \leq 1/2$ ($Pt_3Sn$ and PtSn)

The most platinum-rich compound in the Pt-Sn system, $Pt_3Sn$, has the highest bulk melting temperature (congruent melting point of 1404 $^{o}$C) of all the Pt-Sn phases. In spite of this, $Pt_3Sn$ was found to order at annealing temperatures as low as 200 $^{o}$C when reduced with LBH. The

superlattice peaks (so-called "ordering peaks", indicated by asterisks in Figure 3.6) for the $Pt_3Sn$ phase are quite weak, since the scattering power of Sn and Pt are not too different and because the mole fraction of Sn is low. Nonetheless, these peaks can be used to gauge the degree of ordering in the sample, by comparing the peak height ratios of the annealed samples to the peak height ratios in the reference powder pattern. The scaled peak intensities are shown in Table 3.1.

| **2θ (°)** | **39.0** | **45.4** | **51.0** | **56.5** |
|---|---|---|---|---|
| **(hkl)** | **(111)** | **(200)** | **(210)** | **(211)** |
| **Calculated $Pt_3Sn$** | 100 | 46 | 1.1 | 0.8 |
| **$Pt_3Sn$ 200°C** | 100 | 36 | 4.1±1.1 | 2.3±1.0 |
| **$Pt_3Sn$ 400°C** | 100 | 52 | 2.7±0.6 | 2.7±0.2 |

**Table 3.1** Experimental and calculated X-ray peak intensities for $Pt_3Sn$ samples annealed at 200 and 400 °C, normalized to the large (111) peak taken as 100.

Increasing the temperature from 200°C to 400°C results in a small change in the relative peak intensities, but because the superlattice peaks in $Pt_3Sn$ are so weak, the small difference results in a change in the peak height ratios of 15-40 %, depending on which peaks are compared. Within the signal to noise ratio of the data, these are essentially the same. It is therefore concluded that the $Pt_3Sn$ nanoparticles are nearly 100% ordered in both annealed samples.

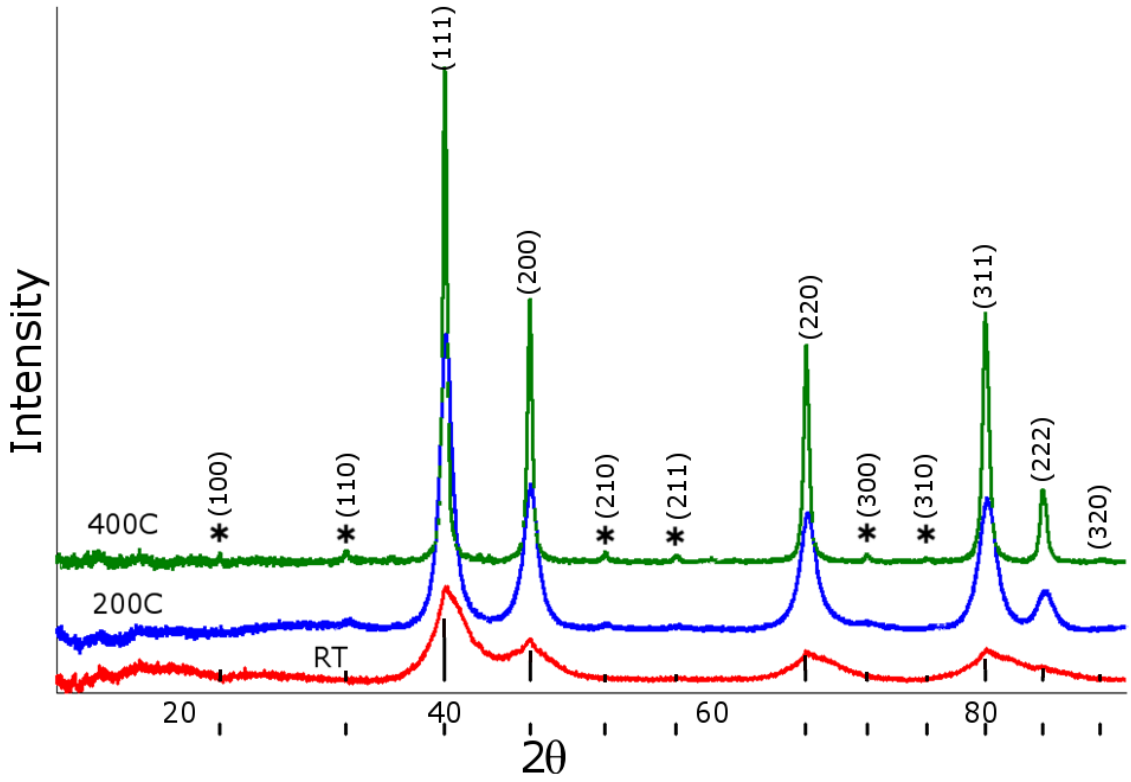


**Figure 3.6** pXRD patterns of $Pt_3Sn$ as-made agglomerated nanoparticles, and nanoparticles annealed without exposure to air for 24 hours at 200 °C and 400 °C. The room temperature peaks are very broad and asymmetric, indicating small particle sizes, compositional variation, and possibly stacking disorder. By 400 °C the domain size has increased to approximately 14.5 ± 0.7 nm**.** Drop lines correspond to $Pt_3Sn$**,** PDF card# 04-007-4093.

In contrast, pXRD patterns of PtSn (x = 0.5) nanoparticles that were obtained by LBH reduction and subsequently exposed to air without any annealing match the reference pattern for the ordered hexagonal PtSn phase reported for bulk samples, as shown in Figure 3.7. No peaks are unaccounted for, excluding the presence of Pt, Sn, Pt-Sn intermetallics of different composition, or crystallized oxides. The large width of the peaks indicates that the crystallization is coherent only on the nanometer scale (domain size of 4.3 nm at RT and 5.5 nm at 200 °C). Note the large

asymmetry in the (102) peak at approximately 42 ° for the RT sample, which likely indicates some kind of disorder or non-stoichiometry.

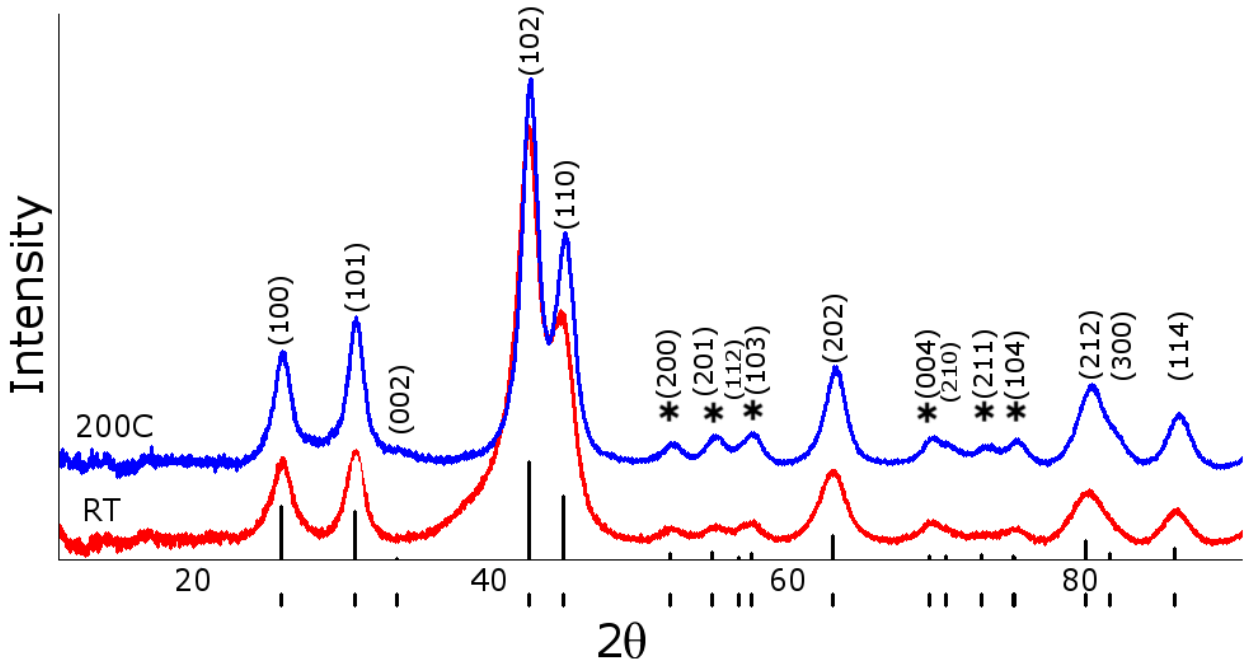


**Figure 3.7** Powder X-ray diffraction pattern of as-made PtSn nanoparticles, and nanoparticles annealed at 200 °C. Major ordering peaks are marked with an asterisk. Domain sizes were calculated to be 4.3 nm via Williamson-Hall. Drop lines correspond to PtSn, PDF card# 04-007-4095.

The presence of superlattice peaks in the region of 50-60 ° and the "splitting" of the expected cubic reflections for a hypothetical cubic alloy shows that the PtSn nanoparticles have adopted the ordered hexagonal structure expected from the bulk phase diagram. However, a more detailed analysis is need to show that the particles are 100% ordered phase, as a disordered hexagonal PtSn also would produce pXRD peaks at very similar values of 2θ. Of course, if fully disordered, there is presumably little driving force to take the structure from cubic to hexagona1. This is demonstrated in Figure 3.8 by a theoretical calculation of the powder patterns of Pt-Sn

1:1 phases with two different structures, similar to Figure 1.5, which compared the (simpler) theoretical pXRD patterns of Pt-Sn 3:1 phases.

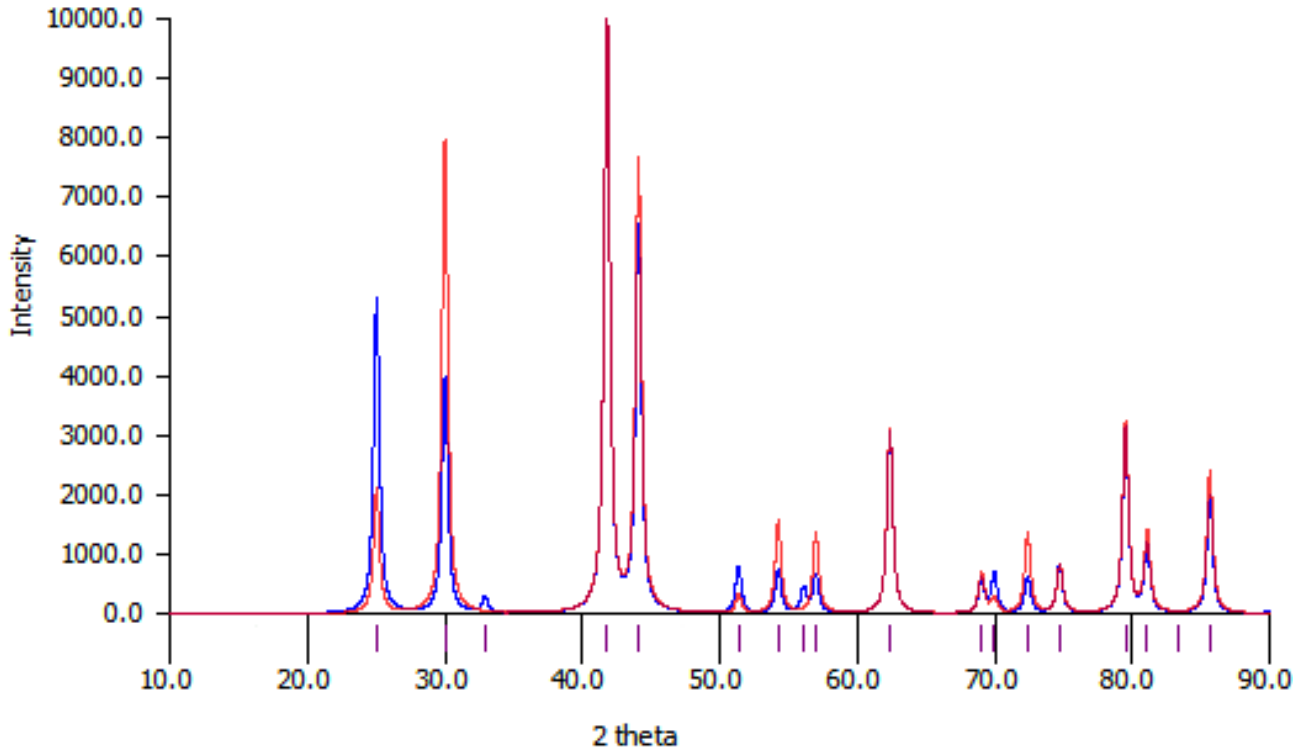


**Figure 3.8** A comparison of theoretical pXRD powder patterns of PtSn in ordered hexagonal (blue) and disordered hexagonal (red). Note the superlattice peaks in the 50-60 $^{o}$ 2θ region are present in both disordered and ordered phases, but have significantly different intensity ratios.

The ordered and disordered XRD spectra can therefore be distinguished through an analysis of the relative intensities of these ordering peaks. To determine if the as-made nanoparticles order at room temperature, the relative peak intensities of three "ordering peaks" were compared to the calculated relative peak intensities for ordered and fully disordered models. This comparison is summarized in Table 3.2. The ratio of the two largest ordering peaks (at 51$^{o}$ and 54$^{o}$ 2θ) was roughly 1:1 in both experimental patterns, which matches well with the calculated pattern for ordered PtSn, whereas the ratio for the disordered calculated pattern was roughly 1:5; this can be

clearly observed in Figure 3.8. This supports the conclusion that the room temperature PtSn sample is fully ordered, particularly since the peak ratios do not significantly change upon annealing.

| **2θ (°)** | **41.8** | **44.1** | **51.4** | **54.3** | **57.0** |
|---|---|---|---|---|---|
| **(hkl)** | **(102)** | **(110)** | **(200)** | **(201)** | **(103)** |
| **PtSn (As-Made)** | 100 | 55 | 4.6 | 4.8 | 5.5 |
| **PtSn (200 °C)** | 100 | 58 | 4.7 | 4.2 | 5.3 |
| **Ordered PtSn** | 100 | 65 | 8 | 7.3 | 6.3 |
| **Disordered PtSn** | 100 | 76 | 3.1 | 16 | 13 |

**Table 3.2** Experimental relative X-ray diffraction peak ratios for PtSn compared to the theoretical patterns for the ordered hexagonal structure and a hypothetical random occupancy model with the same hexagonal structure.

To add further evidence to the existence of room-temperature ordering for PtSn, a Rietveld analysis[10,11] was performed to determine which phase (ordered or disordered) provided a better fit to the whole pXRD pattern. Rietveld analyses are generally used on well crystallized samples with large domain sizes (100 nm or more). Since the products have a broad particle size distribution, the line fitting with standard broadening functions is reasonably expected to produce significant intensity in the difference peaks between the calculated and observed pattern, often attributable to errors in calculating the background signal. Nonetheless, this procedure is the best available for estimating the degree of ordering in small nanoparticles. Obviously, this leads to uncertainties in degree of ordering, which we estimate to be ±20%.

The analysis was carried out for three different hypotheses: first, that the product is 100%

ordered PtSn; second, that the product is 100% disordered but hexagonal PtSn; and third, that the product is some mixture of ordered and disordered hexagonal PtSn. The best fit was found by assuming that the sample was 100% ordered PtSn (see Figure 3.9). When attempting to fit the pXRD to a pattern containing both ordered and disordered PtSn, it was found that the optimized ratio of ordered to disordered PtSn was almost 200:1. Figure 3.10 shows the Rietveld fit for this scenario.

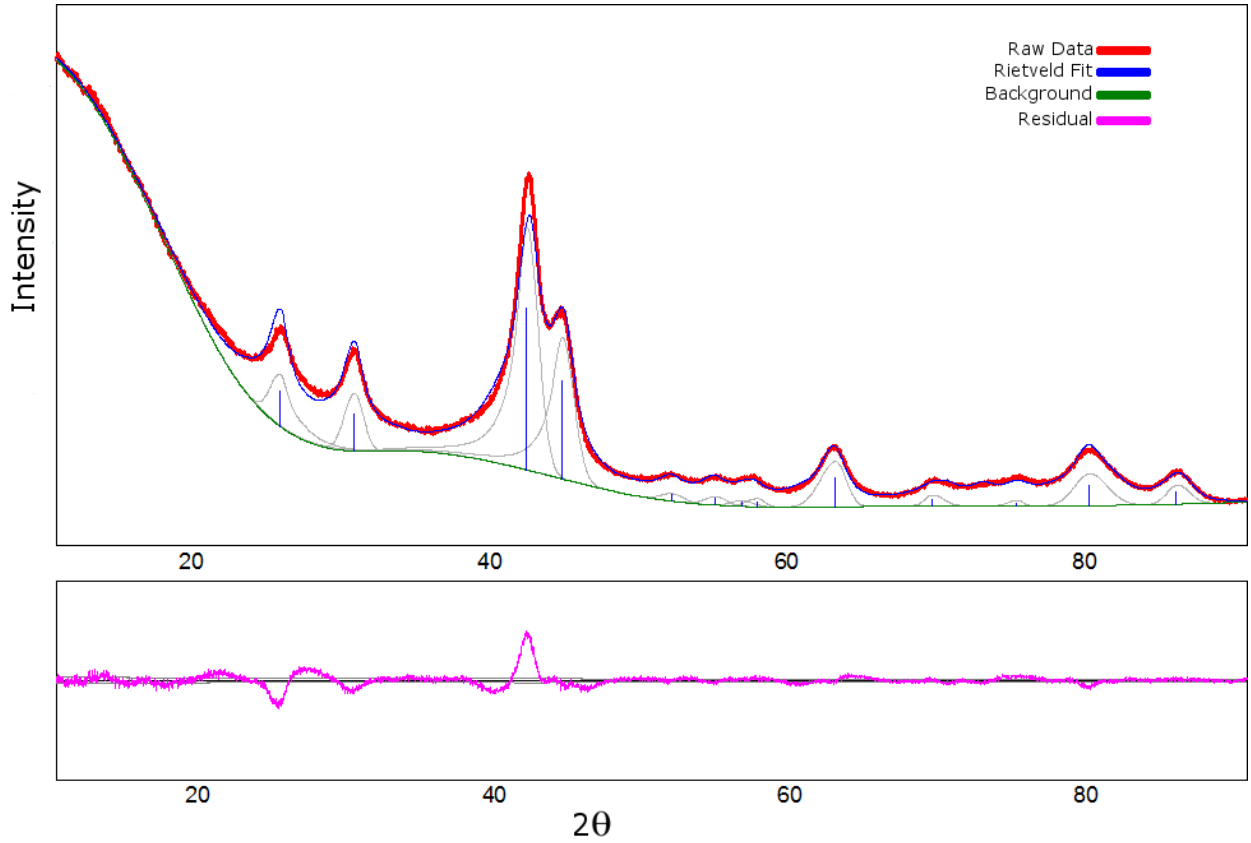


**Figure 3.9** Ordered-only Rietveld analysis of PtSn. Lattice parameters obtained from the fit were: a = 4.12Å, c = 5.46Å. Fitting parameters: wRp = 3.3%, $X^2 = 9.6$.

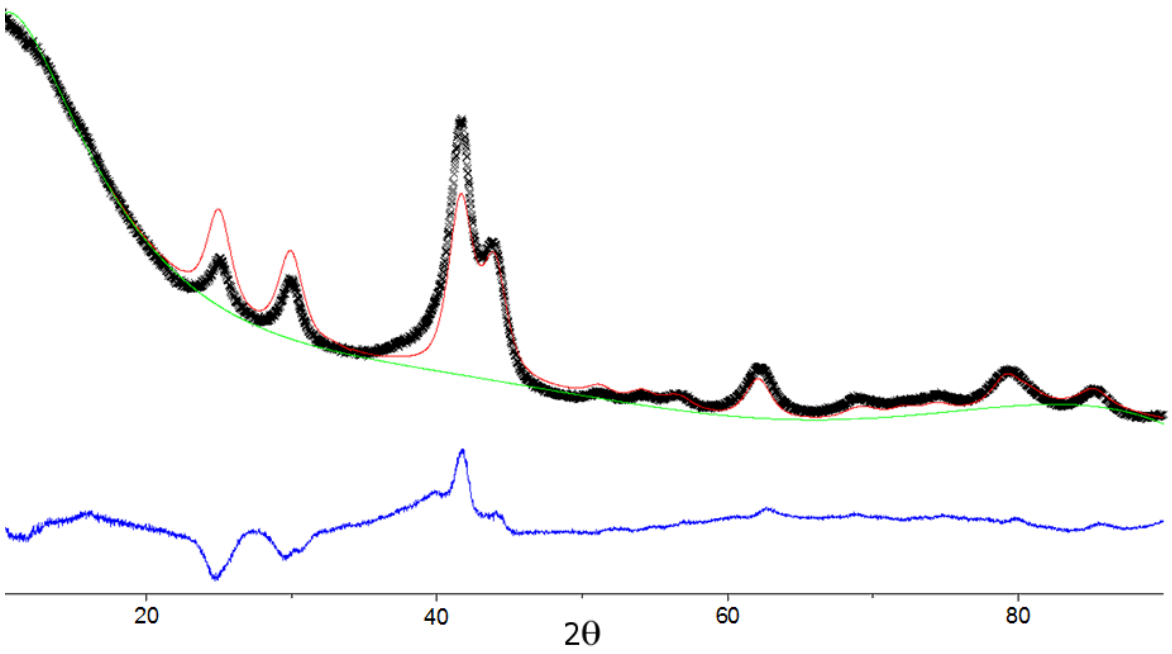


**Figure 3.10** Ordered and disordered mixture Rietveld fit. The green line is the calculated background, the black "X"s are raw pXRD data points, the red line is the calculated fitting pattern, and the blue line is the error between the calculated pattern and the experimental values. Fitting parameters: wRp = 10.2 %, $X^2 = 90$.

A final hypothesis for the apparent formation of the ordered phase was that the as-made nanoparticles were at least partly disordered, but upon exposure to air the surface quickly oxidized, releasing enough heat to briefly raise the temperature of the nanoparticle surface so that the nanoparticles effectively self-annealed. It was determined that this "spontaneous annealing" did not contribute to the apparent formation of the ordered phase at room temperature by repeating the synthesis, with the as-made nanoparticles being gradually exposed to air by first vacuum drying and backfilling with Argon, then inserting a needle into the septum and letting air diffuse into the centrifuge tube overnight. Our previous experience is that this method will avoid any heat buildup (or even sometimes spontaneous air combustion) in air sensitive nanoparticles

containing such elements as Fe or Mn, so that any surface oxidation would occur slowly enough that the local temperature would not rise significantly above room temperature. The diffraction pattern was unchanged by this procedure, indicating that heating due to possible surface oxidation was not important (see Figure 3.11). Lastly, as seen in Figure 3.5, annealing the sample at 200 $^{o}$C produced only minor changes in the XRD pattern, i.e. only a slight improvement in the resolution of weaker peaks above a 2θ of 50 $^{o}$. This indicates that the sample is as ordered at room temperature as it is after annealing to 200 $^{o}$C

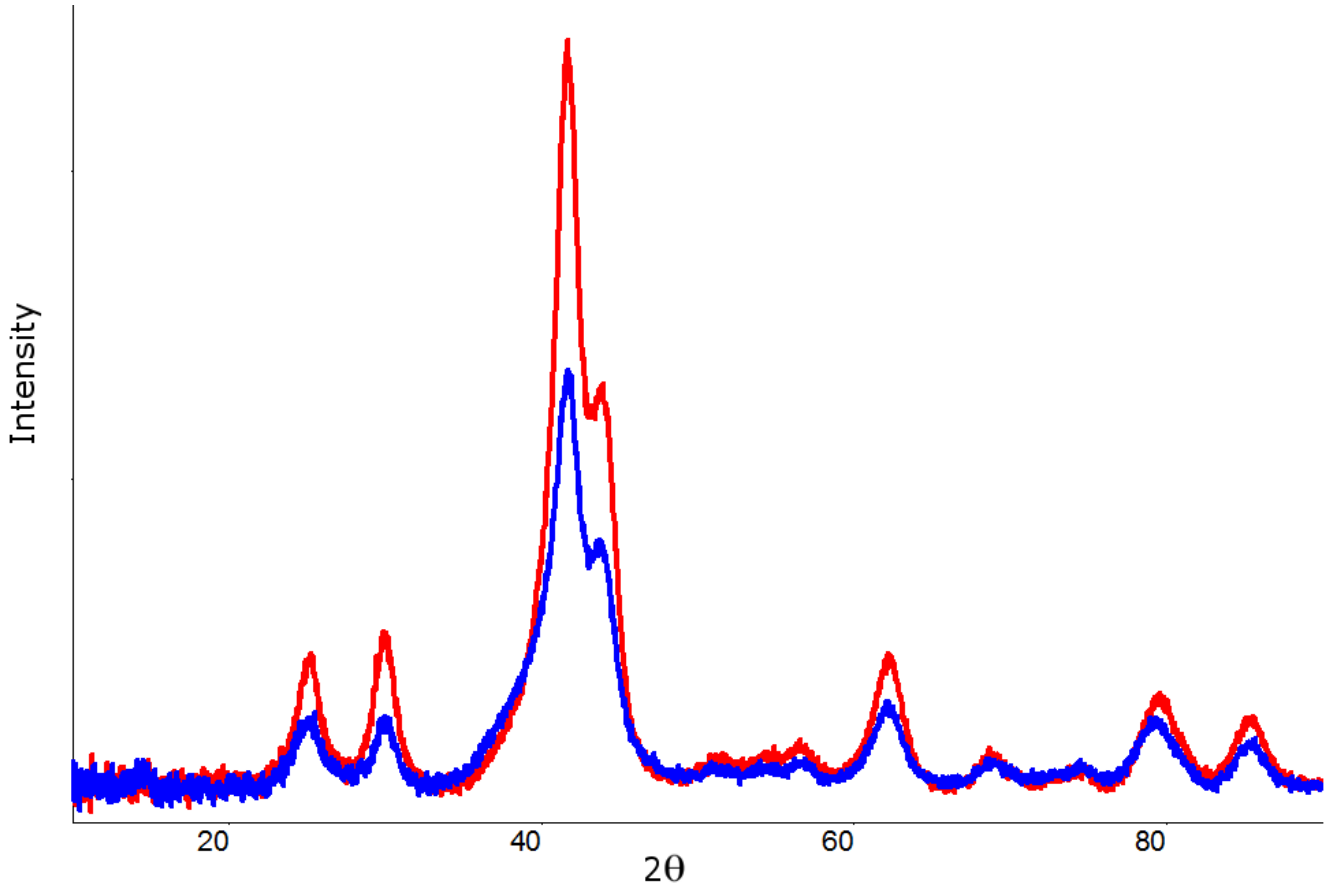


**Figure 3.11** A comparison of ordering between PtSn as-made nanoparticles that are exposed to air quickly (blue) and slowly (red).

*3.1.3 1/2 < x < 1 ($Pt_2Sn_3$, $PtSn_2$, $PtSn_4$)*

The tin-rich phases ($Pt_2Sn_3$, $PtSn_2$, and $PtSn_4$) are all of dubious value as fuel cell catalysts due to the inevitable bulk leaching of the electropositive tin from the nanoparticles that is expected when x > ½[12]. Such bulk leaching will lead to high surface areas as well as compositions richer in Pt, and perhaps unusual particle morphologies[13]. Nonetheless, attempts to synthesize single phase products were undertaken with the intent of exploring the nanocrystallization behavior of the complete Pt-Sn system.

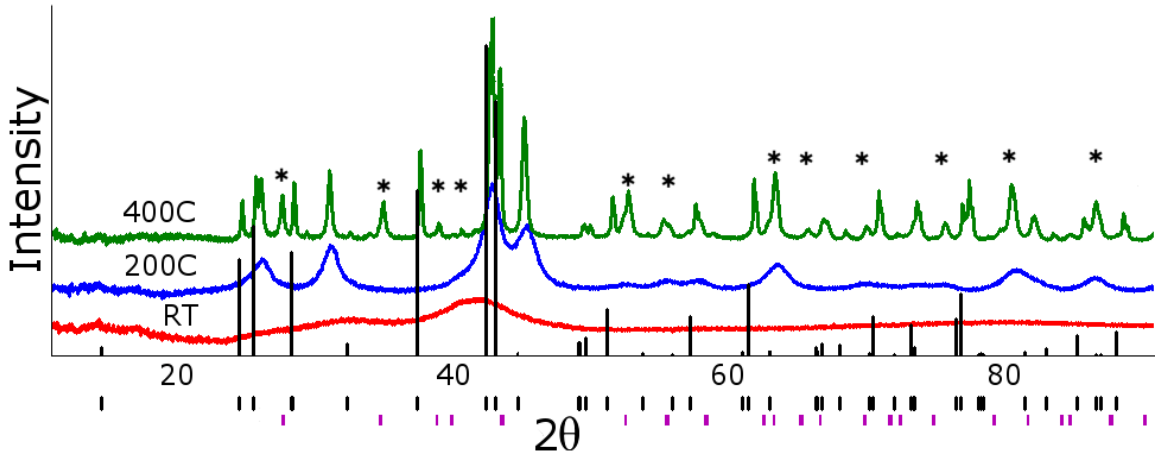


**Figure 3.12** Powder XRD of $Pt_2Sn_3$ nanoparticles. At 400 °C the transition to $Pt_2Sn_3$ (black drop lines) is almost complete. PDF card# 04-007-4094. Purple drop lines and asterisks mark impurity $SnO_2$ in the sample annealed at 400 °C.

$Pt_2Sn_3$ formed the ordered phase only after heating to 400 °C. The diffraction peaks for the product obtained at room temperature sample are very broad, indicating a high degree of disorder (perhaps even an amorphous structure) or very small domain sizes. At 200 °C, the product pXRD pattern shown in Figure 3.12 is close to that expected for PtSn. In this case, there is no evidence for any other crystalline phase expected in the Pt-Sn phase diagram . Since the

room temperature phase is nearly amorphous, the data suggest that the first phase to nucleate on heating has a different stoichiometry than the amorphous 2:3 composition. This behavior is explored in more detail in section 3.5.

Disappointingly, reduction of Pt:Sn::1:2 never resulted in a phase-pure product, independent of the annealing temperature. The product that contained the most $PtSn_2$ (60 wt%) was obtained at 400 $^{o}$C; the remainder consisted of PtSn and some $SnO_2$, with other Pt-Sn phases such as $Pt_2Sn_3$ present in small quantities. The pXRD pattern is shown in figure 3.13.

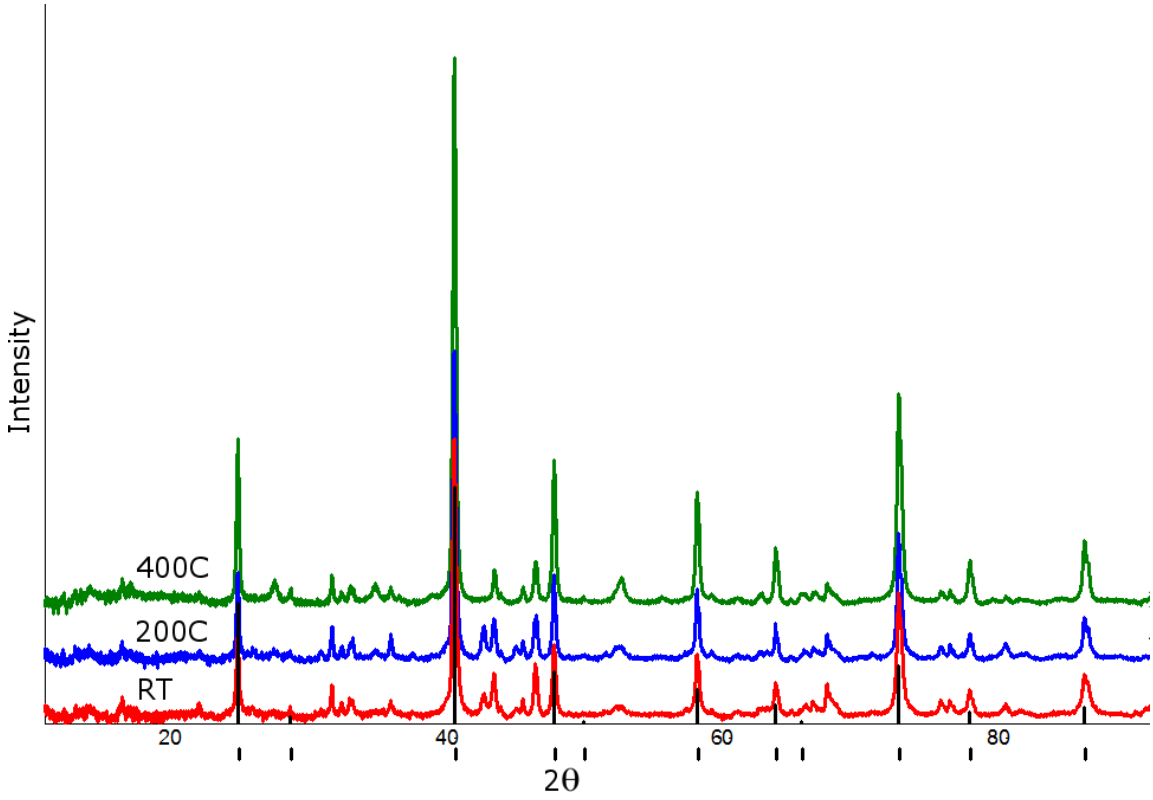


**Figure 3.13** Powder XRD pattern of nanoparticles made from the reduction of $PtCl_4$:$SnCl_2$::1:2 solutions. $PtSn_2$ was identifiable under all annealing conditions, but was always accompanied by other nearby phases (PtSn and $Pt_2Sn_3$). PDF card# 04-007-4096.

In contrast to the previous phase, pXRD patterns of $PtSn_4$ annealed to 200 $^{o}$C (shown in Figure

3.14) showed the expected closely spaced XRD peaks that identify it as the pure orthogonal phase found in bulk materials of the same composition. Small domain sizes at low temperatures make phase identification of impurity phases difficult, but annealed nanoparticles closely match the database pattern for the target phase. It should be noted, however, that the synthesis of this phase is extremely sensitive to air and water contamination of the glovebox atmosphere. In general, a greater tin concentration in a target Pt-Sn phase correlates with an increased difficulty in synthesizing that phase as pure nanoparticles of the target composition and of avoiding the formation of Sn oxides.

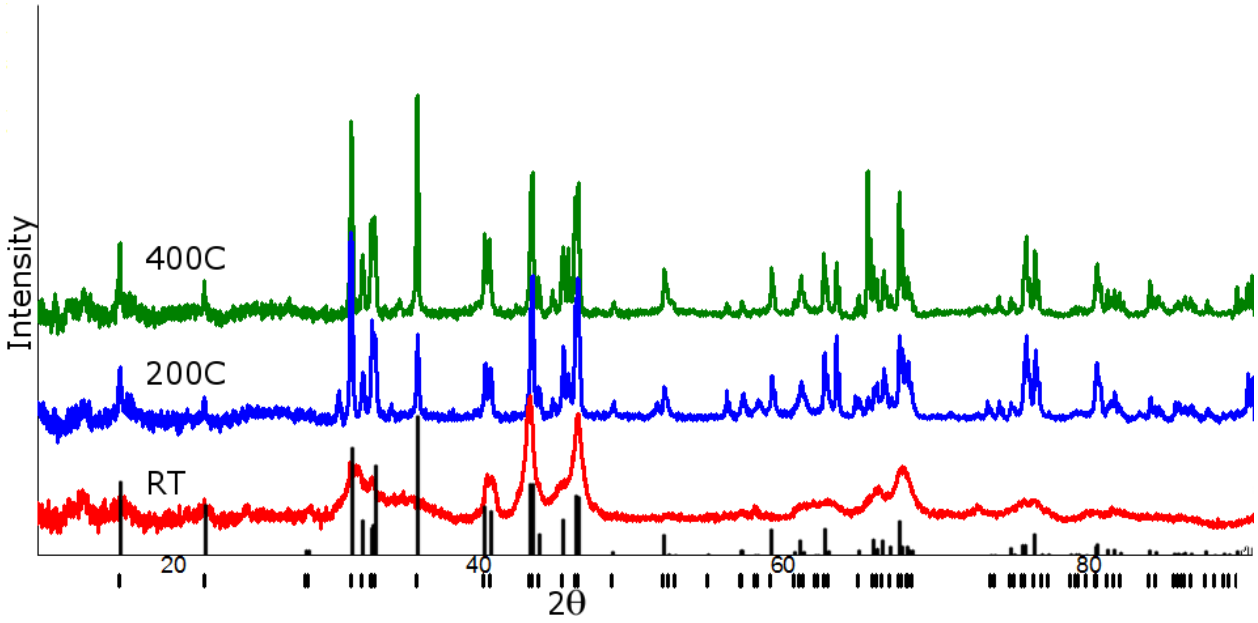


**Figure 3.14** Powder XRD pattern of $PtSn_4$. PDF card# 04-007-4097.

In all of these tin-heavy systems, the bulk peritectic decomposition temperature of the tin-heavy phases are much lower than the congruent bulk melting temperature of either PtSn or $Pt_3Sn$, but the tin-heavy phases order at temperatures on the order of, or higher than, those found for the two Pt-heavy phases.

| Target Phase | SnII / SnIV | $T_{order}$ ($^{o}$C) | Domain Size (nm) | % Target Phase[a] | % Pt (at. %)[b] |
|---|---|---|---|---|---|
| **Pt** | N/A | 25 | 4.5 | 100% | 100% |
| **$Pt_3Sn$** | II | 200 | 5.6 | 100% | 73±3 |
| **PtSn** | II | 25 | 4.3 | 100% | 43±2 |
| | II | 200 | 5.5 | 100% | 45±2 |
| | IV | 200 | 5.8 | 85%*[d] | 38±1 |
| **$Pt_2Sn_3$** | II | 400 | 36.2 | 95%* | 35±1 |
| | IV | 400 | 28.4 | 90%* | 32.2±0.3 |
| **$PtSn_2$** | II | 400 | 44.9 | 60%* | 27.5±0.3 |
| | IV | N/A[c] | N/A | 0%* | 26±2 |
| **$PtSn_4$** | II | 200 | 45.9 | 100%* | 15±3 |
| | IV | 200 | 26.4 | 100%* | 17±2 |
| **Sn** | II | 25 | 21 | 100% | 0% |

**Table 3.3** Summary of nanoparticle products synthesized by LBH reduction and the lowest temperatures at which ordering peaks appear. Percent ordering is calculated from peak area ratios of all phases identified by pXRD. (a) Target phase percent composition determined by Rietveld analysis. (b) Atomic ratios determined by EDX. Reported errors are statistical. Composition ratios partially depend on nanoparticle morphology, and have empirically been found to vary 5-10% from the expected values. (c) Phase not successfully synthesized. (d) Asterisks indicate multiphase products, or products with complex ordering models.

Table 3.3 summarizes the temperatures at which nanoparticles at the stoichiometry of the five bulk Pt-Sn line phase compositions first show ordering behavior, the domain sizes resulting from annealing the samples to those temperatures, and whether or not the sample was phase pure. The percent ordering content is a best estimation based on the results of Rietveld analysis and a comparison of ordering peak ratios, However these methods are unable to satisfactorily distinguish between ordered compounds and disordered alloys for the Sn rich phases that have complex structures and large unit cells, but with the same stoichiometry. This is in part due to the many possible disordered arrangement of Pt and Sn on the occupied sites. These compounds are indicated by an asterisk.

## *3.2 Pre-Reduction Complexation and its Effect on Co-Reduction*

### 3.2.1 UV-Vis Analysis

Room-temperature ordering behavior in binary intermetallic nanoparticles is an unusual occurrence, given that synthesis or annealing at elevated temperatures is often essential to overcome the nucleation and diffusional barriers to ordering. Determining the cause of this ordering behavior is more difficult, as it appears to not be an intrinsic property of the co-reduction method. Of the Pt-M systems that have been investigated in the past, only PtBi and PtPb prepared by specific synthetic pathways showed ordering behavior at room temperature, while other pathways did not show such ordering[14]. Most other metals, including main group metalssuch as Sb and all 3d transition metals combined with Pt, require annealing temperatures of at least 400$^{o}$C before ordered phases are observed via XRD after similar co-reduction syntheses; we will see examples of this in subsequent chapters.

Platinum(IV) and tin(II) chloride are known to make a variety of complexes together in aqueous solution[15]. Qualitatively, one is able to see a color change on mixing these two chlorides in THF - in contrast to all other combinations of metal chlorides from Table 2.1 - which was the first indication that there might be reactions occurring in the pre-reduction Pt-Sn solutions. The formation of such complexes in THF should lead to more compositionally homogenous metal nanoparticle seeds after co-reduction (see Section 3.2.3). Perhaps the existence of these compounds could help to explain the uncharacteristic ordering behavior of the entire Pt-Sn system, including the presence of as-made nanoparticles of certain compositions, specifically of PtSn, that are mostly or wholly ordered. UV-Vis absorbance measurements (see Figure 3.15) were taken of the pre-reduction chloride-containing solutions to determine if there is a noticeable amount of complexation occurring in the THF solution.

The platinum-rich $Pt_3Sn$ solution has very broad peaks in the region of 350 nm, whereas more tin-rich solutions (PtSn, $Pt_2Sn_3$, and $PtSn_2$) have peaks at 390 nm and 450 nm. The pure tin chloride and platinum chloride solutions showed no sign of any absorbance peaks in these regions. A qualitative comparison of peak positions suggests that in each case, there is one major Pt-Sn complex that is limited by either the Platinum (IV) or Tin (II) concentration, thus the composition of this complex changes depending on the ratio of chloride precursors.

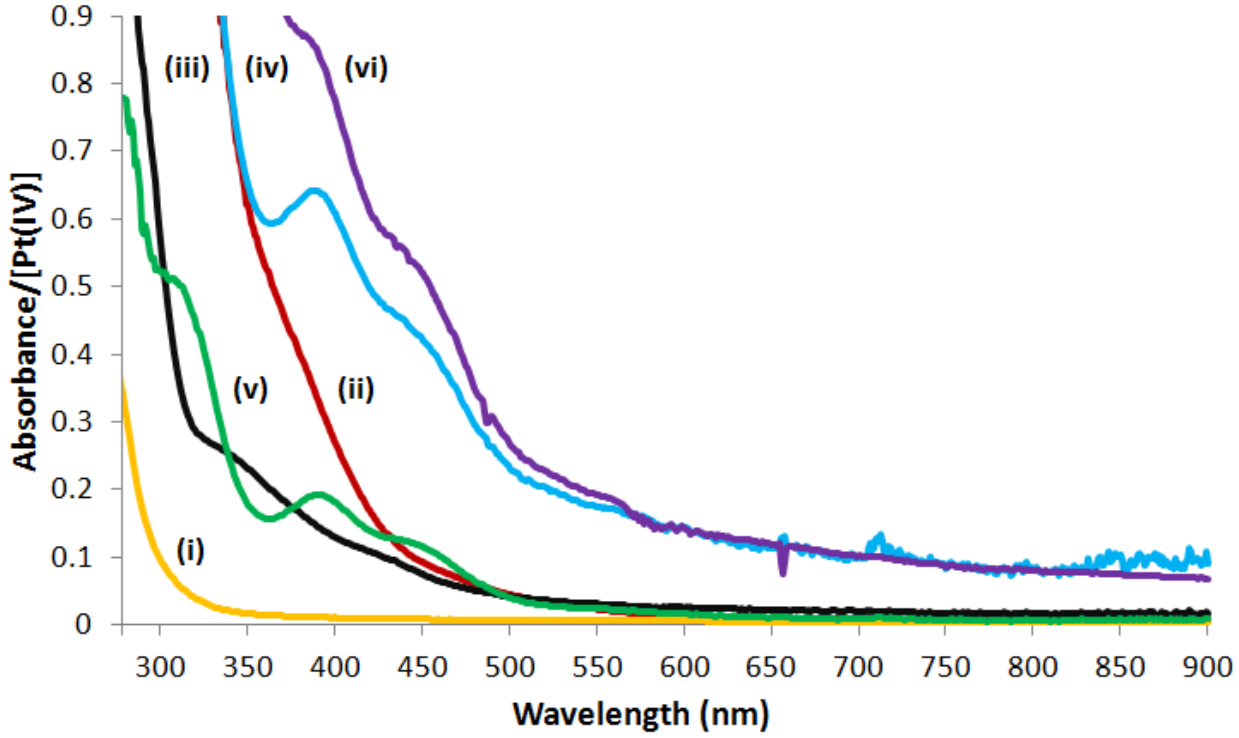


**Figure 3.15** Comparison of UV-Vis absorbance spectra of a range of $PtCl_4$ and $SnCl_2$ pre-reduction solutions. The ratios of the chloride precursors in each solution are equal to the ratios present in the target Pt-Sn line phase. Solutions include pure Sn (i – yellow curve ) and Pt (ii - red curve) chlorides, as well as $PtCl_4$:$SnCl_2$ 3:1 (iii - black curve), 1:1 (iv – blue curve), 2:3 (v – green curve), and 1:2 (vi –purple curve). Absorbencies are scaled relative to the concentration of platinum chloride in each solution. The noisy "tail" for curves iv and vi can most likely be attributed to particulates scattering light.

The fact that the absorbance curves for solutions containing both Pt and Sn cannot be obtained by a linear combination of the pure Sn and Pt curves proves that complexation does occur on mixing and therefore prior to the reduction, and that the complexes that form are dependent on the ratio of platinum to tin in the solution. Further evidence for this fact was obtained via $^{119}Sn$ NMR experiments, which are described in Appendix A. However, as these experimental

methods proved to be insufficient to determine the identities of the pre-reduction complexes (largely due to a lack of literature references), we turned to theoretical studies to provide some insight.

### *3.2.2 Theoretical Study of Pt-Sn Complexation*

Theoretical calculations were a potentially faster and more generalizable method to determine the likely complexes formed by $PtCl_4$ and $SnCl_2$ in THF. A comparison between the experimental UV-Vis data and theoretical predictions could at the least confirm the presence of one or more Pt-Sn complexes in solution, and possibly predict their structure(s). A full treatment of theoretical chemistry techniques is beyond the scope of this dissertation; nonetheless, some background on the capabilities of these techniques is important to understand the power (and limitations) of the method.

This section relies heavily on collaborative efforts with Deniz Gunceler of the Arias theoretical physics group at Cornell University. Energies were calculated ab-initio using Joint Density Functional Theory (JDFT), which was first described by Arias in 2005[16]. The premise of the theory is to treat the solvent as a continuum dielectric environment, which eases the calculations, allowing for precise predictions of molecular structures and energies (particularly at the surfaces of electrodes, which was the original impetus for the creation of the theory).

Since then, the theory has been improved and updated in numerous ways. The ability to treat a solvent as a nonlinear continuum[17] (instead of as a linear or constant continuum) was important because interaction with an electrode often results in nonlinear changes to the solvent's dielectric

field. Recently, these calculations were extended to include non-aqueous solvents[18], which obviously is useful in the context of this work because all UV-Vis measurements were performed in THF. Standard DFT tends to perform poorly when calculating excited states, so a modified DFT method (Delta Self-Consistent Field, ΔSCF) was used, though it is far from the only method that attempts to modify DFT to be more accurate for excited states. ΔSCF has a computational cost only slightly greater than standard DFT, but is equipped to handle excited states reasonably well, including cases of charge transfer[19], This method has been independently developed by numerous individual groups in the past few years; one of the most recent - and the one most similar to that used in this work - was described by Van Voorhis to be used in dye applications[20].

The final piece of the puzzle in the incarnation of JDFT used to calculate the excited state energies of Pt-Sn complexes was the use of the Generalized Gradient Approximation (GGA) over the older Local Spin Density (LSD) method for calculating the exchange-correlation energy ($E_{xc}$) between the solute molecules and the solvent continuum[21]. All calculations were performed using software developed in-house called JDFTx, available at http://jdftx.sourgeforge.net.

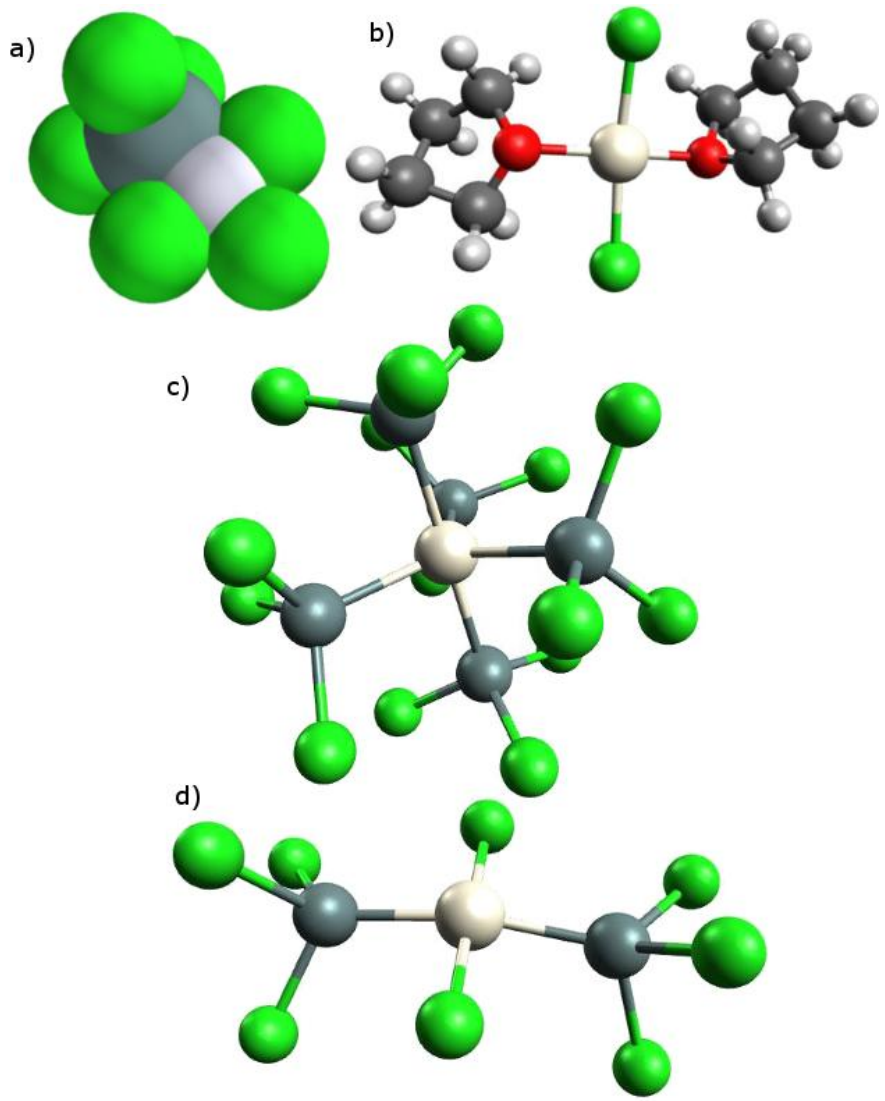


**Figure 3.16** Structures of some hypothesized Pt-Sn complexes. The formulae are a) $[PtCl_3SnCl_3]^0$, b) $[PtCl_2(THF)_2]^0$, c) $[Pt(SnCl_3)_5]^{3-}$, and d) $[PtCl_2(SnCl_3)_2]^{2-}$. White atoms represent Pt, grey represents Sn, green is chloride, black is carbon, and red is oxygen.

Fundamentally, what can be taken away from the above is that JDFT was used to calculate the excited state transition energies of postulated Pt-Sn complex structures (in eV, which were then converted into nm). These excitation energies could be compared against experimental values, determined by UV-Vis absorption. That is what the absorption of a photon entails: an analyte

molecule absorbing a quantized amount of energy to promote an electron into an appropriate excited state (an allowed transition).

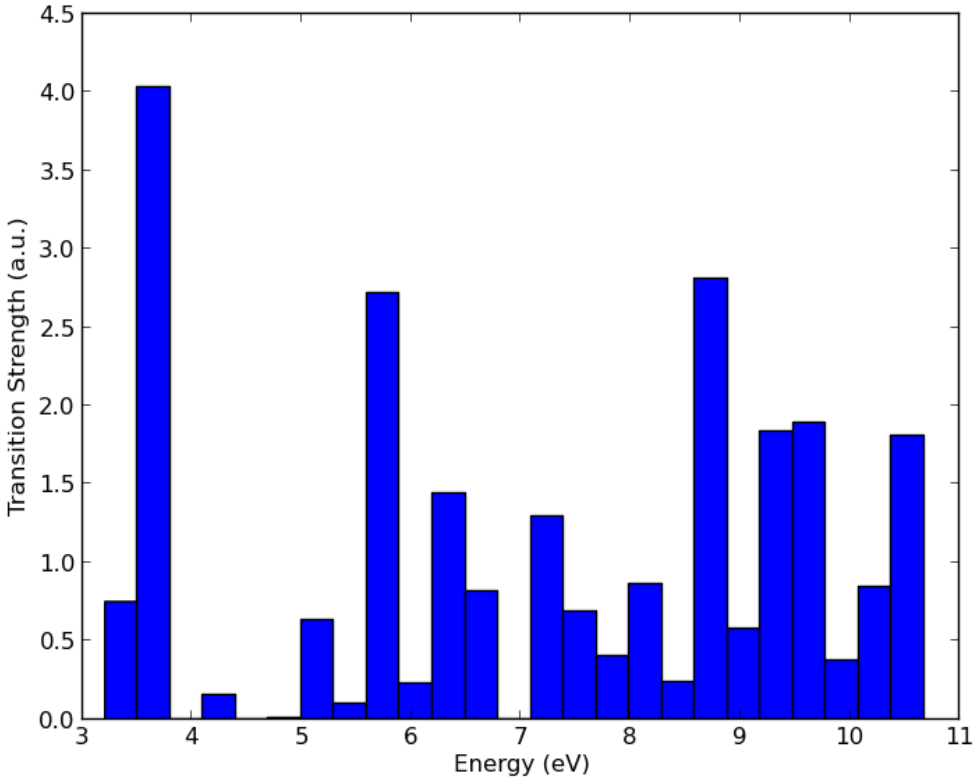


**Figure 3.17** Transition energies between the excited states of $[PtCl_3SnCl_3]^-$.

A number of possible Pt-Sn complex structures were hypothesized and the electronic spectra calculated. Figure 3.16 shows the structures of four representative complexes, which were taken from - or inspired by - known Pt-Sn molecular structures found in literature. One structure (Figure 3.17b) does not contain any tin; it is possible that the complexes formed in the pre-reduction solution are from $PtCl_4$ being partially reduced by THF and forming an adduct. Energy differences were calculated between the ground state and every theoretically available excited state, which resulted in a long list of quantized energies and intensities. These can be sorted by the energy of the excited state and plotted as a histogram. Figure 3.17 shows an example of such

a histogram for $[PtCl_3SnCl_3]^-$ in THF.

Obviously, Figure 3.17 does not look very much like a UV-Vis spectrum. Two things need to change before it can be directly compared to experimental spectra: the units, and the quantization of energy. First, physicists are more comfortable working with energy in terms of eV, but spectra are measured by the wavelength of light absorbed, so it is necessary to convert between the two. These units are inversely related; formula for converting between eV and nm is Eqn 3.1:

$$\lambda\,(nm) = \frac{1240}{E_{ev}} \qquad \text{(Eq. 3.1)}$$

where λ is the wavelength in nm and $E_{ev}$ is the energy in eV. Transition energies below about 1.9 eV were ignored since they do not contributing to the UV-Vis spectrum. Higher energies very well might describe real transitions in the complex; however, since the cutoff wavelength for THF is approximately 250-300 nm, higher energy transitions (above about 4.8 eV) cannot be used for identification. This sets the window for useful transition energies to be the region of 1.9-4.5 eV.

Second, the narrow absorption spectra obtained theoretically from isolated molecules must be broadened. Rotational and vibrational excitations as well as interactions with the solvent result in peaks that are broadened, in a roughly Gaussian manner. This is why UV-Vis spectra do not look like a collection of narrow peaks. Applying Gaussian broadening to the theoretical results produces spectra that superficially look like the UV-Vis spectra. Figure 3.18a shows how the data from Figure 3.17 appears after being processed with specific broadening parameters. The result is a realistic spectrum in the region of interest. Repeating this procedure with the other

complexes gives similar results (see Figure 3.18b-d). Intensities in these measurements are non-physical. The transition energies are self-consistent, but they are not consistent between compounds; there is no way of determining from these calculations which complexes will absorb more strongly in a real solution.

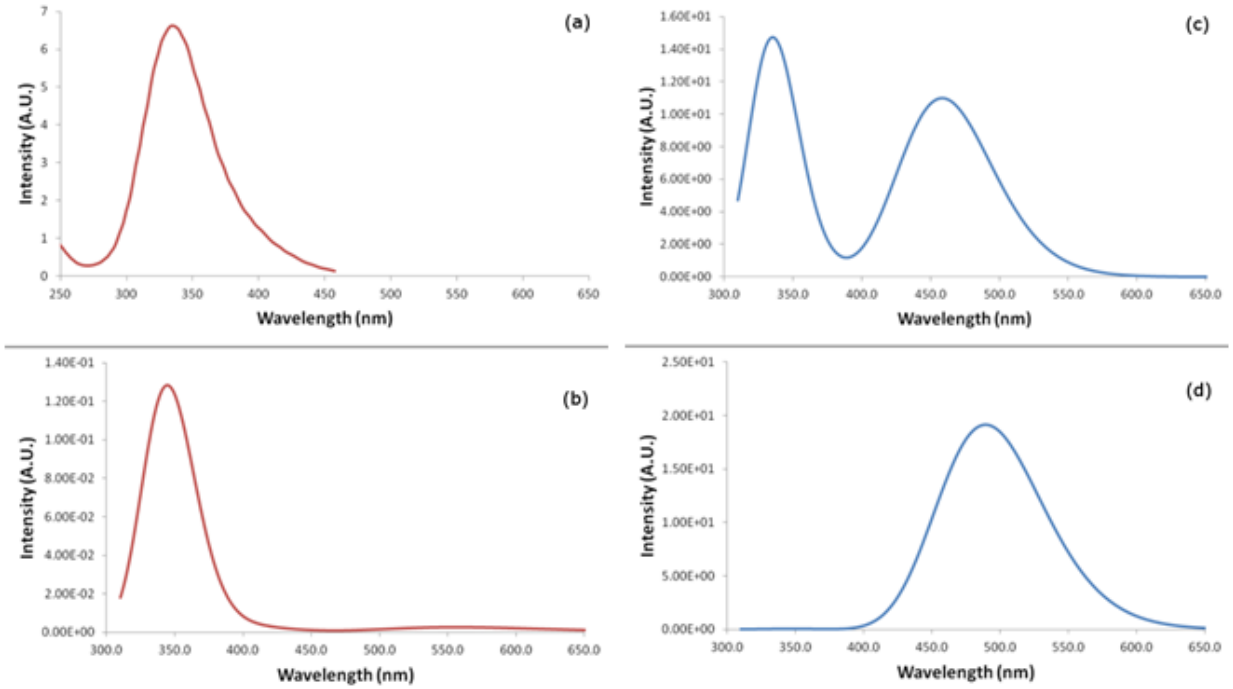


**Figure 3.18** Calculated theoretical UV-Vis spectra of a) $[PtCl_3SnCl_3]^0$, b) $[PtCl_2(THF)_2]^0$, c) $[Pt(SnCl_3)_5]^{3-}$, and d) $[PtCl_2(SnCl_3)_2]^{2-}$.

Finally, bringing Figures 3.15 and 3.18 together, the compilation shown in Figure 3.19 shows how the experimental UV-Vis spectra fit together with the theoretically calculated UV-Vis spectra. In addition to the four compounds above, two additional THF adducts - $[PtCl_2(SnCl_3)(THF)]^-$ and $[Pt(SnCl_3)_4(THF)]^{2-}$ - were investigated. These compounds are of interest because if THF and $SnCl_3^-$ can act as interchangeable labile ligands, the complexes could exist in solution over a range of compositions..

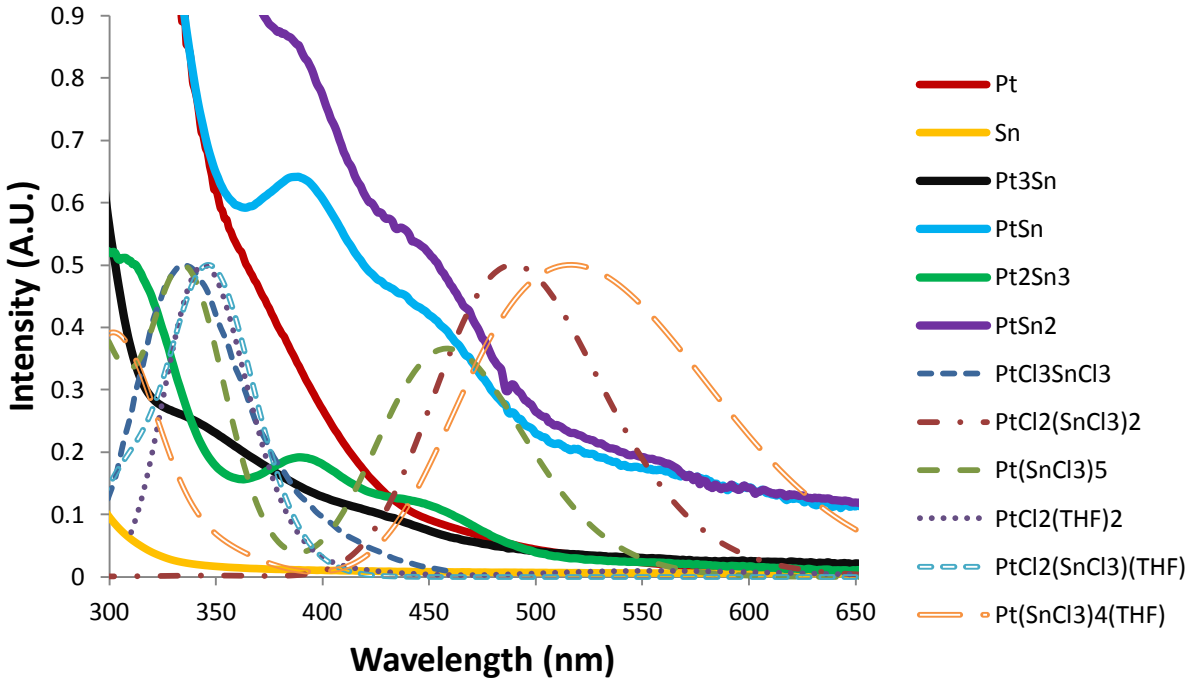


**Figure 3.19** Experimental UV-Vis spectra (bold lines) compared to theoretically calculated UV-Vis spectra (dashed lines). All theoretical spectra are scaled to a maximum absorbance of 0.5 A.U.

Features of interest include the multiple theoretical peaks near the weak Pt3Sn at about 350 nm. While no theoretical peak uniquely matches a given experimental peak, it is still reassuring to see fairly close agreement between the predictions of a method that is not at all optimized for calculating UV-Vis spectra, and actual UV-Vis data. An unfortunate finding is that all examined theoretical spectra have a minimum around 400 nm, which is precisely where the most distinct peak for three Pt-Sn phases is seen in the UV-Vis spectra. While this method was not successful in precisely identifying the Pt-Sn complexes, it has shown promise; simply calculating energies in the correct wavelength region is impressive. More precise calculations (taking weaker energy transitions into account, not just broadening stronger transitions with Gaussian functions) will be

necessary if this approach is ever to work. For now, though, it has been demonstrated that Pt-Sn complexes (and potentially Pt-Sn-THF complexes) definitely absorb in the area of interest, and so the experimentally observed UV-Vis spectra are very consistent with the hypothesized formation of Pt-Sn complexes. Now, the question remains, does the presence of these complexes really matter for the synthesis?

### 3.2.3 Effect on Nanoparticle Nucleation and Growth

In section 3.2.1, it was mentioned that the existence of pre-reduction complexes could improve the seed and growth rate (and even the favorability of ordering) of select phases by reducing the local randomness of the ratio of metal atoms in different nanoparticle seeds. Sections 3.2.2 and 3.2.3, together with the original UV-Vis spectra, form the basis for the claim that Pt(IV) and Sn(II) form such complexes. The next step was to determine if the hypothesized link between complexation and nanoparticle formation and ordering exists.

To test this, $SnCl_4$ was used as the tin precursor in place of $SnCl_2$. There are no peaks to suggest that $SnCl_4$ forms any complexes with platinum chloride, as shown by UV-Vis spectrophotometric measurements (Figure 3.20) that show the $Pt^{IV}$-$Sn^{IV}$ absorbance as roughly the same as pure $Pt^{IV}$ absorbance, in contrast to the $Pt^{IV}$-$Sn^{II}$ solution. The pXRDs comparing the products of these reductions are shown in Figure 3.21; as previously seen, the reduction of a 1:1 ratio of $PtCl_4$ and $SnCl_2$ in THF gives ordered PtSn nanoparticles at both room temperature and upon annealing to 200 $^oC$, whereas the product obtained from the same 1:1 ratio of $PtCl_4$ with $SnCl_4$ is amorphous at room temperature. Annealing these latter nanoparticles to 200 $^oC$ results in the nucleation of several different Pt-Sn phases, and at 400 $^oC$ the pXRD pattern matches the

reference pattern for $Pt_2Sn_3$. This result strongly suggests that the nanoparticles in the latter case have a variety of Pt-Sn compositions when prepared at room temperature.

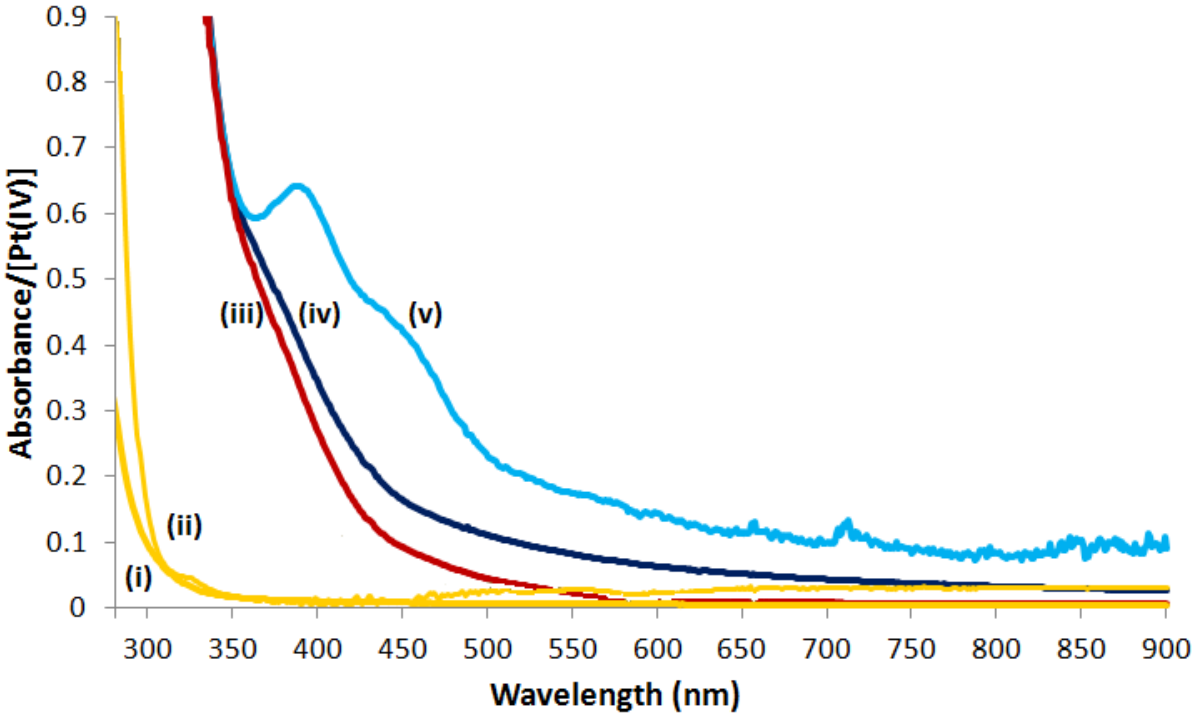


**Figure 3.20** UV-Vis absorbance of pure $SnCl_2$ (i - lower yellow curve), $SnCl_4$ (ii - upper yellow curve), and $PtCl_4$ (iii – red)) in THF. When mixed with $PtCl_4$ in a 1:1 ratio, $SnCl_4$ shows very little change in its absorbance spectra compared to pure $PtCl_4$ (iv - dark blue), while $SnCl_2$ displays prominent peaks due to complexation (v - light blue).

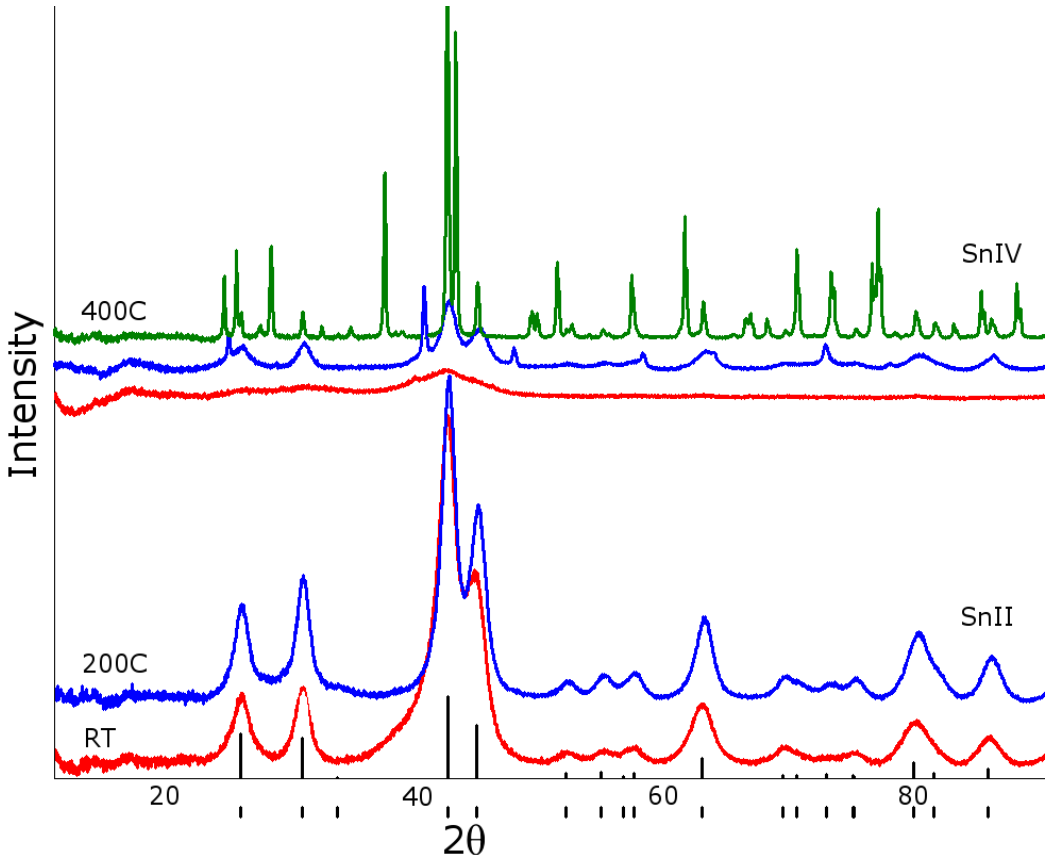


**Figure 3.221** pXRD comparison of 1:1 products using $Sn^{II}$ and $Sn^{IV}$ chloride and $PtCl_4$ precursors reduced with $LiBHEt_3$. Drop lines correspond to PtSn standard.

Reactions with $SnCl_4$ were often found to result in multiphase products, suggesting that the local concentrations of tin and platinum had greater variances than in the samples prepared with $SnCl_2$. $Pt_2Sn_3$ showed such behavior, shown in Figure 3.22. It seems likely, therefore, that the complexation behavior of $PtCl_4$ and $SnCl_2$ plays an integral role in the formation of the ordered phase at room temperature.

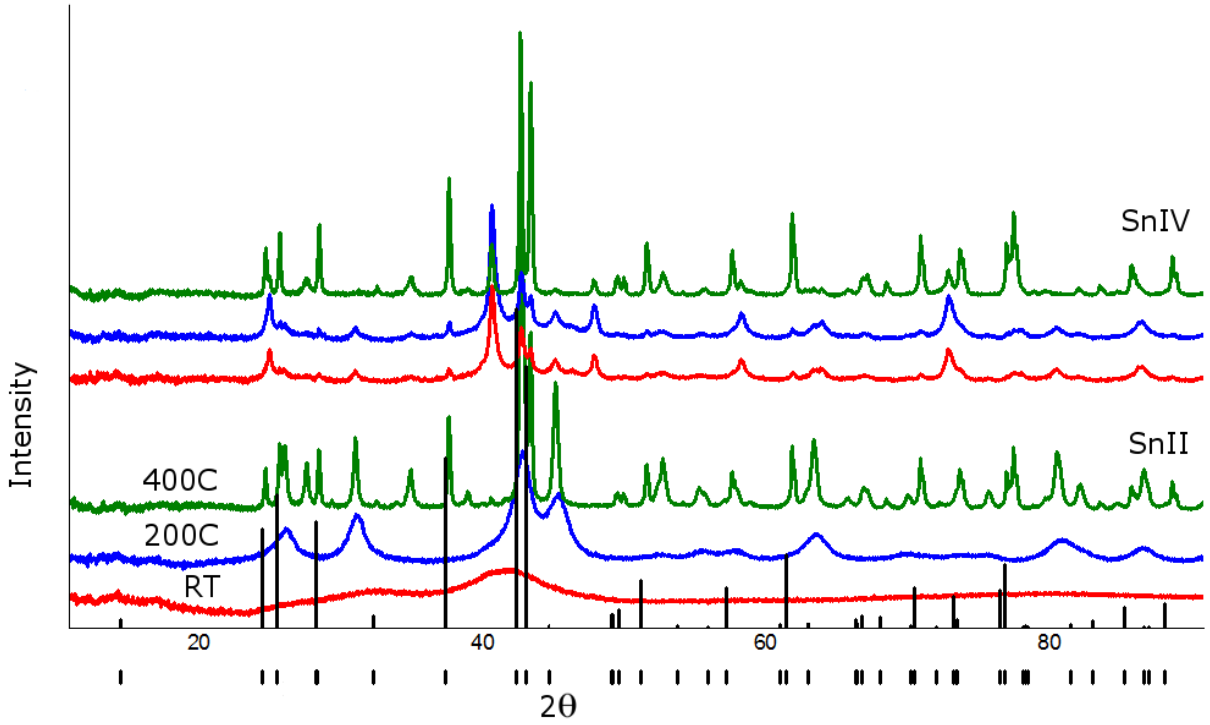


**Figure 3.22** A comparison of $Pt_2Sn_3$ pXRD patterns from samples prepared with $SnCl_2$ or $SnCl_4$. Drop lines correspond to $Pt_2Sn_3$, PDF card# 04-007-4094.

Of note is the contrast between these results and those of $PtSn_4$, where both the $Sn^{II}$ and $Sn^{IV}$ chlorides produced ordered $PtSn_4$ (see Figure 3.23). The major difference between the two products was the presence of $SnO_2$ in the $Sn^{IV}$ sample, but no other Pt-Sn impurity phases were detectable. This is an indication that the specific identities of the pre-reduction Pt-Sn complexes (which depend on the relative concentrations of $PtCl_4$ and $SnCl_2$ in solution) are important factors in whether the co-reduction produces seed nanoparticles with ordered (or close to ordered) structures. It is also possible that the ordered phase formation is hampered by a thin, amorphous surface layer of oxide blocking the diffusion of metal atoms. This surface layer could form due to traces of water or oxygen that are entrapped during the handling of the products in nominally air free environments. However, we did not pursue this idea experimentally.

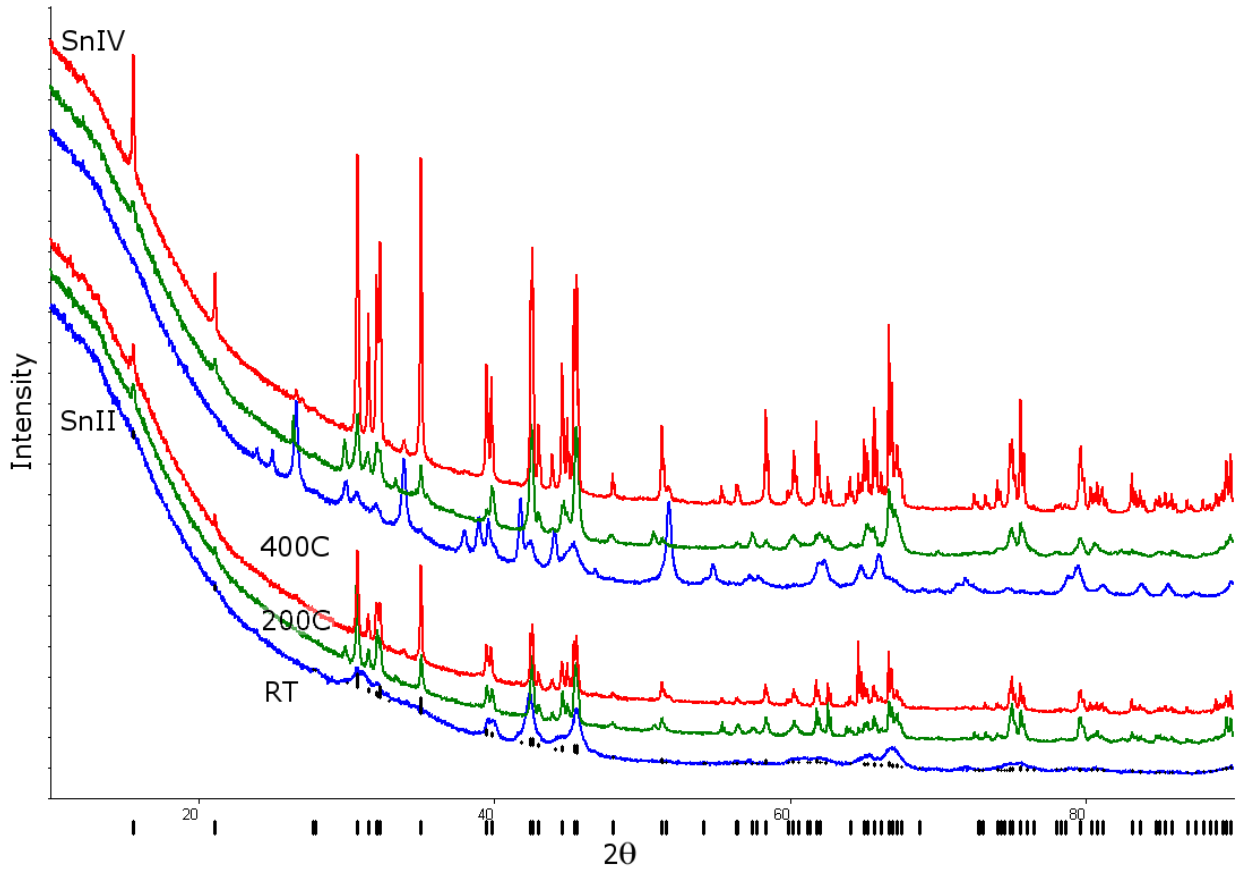


**Figure 3.23** $PtSn_4$ pXRD patterns prepared with $SnCl_2$ and $SnCl_4$. Black lines are the database pattern for $PtSn_4$, (PDF card 04-007-4097).

### *3.3 LBH vs. KBH*

Reductions with KBH were also performed on several Pt-Sn phases to determine if limiting the size of the nanoparticle seeds would have an effect on the identity and ordering behavior of the synthesized phases. As shown in Figure 3.24, ordering behavior was suppressed and required higher annealing temperatures in order to form ordered intermetallics, but domain sizes were kept smaller by the KCl matrix when compared to nanoparticles reduced by LBH and annealed to similar temperatures.

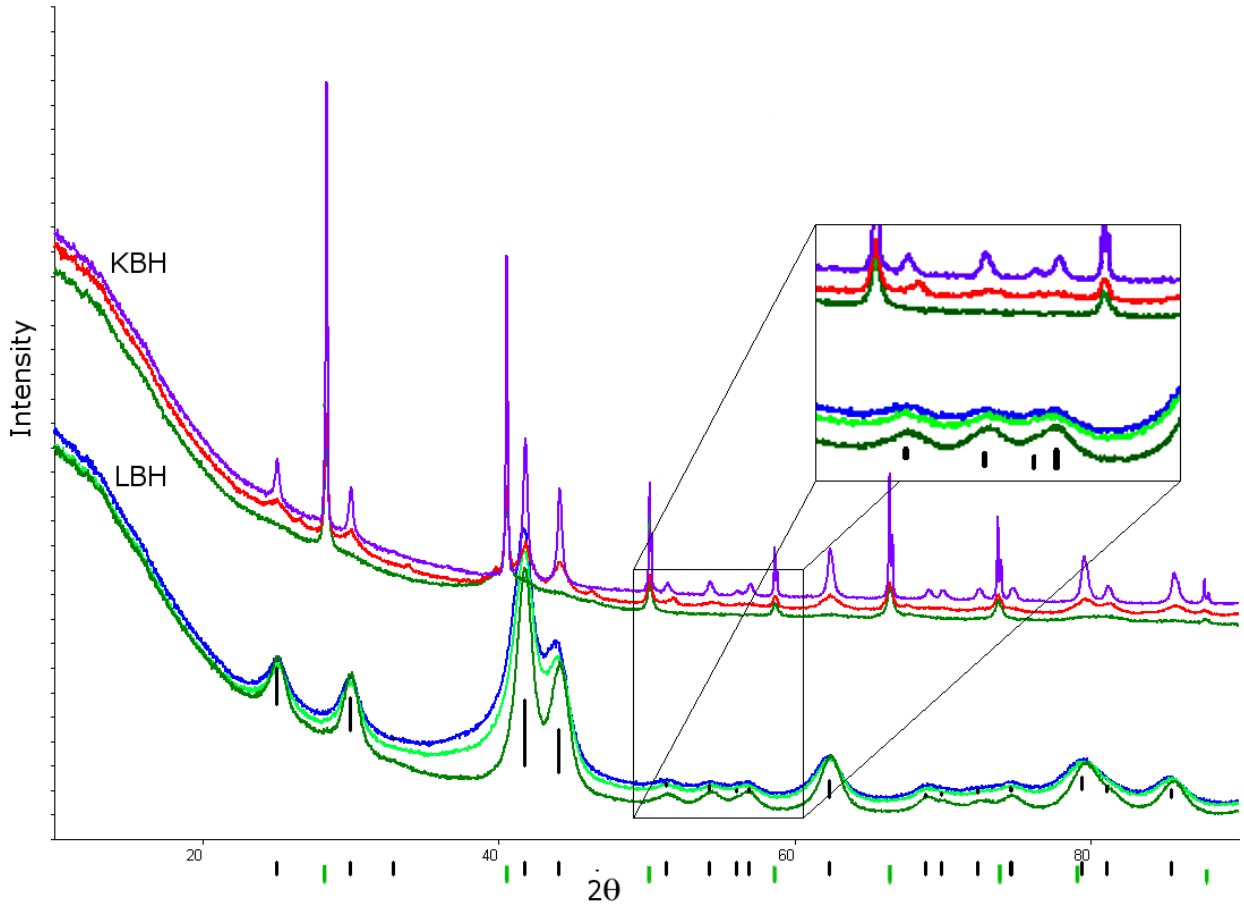


**Figure 3.24** pXRD comparison of PtSn nanoparticles synthesized with $SnCl_2$ using KBH (top) and LBH (bottom) reducing agents. Black drop lines correspond to PtSn, green lines to KCl. LBH annealing temperatures ranged from room temperature (blue) to 200 $^{o}$C (dark green), whereas KBH annealing temperatures ranged from 200 $^{o}$C (dark green) to 600 $^{o}$C (purple).

At 200$^{o}$C the PtSn reduced with LBH has grown about 20% in domain size from the as-made nanoparticles (from 4.3 to 5.5 nm). The particles show clear superlattice peaks. In contrast, PtSn reduced with KBH and annealed to 200 $^{o}$C are barely recognizable as PtSn, since the domain sizes are so small that the peaks are almost indistinguishable from an amorphous pattern. Upon annealing to 400 $^{o}$C the main peaks are resolved, but the narrow, intense KCl peaks dominate the weaker PtSn ordering peaks. It was only upon annealing to 600 $^{o}$C that the ordering peaks are

strong enough to be detected above the noise, with a domain size of 17.4 nm. Unprotected PtSn annealed to this temperature produces nanoparticles with a domain size of 50 nm or more (data not shown).

PtSn made via reduction of $SnCl_4$ similarly showed smaller domain sizes at higher temperatures when reduced with KBH as compared to LBH. However, both reducing agents resulted in multiple phases in addition to, or instead of, the target 1:1 phase. At 600 $^oC$, the sample reduced by KBH produced some peaks that are identifiable as partially ordered PtSn with a domain size of 15.5 nm, comparable to the reduction of $SnCl_2$ and $PtCl_4$ with KBH. This is a minority phase, however, as $PtSn_2$ is the majority product of the reduction.

### *3.4 Nucleation of Non-Stoichiometric Phases*

As mentioned in section 3.1.3, when $PtCl_4$ and $SnCl_2$ are reduced in a 2:3 ratio by LBH, the as-made nanoparticles form a mostly amorphous product that cannot be identified by pXRD because of the small domain size (see Figure 3.10). However, on heating to 200 $^oC$, the 1:1 phase PtSn crystallizes, instead of the stoichiometric phase $Pt_2Sn_3$. We conclude that the rate at which PtSn nucleates and grows from the amorphous nanophase at low temperatures is greater than the rate at which $Pt_2Sn_3$ nucleates and grows. When the same as-made nanoparticles are instead annealed at 400 $^oC$, the expected $Pt_2Sn_3$ forms as a well-crystallized phase; there is no evidence that any PtSn remains.

This behavior is a result of the interplay between the kinetics and thermodynamics of

crystallization. The PtSn synthesized at 200 $^{o}$C using the above synthesis procedure is metastable; annealed to a higher temperature, the residual Sn (which almost certainly exists as an amorphous Sn (or Pt-Sn alloy) undetectable by pXRD), incorporates into the structure. The conclusion is simple: the first phase to nucleate from amorphous products is not necessarily that with the average stoichiomentry of the amorphous phase. Once the "wrong" phase nucleates, the activation energy for growth of that phase can be lower than the activation energy of nucleating a different structure at the average composition. Such behavior has been seen in the nucleation of crystalline domains when amorphous thin films are annealed at low temperature, as seen in Figure 3.25[22].

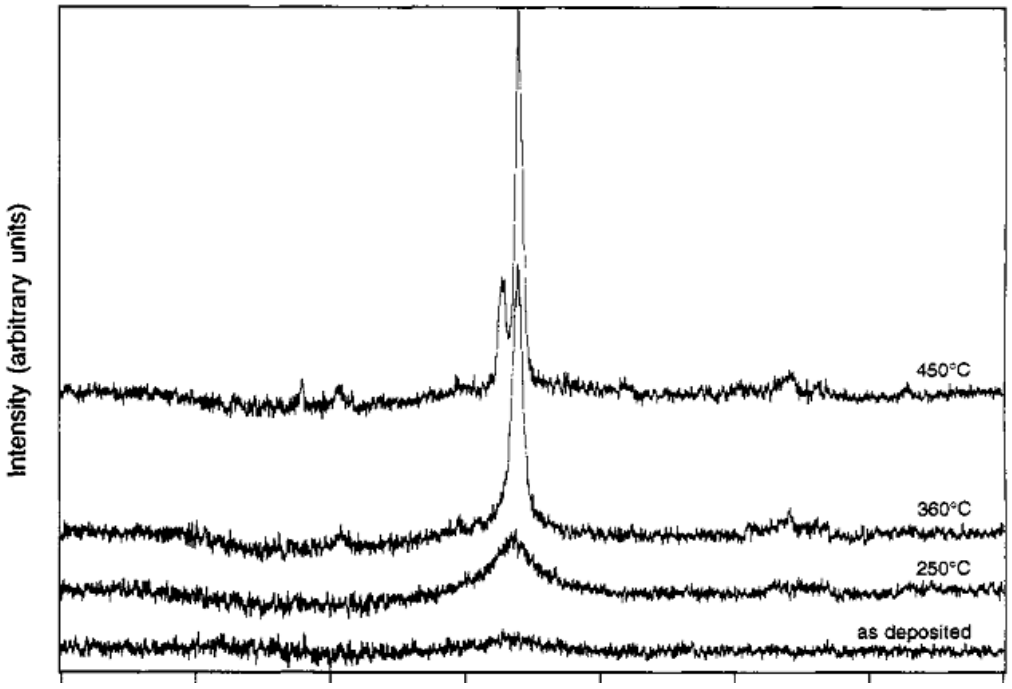


**Figure 3.25** pXRD pattern showing the transition from FeAl to $Fe_2Al_5$ product on annealing to different temperatures, from as-made films to 450 $^{o}$C. Taken from the work of Grant and Johnson[22].

This behavior can be even more pronounced in the co-reduction synthesis used in this work, particularly considering the lack of surfactants or other control agents. Even under ideal circumstances (perfect mixing, perfect molar ratios of precursors, no local concentration variations, no side reactions, and equally fast reduction rates of the two metals), seed crystals will only be composed of the exact stoichiometric ratio of metals on the average. On a particle-by-particle basis, the probability of an individual binary seed crystal having the appropriate ratio of metals is a function of the size of the seed crystal and of the metal ratio itself. This probability should follow a binomial distribution, provided that the reduction and incorporation of each individual metal atom from the solution are a completely independent events.

This effect is demonstrated below using the probability density function in Matlab. Figure 3.26 shows the distribution of nanoseed compositions that would occur when attempting to synthesize any given 1:1 phase via the co-reduction method, following the assumptions given above. Nanoseeds are also assumed to be simple cubic crystals with a given number of atoms (N) per side. For reference, the Pt-Pt bond distance in Pt metal is 2.77 Å, so such simple cubic crystals examined below would have side lengths of 1.4 nm (N = 5) to 8.3 nm (N = 30) if the atoms were the size of Pt.

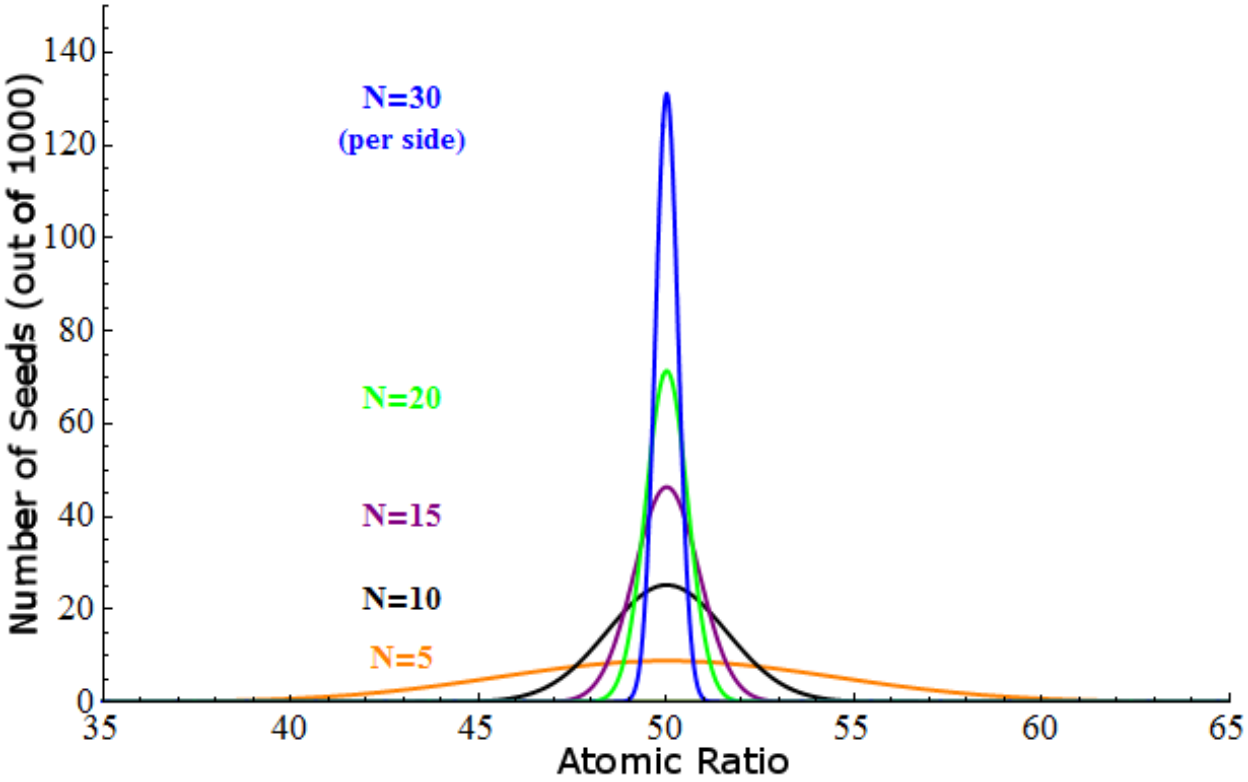


**Figure 3.26**. Probability distribution functions of nanoseeds synthesized via co-reduction from a solution containing a 50:50 mixture of metal chloride precursors. The calculation assumes 1000 total seeds. Five different seed sizes were assumed, all perfect cubes with N=5 (orange), N=10 (black), N=15 (purple), N=20 (green), or N=30 (blue) atoms per side.

From the above figure, it is clear that the size of the seed has a large impact on the breadth of the composition over which nanoseeds are synthesized. Remember, this is mathematically the best case scenario under ideal conditions; under real conditions, the breadth is likely to be larger as local concentration variations and mixing come into play, among other factors. Iterating the same calculation that produced Figure 3.26 over a sample of possible atomic ratios in solution (intended to represent most of the phases that will be synthesized in this work), the number of particles generated with each ratio of metals was calculated, again assuming 1000 total

nanoseeds. The result is Figure 3.27.

Note that the number of seeds generated with the stoichiometric metal ratio increases as one gets further from a 50:50 ratio of metals. To show this explicitly, the full width at half max (FWHM) of the peaks at atomic ratios of 10 %, 25 %, and 50 % were calculated for all nanoseed sizes. These are plotted in Figure 3.28. The FWHM is a good measure of the phase width. If one or more stable phases exist within the FWHM of the probability distribution of the stoichiometric phase, it is entirely unsurprising if the nanoparticles obtained via co-reduction are not phase pure. A good example of this is the synthesis of $PtSn_2$ (see Figure 3.13).

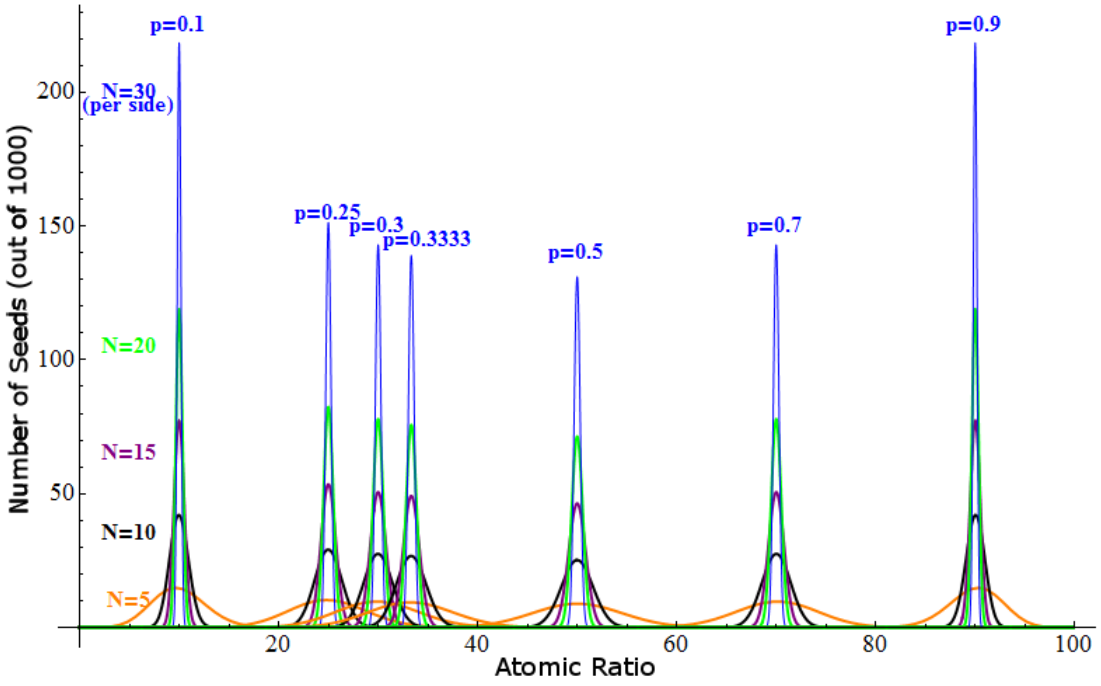


**Figure 3.27** Probability distribution functions of nanoseeds with various dimensions and atomic ratios.

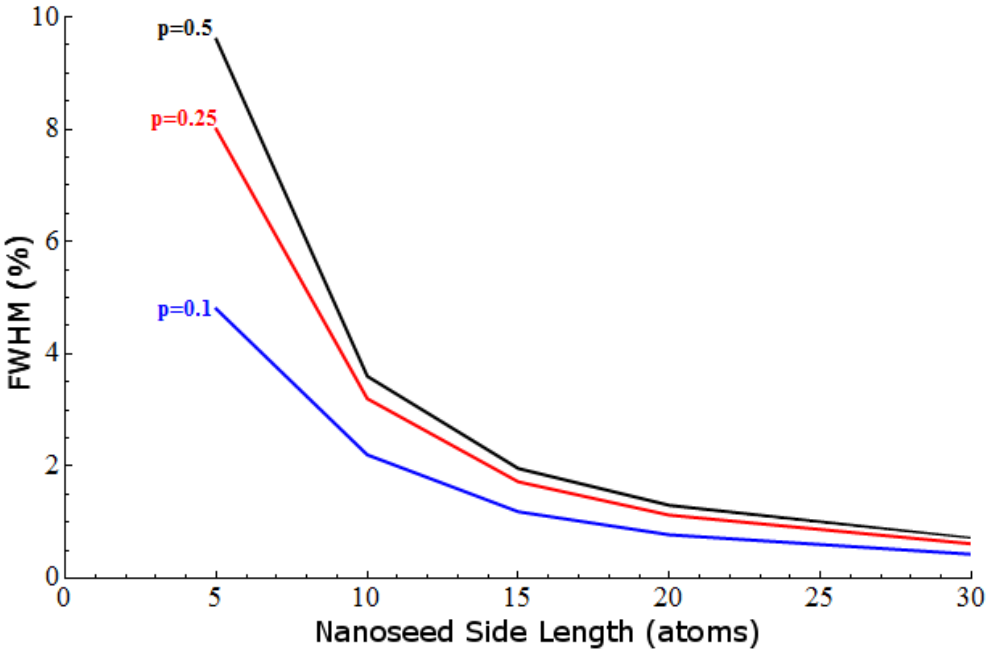


**Figure 3.28** The full-width at half-max of select probability distribution functions from Figure 3.27, plotted over the full range of nanoseed side length.

As the nanoseed size increases, the difference in FWHM between phases becomes minimal, but at small seed sizes - the initial formation of a seed - the probability gap is substantial. And again, these are ideal values for the FWHM of these functions; real values would certainly be larger without some other force directing the reduction of metals (e.g., pre-reduction complexation).

### *3.5 Supported Pt-Sn Nanoparticles*

Supported, well-dispersed nanoparticles are integral in catalysis to best utilize the high surface area of nanoparticles. The low-temperature ordering behavior of the Pt-heavy phases can be leveraged to make well-dispersed supported nanoparticles by a facile and direct synthetic route. More relevant to the goal of this work, however, is the fact that dispersing the nanoparticles on a carbon support prevents agglomeration, which allows the particles to be studied via microscopy

to further probe their ordered structures.

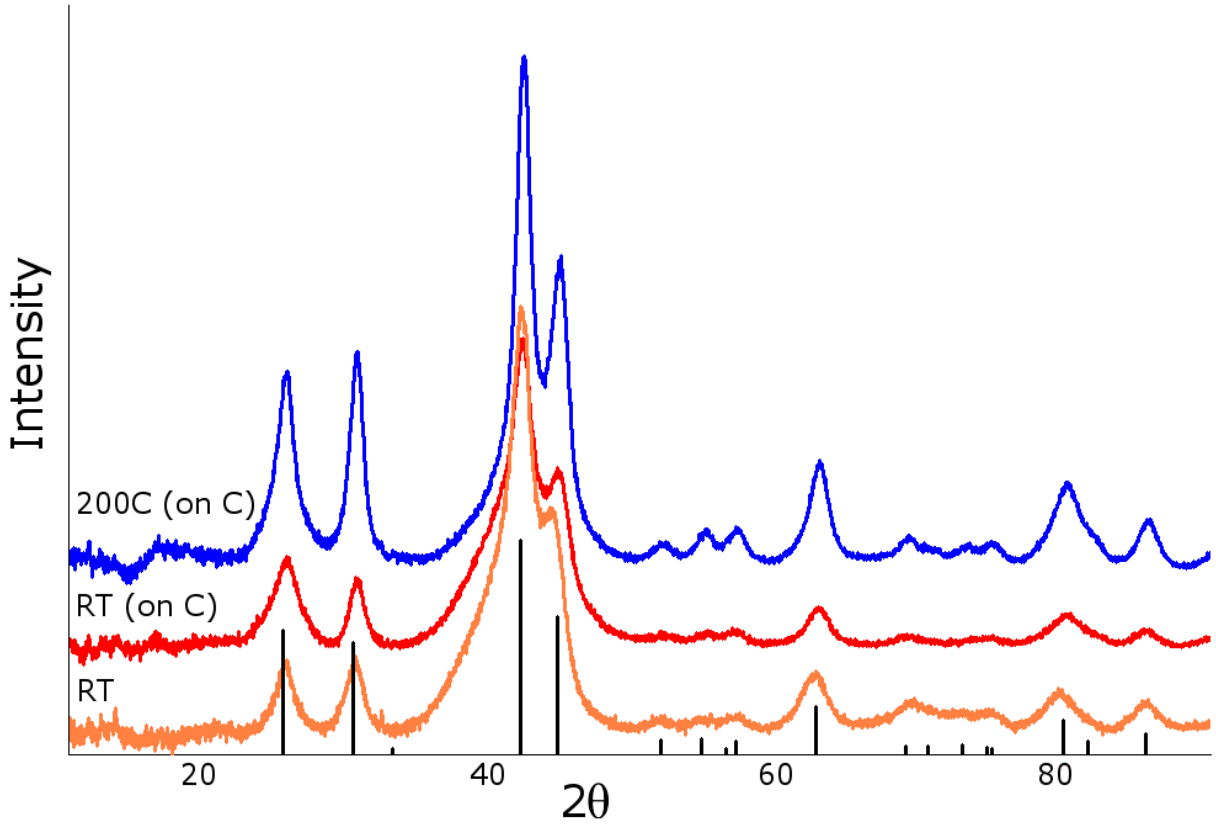


**Figure 3.29** pXRD shows that the reduction of $PtCl_4$ and $SnCl_2$ 1:1 in the presence of carbon black (Vulcan XC-72) produces smaller domain sizes than equivalent reductions of unsupported nanoparticles. The particle domain sizes increase from 4.3 nm to 5.5 nm on annealing the carbon-nanoparticle composite to 200 $^{o}$C.

The process of reducing the metal chloride precursors directly onto the carbon black support has the effect of making the as-made nanoparticles smaller and less well-ordered. For example, the peak at 42$^{o}$ 2θ in PtSn/C prepared at room temperature in the presence of carbon black shows a broader shoulder at smaller angles than the same peak with no carbon black (see Figure 3.29), possibly indicating the presence of some amount of Pt-heavy alloyed phase partially obscured by

the larger PtSn (102) peak. PtSn/C was therefore annealed at 200°C to obtain well-ordered nanoparticles with ordering character equivalent to the unsupported as-made nanoparticles.

The metal:carbon weight ratio in the reaction mixture was 1:5; however, TGA analysis under flowing air oxidizes both Sn and C, which allows one to calculate the mass of PtSn successfully dispersed onto the carbon support. The TGA profiles of PtSn/C (Figure 3.230) shows that 71 % of the mass is lost over the course of heating to 550 °C, which gives a weight percent of 26 % metal for the PtSn/C sample following the procedure detailed in section 2.3.2. The small difference from the 20 % ratio of reactants (C to metal) may be due to the retention of some C in the sample.

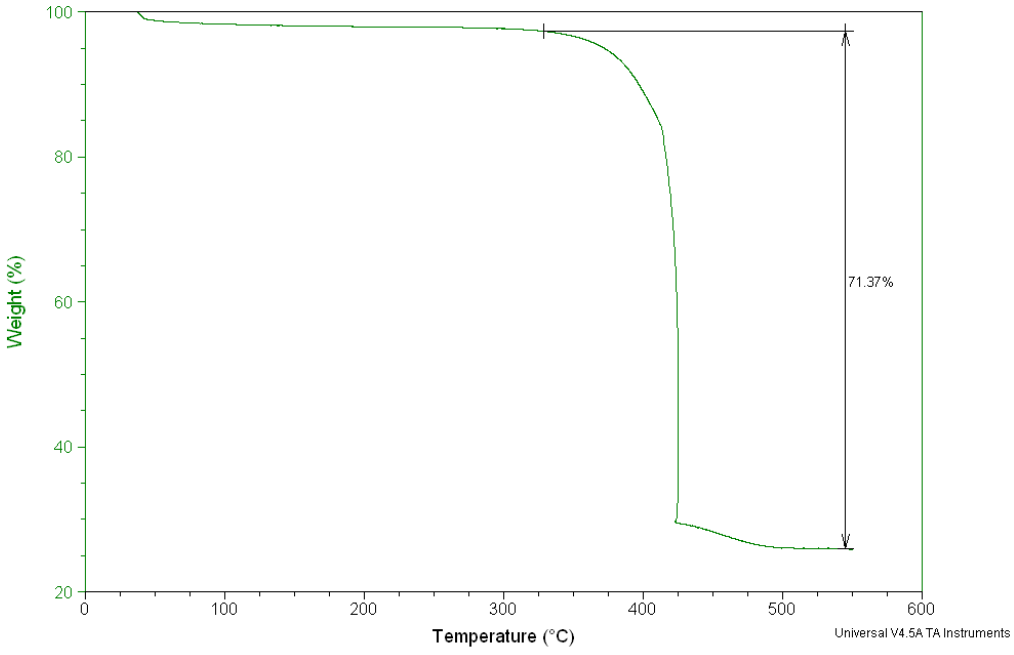


**Figure 3.230** TGA profile of PtSn/C heated in air at 10 °C per hour and held at 550 °C for 30 minutes, showing weight loss of carbon (and "hidden" weight gain of tin oxide).

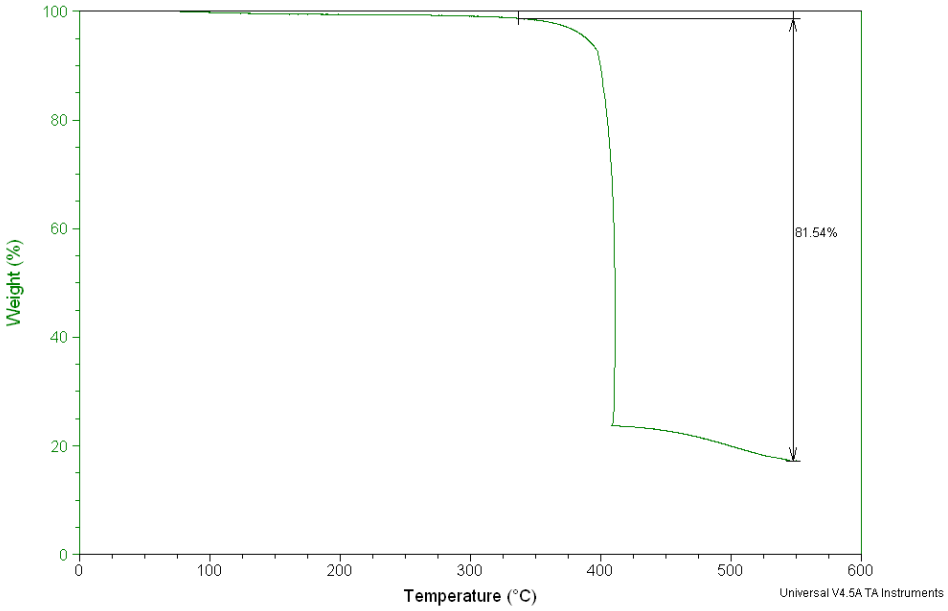


**Figure 3.31** TGA profile of $Pt_3Sn$/C heated in air at 10 $^oC$ per hour and held at 550 $^oC$ for 30 minutes.

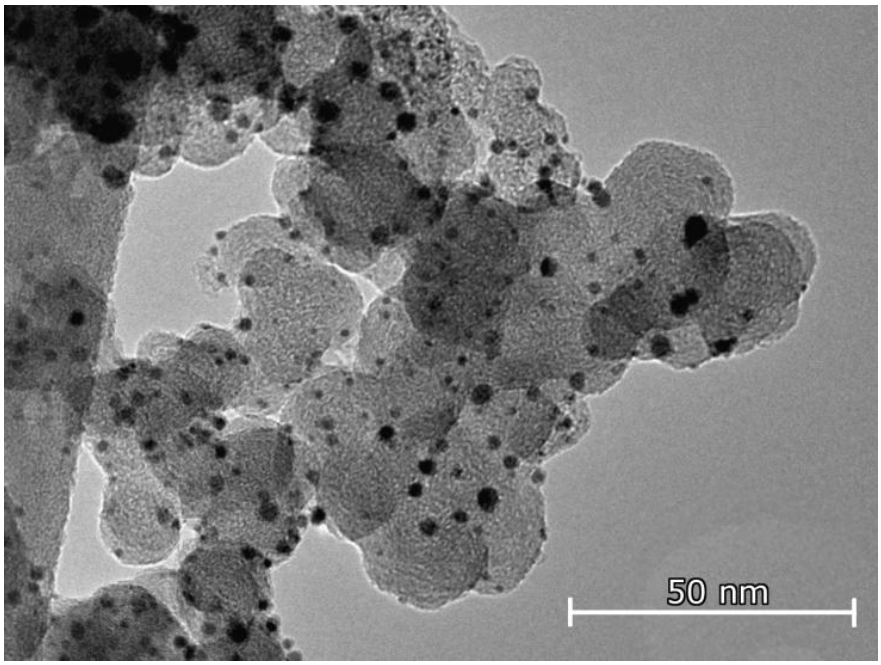


**Figure 3.32** TEM image of $Pt_3Sn$ intermetallic nanoparticles supported on carbon black, annealed at 300 $^oC$.

For $Pt_3Sn/C$, a similar TGA run (Figure 3.31) and calculation gives a weight percent of 18% metal. In both cases, the difference between the theoretical loading of metal on carbon and the experimental value is within expected error for the technique. Figures 3.32 and 3.33 show TEM and SEM images of the $Pt_3Sn/C$ and PtSn/C nanoparticles, respectively. PtSn particle sizes were measured in the TEM to be 5.5 ± 1.7 nm, and $Pt_3Sn$ particles 4.6 ± 1.4 nm, which is in rough agreement with domain sizes measured by pXRD.

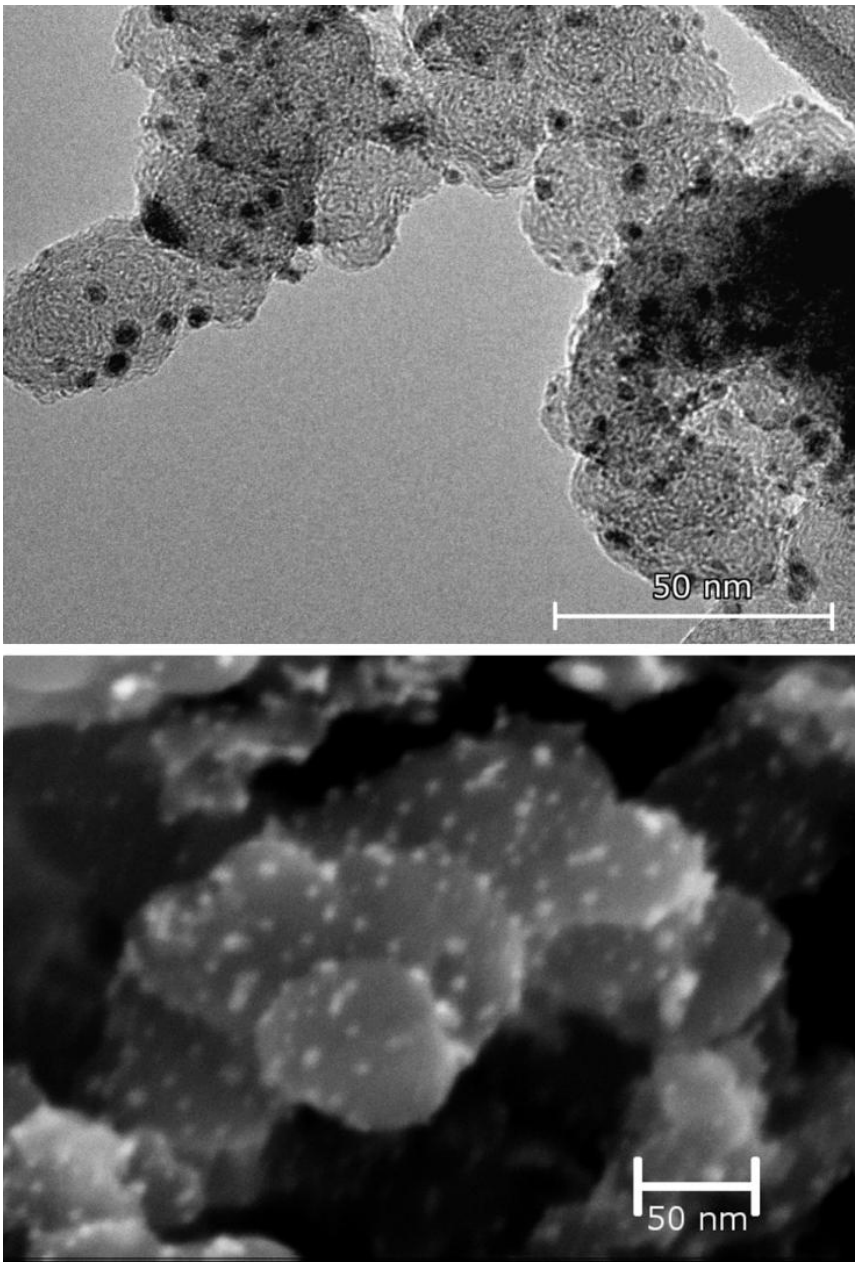


**Figure 3.33** TEM and SEM images of PtSn ordered intermetallic nanoparticles made by reduction of a solution of 1:1 $PtCl_4$ and $SnCl_2$ in the presence of a carbon black support, followed by annealing to 200 $^{o}$C. Bright spots in the SEM indicate metal nanoparticles on the surface of the support.

Finally, HAADF-STEM images and electron diffraction patterns of the PtSn/C particles were acquired to further test the presence of nanoscale ordering. As seen in Figure 3.34, diffraction patterns and Miller planes of two example as-made PtSn nanoparticles match expected values for the 1:1 ordered phase.

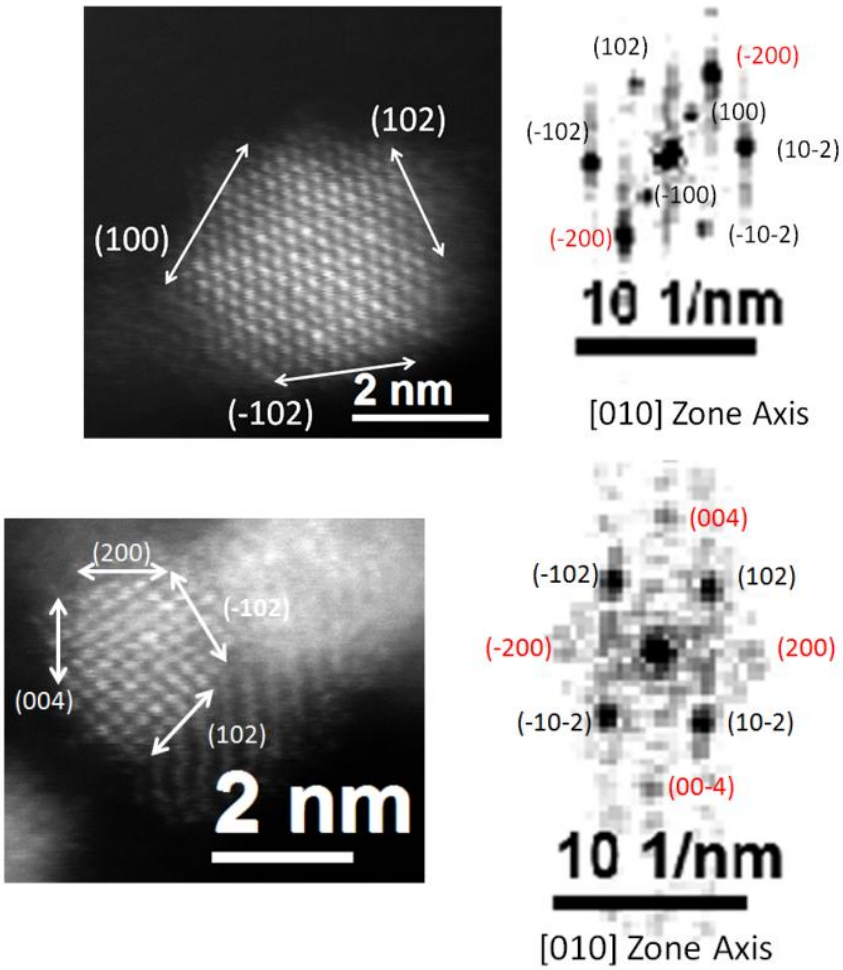


**Figure 3.34** HAADF-STEM images and electron diffraction patterns of individual PtSn/C as-made nanoparticles. Red Miller indices denote superlattice diffraction peaks. Derived distances for identifiable Miller planes: (100) = 4.1 Å, (200) = 2.0 Å, (102) = 2.2 Å, (004) = 1.4 Å.

### *3.6 Conclusions*

The Pt-Sn system was chosen as a model system for investigating the kineticss of co-reduction of Pt-M binary systems. However, after discovering the uncharacteristically low annealing temperatures required for ordering (and ordering behavior present at room temperature for the 1:1 phase), further investigations showed that Pt-Sn is definitely not a typical system. The Pt-Sn complexes that form prior to the co-reduction appear to have a great effect on the subsequent as-made nanoparticles. In order to determine how large a role these complexes played in the observed reduction behavior, other Pt-M systems would need to be explored and compared to Pt-Sn. We have shown that even small changes, such as changing from Sn(II) to Sn(IV) chloride precursors, change the observed behavior dramatically. The following chapter discusses the synthesis and characterization of other Pt-M systems, looking first and foremost at similar systems, to determine if these observations are general trends or are specific to Pt-Sn.

REFERENCES


(1) Okamoto, H.; Cenzual, K. *ASM Alloy Phase Diagrams Center*; ASM International: Materials Park, OH, USA.
(2) Lim, D.-H.; Choi, D.-H.; Lee, W.-D.; Lee, H.-I. *Appl. Catal. B Environ.* **2009**, *89*, 484–493.
(3) Teran, F. E.; Santos, D. M.; Ribeiro, J.; Kokoh, K. B. *Thin Solid Films* **2012**, *520*, 5846–5850.
(4) Tayal, J.; Rawat, B.; Basu, S. *Int. J. Hydrog. Energy* **2011**, *36*, 14884–14897.
(5) Zheng, L.; Xiong, L.; Sun, J.; Li, J.; Yang, S.; Xia, J. *Catal. Commun.* **2008**, *9*, 624–629.
(6) Jeyabharathi, C.; Venkateshkumar, P.; Mathiyarasu, J.; Phani, K. L. N. *Electrochimica Acta* **2008**, *54*, 448–454.
(7) DeSario, D. Y.; DiSalvo, F. J. *Chem. Mater.* **2014**, *26*, 2750–2757.
(8) Chen, H.; Wang, D.; Yu, Y.; Newton, K. A.; Muller, D. A.; Abruña, H.; DiSalvo, F. J. *J. Am. Chem. Soc.* **2012**.
(9) Chen, H. A Surfactant-Free Strategy For Synthesizing And Processing Intermetallic Platinum-Based Nanoparticle Catalysts. Dissertation, Cornell University: Ithaca, NY, 2013.
(10) McCusker, L. B.; Von Dreele, R. B.; Cox, D. E.; Louër, D.; Scardi, P. *J. Appl. Crystallogr.* **1999**, *32*, 36–50.
(11) Rietveld, H. M. *Acta Crystallogr.* **1967**, *22*, 151–152.
(12) Gregoire, J. M.; Kostylev, M.; Tague, M. E.; Mutolo, P. F.; Dover, R. B. van; DiSalvo, F. J.; Abruña, H. D. *J. Electrochem. Soc.* **2009**, *156*, B160–B166.
(13) Cui, C.-H.; Li, H.-H.; Liu, X.-J.; Gao, M.-R.; Yu, S.-H. *ACS Catal.* **2012**, *2*, 916–924.
(14) Antonelli, S. B.; Allen, T. L.; Johnson, D. C.; Dubin, V. M. *J. Electrochem. Soc.* **2005**, *152*, J120–J124.
(15) Nelson, J. H.; Wilson, W. L.; Cary, L. W.; Alcock, N. W.; Clase, H. J.; Jas, G. S.; Ramsey-Tassin, L.; Kenney, J. W. *Inorg. Chem.* **1996**, *35*, 883–892.
(16) Petrosyan, S. A.; Rigos, A. A.; Arias, T. A. *J. Phys. Chem. B* **2005**, *109*, 15436–15444.
(17) Gunceler, D.; Letchworth-Weaver, K.; Sundararaman, R.; Schwarz, K. A.; Arias, T. A. *Model. Simul. Mater. Sci. Eng.* **2013**, *21*, 074005.
(18) Gunceler, D.; Arias, T. A. *ArXiv14036465 Cond-Mat Physicsphysics* **2014**.
(19) Gavnholt, J.; Olsen, T.; Engelund, M.; Schiøtz, J. *Phys. Rev. B* **2008**, *78*.
(20) Kowalczyk, T.; Yost, S. R.; Voorhis, T. V. *J. Chem. Phys.* **2011**, *134*, 054128.
(21) Perdew, J. P.; Burke, K.; Ernzerhof, M. *Phys. Rev. Lett.* **1996**, *77*, 3865–3868.
(22) Grant, C. A.; Johnson, D. C. *Chem. Mater.* **1994**, *6*, 1067–1071.

# CHAPTER 4

# OTHER INTERMETALLIC PHASES: COMPARISONS AND CONTRASTS

In the previous chapter, the reduction and growth of Pt-Sn ordered intermetallic nanoparticles was investigated with the purpose of using it as a model system to describe general factors that influence the formation of ordered structures at low annealing temperatures. Naturally, such predictions and trends need to be tested using other systems. In this chapter, other binary and ternary systems will be investigated and compared to observations from the Pt-Sn system, continuing to focus on making and reinforcing predictions from the bulk phase diagrams when possible. The co-reduction method for each of these phases is described in Chapter 2, with any deviations being noted in the appropriate subchapter.

## *4.1 Other Pt-M Binary Intermetallics*

### *4.1.1 Pt-Sb*

The first phase to be compared to platinum tin is platinum antimony (Pt-Sb). Since the covalent radius of antimony is effectively equal to that of tin (within a picometer), one might expect the phases and crystal structures of Pt-Sb to be very similar to that of Pt-Sn. This is only partially correct. Figure 4.1 is the phase diagram of Pt-Sb in the bulk. Note that Pt again has the highest melting point of all the phases, but the melting point drops sharply as Sb is added, more sharply than in Pt-Sn. It reaches a minimum at roughly 33 % and then dramatically increases to a local maximum at 66 %, again in contrast to Pt-Sn. This local maximum marks the congruent melting point of $PtSb_2$, the only congruently melting phase in the system. This can be attributed to the characteristically strong Sb-Sb bonds present in the cubic $FeS_2$ structure; $PtSn_2$, in contrast, has a

$CaF_2$ prototypical structure.

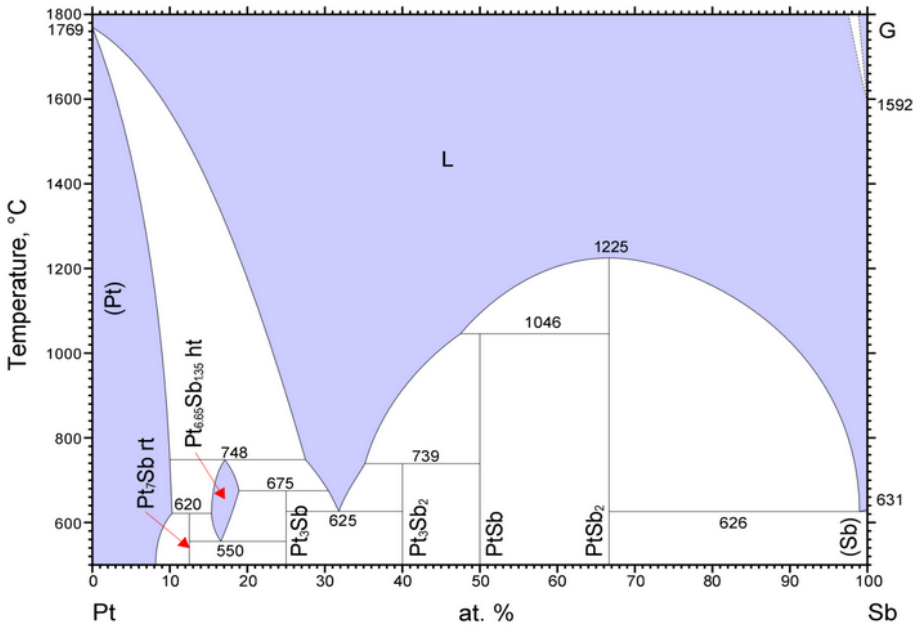


**Figure 4.1** The bulk phase diagram of Pt-Sb. Taken with permission from ASM Alloy Phase Diagram International[1].

Other phases in the system include $Pt_3Sb$ and PtSb, similar to $Pt_3Sn$ and PtSn, though $Pt_3Sb$ adopts a tetragonal structure instead of an ordered primitive cubic structure. Phases that do not have a corresponding phase in Pt-Sn include $Pt_7Sb$, $Pt_3Sb_2$, and a compound with considerable composition width centered near the composition $Pt_5Sb$. This latter phase has a lower peritectoid decomposition temperature and an upper peritectic decomposition (incongruently melting temperature), being thermodynamically stable only above 550 $^oC$ but below 748 $^oC$. Both PtSb and PtSn adopt the hexagonal NiAs structure, with near-identical lattice parameters (a = 4.13 Å, c = 5.48 Å for PtSb; a = 4.10 Å, c = 5.44 Å for PtSn), which results in near-identical pXRD patterns for these two phases; this will be important in Section 4.3.1. In summary, Pt-Sb

contains five binary phases spread across the composition range, which can be compared to the five binary Pt-Sn phases, even though the details of melting or decomposition and their crystal structure type may be different.

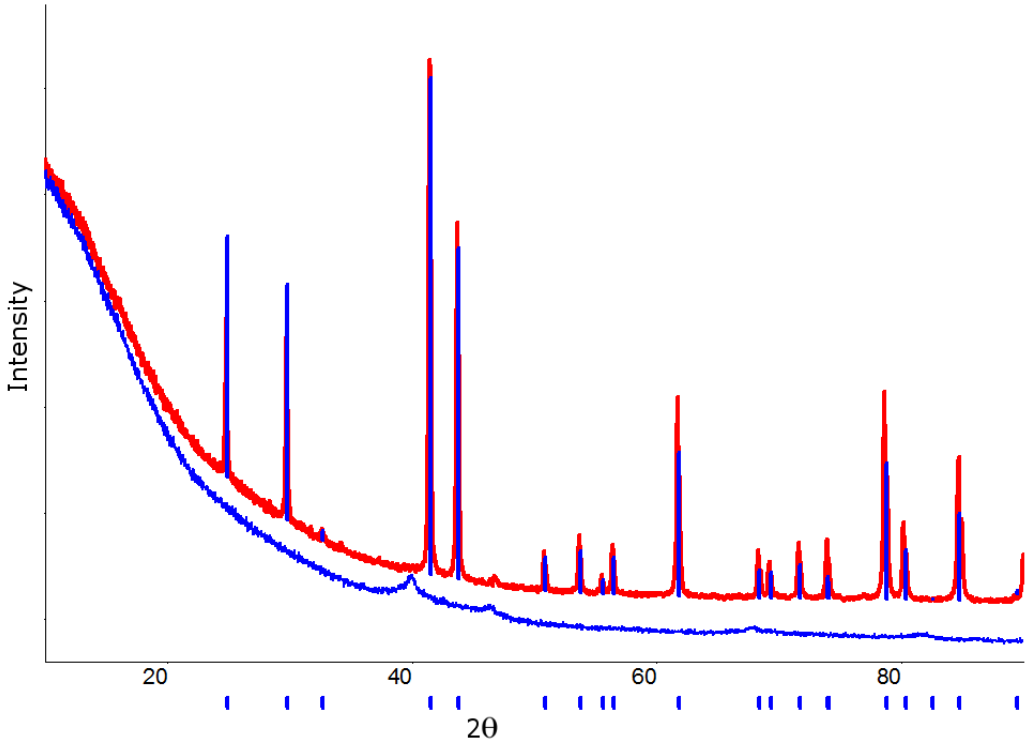


**Figure 4.2** pXRD pattern of PtSb as-made nanoparticles (blue) and annealed at 400 °C (red). Blue drop lines indicate the ordered PtSb phase (PDF card # 03-065-3432).

We begin the exploration of Pt-Sb system with the 1:1 phase. PtSb was synthesized via lithium borohydride (LBH) co-reduction - see Chapter 2 for methods - and annealed to 400 °C to form ordered intermetallic nanoparticles with a large domain size of 47 nm, as shown in Figure 4.2. The pXRD of the same product at room temperature gives a broad, close to amorphous pattern with a few very weak peaks that are close to the expected positions of elemental platinum or

platinum alloy nanoparticles, which indicates that crystalline PtSb does not nucleate and grow near room temperature. This is further supported by annealing at an intermediary temperature (as shown in Figure 4.3), where the product obtained from the same 1:1 ratio of $PtCl_4$ to $SbCl_3$ reactants results in a mixed phase product encompassing multiple crystalline Pt-Sb phases.

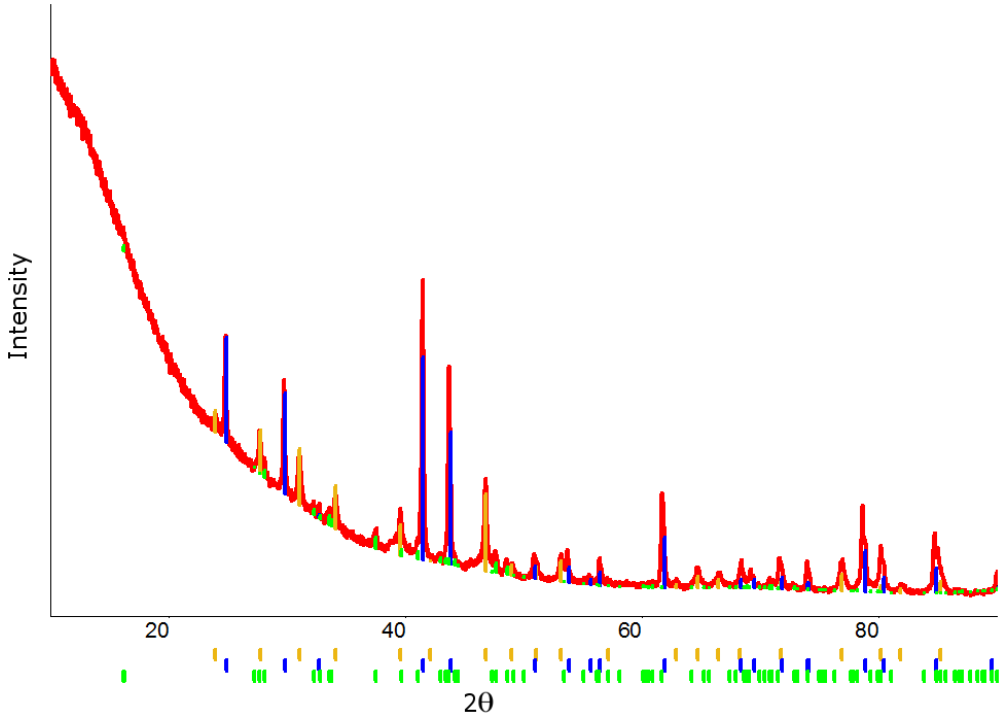


**Figure 4.3** $PtCl_4$:$SbCl_3$::1:1 co-reduced by LBH and annealed to 200 $^oC$, forming multiple Pt-Sb phases. Drop lines correspond to PtSb (blue, PDF card #04-007-7284), $PtSb_2$ (orange, card #04-003-1904), and $Pt_3Sb_2$ (green, card #04-007-1729).

Much like $Pt_2Sn_3$ (and in contrast to PtSn), it appears that the incongruently melting PtSb is not the only phase to nucleate during low temperature annealing, and higher annealing temperatures are necessary to form a (mostly) phase-pure product; small impurity peaks are apparent in Figure 4.2 in the region of 30-50 $^o$ 2θ. These peaks are too small in intensity and number to

identify the impurity phase, but by analysis of the relative peak areas, the sample is at least 95 % pure PtSb.

For Pt-Sn, the congruently melting phases were the most platinum-rich phases, and the tin rich phases were all incongruently melting. In contrast, the only congruently melting Pt-Sb phase is the line phase with the highest percentage of the non-noble element, $PtSb_2$. This makes $PtSb_2$ a good test case for suggesting which parameters may be useful predictors for the ease of nucleation and growth of target phases, such as congruent melting point or the initial stoichiometry of reactants. Additionally, $PtSb_2$ has a cubic crystal structure with the $FeS_2$ structure type (both contain X-X bonded anions), with nearly identical lattice parameters as cubic $PtSn_2$ (which has the $CaF_2$ structure type and no anion-anion pairs).

Figure 4.4 is the pXRD pattern of $PtSb_2$ annealed to 500 $^{o}$C, showing the mostly phase-pure product. Room temperature pXRD scans of this sample consisted of weak unidentifiable Pt alloy peaks, and samples annealed at lower temperatures (around 300 $^{o}$C) were combinations of multiple phases, including of Pt, PtSb, $PtSb_2$, and $Sb_2O_3$.

The domain size of the $PtSb_2$ is 22.1 nm, which is small for agglomerated nanoparticles annealed to such a relatively high temperature, possibly owing to the high melting point of the phase; compare to PtSb annealed to 400 $^{o}$C with a domain size over twice as large. A few weak impurity peaks are visible near 29 $^{o}$, 40 $^{o}$, and 48 $^{o}$ 2θ (also marked by asterisks in Figure 4.4)

possibly correspond to Sb or $Sb_2O_5$, but there are not enough peaks to confirm the identity of the second phase(s). Impurities make up perhaps 5 to 10 wt % of the sample according to pXRD, and the composition of the sample by EDX is 41 ± 9 % Pt, 59 ± 9 % Sb, which is within the range of the theoretical ratio. The sample is therefore mostly phase pure and crystalline, which is in stark contrast to $PtSn_2$. This suggests that the fact that a phase has a congruent bulk melting temperature is more important to forming phase pure ordered products than being platinum rich.

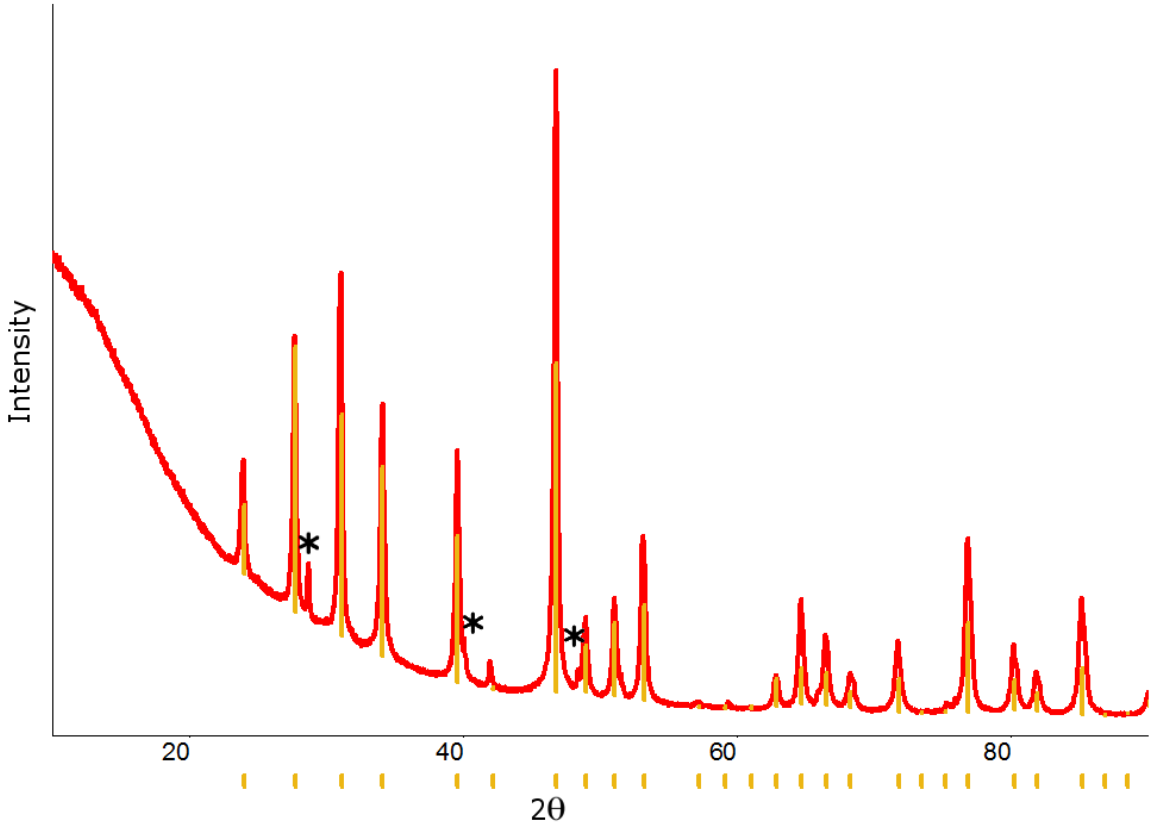


**Figure 4.4** pXRD pattern of $PtSb_2$ annealed at 500 °C. Orange drop lines correspond to $PtSb_2$ (PDF card #04-007-4639). Peaks marked with asterisks are impurity peaks of undetermined identity.

To add support to this hypothesis, the co-reduction of the Pt-heavy phases - $Pt_7Sb$, $Pt_3Sb$, and $Pt_3Sb_2$ - were each met with their own challenges in forming the target phase. The pXRD pattern of $Pt_7Sb$ is unsurprisingly very similar to that of pure Pt. Figure 4.5 shows a section of the full powder pattern highlighting the main peaks; the drop lines show how closely spaced the peaks are from the two phases. A subsequent Rietveld analysis concludes that the sample is mostly $Pt_7Sb$ (87 ± 5 %) with a domain size of 7.0 ± 1.0 nm; however, none of the (extremely weak) ordering peaks show up by pXRD, so which phase are we really seeing here?

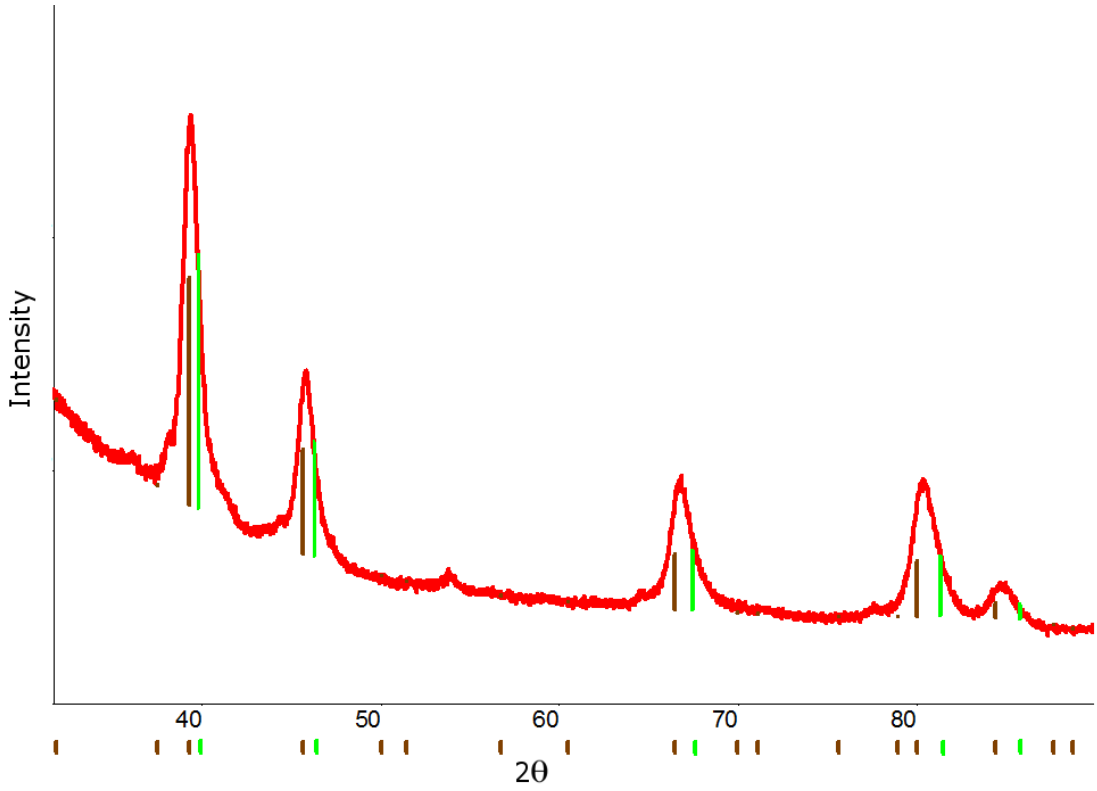


**Figure 4.5** pXRD pattern of $Pt_7Sb$ annealed at 300 °C. Drop lines correspond to $Pt_7Sb$ (brown, card # 04-007-4139) and Pt (green, card # 04-007-2989).

Antimony has a high solubility in platinum (up to 8 %), which means that $Pt_7Sb$ (at a Sb

"concentration" of 12.5 at.%) is not far off from that phase. As shown in Figure 3.27, in a random distribution of two species in solution, probability distributions of local concentrations have substantial width in nanoparticles with sizes less than about 10 nm. Alloy Pt nanoparticles can therefore nucleate easily from co-reduction - it is a statistical certainty that local concentrations of Sb will drop below 8 % - and once formed such nanoparticles could easily incorporate some (or most) of the antimony present in the reaction vessel. The result is that the synthesis of $Pt_7Sb$ inevitably results in Pt-Sb alloys in addition to, or instead of, the intended product. The "lumpy" bases of the peaks shown in Figure 4.5 are the result of peak broadening probably caused by the presence of multiple Pt-Sb alloys with slightly different compositions and lattice parameters.

$Pt_7Sb$ is simply too close to a stable phase to be synthesized consistently as a pure phase; the fact that it decomposes to form a Pt rich alloy and an intermetallic with a short thermal span of stability at 620 $^oC$ means that annealing to higher temperatures will not help to improve its purity. As-made samples have much smaller domain sizes, with peaks so broad that it is impossible to differentiate between Pt and $Pt_7Sb$. We know from EDX that most, if not all, of the antimony ended up in the final product (the product was found to be 14 ± 5 % Sb), so the trouble in forming the proper phase must come from the rate of nucleation of seeds and their subsequent growth in each nanoparticles.

The synthesis of $Pt_3Sb$ is an excellent example of how co-reduction can result in the nucleation of metastable phases that require high temperature annealing in order to produce the desired

product. The as-made nanoparticles from this synthesis had very small domain sizes, and the crystal structure by pXRD is very similar to that expected from pure or alloy Pt (see Figure 4.6). When the same sample was annealed to 200 $^{o}$C, the amount of the Pt-like alloy in the sample decreased to 25 %, and two other phases (PtSb and likely $Pt_3Sb_2$) crystallized, indicating that some of the antimony had preferentially concentrated into growing $Pt_3Sb$ particles through diffusion under annealing. Heating the sample further to 400 $^{o}$C again decreased the amount of the Pt-like alloy in the sample to 7 %, and also increased the amount of PtSb and $Pt_3Sb_2$ in the sample to 52 % and 41 %, respectively. Interestingly, the target stoichiometric phase ($Pt_3Sb$) was never detected. Annealing at much higher temperature would likely decompose the phase in any case, since it peritectically decomposes in bulk at 675 $^{o}$C.

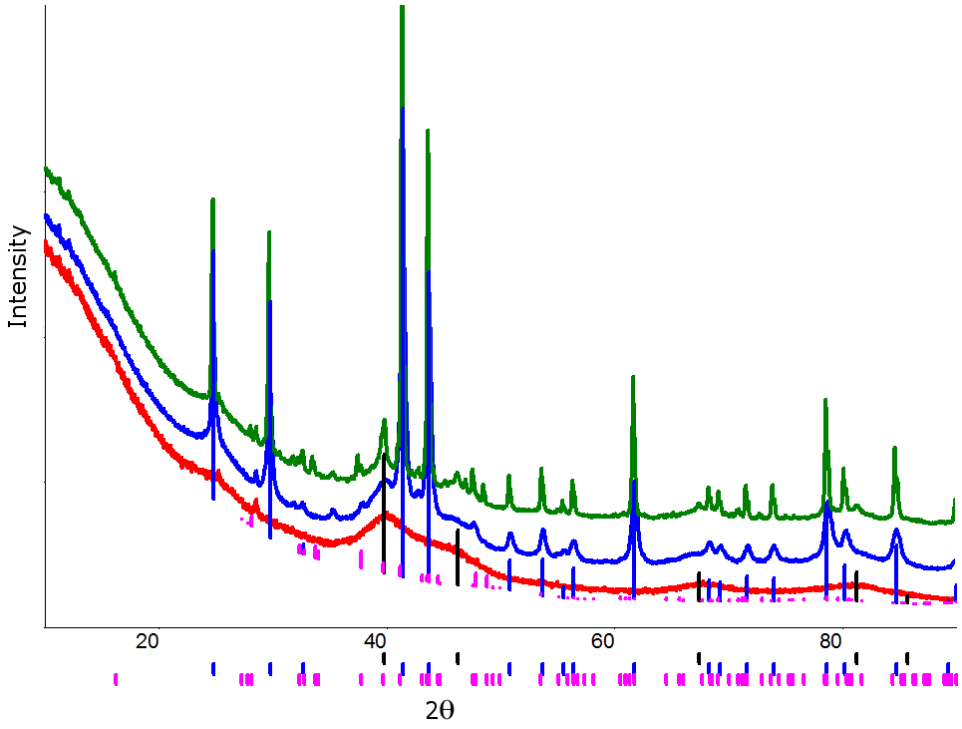


**Figure 4.6** pXRD patterns of $Pt_3Sb$ as-made nanoparticles (red), annealed at 200 $^{o}$C (blue), and annealed at 400 $^{o}$C (green). Drop lines correspond to PtSb (blue, PDF card # 04-008-6110), Pt (black, card # 04-016-6405), and $Pt_3Sb_2$ (pink, card #04-007-7283).

As expected from previous experiments, $Pt_3Sb_2$ proved challenging to synthesize. First, it has an orthorhombic crystal structure. Complex low symmetry structures have been found in our experience to be the most consistently difficult compounds to prepare as single phase nanoparticles. Second, it has a peritectic melting point (739 $^oC$), at which it decomposes to a liquid and a stable hexagonal phase (PtSb), which also has a peritectic melting point.

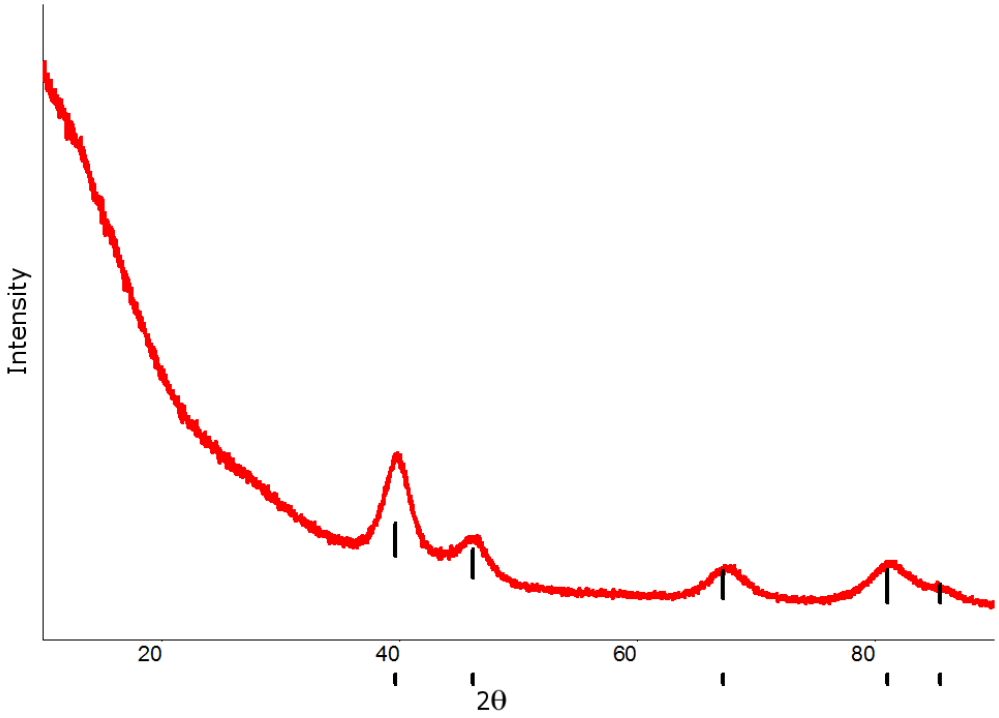


**Figure 4.7** pXRD pattern of $Pt_3Sb_2$ annealed to 200 $^oC$. Black drop lines correspond to Pt.

It was found that, rather than nucleating $Pt_3Sb_2$, co-reduction of precursors in this ratio resulted in nanoparticles with an alloy of Pt (fcc structure). The antimony may also form a second phase, which would have to be amorphous or even may be oxidized to amorphous $Sb_2O_3$ upon air exposure. At higher temperatures most of the Sb must react with the Pt, since Figure 4.7 shows the pXRD pattern of the particles annealed to 200 $^oC$; the product clearly adopt an fcc structure

with a lattice parameter close to that of Pt. The particles have a domain size of 2.9 nm, with no suggestion of impurities. This small domain size is less than that found for pure Pt (4.5 nm, Figure 3.2). This smaller domain size may be a result of alloy formation.

It is interesting that the one Pt-Sb phase that has a congruent melting point is able to be synthesized as a pure intermetallic upon annealing, though it must be annealed to 500 $^{o}$C in order to show a high degree of ordering (in contrast to similar Pt-Sn phases, again supporting the hypothesis that Pt-Sn pre-reduction complexes aid in the formation of ordered structures at low temperatures). The other Pt-Sb phases are all incongruently melting, and only one of them (hexagonal PtSb, with the highest peritectic melting temperature in the phase diagram – 975 $^{o}$C) readily forms phase-pure ordered nanoparticles. The observations on Pt-Sb nanoparticle synthesis are summarized in Table 4.1. Melt behavior, crystal structure, and the presence of any near neighbors on the phase diagram are all important characteristics that potentially correlate with the ease of formation of ordered intermetallic nanoparticles.

| **Phase** | **Crystal Structure** | **Melting Point ($^{o}$C)** | **% Target Phase** |
|---|---|---|---|
| **$Pt_7Sb$** | Cubic | 620 IMP[a] | 88 %[b] |
| **$Pt_3Sb$** | Tetragonal | 675 IMP | 0 % |
| **$Pt_3Sb_2$** | Orthogonal | 739 IMP | 0 % |
| **PtSb** | Hexagonal | 1046 IMP | > 95 % |
| **$PtSb_2$** | Cubic | 1225 CMP | > 95 % |

**Table 4.1** Summary of Pt-Sb phase synthesis. [a]IMP = incongruent melting point, CMP = congruent melting point. [b]This value is possibly inflated because of alloying making it difficult to assess the purity of the target phase via pXRD.

*4.1.2 Pt-In*

As seen in Figure 4.8, the bulk phase diagram of Pt-In comes with its own set of new challenges. There are more ordered phases; in some of these phases, both of the stoichiometry coefficients are three or greater, a situation that has not previously been faced. Another new factor is the introduction of significant composition width in some phases; $Pt_3In$, for example, has a composition width of approximately 2 at.% centered around 75 % Pt. The 1:1 phase PtIn is not thermodynamically stable at low temperatures, but instead is stable only in a narrow high-temperature region; attempts to synthesize this phase resulted in phase segregation with no detectable amount of the target phase. Other Pt-In phases were selected in order to investigate whether or not some of these differences alter the patterns seen thus far.

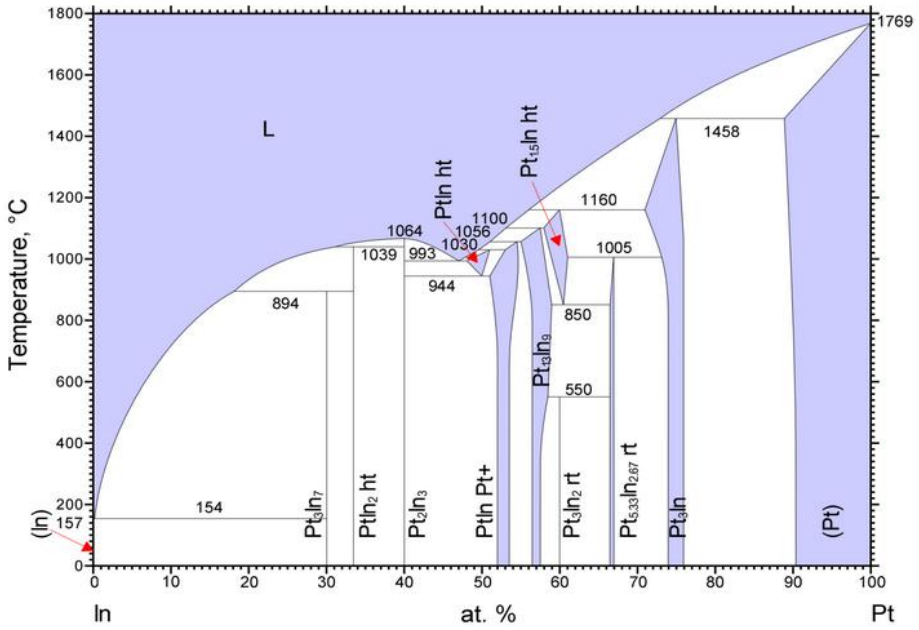


**Figure 4.8** The bulk phase diagram of Pt-In. Taken with permission from ASM Alloy Phase Diagram International[2].

First, we consider the synthesis of the $Pt_3In$ phase from $PtCl_4$ and $InCl_3$. There is no evidence of

complex formation by UV-Vis absorbance, and $PtCl_4$ in THF does not change color upon addition of $InCl_3$. The visible composition width does not appear to negatively affect the synthesis of $Pt_3In$, which forms a phase pure structure upon co-reduction and annealing to 600 $^oC$ with a domain size of 15.7 nm (see Figure 4.9).

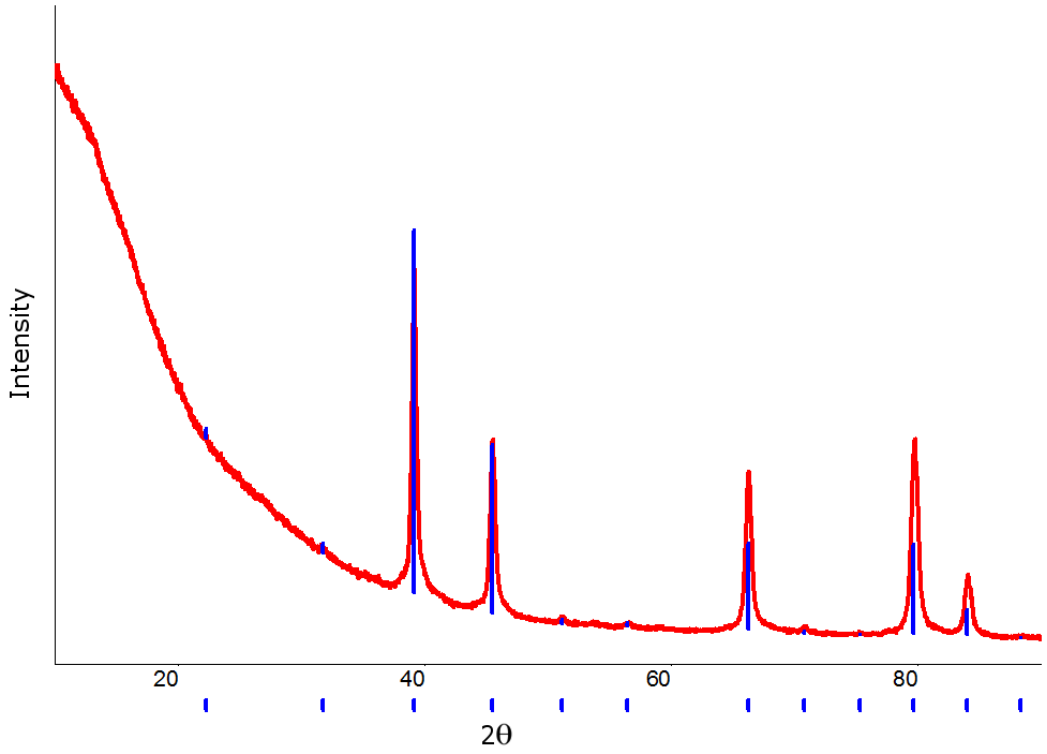


**Figure 4.9** pXRD pattern of $Pt_3In$ annealed at 600 $^oC$. Blue drop lines correspond to $Pt_3In$ (PDF card #04-004-8869).

Note the asymmetric broadening at the base of the peaks. Domain size distribution will cause symmetric broadening; asymmetric broadening is likely the result of particles having a range of very similar lattice parameters. This seems more likely since the $Pt_3In$ structure can incorporate a certain percentage of defects that accommodate the phase width, a width that may be larger in

the nanoparticle regime. The atomic ratio of Pt:In in the sample was found by EDX to be 85:15 with a standard deviation of 10 %. Other than that, $Pt_3In$ looks remarkably similar to $Pt_3Sn$, including the very weak ordering peaks, with the caveat that this sample needed to be annealed to 600 $^oC$ in order to see this degree of ordering.

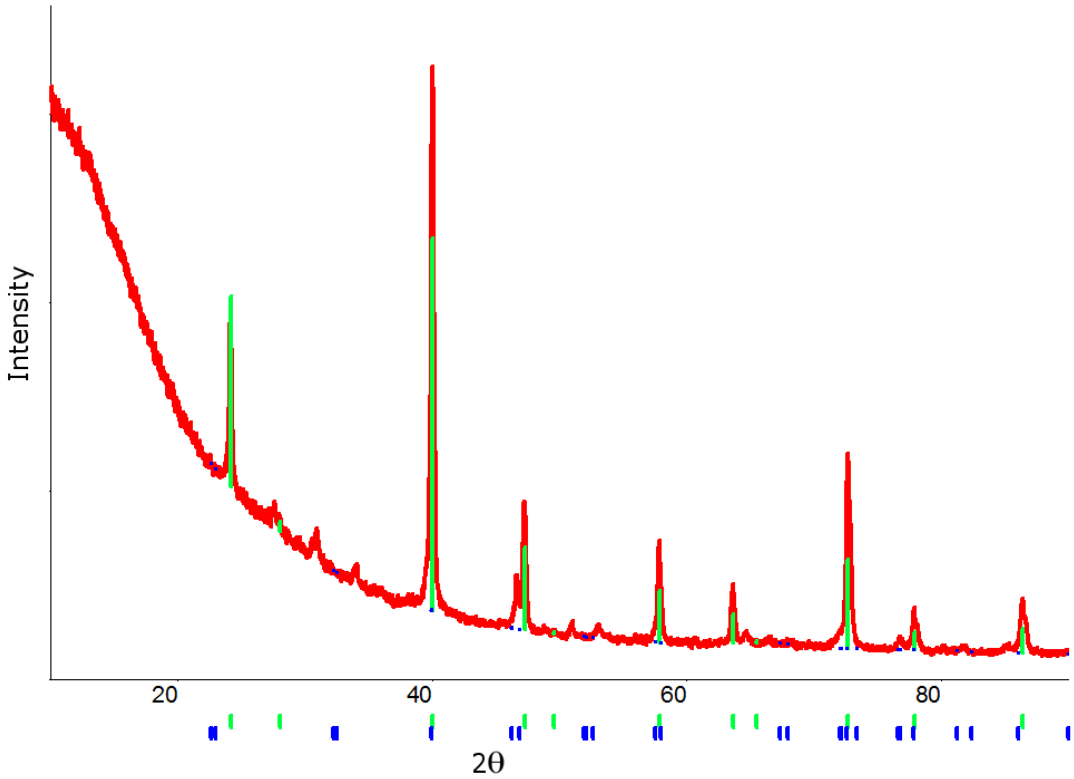


**Figure 4.10** pXRD pattern of $PtIn_2$ annealed at 500 $^oC$. Green drop lines correspond to $PtIn_2$ (PDF card #04-004-8870), blue drop lines correspond to $Pt_3In$ (card #04-001-2903).

$PtIn_2$ is not quite congruently melting; its peritectic melting point lies about 10 $^oC$ below the congruent melting point of its neighbor $Pt_2In_3$ . It is interesting to see from Figure 4.10 that this impacts the synthesis, but only slightly. The majority (73 % by pXRD) of the sample is $PtIn_2$ with a domain size of 31 ± 1 nm after annealing at 500 $^oC$; the remainder is some combination of

$Pt_3In$ and some other phase that could not be identified.

The synthesis of $Pt_2In_3$ resulted in the interesting sequence of pXRD patterns shown in Figure 4.11. Poorly ordered $PtIn_2$ is the first phase to nucleate, as the as-made nanoparticles match very closely to the pattern for $PtIn_2$ with a domain size of 6.6 ± 0.2 nm (though note how weak the ordering peaks are compared to Figure 4.10, and the large domain size distribution evidenced by the broad bases of the main peaks). The two phases are so close in terms of Pt:In ratio that it is entirely probable that this is another effect of the local concentration distribution being broad enough that a non-stoichiometric phase is allowed to seed before the stoichiometric phase; the fact that $PtIn_2$ decomposes at its peritectic melting point to $Pt_2In_3$ (see Figure 4.8) at a temperature only 25 $^oC$ lower than the congruent melting point of $Pt_2In_3$ only serves to help blur the synthetic boundary between these phases, particularly when relying as heavily on the statistical incorporation of reduced metal atoms that produce particle growth as we are in this procedure. However, $Pt_2In_3$ is still the thermodynamically favorable phase at this composition; when the same sample is annealed to 400 $^oC$, the $PtIn_2$ disappears and the product is pure $Pt_2In_3$ with a domain size of 16.2 ± 3.0 nm.

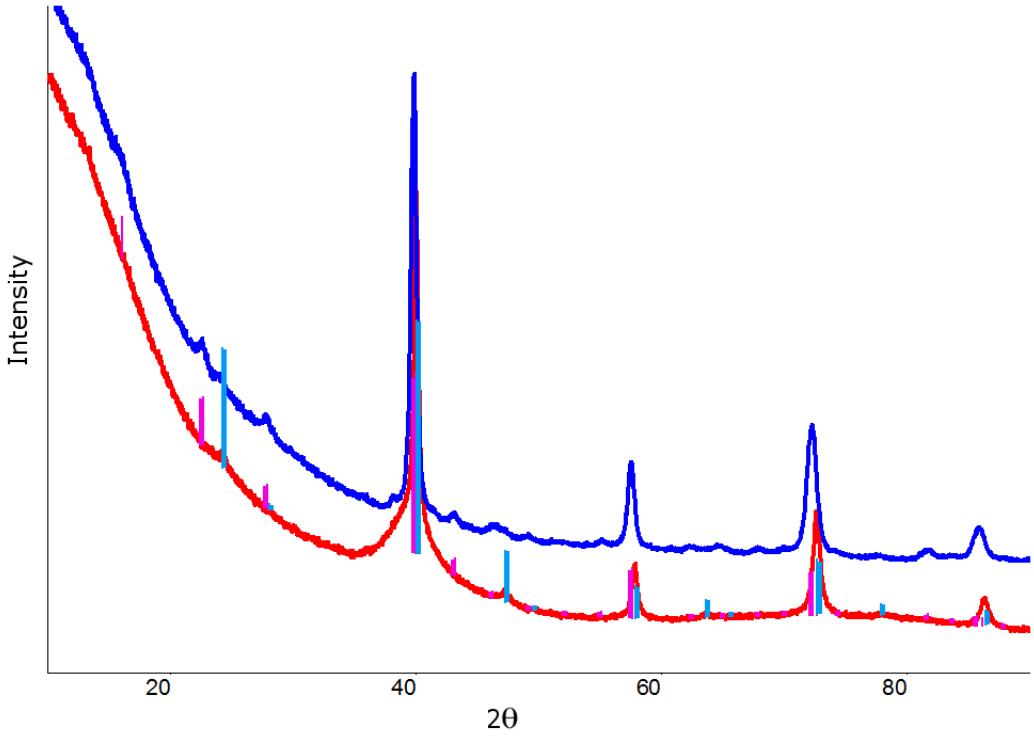


**Figure 4.11** pXRD pattern of $Pt_2In_3$ as-made nanoparticles (red) and annealed at 400 $^oC$ (blue). Teal drop lines correspond to $PtIn_2$ (PDF card#04-006-3482), pink drop lines correspond to $Pt_2In_3$ (card #04-006-3483).

Another example of co-reduction resulting in non-stoichiometric phases (particularly for the closely-spaced In-heavy Pt-In phases) is the next sample shown in Figure 4.12. The target phase here is $Pt_2In_3$, but upon annealing at 350 $^oC$, the phase that is visible by pXRD is $Pt_3In_7$ with a domain size of 24 ± 3 nm.

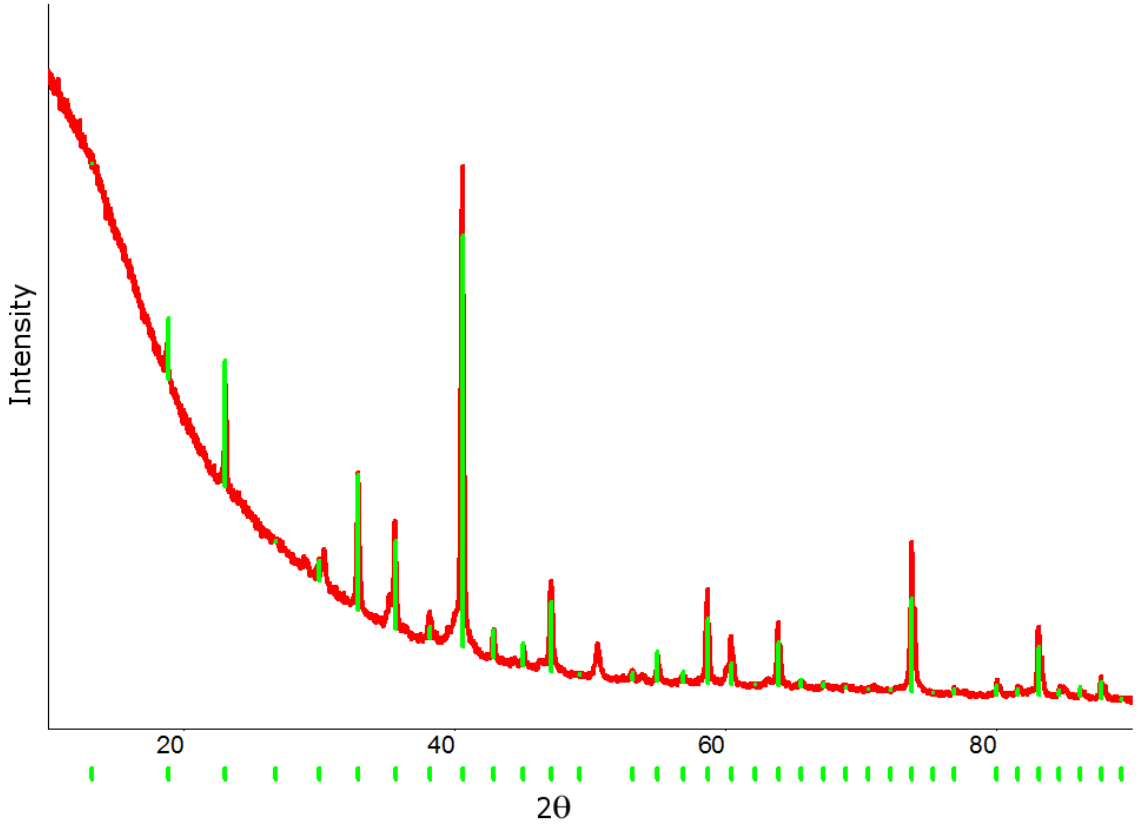


**Figure 4.12** pXRD pattern of $Pt_3In_7$ annealed at 350 $^oC$.

This is the first phase with both coefficients greater than 2 that has formed spontaneously (and it must form seeds easily if it dominates the crystallization as the non-stoichiometric phase in solution), so in that sense this is a deviation from previous trends. On the other hand it is a cubic phase, and Pt-In phases have shown a propensity to seed non-stoichiometric phases whenever another line phase is close enough in composition to overlap random distribution functions in the pre-reduction solution. The difference between $Pt_3In_7$ and $Pt_2In_3$ is a difference between 30 and 40 % Pt; by EDX, the phase below straddles the line between them at 38 ± 3 %. Figure 4.13 is an SEM image showing the relatively homogenous (for agglomerated particles synthesized with no capping agents) nanoparticles.

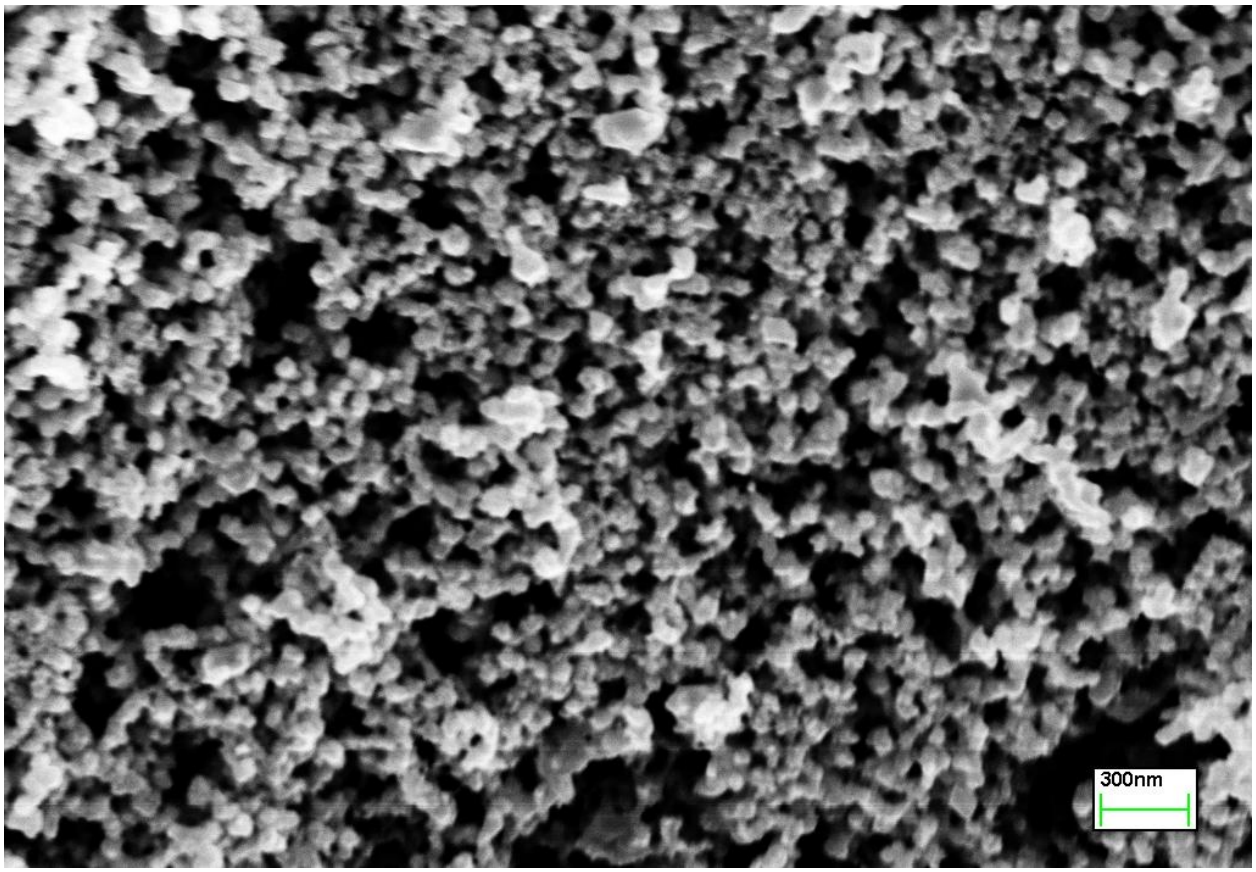


**Figure 4.13** SEM image of $Pt_3In_7$ annealed at 350 $^oC$.

The next phase to be synthesized was intended to be $Pt_3In_2$. However, upon annealing to 500 $^oC$, the phase that was synthesized was actually the high-temperature phase $Pt_{1.5}In$ (domain size 23 ± 2 nm, see Figure 4.13) which has the same stoichiometry, but (in the bulk, as far as we know) is only thermodynamically stable above 850 $^oC$. It is readily apparent that the stability of this phase and the low temperature phase are affected by moving to the nanoparticle regime. Both $Pt_3In_2$ and $Pt_{1.5}In$ are hexagonal phases; there is no readily apparent reason why this synthesis would favor one phase over the other. The small impurity peaks are difficult to identify (interestingly, the one phase they definitely do not match is $Pt_3In_2$); the best fit appears to be $Pt_{13}In_9$, which is

compositionally very close to $Pt_{1.5}In$. Given this, the product is about 80 % $Pt_{1.5}In$ by Rietveld analysis.

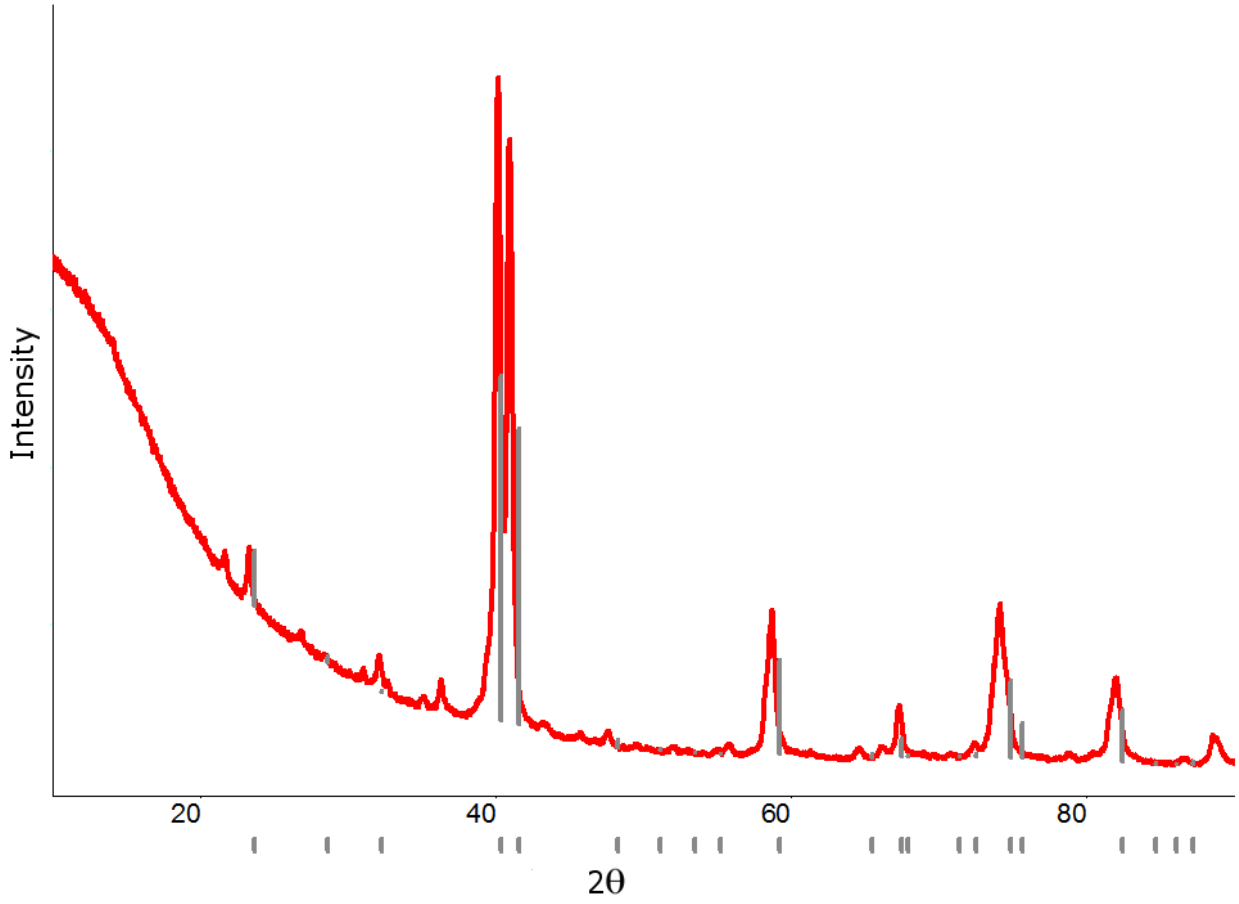


**Figure 4.13** pXRD pattern of Pt:In::3:2. Grey drop lines correspond to $Pt_{1.5}In$ ht (PDF card #04-004-8871). Drop lines are shifted slightly from the experimental peaks perhaps due to the phase width of the compound (about 3 % Pt).

Table 4.2 is a summary of the Pt-In system. This binary system has produced many strange reaction sequences - such as multiple instances of getting a pure phase at a composition different from that suggested by the molar ratio of metal precursors in the reduction step and forming high-temperature phases preferentially over low-temperature phases - but nonetheless appears to follow certain patterns that are, at this point, familiar.

| Phase | Crystal Structure | Melting Point ($^{o}$C) | % Target Phase |
|---|---|---|---|
| **$Pt_3In$** | Cubic | 1458 NCMP[a] | 100 % |
| **$Pt_{1.5}In$ (ht)[b]** | Hexagonal | 1160 IMP | 80 % |
| **PtIn (ht)[c]** | Cubic | 1030 IMP | 0 % |
| **$Pt_2In_3$** | Hexagonal | 1064 CMP | 100 % |
| **$PtIn_2$** | Cubic | 1039 NCMP | 73 % |
| **$Pt_3In_7$** | Cubic | 894 IMP | > 95 % |

**Table 4.2** Summary of Pt-In phase synthesis. [a]IMP = incongruent melting point, CMP = congruent melting point, NCMP = nearly congruent melting point [b]This high-temperature phase was synthesized preferentially over the low-temperature $Pt_3In_2$ phase. [c]Not a line phase, unstable at room temperature.

### 4.1.3 Pt-Bi

The Pt-Bi system contains the fewest number of line phases seen so far. The only phases that exist below 570 $^{o}$C are PtBi and $PtBi_2$ (Figure 4.14), though it should be noted that $PtBi_2$ actually exists as four distinct phases in different temperature regions. PtBi is a congruently melting phase that has previously been synthesized by our group as an ordered intermetallic, at room temperature, using a slightly different co-reduction method[4].

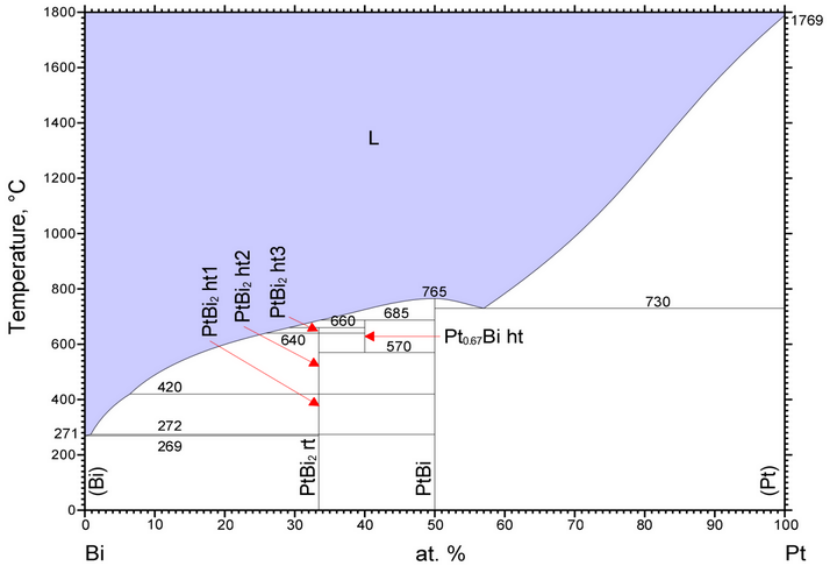


**Figure 4.14** The bulk phase diagram of Pt-Bi. Taken with permission from ASM Alloy Phase Diagram International[3].

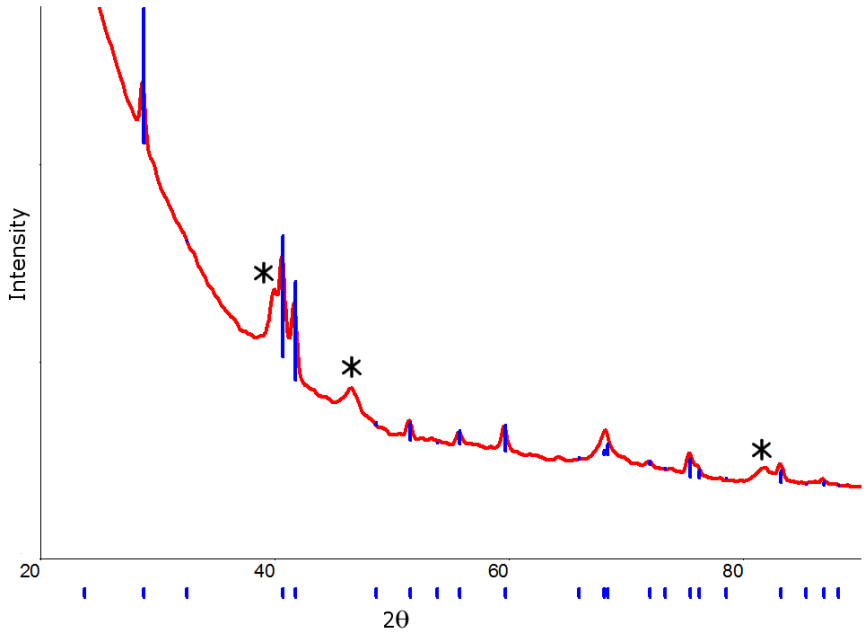


**Figure 4.15** pXRD pattern of PtBi annealed at 400 °C. Blue drop lines correspond to PtBi (PDF card #04-007-4117). Peaks marked with asterisks are known to be the result of a contaminated sample holder, and are not part of the sample.

As seen in Figure 4.15, PtBi is readily synthesized as a pure ordered phase via LBH co-reduction of $PtCl_4$ and $BiCl_3$ upon annealing to 400 $^oC$. Unannealed particles, in contrast, have the familiar Pt-alloy pXRD pattern (not shown). The non-indexed peaks were confirmed to be background contamination from the sample holder; the product is 100 % PtBi. The domain size by Williamson-Hall analysis is 13.3 ± 1.1 nm. Again, a congruently melting Pt-M binary phase is demonstrated to be easily synthesized by co-reduction.

### *4.2 Pd-Sn*

The next step towards generalizing the observed trends of nanoparticle reduction was to expand beyond platinum-containing binaries. The logical extension was to look at one of the near neighbors of Pt-Sn: Pd-Sn. Palladium dichloride is much less soluble than platinum chloride in THF (forming a cloudy suspension of particles that does not fully dissolve after an hour of stirring). The lithiated palladium-chloride complexes that are required to get Pd cations into solution at all do not react or form complexes with $SnCl_2$, so this system is another good test of the effect of the pre-reduction complexes on the reduction and ordering behavior of the as-made nanaoparticles. The phase diagram of Pd-Sn is shown in Figure 4.15.

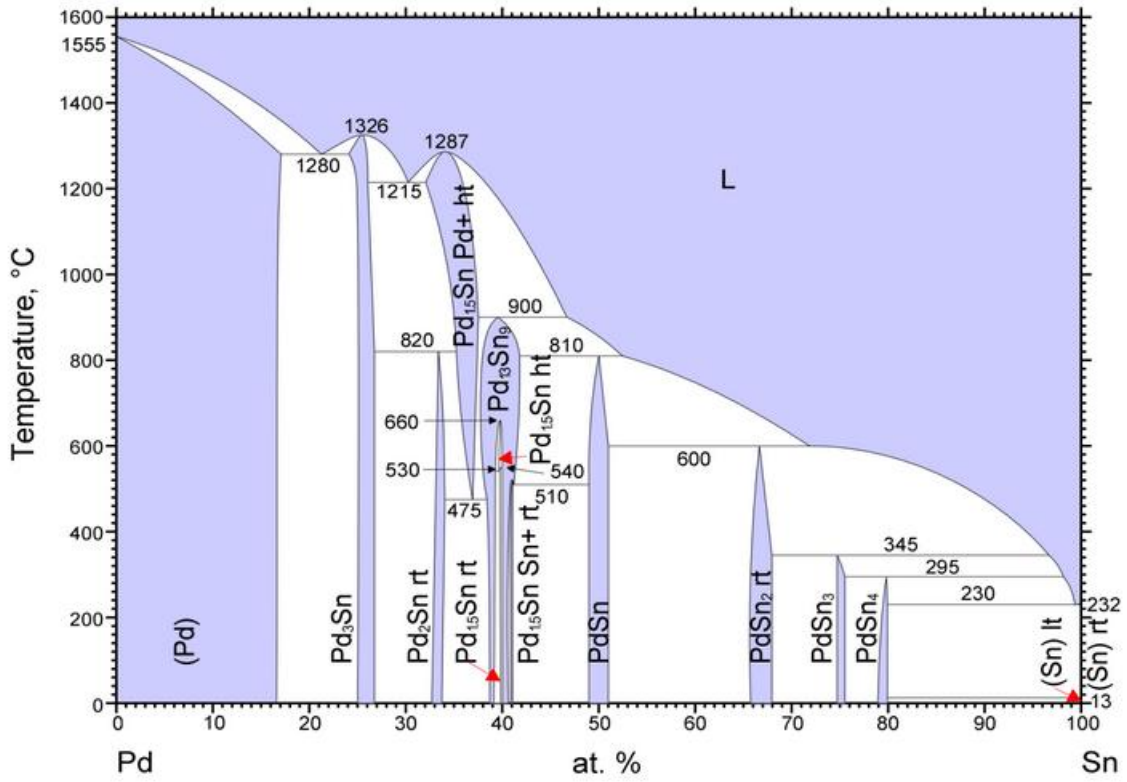


**Figure 4.15** The bulk phase diagram of Pd-Sn. Taken with permission from ASM Alloy Phase Diagram International[5].

The target phases for this system were the palladium-rich phases stable at room temperature ($Pd_3Sn$, $Pd_2Sn$, and PdSn). $Pd_3Sn$ is a congruently melting cubic structure, while $Pd_2Sn$ and PdSn are both incongruently melting (peritectoid and peritectic, respectively) orthorhombic phases. $Pd_2Sn$ is also closely neighbored on both sides of the phase diagram by other, stable phases. From previous observations of other phases, one would predict Pd3Sn to easily order as a pure compound, PdSn to have some trouble ordering but possibly being successful at higher temperatures, and $Pd_2Sn$ to form a mixture of phases at any annealing temperature. This is, on the whole, what is observed. The pXRD of $Pd_3Sn$ (Figure 4.16) shows that the as-made

nanoparticles are an amorphous indeterminate Pd alloy, and upon annealing to 600 °C both $Pd_3Sn$ and $Pd_2Sn$ nucleate (75 % $Pd_3Sn$ by pXRD refinement). This discrepancy could be caused by the substantial phase width of $Pd_3Sn$ and the proximity to $Pd_2Sn$, but it's also possible that it is simply the result of the low solubility of Pd resulting in nanoparticles with insufficient Pd to completely form the $Pd_3Sn$ phase. The domain size of $Pd_3Sn$ was quite large at 45 ± 3 nm.

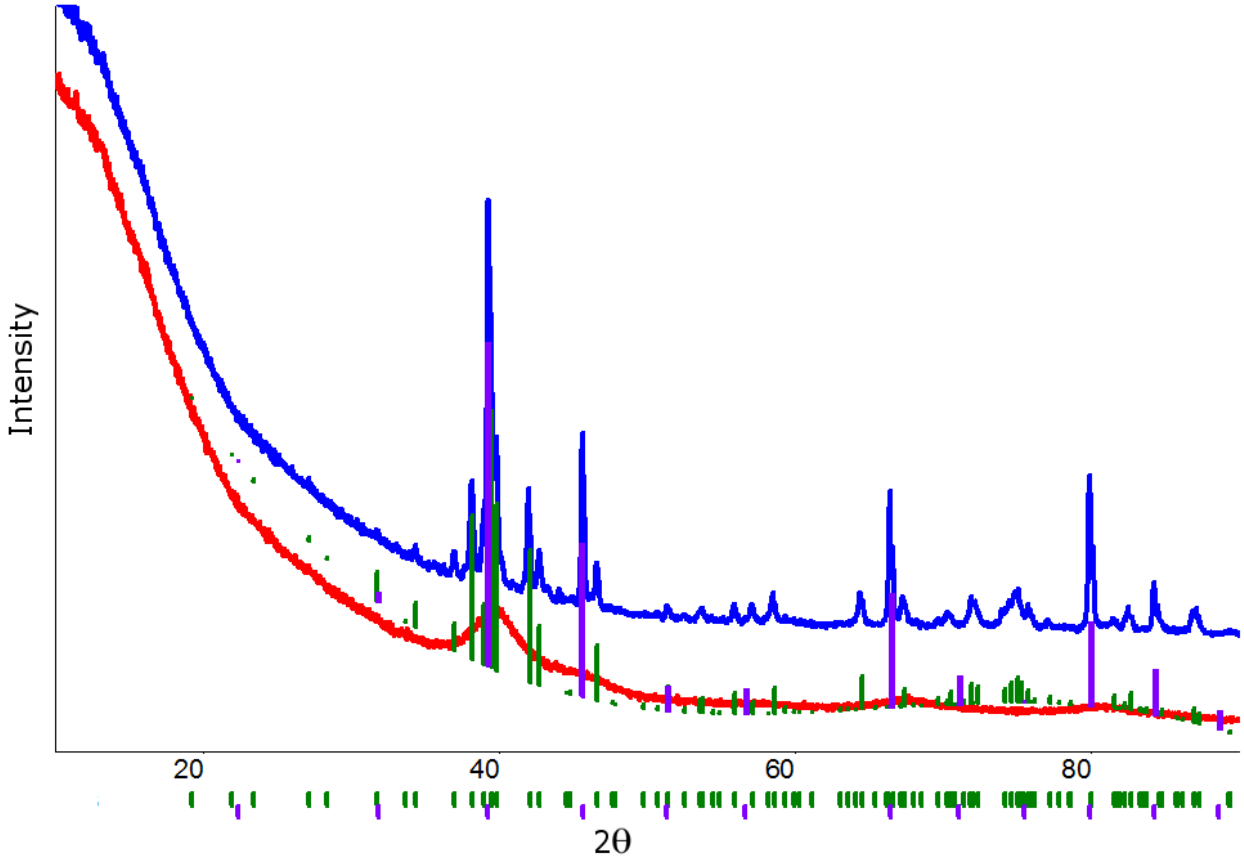


**Figure 4.16** pXRD pattern of $Pd_3Sn$ at room temperature (red) and annealed at 600 °C. Purple drop lines correspond to $Pd_3Sn$ (PDF card # 04-001-0514), green lines correspond to $Pd_2Sn$ (card# 00-052-1515).

The other two phases of interest ordered as we expected them to. $Pd_2Sn$ forms amorphous

nanoparticles at room temperature, and a mixture of $Pd_2Sn$ and other unidentified phases when annealed to 600 $^{o}$C, while PdSn (Figure 4.17) forms an unidentifiable mixture of as-made nanoparticles that anneal into a mostly pure well-defined product at 600 $^{o}$C with a domain size of 41 ± 5 nm.

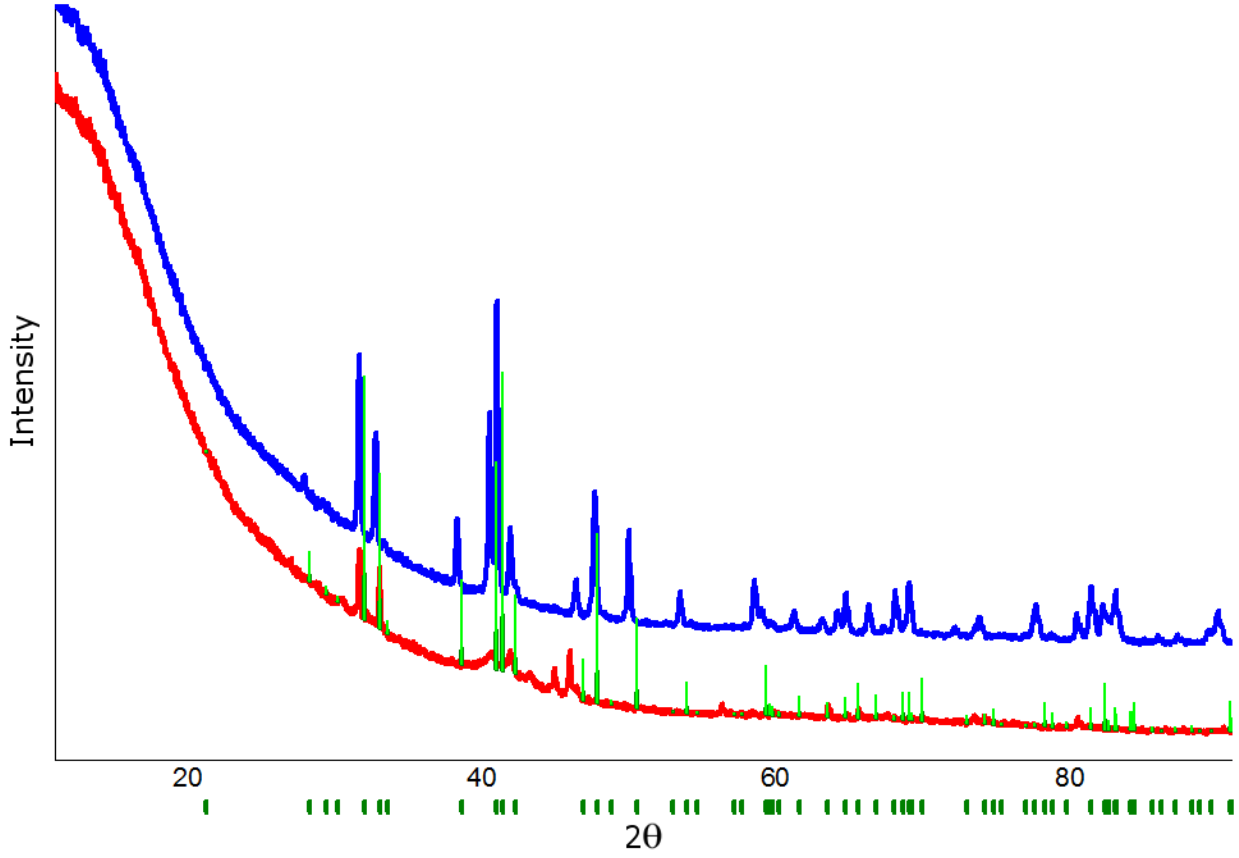


**Figure 4.17** pXRD pattern of PdSn as-made nanoparticles (red) and annealed at 600 $^{o}$C (blue). Green drop lines correspond to PdSn (PDF card # 04-013-6682).

These results were also reproducible when Pd-Sn phases were annealed onto carbon black supports. In summary, while not explored in great detail, Pd-Sn was the first example of how the predictions of co-reduction could be applied beyond Pt-M binary materials. Co-reduction with

LBH was also shown to have a wider field of applications than the fairly narrow range of materials previously discussed. The next section discusses some examples of how we further pushed LBH co-reduction synthesis, this time to ternary metal nanoparticles.

## *4.3 Ternaries and Pseudoternaries*

### *4.3.1 Pt-Sn-Sb*

The first ternary compound under investigation is actually a pseudoternary, which can be called either $PtSn_{0.5}Sb_{0.5}$ or - perhaps more accurately - Pt(Sn,Sb). The ternary phase diagram, seen in Figure 4.18, will clarify this nomenclature. Starting from PtSn on the base of the triangle, a blue region runs in a straight line through the phase diagram and intersects the left side at PtSb. This means that Sn and Sb are completely interchangeable in the hexagonal NiAs structure that has a metal ratio Pt:M::1:1. So, while there is long-range order in the structure, on an atomic level there are inhomogeneities due to local variations in the placement of Sb and/or Sn on the As site in the structure. There is a similar region - with a smaller phase width and some gaps in the single-phase region - between $PtSn_2$ and $PtSb_2$. The gaps are expected, since the end members do not have the crystal structure, as mentioned previously.

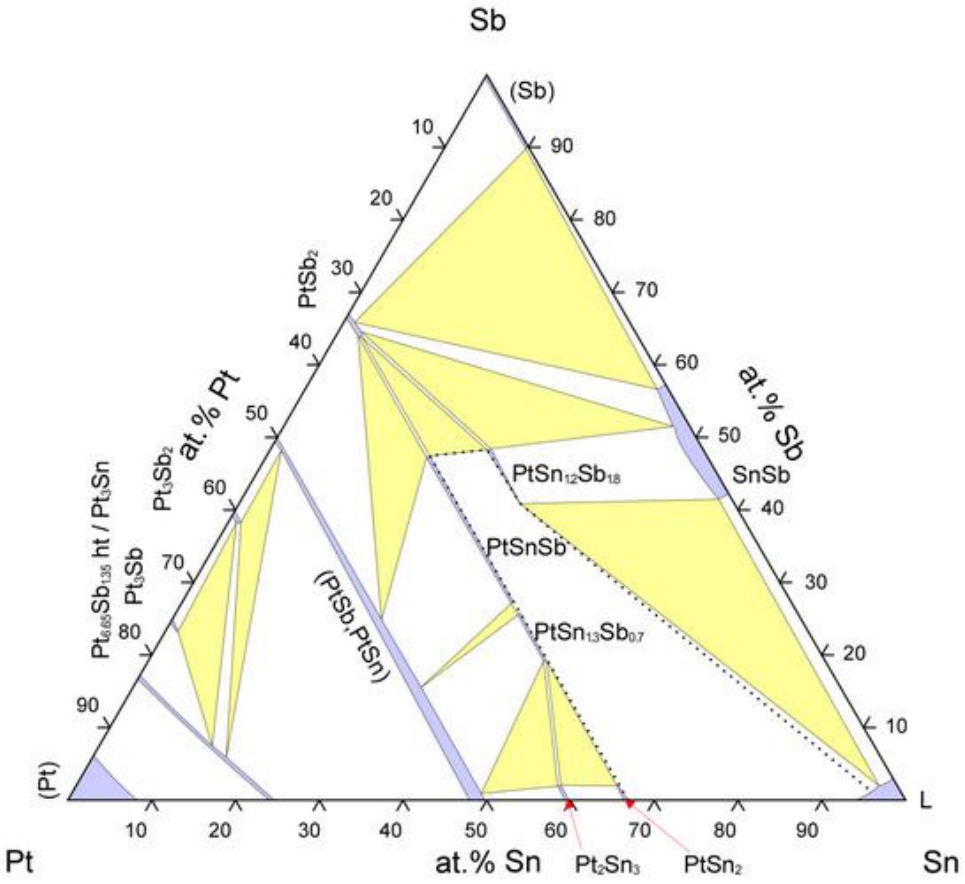


**Figure 4.18** Ternary phase diagram of the Pt-Sn-Sb system. The blue areas represent single-phase regions, white represents a two-phase region, and yellow represents a three-phase region. This phase diagram is representative of the temperature range 500 to 830 $^{o}$C. Taken with permission from ASM Phase Diagram International[6].

Additionally, it is not necessarily true that the resulting nanoparticles have a perfect ratio of 1:1 Sn:Sb; it is entirely possible that the reduction or incorporation rates of the two elements differ enough that the resulting nanoparticles will end up being enriched in one element while maintaining the same structure. The usual statistical uncertainty is likely in any case. An analysis of the lattice parameters (via pXRD) and the atomic ratios (via EDX) will help determine if this

is the case, though they are ensemble analytical methods, so variations from one particle to another may be lost in the average.

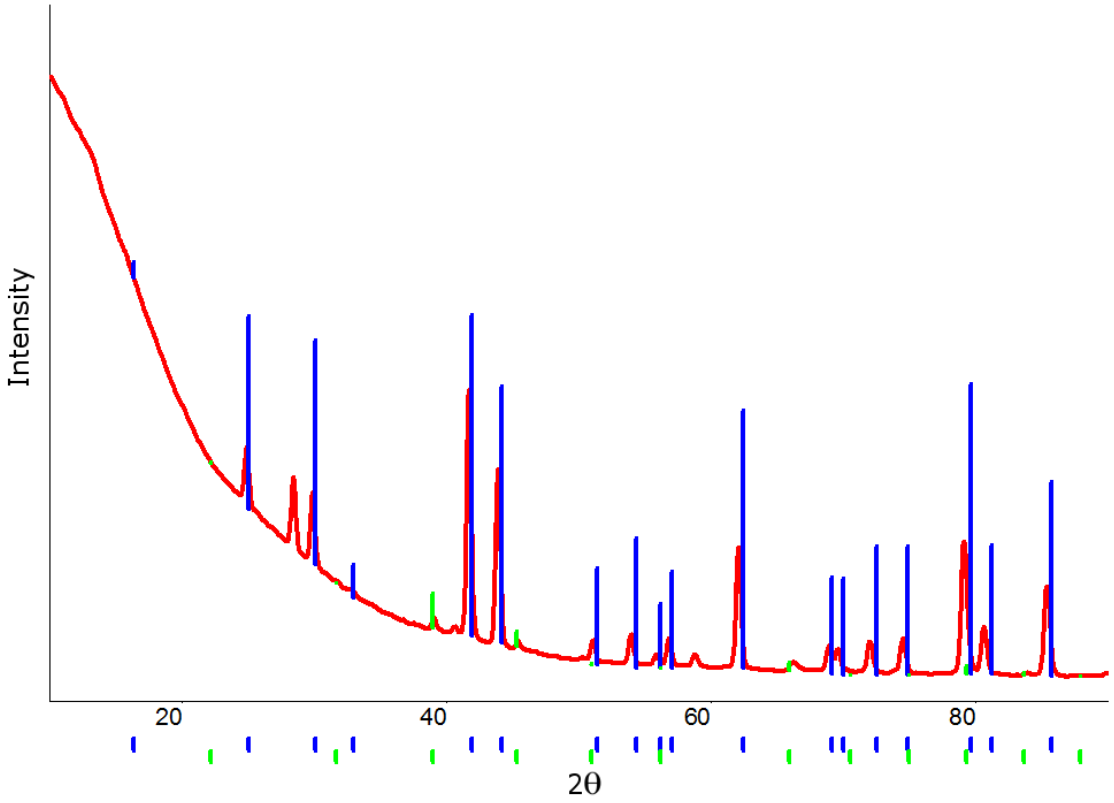


**Figure 4.19** pXRD pattern of $PtSn_{0.5}Sb_{0.5}$ annealed at 600 $^{o}$C. Blue drop lines correspond to PtSn (note that the main peaks are all shifted off of the pattern for PtSn), green drop lines correspond to $Pt_3Sn$.

When $PtCl_4$, $SbCl_3$, and $SnCl_2$ are reduced in a 2:1:1 molar ratio and annealed at 600 $^{o}$C, the resulting powder pattern (Figure 4.19) consists of 88 % PtSn or PtSb. The peaks lie between those expected for the two PtM 1:1 phases; however, they are not halfway between them, indicating that the phase may not have precisely the 2:1:1 Pt:Sn:Sb ratio. The lattice parameter calculated by Rietveld analysis that best fits the peaks is 4.126 Å, which is closer to PtSb (4.130

Å) than PtSn (4.101 Å). This can be partially explained by the presence of some impurity $Pt_3Sn$ (about 12 % by Rietveld).

Figure 4.20 is a compilation of SEM images of the $PtSn_{0.5}Sb_{0.5}$ phase above. EDX data of the elemental composition of this phase is summarized in Table 4.3.

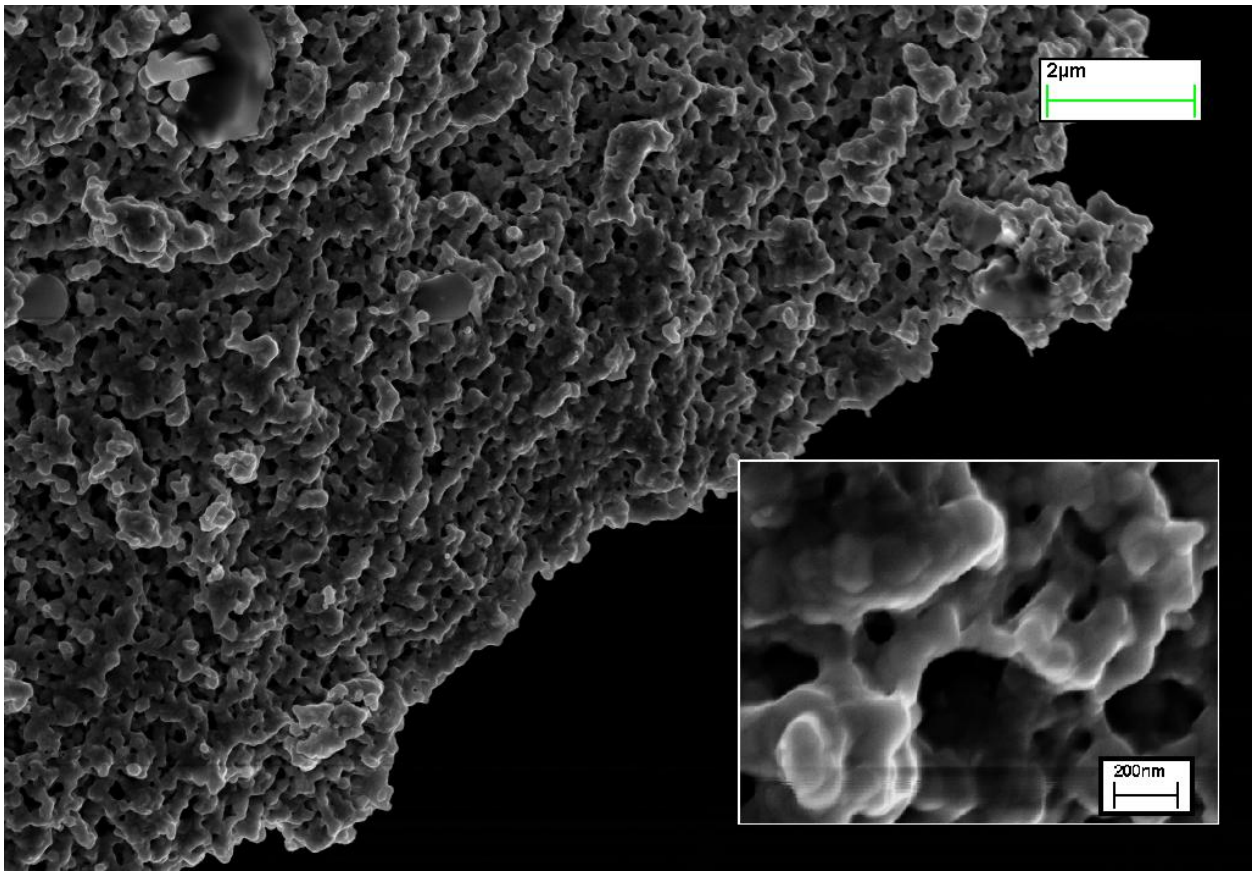


**Figure 4.20** SEM image of Pt(Sn,Sb) annealed to 600 $^{o}$C. Inset shows a magnified view of the agglomerated nanoparticles.

| Element | Percentage Composition (%) | Standard Deviation (%) |
|---|---|---|
| **Pt** | 66 | 8 |
| **Sn** | 18 | 5 |
| **Sb** | 16 | 3 |

**Table 4.3** Atomic percentages of the three elements in $PtSn_{0.5}Sb_{0.5}$ annealed at 600 $^{o}$C.

*4.3.2 Pt-Ni-Sn*

To create a stable Pt-Sn-M true ternary phase, the third metal M must be sufficiently different from both Pt and Sn that it cannot freely exchange lattice sites with one element or the other. Antimony obviously does not fit this description, based on the previous section. There are remarkably few published ternary phase diagrams. The phase space in which ternaries exist is huge, and few researchers are currently working on the problem of creating a library of bulk phase diagrams (but not diagrams that relate to the nanoparticle regime), so the choice of metals at this point is based on very little solid evidence that an ordered ternary nanoparticle compound is favorable, or even exists.

Therefore, the next metal to be examined was nickel, based on a promising paper by Correa et al.[7] describing two Pt-Sn-Ni alloys for use as a catalyst for ethanol oxidation. If a phase cannot be chosen that is known to be stable in the bulk, the next best option is to pursue phases that are more likely to have good catalytic properties. The alloys that Correa investigated had nominal elemental ratios of 75:15:10 (denoted alloy A) and 55:17:28 (alloy B). The powder patterns of the phases synthesized by Correa (see Figure 4.21) all appear to be cubic, nearly identical to Pt/C

with slightly shifted lattice parameters. There is no evidence of ordering.

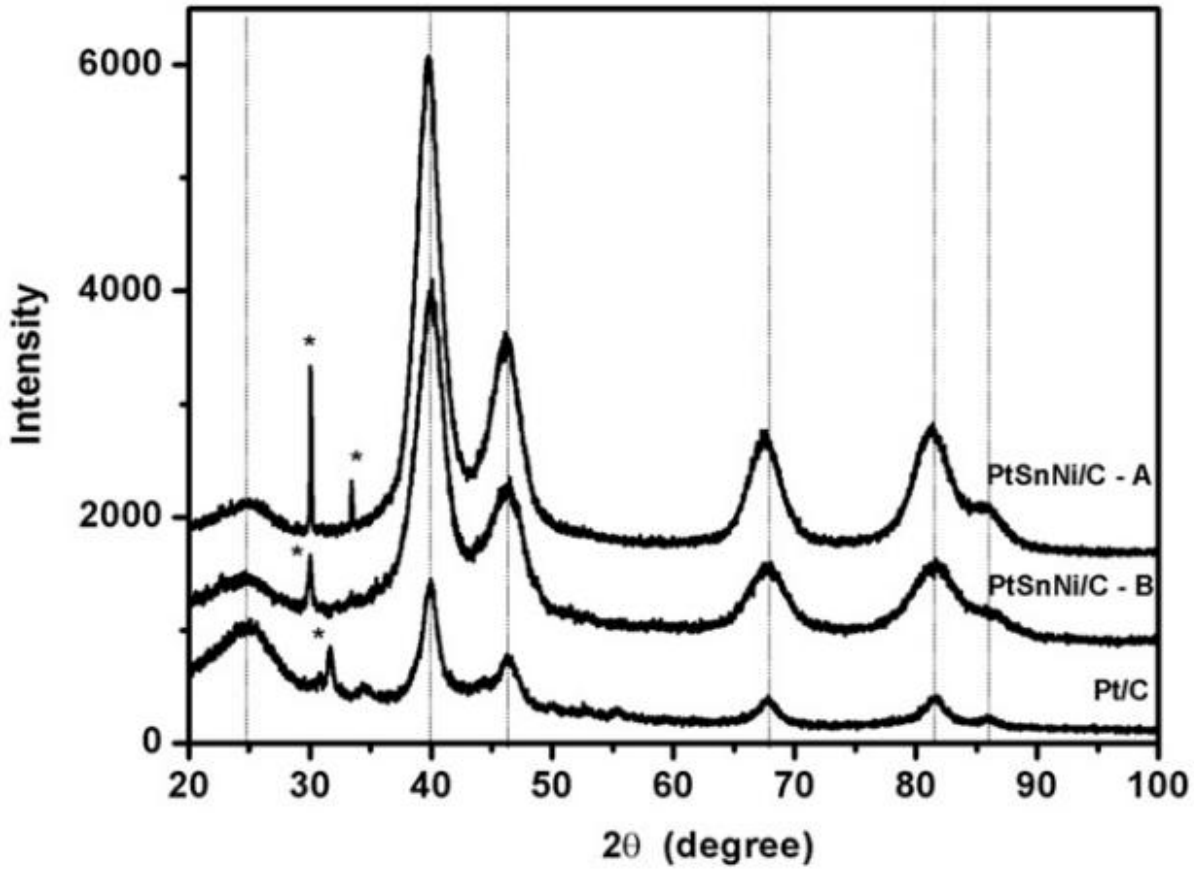


**Figure 4.21** pXRD patterns of $Pt_{75}Sn_{15}Ni_{10}$/C (top), $Pt_{55}Sn_{17}Ni_{28}$/C (middle), and Pt/C (bottom). Asterisks mark unknown peaks. Taken from Correa et al[7].

Both composition A and B looked similar to the powder patterns in Figure 4.21 before annealing - i.e., like Pt/C - but after annealing at 600 $^{o}$C, the broad platinum peaks split into multiple phases. Composition A is shown first in Figure 4.22. As you can see, the main phase is structurally similar to $Pt_3Sn$ (the green drop lines), but shifted towards Pt (black drop lines). This suggests that the intended product (which looks to be a variant of $Pt_3M$, where M is a

combination of Sn and Ni) was synthesized. The calculated lattice parameters fit this hypothesis. $Pt_3Sn$ has a lattice constant of 4.002 Å, the theoretical lattice constant of $Pt_{75}Sn_{15}Ni_{10}$ is 3.923 Å based on calculations using the program Mercury, and the experimental lattice constant from the pattern below was calculated to be 3.983 Å. Some impurity phase PtNi was also detected. This implies that the main phase is deficient in Ni, which would explain why the experimental lattice constant is shifted closer to $Pt_3Sn$ than expected.

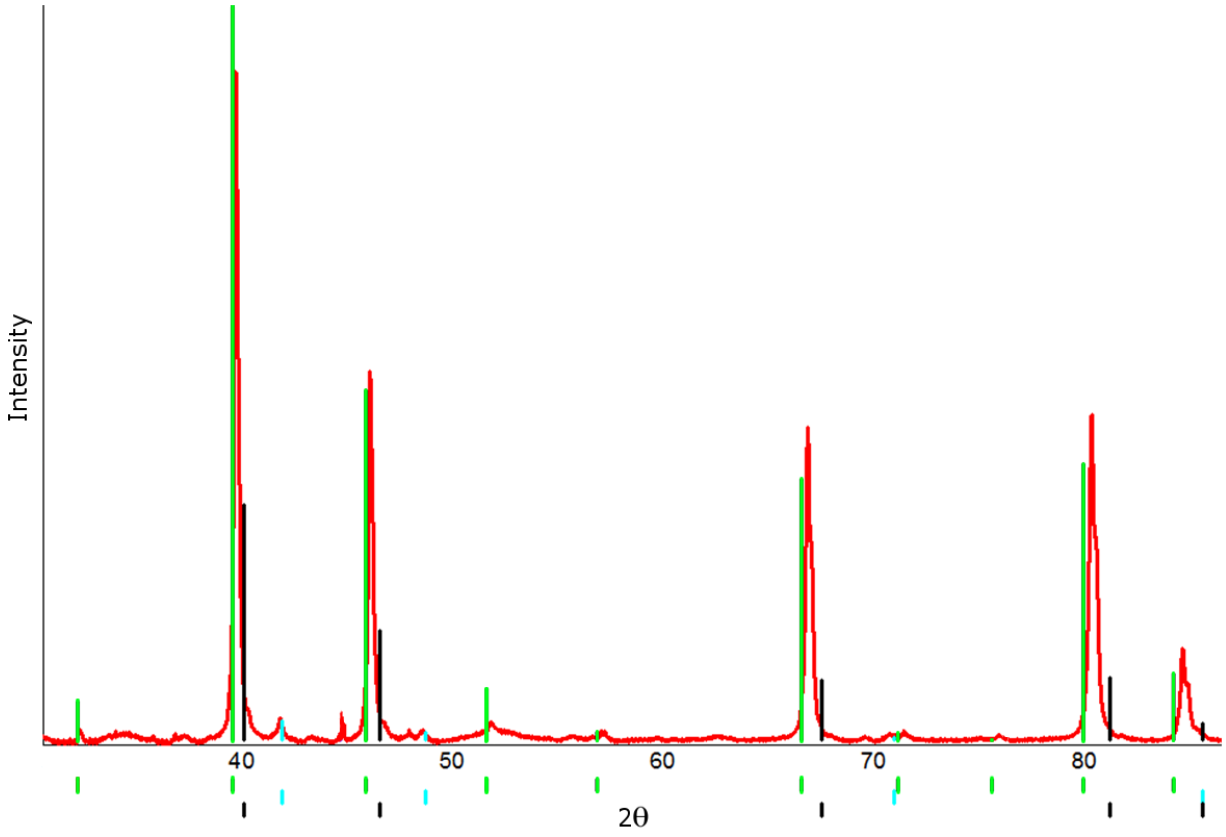


**Figure 4.22** pXRD pattern of $Pt_{75}Sn_{15}Ni_{10}$, known as composition A, annealed at 600 $^{o}$C. Green drop lines correspond to $Pt_3Sn$, black lines to Pt, and blue lies to PtNi.

When observed under a microscope (see Figure 4.23), the surface of composition A appeared to

mostly consist of homogenous agglomerated nanoparticles interspersed with larger pieces of a material that looks smooth under these conditions, a trait often characteristic of metal oxide impurities. EDX data confirmed that all three elements were present in the sample in approximately the correct ratios (see Table 4.4)

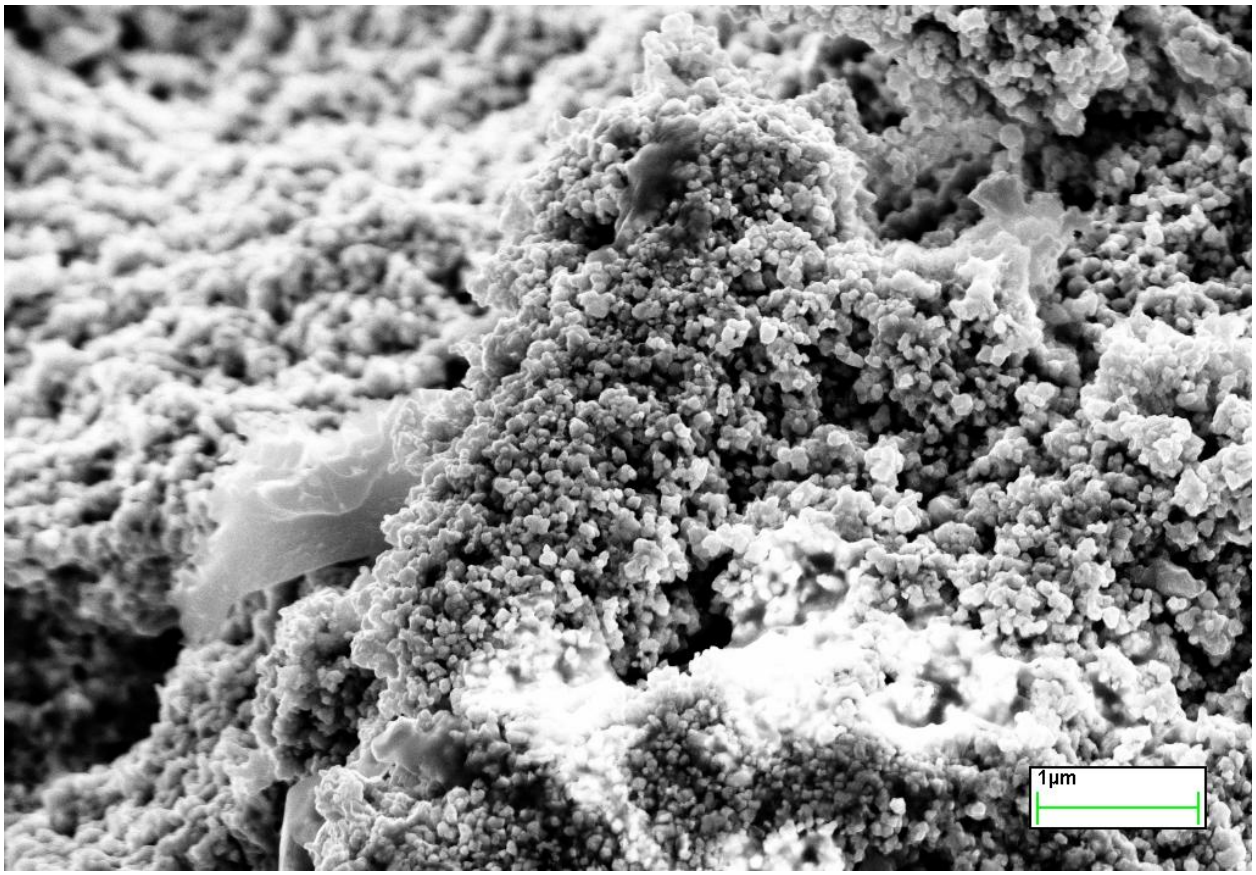


**Figure 4.23** SEM image of Pt-Sn-Ni composition A (75:15:10) annealed at 600 $^{o}$C.

Composition B ($Pt_{55}Sn_{17}Ni_{28}$) was synthesized under the same conditions, but the pXRD (Figure 4.24) belies a more complicated synthesis. There are at least four phases in this sample, none of which have a simple reference phase to which they can be compared as the previous composition was.

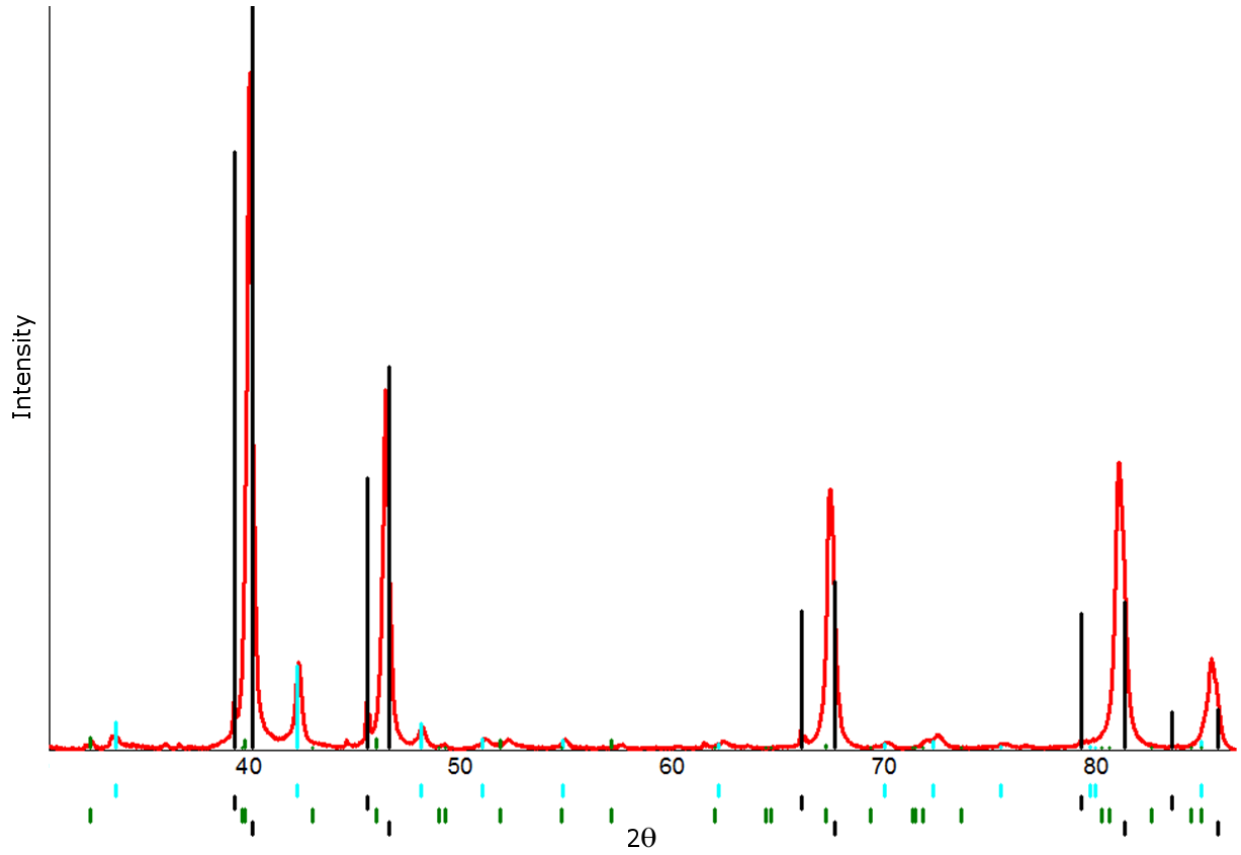


**Figure 4.24** pXRD pattern of $Pt_{55}Sn_{17}Ni_{28}$, known as composition B, annealed at 600 $^{o}$C. Black drop lines correspond to fcc Pt alloys (two different phases), blue drop lines correspond to PtNi, and green drop lines correspond to $Ni_2O_3$.

The SEM images of this sample are even more striking in their variety. Visible are globular structures layered over the more "popcorn-shaped" agglomerated nanoparticles familiar to most of the syntheses presented in this work, as well as angular crystallites and a smaller, less well-crystallized phase (see Figure 4.25a-c). This sample unequivocally did not form a single phase.

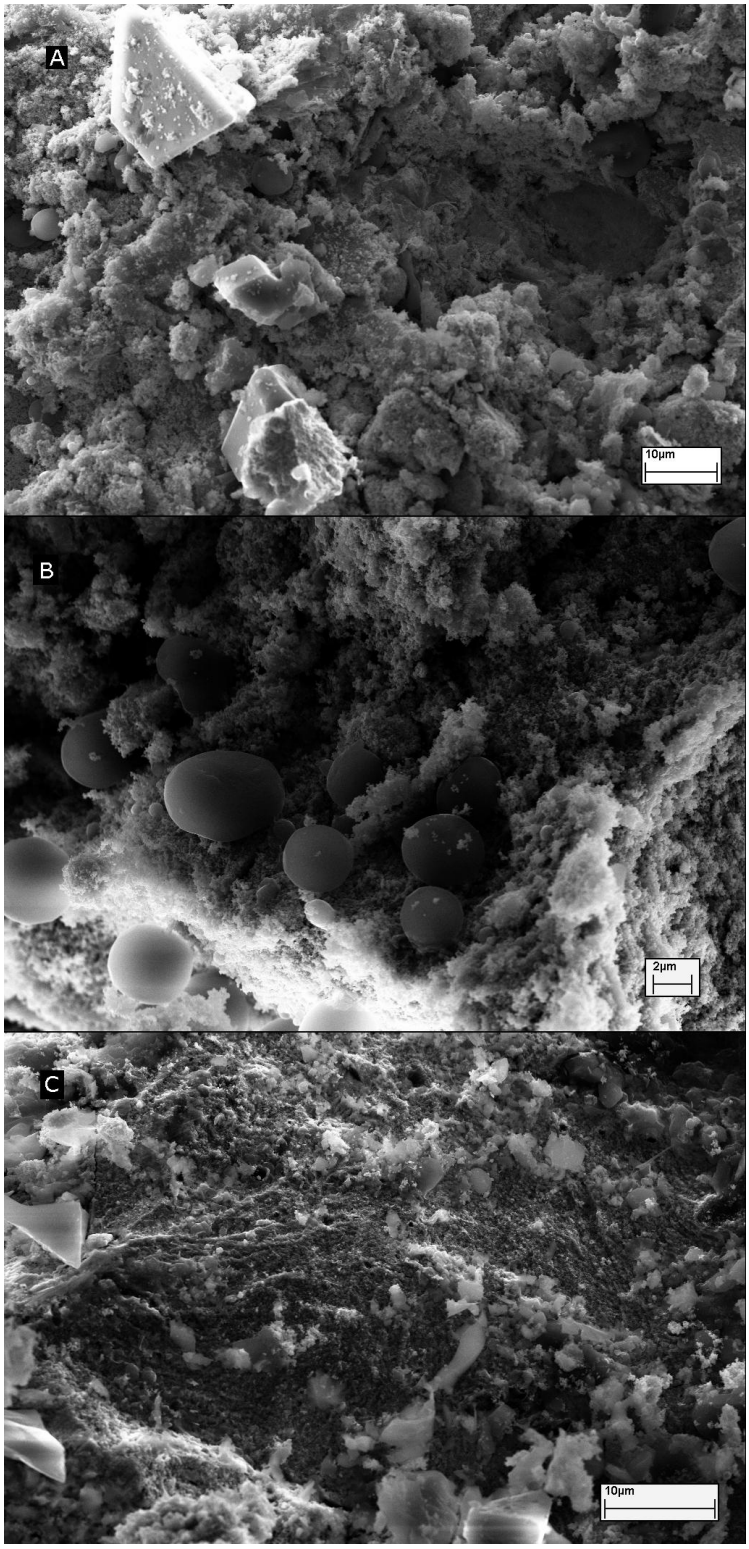


**Figure 4.25** SEM images of Pt-Sn-Ni composition B (55:17:28). Images are taken from different particles present in the same sample annealed at 600 $^{o}$C.

This is not surprising, considering the stoichiometric ratios of the metals; almost no phase that we have seen so far will readily order at such compositions. Even if a single-phase ternary alloy is favorable under these conditions and at this composition, it is far more favorable during the reduction and nucleation step for stable, consistent intermetallic phases like pure alloys of Pt or PtM binary materials to form. It is uncertain whether composition B in Correa's work is a stable alloy, or if it actually consists of multiple separate phases which cannot be distinguished because of the small domain sizes of the nanoparticles and are therefore hidden underneath the large Pt-like pXRD peak. What is certain is that fast co-reduction cannot produce such a material at this composition.

*4.3.3 Pt-Sn-Fe*

The Pt-Fe system has been under investigation in our group as a product of co-reduction for some time[8], so it is known to be possible to synthesize via co-reduction. For that reason, Pt-Sn-Fe was the next ternary system to be investigated. Two phases were targeted: the 1:1:1 phase PtSnFe, and the analog of Pt-Sn-Ni composition A, $Pt_{75}Sn_{15}Fe_{10}$.

The 1:1:1 phase PtSnFe is a pseudoternary phase, like Pt-Sn-Sb, but it is different from the previously explored pseudoternaries because iron substitutes onto both platinum and tin sites in the hexagonal PtSn crystal structure. The resulting material looks, by pXRD, like PtSn with a shifted lattice constant (with lattice parameters of 4.12 Å and 5.42 Å according to PDF card #00-038-0533). Figure 4.26 is the pXRD pattern of PtSnFe synthesized via co-reduction and annealed at 400 $^{o}$C; the resulting particles have domain sizes of 23.7 ± 0.6 nm. The small peaks in the region of 35 $^{o}$ 2θ match well to $FeSn_2$, but there are not enough visible peaks to get a positive

identification.

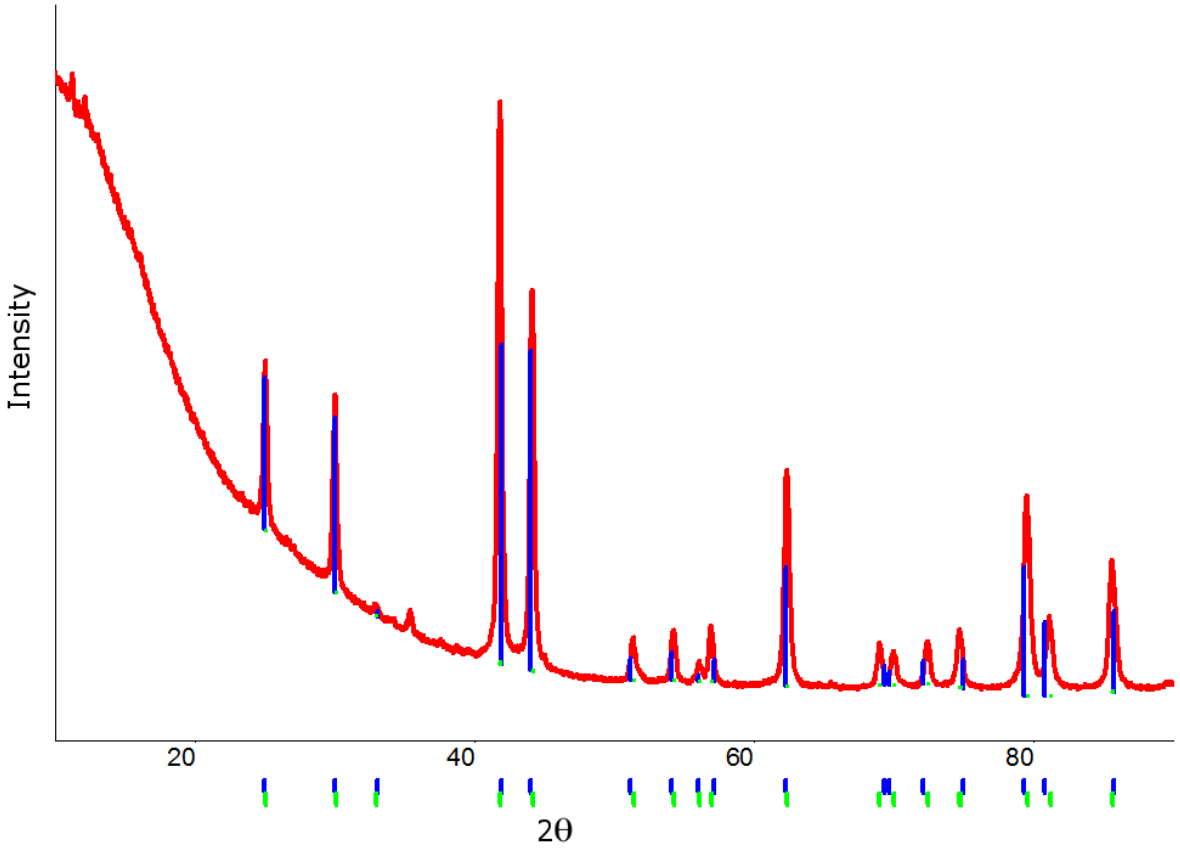


**Figure 4.26** pXRD pattern of PtSnFe 1:1:1. Blue drop lines correspond to PtSnFe (PDF card #00-038-0533), green drop lines correspond to PtSn.

SEM images of these nanoparticles showed homogenous agglomerated nanoparticles (Figure 4.27). EDX data supports the conclusion that the synthesized phase includes iron, though the iron content is slightly diminished from the theoretical value of 33 %. Experimental atomic percents were 39 ± 5 % Pt, 33 ± 3 % Sn, and 28 ± 3 % Fe. This is unsurprising; considering that PtSn forms at room temperature. When the pXRD pattern was checked via Rietveld refinement, it was found that the lattice parameters of the hexagonal phase (4.1044 Å and 5.4391 Å) were closer to

that of PtSn than that of PtSnFe. Nonetheless, the evidence shows that there was at least some successful incorporation of Fe into the PtSn structure to form the pseduoternary PtSnFe.

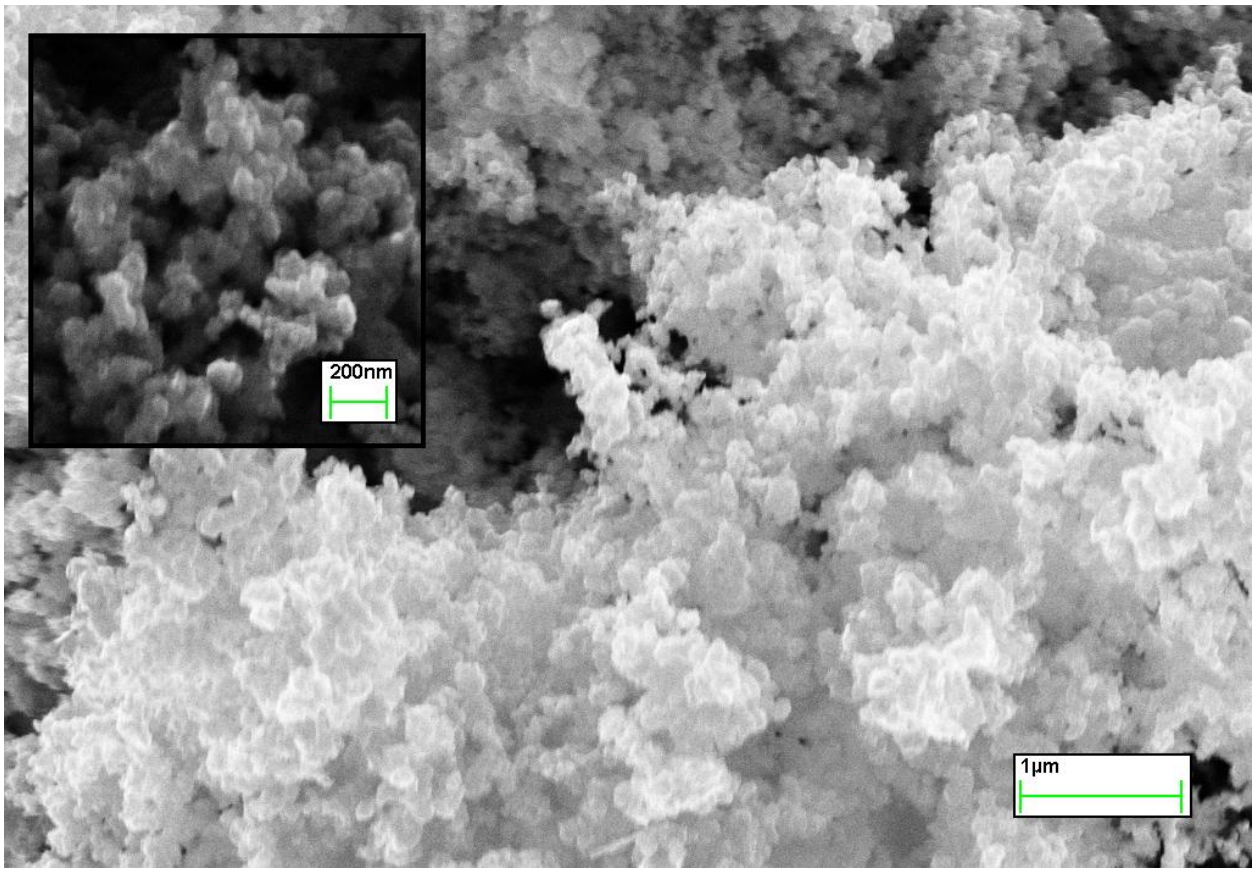


**Figure 4.27** SEM image of PtSnFe nanoparticles annealed at 400 $^{o}$C. Inset: higher magnification image of same phase.

The next phase, $Pt_{75}Sn_{15}Fe_{10}$, is very similar to the corresponding Pt-Sn-Ni alloy. The structure is simply $Pt_3Sn$ with iron substituted onto some of the tin sites (see Figure 4.28). As expected, the lattice constant found by Rietveld refinement (3.9898 Å) lies between that of $Pt_3Sn$ (4.004 Å) and $Pt_3Fe$ (3.892 Å). By EDX, this phase appears to actually be deficient in platinum; atomic percents were found to be 69 ± 1 % Pt, 20 ± 1 % Sn, and 12 ± 1 % Fe. As discussed in Chapter 2,

these experimental atomic percents have a much larger margin of error than the mathematical standard deviations given above; it is entirely possible that the apparent deficiency in platinum is non-physical.

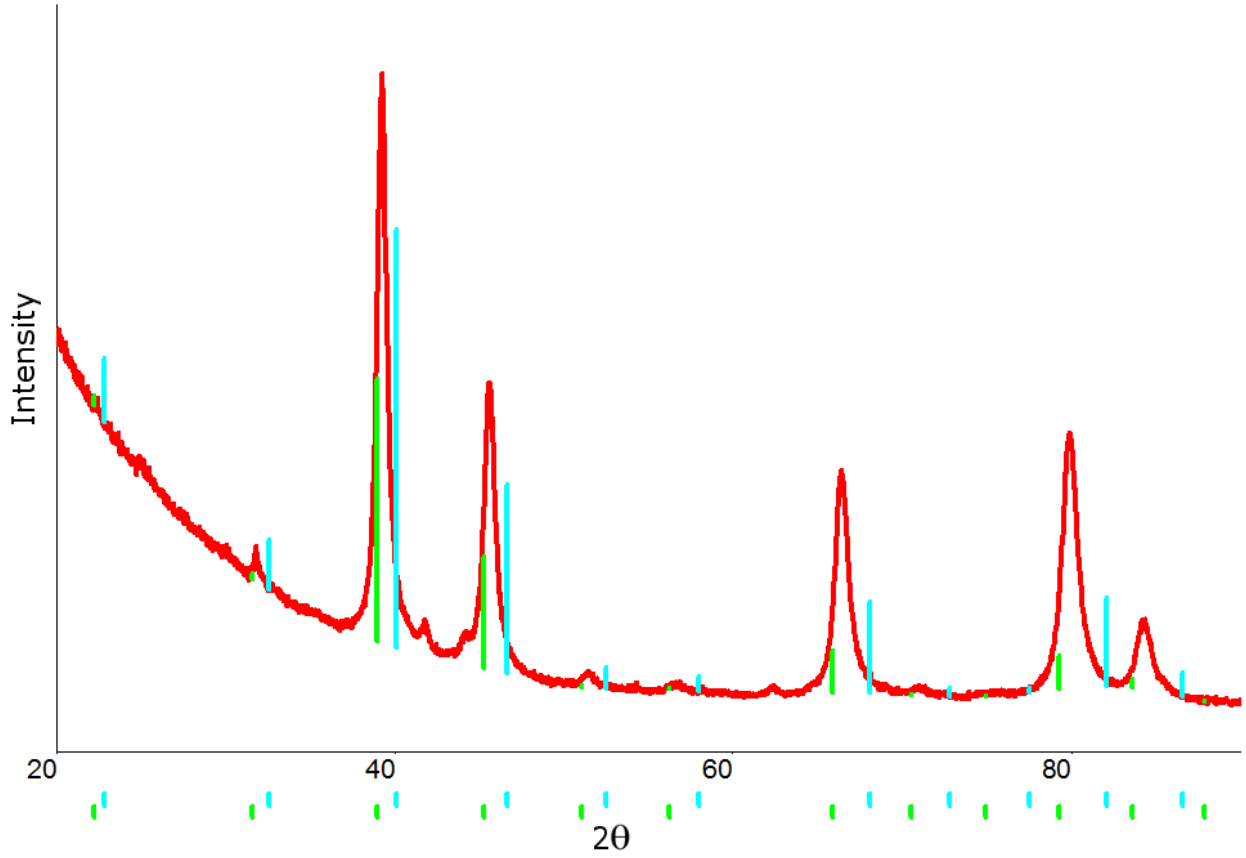


**Figure 4.28** pXRD pattern of Pt-Sn-Fe 75:15:10 annealed at 400 $^{o}$C. Green drop lines correspond to $Pt_3Sn$, blue drop lines correspond to $Pt_3Fe$ (PDF card #04-017-4976).

The same Pt-Sn-Fe alloy could be synthesized directly onto carbon black, as shown in Figure 4.29. Annealing the nanoparticles to 400 $^{o}$C, the same temperature as the sample Figure 4.28, results in nanoparticles with a decreased domain size, undoubtedly caused by the carbon support slowing the sintering of nanoparticles. However, this reduction in the diffusion of nanoparticles

seems to have also resulted in an increased composition spread, as evidenced by the asymmetry of the main peaks. That particular shape is most likely caused by a combination of peaks of slightly different lattice parameters. This spread of lattice parameters is expected in a sample that is, in essence, a mixture of $Pt_3Sn$ and $Pt_3Fe$; the fact that such peak splitting is not more common in the previous pseudoternaries is remarkable.

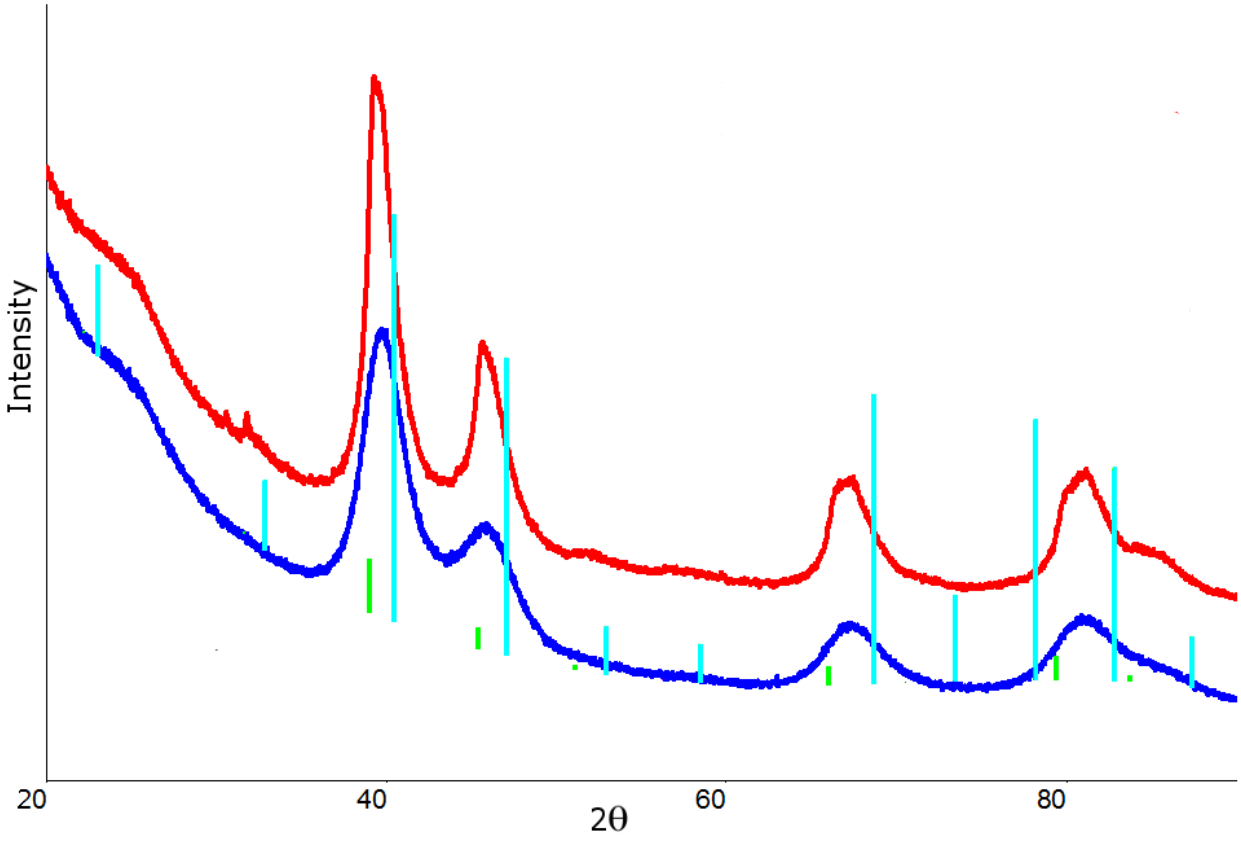


**Figure 4.29** pXRD pattern of Pt-Sn-Fe 75:15:10 annealed at 200 $^{o}$C (blue) and 400 $^{o}$C (red). Green drop lines correspond to $Pt_3Sn$, blue drop lines correspond to $Pt_3Fe$.

### *4.4 Conclusions*

Multiple binary (Pt-Sb, Pt-In, Pt-Bi) and ternary (Pt-Sn-Sb, Pt-Sn-Ni, Pt-Sn-Fe) phases were synthesized via co-reduction. While none of these phases showed ordering behavior at the same low temperatures as Pt-Sn, there were nonetheless many of the same links between the bulk phase diagrams and reduction, seeding, and growth behavior in the nanoparticle regime. Congruent melting points, cubic or hexagonal structures, and separation from nearest neighboring phases are all factors that predict the facile synthesis of ordered phases and phase-pure products.

Though this qualitative analysis is useful in and of itself, a more quantitative approach might be useful for predicting definitively the reduction behavior of other phases, particularly if the synthesis is to be extended beyond platinum binaries and ternaries. The following chapter will attempt to present a model using the synthetic data presented in Chapters 3 and 4 that can identify the most important factors that contribute to the successful synthesis of any given phase.

REFERENCES


(1) Okamoto, H.; Villars, P.; Cenzual, K. *Pt-Sb Phase Diagram*; ASM Alloy Phase diagrams Center; ASM International: Materials Park, OH, USA, 2013.
(2) Okamoto, H.; Villars, P.; Cenzual, K. *Pt-In Phase Diagram*; ASM Alloy Phase diagrams Center; ASM International: Materials Park, OH, USA, 2013.
(3) Okamoto, H.; Villars, P.; Cenzual, K. *Pt-Bi Phase Diagram*; ASM Alloy Phase diagrams Center; ASM International: Materials Park, OH, USA, 2013.
(4) Roychowdhury, C.; Matsumoto, F.; Zeldovich, V. B.; Warren, S. C.; Mutolo, P. F.; Ballesteros, M.; Wiesner, U.; Abruña, H. D.; DiSalvo, F. J. *Chem. Mater.* **2006**, *18*, 3365–3372.
(5) Okamoto, H.; Villars, P.; Cenzual, K. *Pd-Sn Phase Diagram*; ASM Alloy Phase diagrams Center; ASM International: Materials Park, OH, USA, 2013.
(6) Okamoto, H.; Villars, P.; Cenzual, K. *Pt-Sn-Sb Phase Diagram*; ASM Alloy Phase diagrams Center; ASM International: Materials Park, OH, USA, 2013.
(7) Correa, P. dos S.; da Silva, E. L.; da Silva, R. F.; Radtke, C.; Moreno, B.; Chinarro, E.; Malfatti, C. de F. *Int. J. Hydrog. Energy* **2012**, *37*, 9314–9323.
(8) Nguyen, M. T. Synthesis of Carbon Supported Ordered Intermetallic Nanoparticles as Oxygen Reduction Catalysts in Polymer Electrolyte Membrane Fuel Cells. Dissertation, Cornell University: Ithaca, NY, 2014.

# CHAPTER 5

# PHASE CLUSTERING AND PREDICTING ORDERING BEHAVIOR

The previous two chapters have focused on the synthesis, processing and characterization of various binary and ternary ordered intermetallic metal nanoparticles, and connecting observations concerning said syntheses to the bulk phase diagram. Qualitatively, we can say that there have been overarching trends - among them, the link between congruent melting points, crystal structure, and nearby phases with similar compositions and the ease or difficulty of preparing the associated ordered phases as nanoparticles - but with this many potential variables, it is still be difficult to predict ordering trends from the phase diagram alone.

This chapter is focused on reducing the field of variables and creating a predictive model capable of determining, using only known physical properties, how easily a phase can be formed in the nanoparticle regime by co-reduction. Ideally this model would be able to be extended to phases beyond the Pt-M binaries that have been the subject of most of this work. To achieve this goal, we must use all of the data at our disposal. To that end we have applied multiple multivariate analytical techniques: Principal Components Analysis (PCA), Partial Least Squares (PLS) regression, and Logistic regression.

## *5.1 Introduction to Principal Components Analysis*

At its most fundamental level, PCA is a mathematical algorithm that takes a large collection of data and attempts to find the most relevant and descriptive patterns that describe the data[1,2]. It can be used on multidimensional data that defies traditional graphing methods, which are limited

to two or three dimensions, in order to reduce the number of dimensions (or *components*) needed to describe the data to the most important (or *principal*) ones.

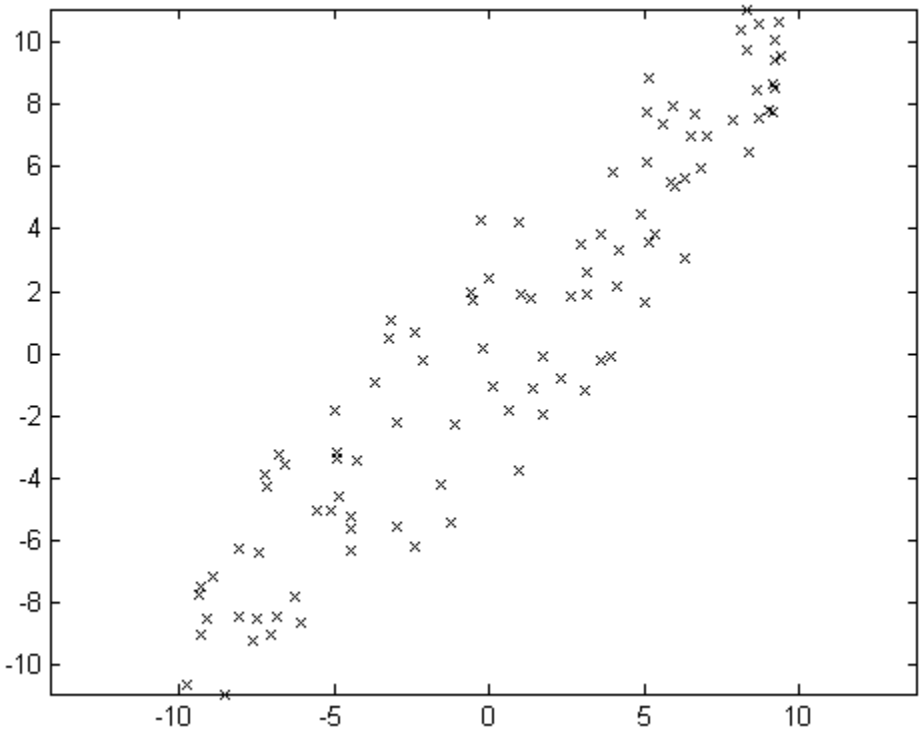


**Figure 5.1** A scatter plot of randomly distributed points in a shifted ellipsoid area.

These new components can be described as shifted set of axes. If a scatter plot is made in two dimensions (see Figure 5.1), each point can naturally be defined in terms of its coordinates on the x and y axis. This is, however, only one out of infinitely many basis sets that can be used to define these points. The simple x, y coordinates are often the most sensible basis set for visualization purposes, but it is possible to define axes that describe the data more fundamentally.

One possible way to define a new set of axes is to choose the vectors that describe the most

variance in the data. Variance is a measure of the spread of data in a data set. The formula for variance is:

$$\sigma^2 = \frac{\sum_{i=1}^{n}(\mathrm{x_i} - \hat{\mathrm{x}})^2}{(n-1)} \qquad \text{(Eq. 5.1)}$$

where $\sigma^2$ is the variance ($\sigma$ is the standard deviation) , $x_i$ is the i-th element in a data set, $\hat{x}$ is the mean of the data set, and n in the number of elements in the data set. Variance only describes spread in one dimension; in order to measure how much two variables vary with respect to one another, one must use covariance. Covariance is always measured between exactly two dimensions. The equation for covariance is similar to Equation 5.1:

$$cov(x,y) = \frac{\sum_{i=1}^{n}(x_i - \hat{x})(y_i - \hat{y})}{(n-1)} \qquad \text{(Eq. 5.2)}$$

For an N-dimensional data set, the "covariance matrix" C can be defined to be an NxN matrix with the value of each element (i,j) equal to the calculated value cov(i,j). For a three-dimensional data set:

$$C = \begin{pmatrix} cov(x,x) & cov(x,y) & cov(x,z) \\ cov(y,x) & cov(y,y) & cov(y,z) \\ cov(z,x) & cov(z,y) & cov(z,z) \end{pmatrix} \qquad \text{(Eq. 5.3)}$$

Note that the diagonals of this matrix are equal to the covariance of a dimension with itself; in other words, the variance of that dimension. Also, cov(a,b) = cov(b,a), so C is symmetrical about the main diagonal.

Now we have a matrix of values describing the spread of the data, but we still do not have a new basis set. For that, we must find the eigenvalues and eigenvectors of the data. For any square matrix A of dimensions nxn, there exists n column vectors $v_{i..n}$ of length n, and n scalars $\lambda_{i..n}$, such that:

$$Av_i = \lambda v_i \qquad \text{(Eq. 5.4)}$$

where the column vectors $v_i$ are known as the eigenvectors, which are always orthogonal to each other, and the scalars $\lambda_i$ are the corresponding eigenvalues. The covariance matrix C is a square matrix, so it is possible to calculate its eigenvalues and eigenvectors. The eigenvectors of the covariance matrix form a complete basis set where one vector is in the direction of the most descriptive pattern in the data - like a regression line - another vector describes the second most descriptive pattern in the data orthogonal to the first, and so on for n vectors for a data set with n variables. The relative magnitudes of the corresponding eigenvalues determine which eigenvectors describe the most variance.

As mentioned before, for our two-dimensional sample data, the new basis set must also be two dimensions. Figure 5.2 overlays the two eigenvectors of the covariance matrix of the data set onto the scatter plot from Figure 5.1. The larger vector describes the majority of the variance in the data, while the second vector (which must be orthogonal to the first) describes the remainder of the variance. Only two vectors are needed to completely describe all of the data points, as only two axes (x and y) were used to completely define them in the first place.

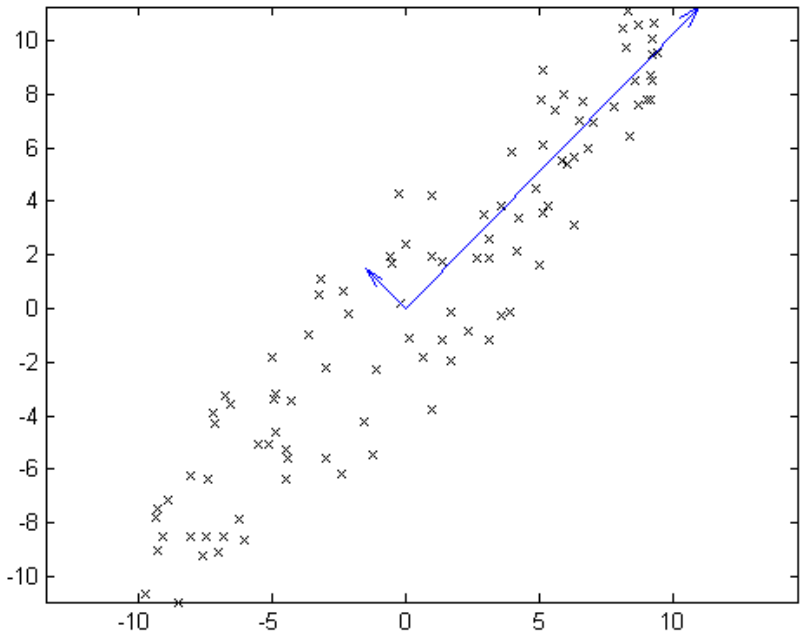


**Figure 5.2** Plot of random data with two eigenvectors (scaled by their corresponding eigenvalues).

Now, the coordinates of each point can be written in terms of these new vectors by dropping a perpendicular line to connect each point to each vector. Re-plotting the data with these coordinates has the effect of rotating the data onto this new basis set, where the new x-axis is the eigenvector of the covariance matrix of the original data with the largest eigenvalue (see Figure 5.3).

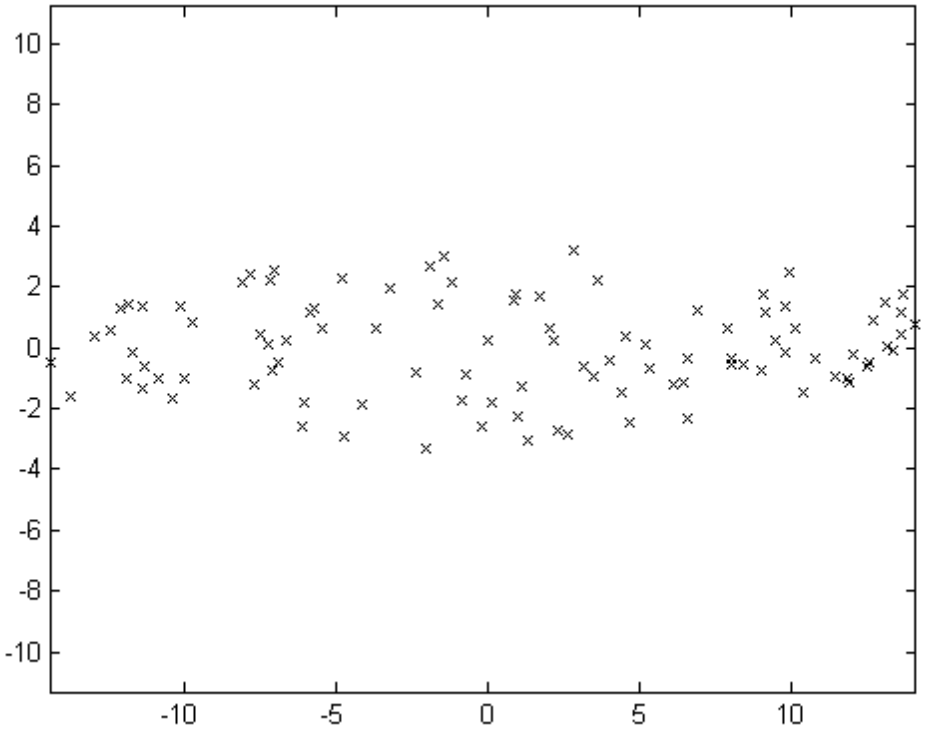


**Figure 5.3** Original data set rotated onto new basis set describing the spread of the data most efficiently.

The coordinates plotted in Figure 5.3 (F) are found by multiplying a matrix of eigenvectors *in the rows* (R) by the transpose of the original data D:

$$F = R \times D^T \qquad \text{(Eq. 5.5)}$$

The rotated data points F can be directly transformed back into the original data D by reversing the calculation. Alternatively, since the majority of the variance (in this example, over 90 %) is described by the position on a point along one vector, the information in the second coordinate could be thrown out entirely, turning the two-dimensional data set into a one-dimensional data set but retaining the majority of the information in the sample. To condense the data in this way, R is chosen to contain only the most important eigenvectors as determined by the eigenvalues. In

this case, just the first eigenvector is chosen since there are only two eigenvectors total. Then, the data can be converted back into the original basis set (the x and y axes) by taking the matrix F and multiplying it by the transpose of the eigenvector matrix R. This calculation gives the adjusted data matrix $D_A$

$$D_A = R^T \times F \qquad \text{(Eq. 5.6)}$$

The dimensionality of the data has been reduced. As seen in Figure 5.4, all of the points now sit on the eigenvector. While some information has obviously been lost, the data are now much easier to organize, sort, and group.

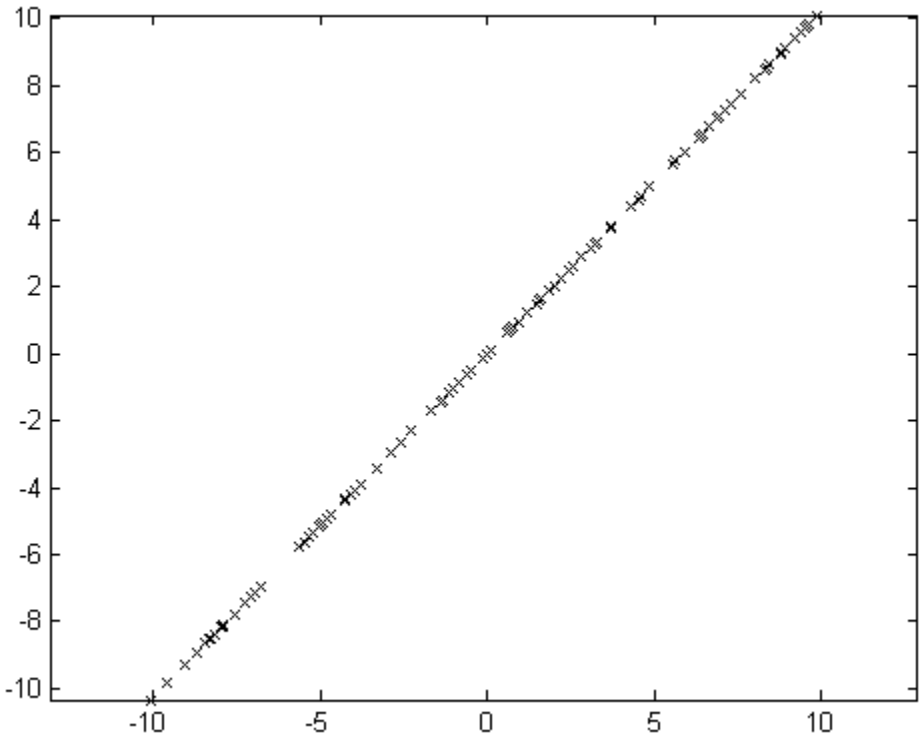


**Figure 5.4** Rotated data transformed back to the original basis set, with the variance along the second eigenvector removed.

This entire process, from original data to the shifted basis set and back to the original basis set, describes the majority of what goes on during a Principal Components Analysis. The benefit of this analysis is the ability to take a large data set comprised of many different trials and variables (in the context of this work: phases and physical properties) and be able to cluster them according to the variables that hold the most predictive property, thereby reducing the complexity of the overall data set to something that can be visualized easily. Reducing a data set with two dimensions down to one dimension is of limited utility - after all, we can discern patterns in two dimensions perfectly well - but reducing a field of eight or more variables down to a number of components that can be plotted (between one and three) makes the cluster analysis of those phases substantially easier.

Later, we will see techniques that build from PCA to perform regression on the data acquired through the reduction experiments of chapter 3s and 4, by referencing the properties identified by PCA to be the most important in separating the reduction behavior of the different phases.

### *5.2 PCA Cluster Analysis of Binary Phase Properties*

The first step is to determine which properties are of potential value in categorizing phases in a cluster analysis. One of the best aspects of PCA is that variables that have little predictive value are identified and can be ignored, while variables that have strong co-variance can be combined. Both of these steps reduce the dimensionality of the data; therefore, it is unlikely that one can ever start with too many variables. The full list of variables and phases is given in Table 5.1.

The mean values and ranges of the variables in Table 5.1 vary by orders of magnitude. This spread can disrupt the PCA algorithm, which depends on comparing the covariance values of different variables, because the magnitude of the covariance depends on the magnitude of the variables. Therefore, it is necessary to pre-process the data by a process called autoscaling, which centers all of the data (sets the mean to zero) and scales the range of the data so that all variables can contribute equally to the variance.

The next step uses the PCA function created by Barry M. Wise in 1992 to perform roughly the same calculations outlined in Section 5.1. The function outputs a plot showing the values of the eigenvalues of the covariance matrix, sorted from largest to smallest. The user then selects the number of principal components to use that covers most of the variance in the data. For this data set, three eigenvectors (components) were chosen to be sufficient, as they explained 77 % of the variance in the data and the fourth eigenvalue was not deemed useful enough to be included when three components are so much easier to work with visually.

| Phase | Coefficient Ratio (x:1) | Bulk Melt Temp (K) | Annealing Temp (K) | Bulk Melt - Anneal (K) | Crystal Structure (1=cubic, 2=hex, 3=tetra, 4=ortho) | Nearest phase distance (%) | Nearest phase distance to stable phase (%) | Congruently Melting? (1=Y) |
|---|---|---|---|---|---|---|---|---|
| **$Pt_3Sn$** | 3 | 1677 | 473 | 1204 | 1 | 23 | 25 | 1 |
| **PtSn** | 1 | 1541 | 298 | 1243 | 2 | 10 | 25 | 1 |
| **$Pt_2Sn_3$** | 0.66 | 1171 | 673 | 498 | 2 | 6.6 | 10 | 0 |
| **$PtSn_2$** | 0.5 | 1021 | 673 | 348 | 1 | 6.6 | 16 | 0 |
| **$PtSn_4$** | 0.25 | 813 | 673 | 140 | 4 | 13.4 | 30 | 0 |
| **$Pt_7Sb$** | 7 | 893 | 573 | 320 | 1 | 6 | 6 | 0 |
| **$Pt_3Sb$** | 3 | 948 | 673 | 275 | 3 | 11 | 17 | 0 |
| **$Pt_3Sb_2$** | 1.5 | 1012 | 473 | 539 | 4 | 10 | 10 | 0 |
| **PtSb** | 1 | 1319 | 673 | 646 | 2 | 10 | 16 | 0.5[a] |
| **$PtSb_2$** | 0.5 | 1498 | 773 | 725 | 1 | 16 | 16 | 1 |
| **$Pt_3In$** | 3 | 1731 | 873 | 858 | 1 | 8.4 | 15 | 0.5 |
| **$Pt_3In_2$** | 1.5 | 1433 | 873 | 560 | 2 | 3 | 15 | 0 |
| **$Pt_2In_3$** | 0.66 | 1337 | 673 | 664 | 2 | 6.7 | 6.7 | 1 |
| **$PtIn_2$** | 0.5 | 1312 | 773 | 539 | 1 | 3.3 | 6.7 | 0.5 |
| **$Pt_3In_7$** | 0.43 | 1167 | 623 | 544 | 1 | 3.3 | 3.3 | 0 |
| **PtBi** | 1 | 1038 | 673 | 365 | 2 | 16.7 | 16.7 | 1 |

**Table 5.1** A list of the physical properties that will be used to perform a cluster analysis on the listed phases, using PCA.
[a]Phases with melting points that were close to congruently melting (ie, peritectics that were less than about 40 $^{o}$C from a congruent melting point) were given a value of 0.5.

After the first three components are selected, it is useful to see which variables contribute the most to the variance. To visualize the contribution of the eight variables, we plot the weights by which each original variable is multiplied to obtain the new principal components (the weight is also known as the "loadings"). In the example in section 5.1, both of the original variables (x and y) are equally loaded onto the first and second principal components, because the component vectors lie almost directly on top of the lines y = x and y = -x. The important factor in whether or not a variable is important in a particular principal component is the magnitude of the loading; the sign indicates whether the variables are directly or inversely proportional. In Figure 5.5a, the loadings of the variables are plotted against principal components one and two. The further away a variable is positioned from the green axes, the more it contributes to that principal component.

For example, principal component 1 mainly contains the variance due to whether or not a phase is congruently melting, the bulk melting temperature, and the difference between the bulk melting temperature and the annealing temperature. Principal component two depends partially on the bulk melting temperature (but not the other two variables), but more strongly on the structure of the phase and whether or not it is near a "stable phase" (here defined as phases that are experimentally determined to easily nucleate and grow phase-pure compounds, e.g. congruently melting phases, many cubic compounds, etc). Remember, these are measures of what variables are most useful in separating phases into similar and dissimilar groupings. The loadings on the third principal component can be plotted similarly (see Figure 5.5b).

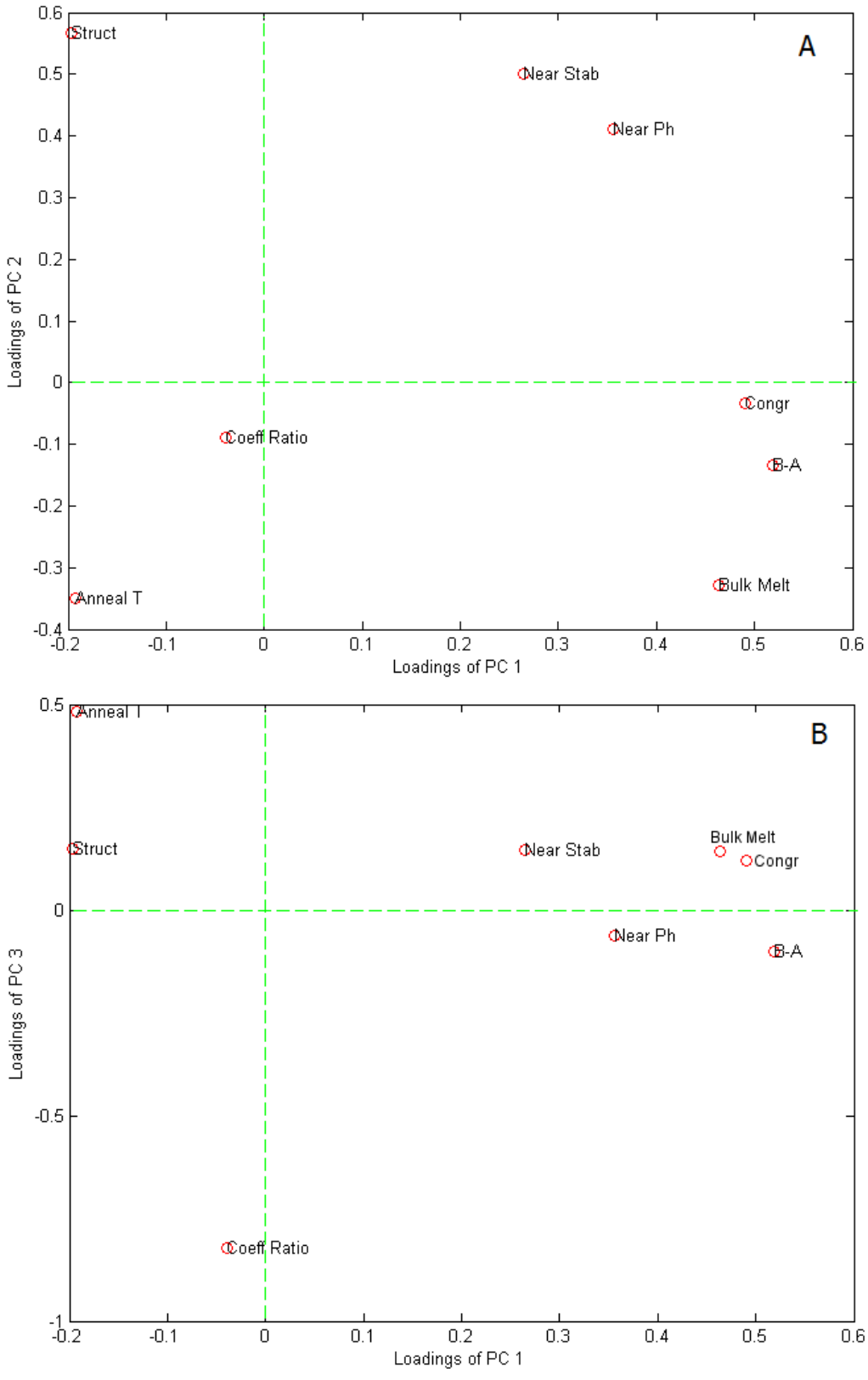


**Figure 5.5** Loadings of variables on principal components a) one and two, and b) one and three.

Note that the position of the variables along the x-axis remains constant between Figures 5.5a and 5.5b, but their position on the y-axis changes. Principal component three is heavily dominated by the stoichiometric coefficient ratio between the two metal reactants in the binary intermetallic, no other variable comes close. Considering that the coefficient ratio does not factor heavily into either principal component one or two, it makes sense that principal component three depends on it.

The phases in the first column of Table 5.1 can now be plotted according to their placement along the axes defined by these three principal components (also called their "scores" for each principal component). This is akin to the rotation performed in Figure 5.3, except that we have also reduced the number of axes necessary to sufficiently describe the data from eight to three. When this is done, the resulting two dimensional plots shown in Figure 5.6a-b are obtained.

Figure 5.6a shows remarkably good separation of phases. The platinum-rich Pt-Sn phases are far off to the right, $PtSn_2$ and $Pt_2Sn_3$ are clustered together in the middle, while $PtSn_4$ (the only tin-rich phase to show a large degree of ordering behavior without forming non-stoichiometric phases) is isolated in the top left corner. $PtSb_2$ is another well-isolated phase that orders unexpectedly well for a non-Pt rich intermetallic. There is also a cluster of similarly-behaving Pt-In compounds in the bottom left corner. In contrast, Figure 5.6b shows very little in the way of descriptive clustering, primarily (as shown in Figure 5.5b) because this component is dominated by the coefficient ratio, which means that the phase that is most unlike any other phase ($Pt_7Sb$) scored by far the highest in this component.

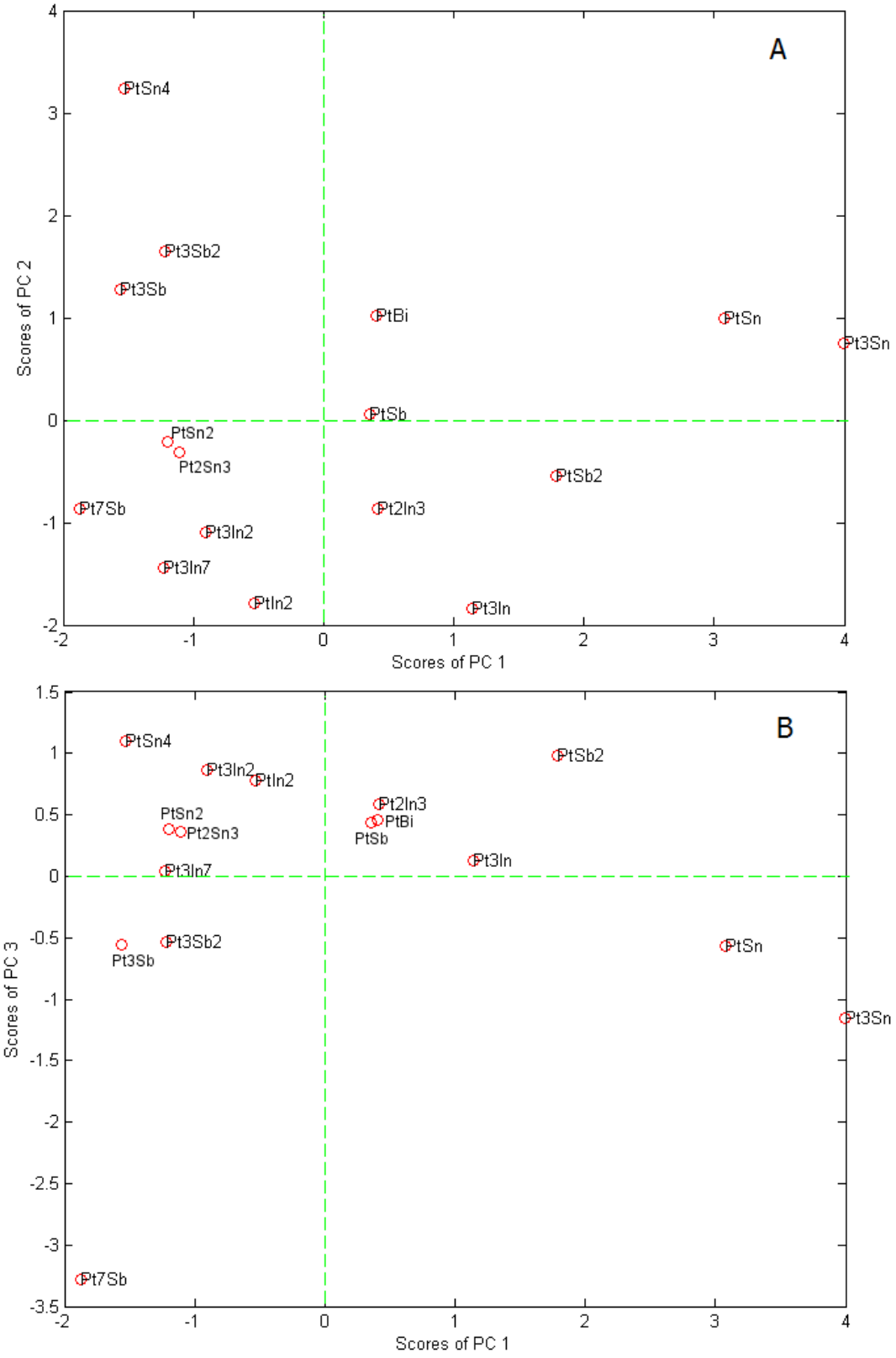


**Figure 5.6** Scores of phases on principal components a) one and two, and b) one and three.

As a result of this analysis, one could decide that the stoichiometric coefficient ratio variable is skewing the variance in such a way as to hide potentially more important information. Going back to the original data table and removing coefficient ratio allows us to repeat the analysis, this time with three principal components that describe more of the variance (84 %). The loadings of the first two principal components are largely unchanged, though the values have been inverted so the plot appears to be reflected across the y-axis; remember, the magnitude of the loading is what matters for this analysis. The loading of the third component is dominated by the annealing temperature (see Figure 5.7).

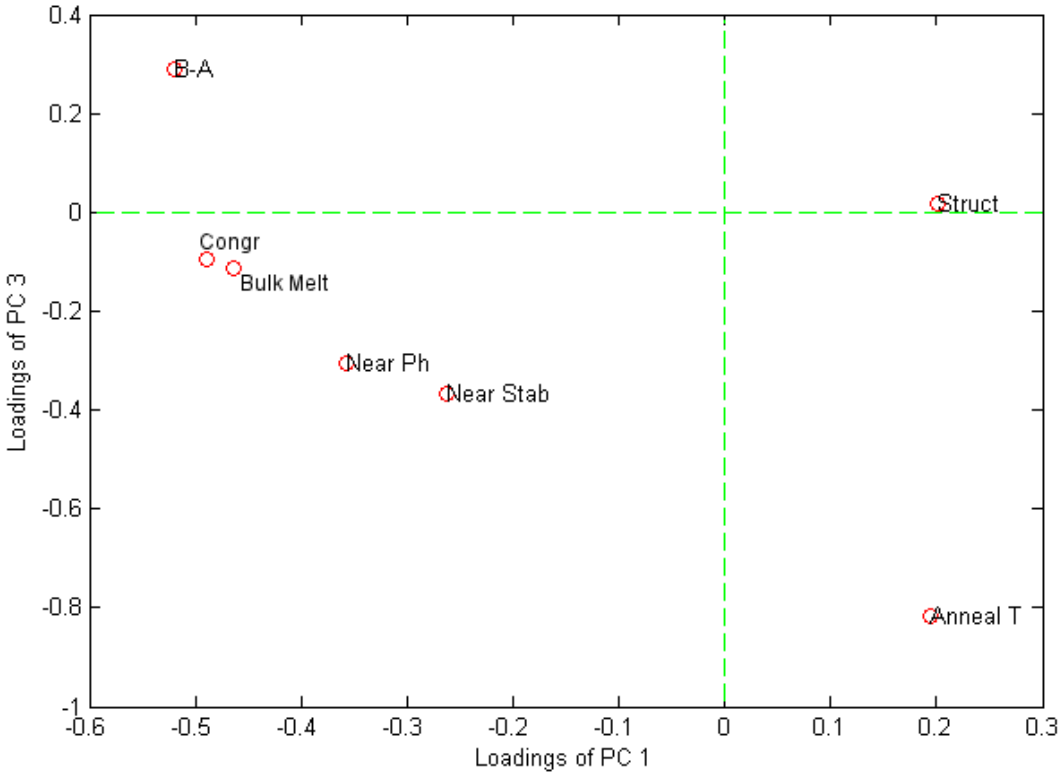


**Figure 5.7** Loadings of variables on principal components one and three, after the removal of coefficient ratio from consideration.

When plotting all three principal components together (see Figure 5.8), we can see the full cluster analysis of the target phases. Obviously, with only sixteen phases (all of which are Pt-M binaries, with M being a main-group element) many of these phases will have many similar variables, but nonetheless some patterns have emerged. The tin-rich Pt-Sn phases, $Pt_3In$, and $PtSb_2$ are clear standouts. $PtSn_4$ is also in a category of its own. The other Pt-In and Pt-Sb phases are scattered in a much tighter grouping; considering their similar reduction behavior, this is expected.

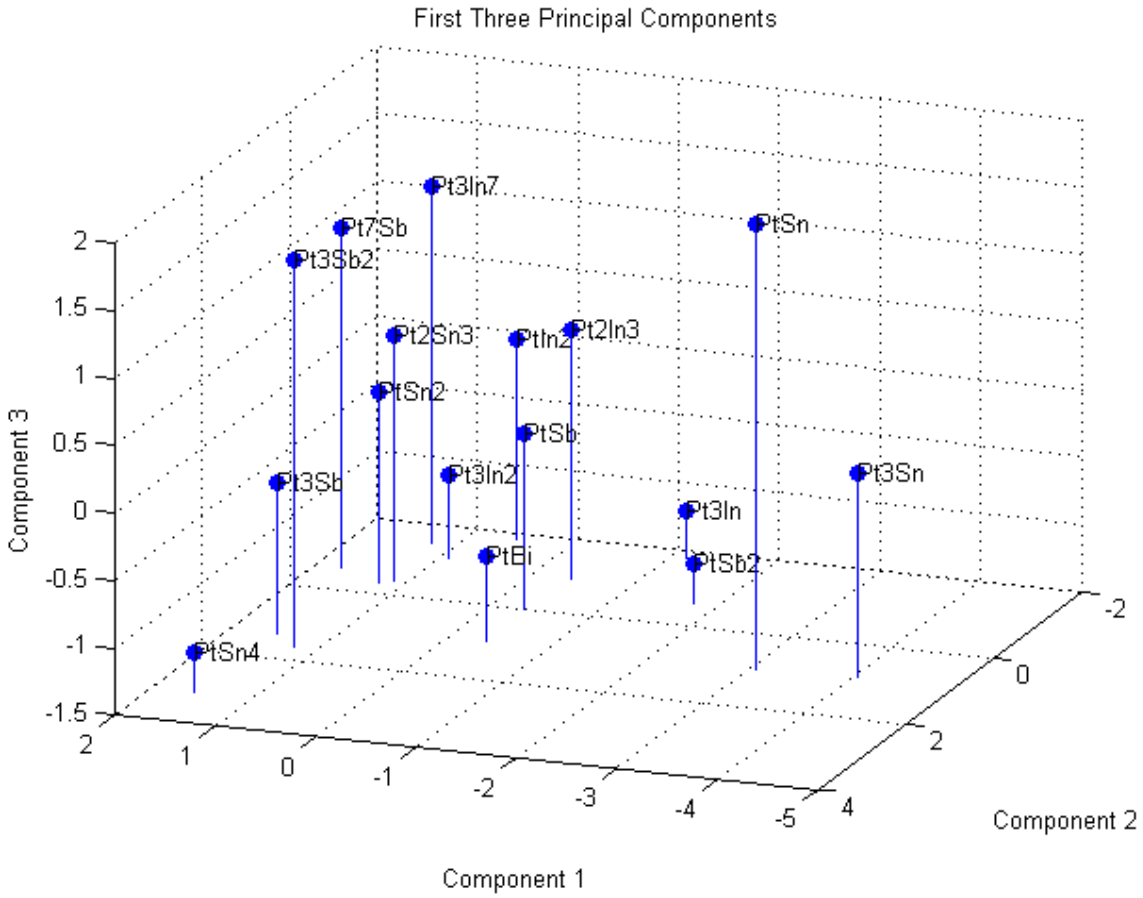


**Figure 5.8** Cluster analysis of all Pt-M phases obtained by plotting scores against the first three principal components.

The analysis so far has succeeded in separating the phases according to a number of physical properties. While it is certainly possible to add additional phases and plot them according to their scores on these three components - just as one would plot any new data in three dimensional space - technically this is not an predictive model just yet. Data points that lie closely to well-ordered phases like PtSn and $PtSb_2$ might very well be phases that are easily co-reduced into ordered intermetallics, but there are additional analyses that we can do to make this model less qualitative.

### *5.3 Partial Least Squares Regression*

Now we can finally start to use experimental data from the co-reductions to help make a model for what factors predict ordering behavior. Ordering character is very difficult to quantify for many phases, particularly non-cubic phases, so instead the phase composition (expressed as a percentage of the total material in the sample, measured by pXRD) was used. The domain size calculated by the Williamson-Hall method (see Section 2.3.1) was also included in the regression, primarily because annealing temperature has such a strong effect on the domain size and larger domain sizes are indications that it would be possible to reduce the annealing temperature and still obtain the ordered phase (tuning of the annealing temperature is an area where this work could be refined in the future).

The first step of the Partial Least Squares (PLS) regression method[3] is to do a PCA on both the independent variables (the same variables from Section 5.2, called the x block or X) and the dependent variables (called the y block or Y). In this analysis, Y is the results of the co-

reduction, here defined as a matrix containing the phase purities expressed as a percentage in one column, and the domain sizes (in nm) in the second column. The independent variables use three principal components to fit the data, and both of the possible principal components were used to describe the dependent variables. Technically, the components obtained via PLS (also called "latent variables") are not exactly the same as those obtained via PCA; instead of simply maximizing the variance of the independent variables, PLS specifically seeks to maximize the variation in X that is useful for predicting Y.

PLS calculates the scores and loadings of X and Y, and the weight matrix W that is used to maintain orthogonality in the scores, through the NIPALS (Non-Iterative PArtial Least Squares) algorithm. If X is the matrix of independent variables, Y is the matrix of dependent variables, W are the weights, T and U are the scores of X and Y respectively, and P and Q are loadings of X and Y respectively, the NIPALS algorithm works by picking one column of Y as the starting estimate for $u_1$ and sequentially solving the following series of equations:

$$w_1 = \frac{X^T u_1}{\|X^T u_1\|} \quad \text{(Eq. 5.7)}$$

$$t_1 = X w_1 \quad \text{(Eq. 5.8)}$$

$$q_1 = \frac{Y^T t_1}{\|Y^T t_1\|} \quad \text{(Eq. 5.9)}$$

$$u_1 = Y q_1 \quad \text{(Eq. 5.10)}$$

After solving Equation 5.10, the new $u_1$ is compared to the $u_1$ from Equation 5.7; if there is a significant difference, the series of equations is repeated with the new $u_1$ taking the place of the old. Next, the X block loadings need to be calculated, and the scores and weights rescaled:

$$p_1 = \frac{X^T t_1}{\|t_1^T t_1\|} \quad \text{(Eq. 5.11)}$$

$$p_{1,new} = \frac{p_{1,old}}{\|p_{1,old}\|} \quad \text{(Eq. 5.12)}$$

$$t_{1,new} = t_{1,old}\|p_{1,old}\| \quad \text{(Eq. 5.13)}$$

$$w_{1,new} = w_{1,old}\|p_{1,old}\| \quad \text{(Eq. 5.14)}$$

And the regression coefficient for the relationship between the X and Y block scores, b, must also be calculated:

$$b_1 = \frac{u_1^T t_1}{t_1^T t_1} \quad \text{(Eq. 5.15)}$$

The last step before moving on to the next latent variable (the optimum number of latent variables was found before beginning this procedure, via PCA) is to calculate the residuals of the X block (E) and Y block (F).

$$E_1 = X - t_1 {p_1}^T \quad \text{(Eq. 5.16)}$$

$$F_1 = Y - b_1 t_1 {q_1}^T \quad \text{(Eq 5.17)}$$

The entire process is then repeated (from Equation 5.7) with $E_1$ and $F_1$ substituting in for X and Y, respectively, for the next latent variable. This process is repeated for as many latent variables as were initially chosen. As the fit improves, the residuals approach zero. The model's prediction of the original Y (based on the original X) can then be reconstructed using the calculated weights, loadings, and scores.

Figure 5.9 is a comparison of the calculated values (via PLS regression) for both phase purity and domain size to the actual experimental values. Note that this is not a linear regression, and these points are not intended to be sorted in any particular order; the lines connecting points are there for visualization purposes only. The real test is how closely the actual and predicted values trend together. One way of evaluating a model is to use the root-mean-squared error of cross-validation (RMSECV) which is defined as

$$RMSECV = \sqrt{\frac{\sum_{i=1}^{n}\left(y_{pred,i} - y_{actual,i}\right)^2}{n}} \quad \text{(Eq. 5.18)}$$

where n is the number of trials (phases, in this case). RMSECV is calculated for each individual assessment value (phase purity and domain size, in Figure 5.9). If each column RMSECV is divided by the mean of Y for that assessment value, the resulting value (expressed as a percentage) can be used to quantitatively determine the goodness of fit of the model to the data. This calculation for the model shown in Figure 5.9 gives a percent error of 9.5 % for the phase purity assessment value, and 44 % for the domain size. Removing the fourth phase ($PtSn_2$) from consideration lowers the percent error of the phase purity value to 6.3 %.

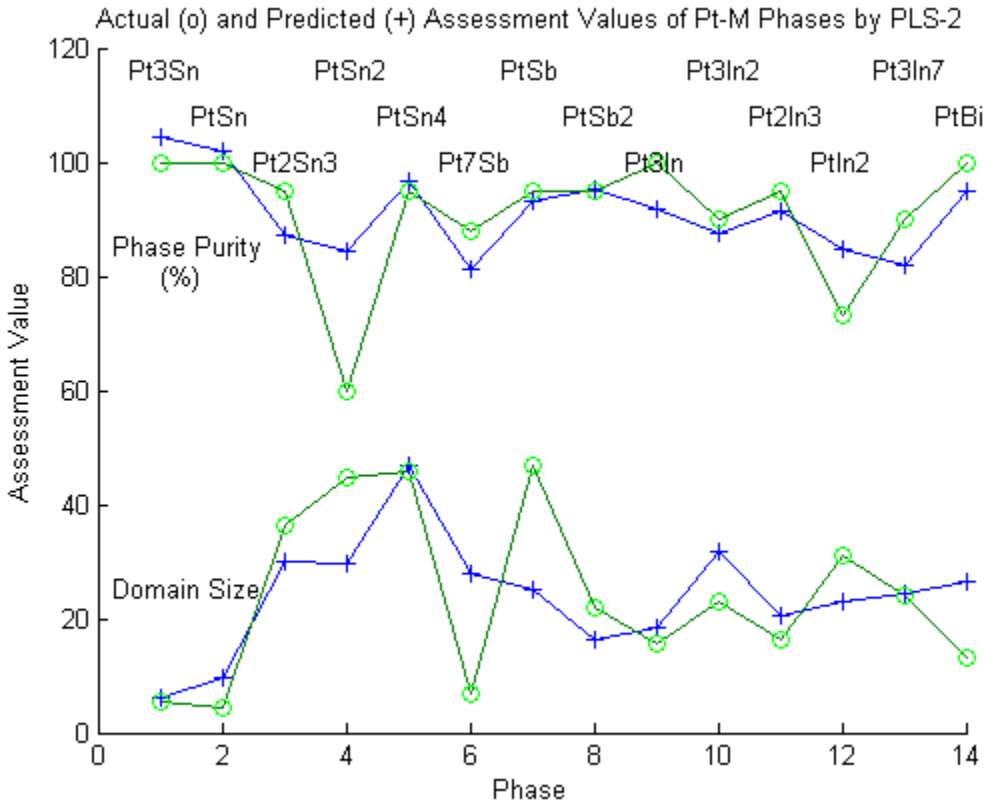


**Figure 5.9** Comparison of actual values of phase purity and domain size versus values predicted from PLS regression model using three latent variables.

This is a model with potential. The domain size fitting is wildly off - among other reasons,

because the products were not annealed at the lowest temperatures necessary for ordering to occur - but simply making an estimate of the purity of a phase just from its physical properties is an impressive first step towards developing a model that can predict whether or not a phase will form an ordered phase. With more gradated annealing temperature data, it is conceivable that the model could even be extended to include a "prediction" of the temperatures at which as-made particles must be annealed for ordering to occur.

### *5.4 Logistic Regression*

The previous regression does an acceptable job of predicting phase purity of synthesized intermetallics, but it has some limitations. For one thing, phase purity is a percentage value with a hard cap of 100 % (any predicted values greater than 100 % make no physical sense). However, the regression can't take this into account. We were also obligated to remove from the analysis compounds that we were unable to synthesize as pure phases, such as $Pt_3Sb$, because no estimate could be made of the phase purity. This could be represented as a "0 %" phase purity, but attempts to fit that into the model just created a large instability in the regression and made the predictions for the other phases less accurate.

Instead, what is needed is a way to give a quantitative answer to the question: how likely is this phase to be successfully synthesized (where a "successful synthesis" is here defined as a product that is over 90 % pure by pXRD and has formed the targeted stoichiometric ordered phase)? The answer to this question is a categorical variable, with a value of 1 for a successful synthesis and 0 for an unsuccessful synthesis. There are a number of different models that are able to perform a

regression capable of answering this question; for our purposes, a logistic regression is appropriate.

A logistic regression is a member of a set of models called generalized linear methods (GLM). These models seek first to explain the data trend with a linear model, and then account for the rest of the variation with a "link function". In a logistic regression, the link function is a series of weights multiplied by variations in the independent variables, which are then summed and run through the logistic function.

The logistic function (shown in Figure 5.10) maps input values to a range of values between 0 and 1. Output values approach 1 as input values approach positive infinity, and 0 as input values approach negative infinity. When the input is zero, the logistic function returns 0.5. Link functions do not always return a value between 0 and 1, but it is essential for the regression that we want to do. The equation of the logistic function is given below.

$$Logistic(x) = \frac{1}{1 + e^{-x}} \qquad \text{(Eq. 5.19)}$$

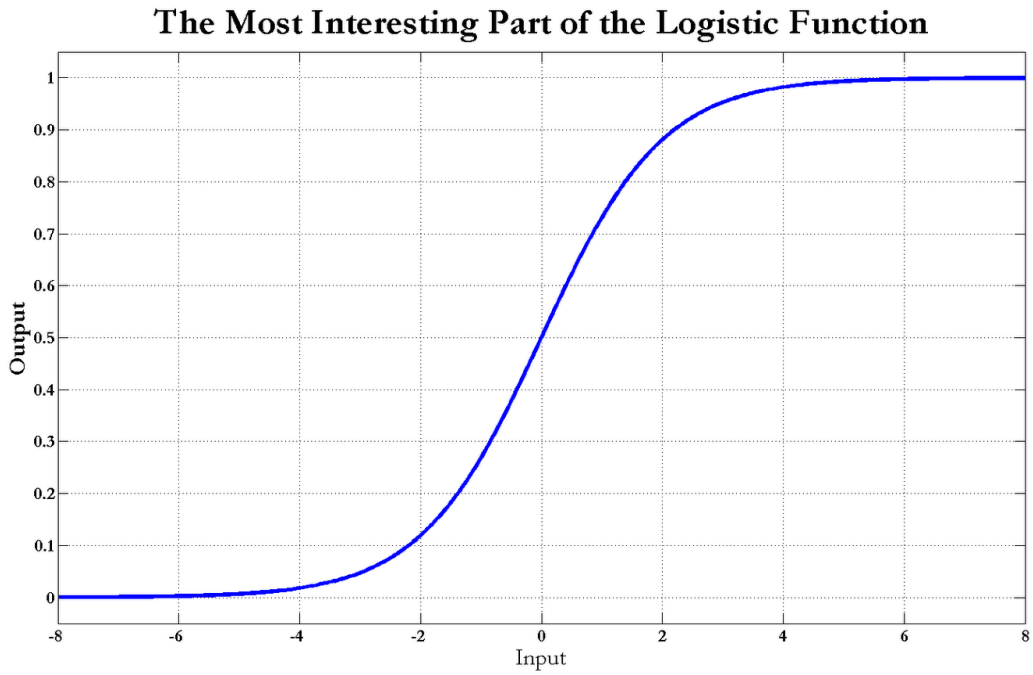


**Figure 5.10** A section of the logistic function, showing the inflection point at (0,0.5). Taken from Will Dwinnel's data mining blog[4].

A logistic regression will have one linear term, and as many weighted terms as there are independent variables, all of which is set as "x" in Equation 5.19. Unfortunately, there is no definite mathematical formula that is able to calculate the weights (also called regression coefficients) in terms of how well they fit the dependent variables after a logistic regression. Fortunately, they can be solved for iteratively, and MATLAB is excellent for iterating over matrices of data.

As mentioned before, one of the benefits of using this analysis over the previous PLS approach is that we can use every experiment to make the model. All trials are useful here, which means that we should be able to get a clearer picture of how the annealing temperature affects ordering

because we can track each phase, and at what temperature the phase goes from an "unsuccessful synthesis" to a "successful synthesis". The data used in this regression are not optimized for this task - this is why experimental design is an important topic! - but the door is open for such data to be added to the model in the future. Multiple trials of the same synthesis can also easily be incorporated into the regression.

It is also important to not over-parameterize our data set, as well. This is where the PCA analysis shines; we can skip a lot of tedious manual iteration of our regression and choices on independent variables because we already know for a fact which variables are most important, which are unimportant, and which are closely related (and therefore redundant). For this regression, the following six variables were chosen as the most unique and important: bulk melting temperature, annealing temperature, structure (expressed as a categorical: 1 = cubic, 2 = hexagonal, 3 = trigonal, 4 = orthorhombic), phase distance to nearest stable phase (expressed as a percent), whether the phase is congruently melting (1 = yes, 0.5 = within 40 $^{o}$C, 0 = no), and whether or not there is complexation prior to the reduction (1 = yes, 0 = no). Table 5.2 lists the phases used in the regression, the predictor variables, and the responses for each synthesis. The Pd-Sn phases were also included.

| Phase | Bulk Melt Temp (K) | Anneal Temp (K) | Crystal Structure[a] | D (stab. ph.) (%) | Congruent Melting? | Complex? | Successful Synthesis? |
|---|---|---|---|---|---|---|---|
| $Pt_3Sn$ | 1677 | 298 | 1 | 25 | 1 | 1 | 0 |
| $Pt_3Sn$ | 1677 | 473 | 1 | 25 | 1 | 1 | 1 |
| $Pt_3Sn$ | 1677 | 673 | 1 | 25 | 1 | 1 | 1 |
| PtSn | 1541 | 298 | 2 | 25 | 1 | 1 | 1 |
| PtSn | 1541 | 473 | 2 | 25 | 1 | 1 | 1 |
| $Pt_2Sn_3$ | 1171 | 298 | 2 | 10 | 0 | 1 | 0 |
| $Pt_2Sn_3$ | 1171 | 473 | 2 | 10 | 0 | 1 | 0 |
| $Pt_2Sn_3$ | 1171 | 673 | 2 | 10 | 0 | 1 | 1 |
| $PtSn_2$ | 1021 | 298 | 1 | 16 | 0 | 1 | 0 |
| $PtSn_2$ | 1021 | 473 | 1 | 16 | 0 | 1 | 0 |
| $PtSn_2$ | 1021 | 673 | 1 | 16 | 0 | 1 | 0 |
| $PtSn_4$ | 813 | 298 | 4 | 30 | 0 | 1 | 0 |
| $PtSn_4$ | 813 | 473 | 4 | 30 | 0 | 1 | 1 |
| $PtSn_4$ | 813 | 673 | 4 | 30 | 0 | 1 | 1 |
| $Pt_7Sb$ | 893 | 298 | 1 | 6 | 0 | 0 | 0 |
| $Pt_7Sb$ | 893 | 573 | 1 | 6 | 0 | 0 | 0 |
| $Pt_3Sb$ | 948 | 298 | 3 | 17 | 0 | 0 | 0 |
| $Pt_3Sb$ | 948 | 473 | 3 | 17 | 0 | 0 | 0 |
| $Pt_3Sb$ | 948 | 673 | 3 | 17 | 0 | 0 | 0 |
| $Pt_3Sb_2$ | 1012 | 473 | 4 | 10 | 0 | 0 | 0 |
| PtSb | 1319 | 298 | 2 | 16 | 0.5 | 0 | 0 |
| PtSb | 1319 | 473 | 2 | 16 | 0.5 | 0 | 0 |
| PtSb | 1319 | 673 | 2 | 16 | 0.5 | 0 | 1 |
| $PtSb_2$ | 1498 | 773 | 1 | 16 | 1 | 0 | 1 |
| $Pt_3In$ | 1731 | 873 | 1 | 15 | 0.5 | 0 | 1 |
| $Pt_3In_2$ | 1433 | 873 | 2 | 15 | 0 | 0 | 1 |
| $Pt_2In_2$ | 1337 | 298 | 2 | 6.7 | 1 | 0 | 0 |
| $Pt_2In_3$ | 1337 | 673 | 2 | 6.7 | 1 | 0 | 1 |
| $PtIn_2$ | 1312 | 773 | 1 | 6.7 | 0.5 | 0 | 1 |
| $Pt_3In_7$ | 1167 | 623 | 1 | 3.3 | 0 | 0 | 1 |
| PtBi | 1038 | 673 | 2 | 16.7 | 1 | 0 | 1 |
| $Pd_3Sn$ | 1599 | 298 | 1 | 9 | 1 | 0 | 0 |
| $Pd_3Sn$ | 1599 | 873 | 1 | 9 | 1 | 0 | 1 |
| $Pd_2Sn$ | 1093 | 293 | 4 | 7 | 0 | 0 | 0 |
| $Pd_2Sn$ | 1093 | 873 | 4 | 7 | 0 | 0 | 0 |
| PdSn | 1083 | 298 | 4 | 23 | 0.5 | 0 | 0 |
| PdSn | 1083 | 873 | 4 | 23 | 0.5 | 0 | 1 |

**Table 5.2** Predictor data and response variables used in logistic regression. [a]See text for explanation.

If the response variables - again, either 1 for successful or 0 for unsuccessful - are contained in a vector Y, and the predictor data are held in a matrix X with a number of rows n equal to the number of trials and a number of columns m equal to the number of independent variables (m = 6 in this case), the regression seeks to minimize the sum of the squared residuals R:

$$R = Y - Logistic(Z) \quad \text{(Eq. 5.20)}$$

where Z is the sum of the linear and link functions:

$$Z = B_0 + \sum_{i=1}^{m} B_i X_i \quad \text{(Eq. 5.21)}$$

The coefficients $B_0$ through $B_m$ are the previously mentioned regression coefficients, and they are what the algorithm iterates. The final values for B tell us which variables are most important, and if they are positively or negatively correlated to the response variable.

The values of the coefficients obtained from the regression, their standard errors, and their p-values (a measure of the probability that the apparent contribution from a particular variable is due to chance alone and not real) are listed in Table 5.3.

| **Variable** | **$B_i$** | **Error** | **p-value** |
|---|---|---|---|
| **(Linear Coeff.)** | -10.4 | 5.9 | 0.081 |
| **Bulk Melt.** | $-5.0*10^{-4}$ | $4.4*10^{-3}$ | 0.910 |
| **Anneal T.** | $1.4*10^{-2}$ | $4.5*10^{-3}$ | 0.003 |
| **Struct** | $-1.8*10^{-1}$ | $7.6*10^{-1}$ | 0.812 |
| **Near Stab. Ph.** | $1.1*10^{-1}$ | $1.2*10^{-1}$ | 0.361 |
| **Congr?** | 3.8 | 2.9 | 0.187 |
| **Complex?** | 1.4 | 1.6 | 0.387 |

**Table 5.3** Regression coefficients and their associated errors.

Obviously, the error bars on most of these coefficients are enormous, and the p-values (which should be below 0.1 to have even a low presumption against the null hypothesis) are almost as bad. If we can ignore those for a moment - partially the result of bad experimental design; we are missing a lot of data for intermediary temperatures - what do the general trends tell us? The two variables that are an order of magnitude more important in determining the whether or not a particular phase will order are, unsurprisingly, whether or not it is a congruently melting phase and whether or not it forms complexes in solution prior to the reduction (basically, Pt-Sn gets a boost that no other phase system sees). After that, the structure is the next most important factor (with the lowest p-value as well).

The regression does not actually output a simple binary value, remember. The output is in the range between zero and one, which we can interpret as a measure of how likely it is that a particular phase belongs to one category or the other. Looking at the output for Logistic(Z) for each phase shows how the phases are grouped (see Table 5.4).

We again see $PtSn_2$ and $PtSn_4$ defying expectations; $PtSn_2$ by being more difficult to synthesize and $PtSn_4$ by being more readily synthesized than they both are predicted to be. $Pt_3In_7$'s ability to be synthesized as a pure compound also would be an unexpected result, based on this regression. For all other phases, the demarcations are clear: below a predicted response of 0.5 is a clear sign that a phase is going to be difficult, or impossible, to synthesize successfully; above 0.8 the opposite is true. A handful of phases in the 0.6 to 0.75 region muddy the waters somewhat, but going by the above rule, thirteen out of seventeen successfully synthesized phases are definitively predicted correctly, and seventeen out of twenty unsuccessfully synthesized phases

are also predicted correctly.

| Successful (Y=1) | | Unsuccessful (Y=0) | |
|---|---|---|---|
| **Phase** | **Logistic(Z)** | **Phase** | **Logistic(Z)** |
| $Pt_3Sn$ | 0.95, 1.00 | $Pt_3Sn$ | 0.62 |
| PtSn | 0.59, 0.94 | $Pt_2Sn_3$ | 0.01, 0.08 |
| $Pt_2Sn_3$ | 0.56 | $PtSn_2$ | 0.02, 0.17, 0.75 |
| $PtSn_4$ | 0.37, 0.90 | $PtSn_4$ | 0.05 |
| PtSb | 0.78 | $Pt_7Sb$ | 0.01, 0.07 |
| $PtSb_2$ | 0.99 | $Pt_3Sb$ | 0.01, 0.04, 0.37 |
| $Pt_3In$ | 0.98 | $Pt_3Sb_2$ | 0.02 |
| $Pt_3In_2$ | 0.87 | PtSb | 0.02, 0.19 |
| $Pt_2In_3$ | 0.90 | $Pt_2In_3$ | 0.05 |
| $PtIn_2$ | 0.86 | $Pd_3Sn$ | 0.07 |
| $Pt_3In_7$ | 0.08 | $Pd_2Sn$ | 0.01, 0.70 |
| PtBi | 0.97 | PdSn | 0.04 |
| $Pd_3Sn$ | 0.99 | | |
| PdSn | 0.99 | | |

**Table 5.4** Comparison of response values to predicted responses for target phases.

This is as far as this analysis has been taken, though it should be stressed that there is more ground to cover here. There is always room to add additional phases to improve the model of general trends, increase the number of trials to hopefully narrow those enormous error bars, or add additional predictors (for example, something to incorporate elemental differences, such as differences in electronegativity or Mendeleev number) that may better explain the variations. There exist variations on the regression model that are mathematically more appropriate for categorical predictor variables (e.g. whether a phase is congruently melting, the type of crystal structure, etc). And of course, a model's real test is its ability to accurately predict properties, not just explain the properties of the phases used to create the model. To that end, incorporating the large existing synthetic datasets of previous DiSalvo group members who have utilized the co-reduction method to form ordered intermetallics[5,6] would be an excellent first step in validating the model presented here. There is rarely a defined endpoint in multivariate analysis, just a series of best fits and predictions that are constantly reevaluated and revised.

### *5.5 Conclusions*

The multivariate analysis of the ordered intermetallic nanoparticle syntheses presented in chapters 3 and 4 quantified a number of trends that were previously only anecdotal observations. The most important factors for ordering and phase purity were found to be whether a phase is congruently melting, how closely it lies on the phase diagram to other phases of a different structure type, what structure type is adopted (with cubic and hexagonal being far superior in general for ordering), and whether or not the reactants form complexes in solution prior to the reduction (specific to Pt-Sn).

The relative importance of these trends varied depending on the phases that we analyzed and how the analysis was performed, but a congruent melting point was the one property that was consistent throughout all analyses as a primary differentiator between phases that easily order and phases that require high temperature annealing to order (or, for one reason or another, never order). This is expected, as a congruent melting point is indicative that the compound as a "significantly" lower free energy than its near neighbors in the phase diagram. This energy is usually dominated by the enthalpy of ordering, which is more negative for the congruently melting composition than nearby compositions. However, it is still desirable to quantify this effect, and to be able to look at congruent melting points in the context of a wider series of properties that may all contribute in their own way to the formation of the ordered intermetallic phase. While this thesis has been decidedly light on the discovery of new, more efficient fuel cell catalysts, the original impetus for looking at these materials harking back to chapter 1, the author hopes that such analyses could make the task of synthesizing a new intermetallic phase for

energy materials easier. At the very least, this work has been an interesting study on the myriad forces influencing the synthetic and processing behavior of nanoparticles from just this small corner of the periodic table, and a reminder that a train of scientific inquiry rarely takes you where you think you will go.

REFERENCES


(1) Pearson, K. *Philosophical Magazine* **1901**, *2*, 559–572.
(2) Ringnér, M. *Nat Biotech* **2008**, *26*, 303–304.
(3) Mevik, B.-H.; Wehrens, R. *Journal of Statistical Software* **2007**, *18*, 1–24.
(4) Dwinnell, W. Data Mining in MATLAB: Logistic Regression. *Data Mining in MATLAB*, 2009.
(5) Nguyen, M. T. Synthesis of Carbon Supported Ordered Intermetallic Nanoparticles as Oxygen Reduction Catalysts in Polymer Electrolyte Membrane Fuel Cells. Dissertation, Cornell University: Ithaca, NY, 2014.
(6) Chen, H. A Surfactant-Free Strategy For Synthesizing And Processing Intermetallic Platinum-Based Nanoparticle Catalysts. Dissertation, Cornell University: Ithaca, NY, 2013.

# APPENDIX A

## 119-SN NMR ANALYSIS OF PRE-REDUCTION SOLUTION

This Appendix builds off of the observations of Pt-Sn apparent complexation described in section 3.2 Determining the identities of these complexes proved to be more complicated than the initial step of observing them in the first place. Spectroscopic measurements on Pt-Sn chloride solutions under aqueous conditions confirm that multiple complexes exist, and that they have distinguishable spectra with peaks occurring in the region of 300 to 550 nm[1,2]. However, literature on the UV-Vis spectra of Pt-Sn complexes in THF could not be found; to our knowledge, such studies have not been carried out, and while the literature data for Pt-Sn complexes in water are useful for demonstrating the hypothetical range where Pt-Sn complexes might absorb, they are not useful for identifying the structures of individual complexes.

To that end, further analytical techniques were employed. Drawing inspiration from long-dormant organic chemistry methods, NMR was pursued as a method to elucidate the structures of the complexes. Obviously, the standard $^{13}C$ NMR and $^{1}H$ NMR would be useless in this case, as the bonds of interest (in most of the possible structures) do not incorporate those nuclei. However, $^{195}Pt$- and $^{119}Sn$ are both heteroatoms that have received some degree of attention in the literature as active centers for structure determination via NMR, including structures with Pt-Sn bonding[1,3,4]. In addition to the chemical shifts (measured in ppm) and the broadening of the peaks (measured in either ppm or Hz, which are interchangeable), another source of structure information is the J coupling constants, which are a measure of the degree of splitting of the peaks. Figure 3.14 is an example spectrum of two very similar Pt-Sn compounds, showing how peak splitting, shifting, and broadening can be used to fingerprint, and in some cases identify, Pt-

Sn complexes.

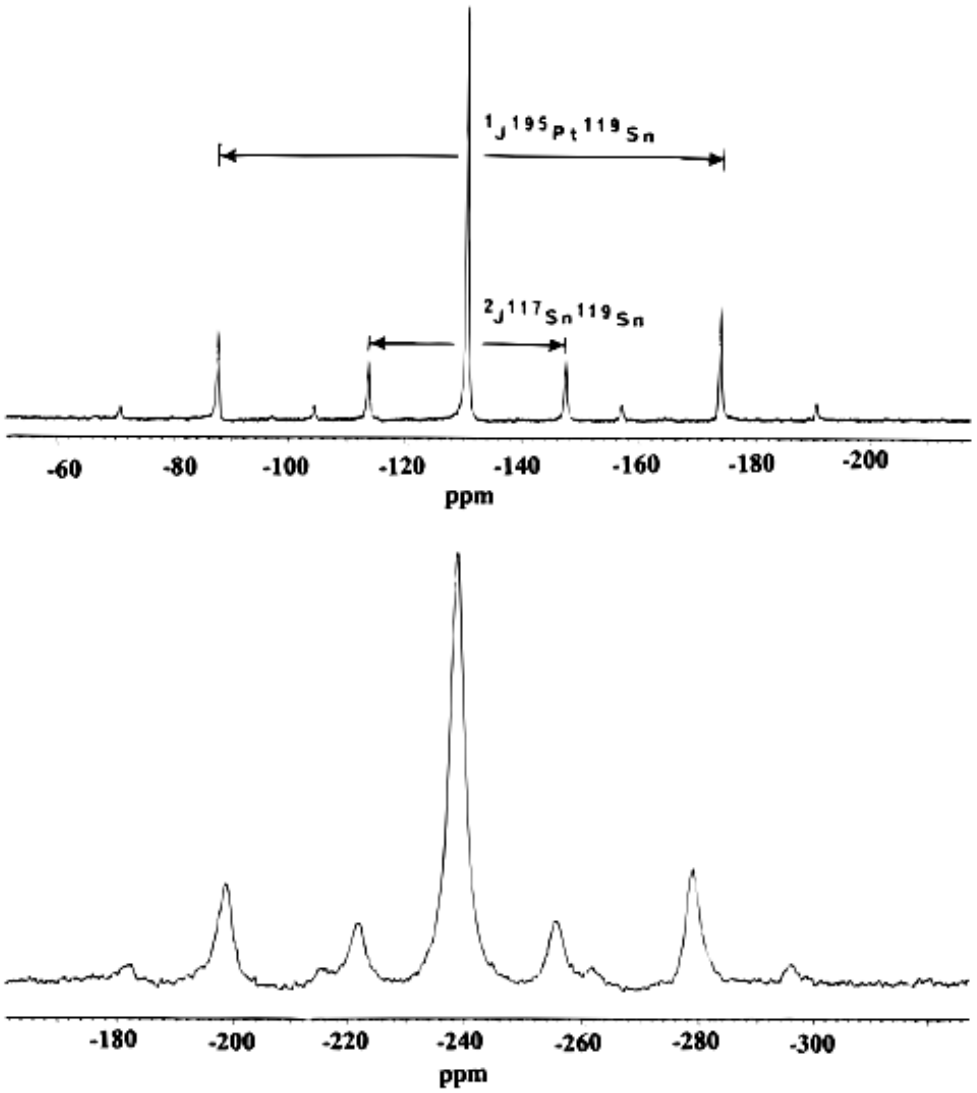


**Figure 3.14** $^{119}$Sn NMR spectra of $[PhCh_2PPh_3]_3[Pt(SnCl_3)_5]$ (top) and $[PhCh_2PPh_3]_3[Pt(SnBr_3)_5]$ (bottom) in acetone-$d_6$. The sources of peak splitting (coupling between spin-active heteroatoms) are labeled on the top spectrum. Taken from Nelson et. al[1].

Unfortunately, $^{119}$Sn NMR chemical shifts have an enormous range of reported values. For comparison, $^{13}$C NMR has at most a range of about 220 ppm to scan. This is small enough to scan the entire range in an afternoon with excellent signal to noise on a standard 600 MHz instrument. $^{119}$Sn NMR can range from -2000 to 700 ppm. The chemical shifts of tin-transition

metal complexes are reported to span -400 to 300 ppm, and tin halides alone have a vast span from -1600 to 0 ppm. These shifts are also highly solvent and temperature dependent. . With regions of interest an order of magnitude or more larger than $^{13}C$ NMR, the first problem with $^{119}Sn$ NMR is determining where to focus. $^{195}Pt$ has potential shifts as large, or larger, and it also has the disadvantage of having an inherently weaker NMR resonance, so for these experiments the focus was on tin.

The first experiments were each six hours in length, over a ppm window of 550 ppm. This window was shifted incrementally from -1050 to 150 ppm, overlapping slightly each time, in order to assemble a complete picture of the NMR window. 550 ppm was roughly the largest window that could be scanned in a single experiment while maintaining a reasonable signal. These scans are shown in Figure 3.15.

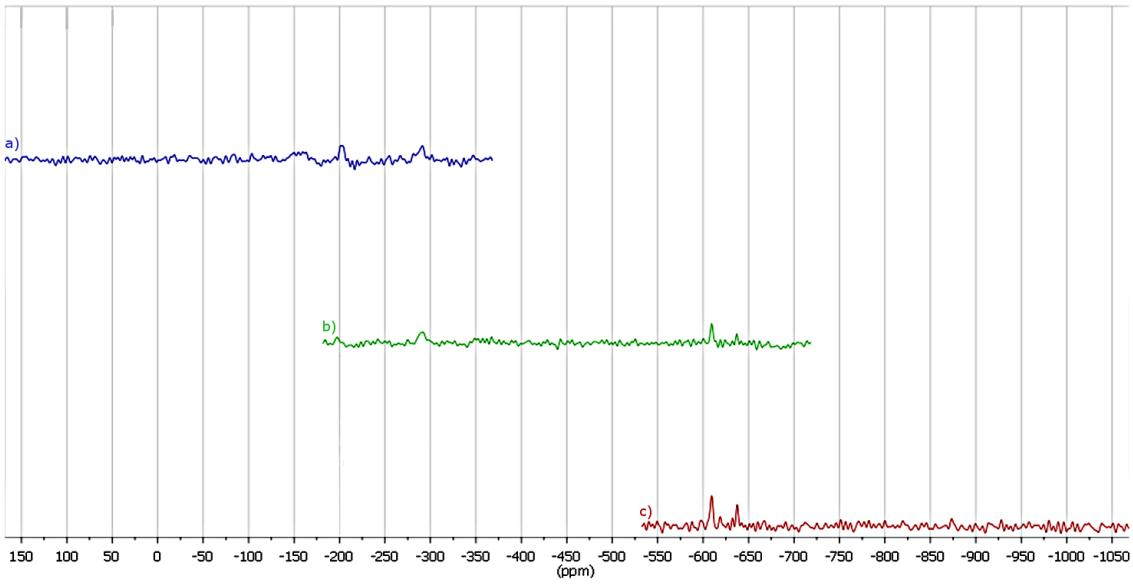


**Figure 3.15** Three separate six-hour $^{119}Sn$ NMR scans of $PtCl_4$:$SnCl_2$ 1:4 solution in THF.

From the previous exploratory scans, possible Sn complex or halide peaks were identified in the

region of -550 to 0 ppm. The very weak signals seen in Figure 3.15a and 3.15b fall in the expected region for Sn bonded to Pt. The sharper peaks further upfield (towards more negative ppm values) did not fit in this range and therefore were ignored for the following scan. In order to increase the signal-to-noise ratio, a subsequent experiment was conducted overnight. Figure 3.16 is the resulting $^{119}$Sn NMR trace.

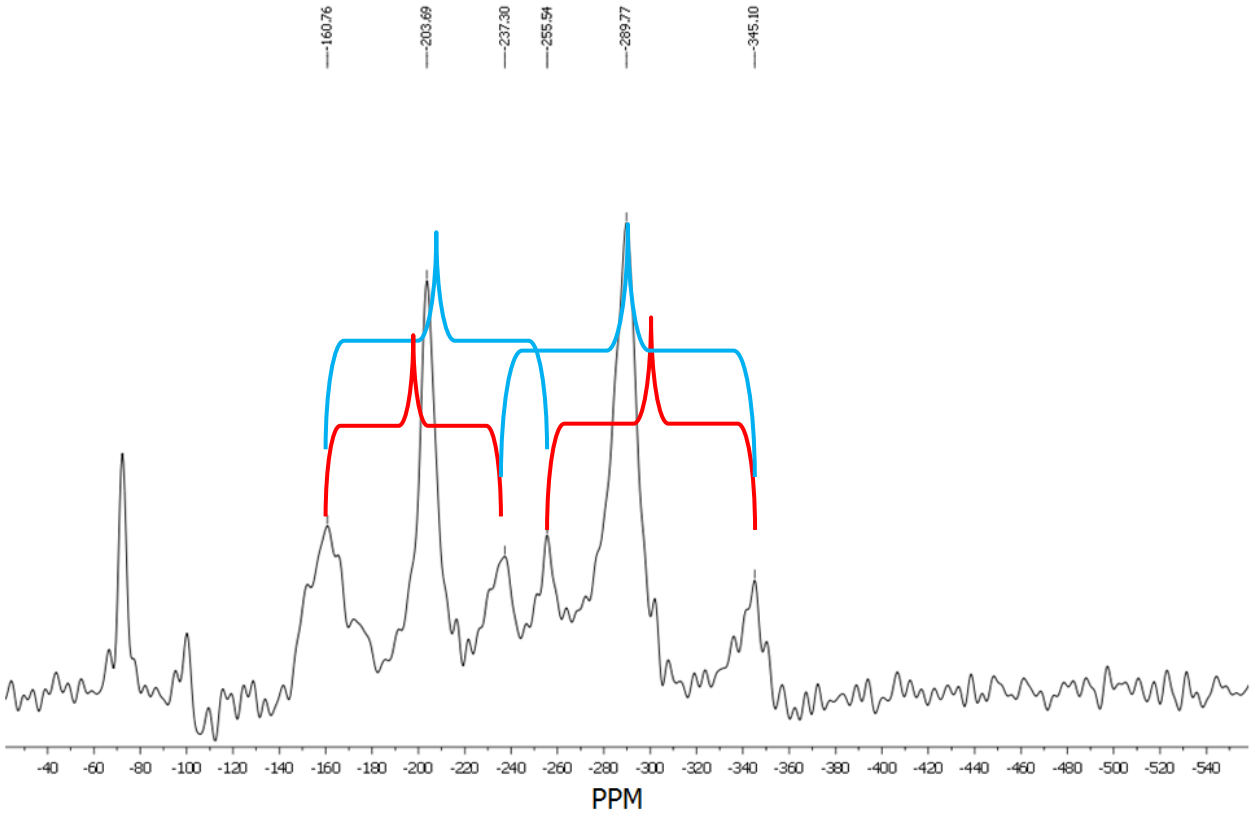


**Figure 3.16** Overnight $^{119}$Sn NMR of $PtCl_4$:$SnCl_2$ 1:4 solution in THF. Red and blue lines signify the two possible J-coupling groupings.

Fortunately, the presence of coupling peaks (most likely, but unproven to be, the result of Pt-Sn bonding) was confirmed by this overnight scan. Unfortunately, the resolution of these peaks is insufficient to identify the specific Pt-Sn complex(es) in solution. The uncertainty in the

chemical shifts of the side peaks results in the two possible groupings seen Figure 3.16. The two red lines represent one possible scenario, and the two blue lines represent another unique configuration. It is impossible to tell from this data which is correct.

Additionally, after this overnight scan, the NMR tube was removed from the instrument and a layer of brown precipitate was seen on the bottom and interior walls. It seems likely that $Pt^{IV}$ was being reduced to the neutral metal by $Sn^{II}$ after an extended period of time left in solution. The reduction potentials of these elements show that this is thermodynamically favorable. This means that longer experiments are out of the question to increase the signal-to-noise. Since this solution is already operating at near the solubility limit of these precursors in THF, that essentially gives us nowhere left to go in order to improve the resolution on these scans.

Therefore it is impossible to determine the identity of the complex from $^{119}$Sn NMR. While it could be useful as a fingerprint, the best case scenario from more $^{119}$Sn NMR experiments of different ratios of Pt and Sn precursors would be to further confirm the presence of Pt-Sn complexes. That seems redundant given the other evidence, but nonetheless the method was interesting enough to warrant inclusion here, if for no other reason than as a road marker describing the path taken in our attempts to identify the pre-reduction complexes of platinum and tin.

REFERENCES

(1) Nelson, J. H.; Wilson, W. L.; Cary, L. W.; Alcock, N. W.; Clase, H. J.; Jas, G. S.; Ramsey-Tassin, L.; Kenney, J. W. *Inorg. Chem.* **1996**, *35*, 883–892.
(2) Tarozaitė, R.; Tamašauskaitė Tamašiūnaitė, L.; Jasulaitienė, V. *J. Solid State Electrochem.* **2008**, *13*, 721–731.
(3) Starzewski, K. A. O.; Pregosin, P. S. In *Catalytic Aspects of Metal Phosphine Complexes*; Alyea, E. C.; Meek, D. W., Eds.; AMERICAN CHEMICAL SOCIETY: WASHINGTON, D. C., 1982; Vol. 196, pp. 23–41.
(4) Kesanli, B.; Fettinger, J.; Gardner, D. R.; Eichhorn, B. *J. Am. Chem. Soc.* **2002**, *124*, 4779–4786.